



UNIVERSITÀ
DEGLI STUDI
FIRENZE

PhD in
Physics and Astronomy

CYCLE XXXVI

COORDINATOR Prof. Giovanni Modugno

Can a superfluid be solid? A study of the supersolid
phase in a dipolar quantum gas

Academic Discipline (SSD) FIS/03

Doctoral Candidate

Dr. Giulio Biagioni

Giulio Biagioni

Supervisor

Prof. Giovanni Modugno

Modugno

Coordinator

Prof. Giovanni Modugno

Modugno

The consultation of the thesis is free. Unless a specific authorization is obtained from the author, the thesis can be, however, downloaded and printed only for strictly personal purposes related to study, research and teaching, with the explicit exclusion of any use that has – even indirectly – a commercial nature.

Giulio Biagioni

Can a solid be superfluid?

A study of the supersolid phase in a dipolar quantum gas

PhD thesis, University of Florence. October 2023.

giulio.biagioni@unifi.it

*There is no science without fancy,
and no art without facts.
Non c'è scienza senza immaginazione,
nè arte senza fatti.*

V. Nabokov

Ringraziamenti

Sono trascorsi all'incirca quattro anni da quando ho messo piede per la prima volta nel laboratorio disprosio a Pisa. Da quel giorno, penso di essere cresciuto molto, sia da un punto di vista scientifico che personale. Ho imparato che, probabilmente molto più che in altre attività, nella ricerca si alternano momenti di improvviso entusiasmo, slancio positivo verso obiettivi futuri e fiducia nei propri mezzi, a momenti di scoraggiamento, quando sembra che tutto congiuri contro di te e pensi di non farcela.

I miei ringraziamenti vanno in primo luogo al gruppo con il quale ho condiviso, ancora prima dei risultati scientifici, questo caleidoscopio di emozioni. Nicolò, il mio compagno nell'avventura del dottorato, senza il quale questi quattro anni sarebbero stati molto più solitari. Luca e Carlo, guide sicure nel laboratorio da cui ho imparato tanto. Andrea, che mi ha coinvolto in divertenti attività di divulgazione. Niccolò, che si è rivolto a me per la prima volta per cercare risposte, anziché per rispondere a mie domande. Non so se ha imparato della fisica da me, ma sicuramente ha assistito a delle belle partite di basket. Ci tengo anche a ringraziare Marco, con il quale sono stato felice di avere condiviso una parte del dottorato, sia in attività di ricerca che di insegnamento.

Infine un grazie speciale a Giovanni, la mia guida durante il dottorato. Se quattro anni fa ero un buono studente di fisica e ora sono un buon fisico, è merito tuo.

Non c'è bisogno di sottolineare che, senza di voi, non avrei potuto scrivere questa tesi.

Un ringraziamento a parte va ai miei angeli custodi a Pisa: Chicca e Sandra, senza il vostro calore, entusiasmo e affetto, questi anni non sarebbero stati gli stessi.

Contents

Introduction	v
List of publications	x
1 The supersolid phase of matter	1
1.1 Superfluidity and supersolidity: first proposals and experiments	1
The search in solid helium	5
1.2 Supersolidity in dipolar quantum gases	6
Dipole-dipole interaction	7
Dipolar BECs and roton instability	8
Beyond mean-field stabilization and quantum droplets	11
The supersolid phase	13
1.3 Spontaneously modulated superfluid phases in recent experiments	18
2 Experimental realization and detection of a dipolar supersolid	27
2.1 Cooling and trapping Dy	27
Tuning the interactions	29
2.2 Characterization of the supersolid phase: time of flight imaging	32
2.3 Characterization of the supersolid phase: in situ imaging	36
Test of the imaging system	36
Phase-contrast imaging	38
In situ imaging of the supersolid phase	40
3 The superfluid-supersolid quantum phase transition	45
3.1 Landau theory for the superfluid-supersolid transition	47
3.2 Phase diagram from ground-state simulations	52
3.3 Experimental evidence of continuous and discontinuous phase transitions	56
Excitation of collective modes	59
Fluctuations and Landau energy	64
4 Supersolidity and rotations	69
4.1 Leggett model for a rotating supersolid	70
4.2 The scissors mode	74
4.3 Moment of inertia of the supersolid	77
4.4 Discussion about the superfluid fraction	82

5	Sub-unity superfluid fraction from self-induced Josephson effect	87
5.1	Superfluid fraction and Josephson oscillations	88
5.2	Excitation of Josephson oscillations: phase imprinting	91
5.3	Detection of Josephson oscillations: phase and imbalance	94
5.4	The supersolid as an array of Josephson junctions: a model	101
5.5	Sub-unity superfluid fraction	105
5.6	A self-induced Josephson junction: the Goldstone mode	109
6	Towards a supersolid in a ring	113
6.1	Optical scheme for a ring-shaped potential	115
	The DMD	116
	Optical trap and imaging	118
6.2	A laser source at 404 nm for repulsive optical potentials	119
6.3	Dysprosium polarizability at 404 nm	123
6.4	Persistent currents in the ring: preliminary numerical studies	127
	Outlook	133
	Bibliography	135

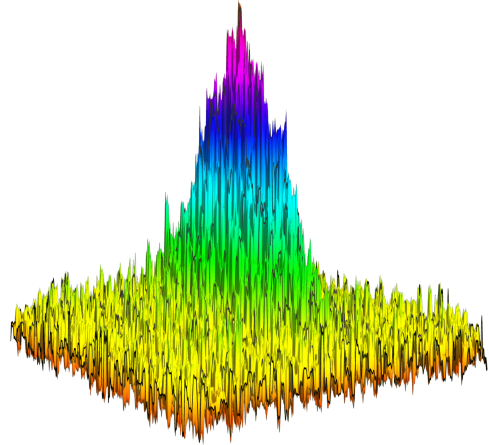
Introduction

”Can a solid be superfluid?” This question is the title of a famous 1970 paper from the Nobel laureate A. J. Leggett, in which he proposed some of the first ideas related to the possible existence of a supersolid phase of matter [1]. Superfluidity was well established at the time, both theoretically and experimentally, thanks to the successful pioneering investigations of liquid helium at low temperatures. A superfluid, as the word itself says, is a state of matter somewhat related to fluids but with extraordinary properties: the possibility of moving without friction, rotating without inertia, and sustaining quantized vortices are some of them [2, 3]. The tantalizing question that started to be discussed in some papers around 1970 (by Gross [4], Chester [5], Andreev and Lifshitz [6]), and that is so efficiently condensed in the title of Leggett’s paper, is whether it is possible to extract the concept of superfluidity from its native environment of liquid helium, from which it bears its name, and investigate the emergence of superfluidity in another state of matter, namely a solid. At first glance, this idea seems highly doubtful: a solid, for definition, is a piece of matter that can resist shear stress, contrary to liquids, while a superfluid can flow without friction, like an ideal fluid. The two phases seem incompatible. However, since the first proposals it appeared that it is possible to conceive the coexistence of superfluidity and a crystal structure in the same phase of matter: the supersolid.

Similar to superfluidity, it is very hard to give a satisfying and general definition of supersolidity able to capture all the subtle phenomenology related to the merging of solid and superfluid natures, regardless of the actual physical system in which such a phase could emerge. A possible route is to follow a classification of the phases of matter based on the kind of order that they bring along and the broken symmetries for which they are responsible [7]. In a crystalline solid, atoms or molecules are arranged in periodic structures, breaking the translational invariance of space. Macroscopic consequences of the broken symmetry are the aforementioned resistance to shear stress, or the diffraction pattern of light scattered from the crystal. In equations, the emerging spatial order in a solid can be written as

$$\rho(\mathbf{r}) = \rho(\mathbf{r} + \mathbf{a}),$$

where $\rho(\mathbf{r})$ is the density at position \mathbf{r} and \mathbf{a} is a lattice vector. This periodicity condition, absent in liquids for which the density is uniform, expresses the long-range order of a crystalline solid. A different kind of order exists in the superfluid phase, related to its quantum-mechanical nature: each particle inside the superfluid loses its individuality and takes part in a global wavefunction, which determines the collective properties of the system. All the particles are undistinguishable and are delocalized over the whole system.



Can a superfluid be solid, or can a solid be superfluid ?

Since the wavefunction is a complex quantity, the broken symmetry is related to its global phase, the so-called $U(1)$ symmetry. Again, we can condense the superfluid order in one equation employing the one-particle density matrix $n(s)$:

$$\lim_{s \rightarrow \infty} n(s) = n_c,$$

where $s = |\mathbf{r} - \mathbf{r}'|$ is the distance between two points and n_c is a finite value, the condensed fraction [3]. This equation means that the quantum mechanical amplitude between two states in which a particle is removed at position \mathbf{r} or in a different, far apart, position \mathbf{r}' , is larger than zero. It expresses, therefore, the essence of the superfluid order, also called off-diagonal long-range order, related to the delocalization of the single particle over the whole system. The supersolid is a phase in which the crystalline and superfluid order coexist, meaning that the particles are delocalized but also arrange in a crystal structure. Note that both orders must be spontaneous, meaning that they cannot be induced and fixed externally. Possessing both superfluid and crystalline properties doesn't mean that the supersolid is simply a sum of the two because the two orders influence each other and give rise to novel phenomena, some of them I investigate in this thesis: the anomalous rotational properties, the self-induced Josephson effect and partially-quantized persistent currents.

A possible route to supersolidity consists of searching for superfluid behavior in a crystal at low temperatures. The natural candidate, bringing in mind the history of superfluidity, was the solid phase of helium. Solid helium was also the reference system for the first theoretical proposals of supersolids, and indeed the question asked by Leggett is if a solid (like helium) can also be superfluid. The research in solid helium has been very rich for many years but without a demonstration of supersolidity [8]. On the other hand, quantum gases at ultralow temperatures offer an alternative route to supersolidity. Bose-Einstein condensates (BECs) in dilute quantum gases are a superfluid phase that

can be controlled and manipulated both experimentally and theoretically with a high tunability, and offer an extraordinary platform to study condensed matter problems that can be very complicated in real materials, such as solid helium. Regarding the search for supersolidity, the original Leggett's question is reversed: now we wonder if a superfluid, a BEC for example, can develop a crystal structure and become a solid.

Then, the question changes to "Can a superfluid be solid?" In the last few years, the answer has become positive. The spontaneous crystallization of a BEC requires a combination of different factors: an attractive contribution to the interatomic interactions, which induces an instability for some wavevector k ; a repulsive interaction strong enough to arrest the instability and ensure a new equilibrium configuration at higher densities; the possibility for atoms in different lattice sites to interact, hence a long-range nature of the interactions typically absent in the usual contact-like interactions characterizing dilute ultracold atoms. Remarkably, all these ingredients are naturally present, without any need to be externally engineered, in dipolar quantum gases. The dipolar interaction is long-range, has an attractive component, and creates the conditions for the repulsive zero-energy of quantum fluctuations, usually negligible, to play the role of the stabilizing mechanism. The crystallization of dipolar BECs has been demonstrated by realizing lattices made up of self-bound droplets [9]. However, a crucial ingredient was lacking: the different clusters forming the lattice must preserve global phase coherence to allow a superfluid flow across the whole system. Otherwise, the droplets are independent superfluids, each with its own phase. In 2019, the Pisa-Florence group discovered an experimental region of parameters in which the crystal structure coexists with global phase coherence, a hallmark of supersolidity [10]. The results were promptly confirmed by the Stuttgart [11] and Innsbruck groups [12]. Supersolid phases have been observed also in other BEC-based platforms: BECs coupled to optical cavities [13] and BEC with spin-orbit coupling [14].

This thesis contains the research work I carried out in the Pisa-Florence group after the discovery of the supersolid phase. Of course, many fundamental questions about supersolids are still open and are the subject of debate in the scientific community, which I think is a signal of the exciting activity inside the heterogeneous and growing field of supersolidity. For this reason, I often complement the published results which are the main corpus of my thesis with outlook and perspectives for future research.

One could naturally think about the supersolid-related research conducted in the field of quantum gases as a remarkable example of the general quantum simulation program: simulating in a clean and controllable environment phenomena that occur in condensed matter physics, but that are hard to study in real-world materials due to their complexity. However, in the case of the supersolid, we are in front of something that is beyond standard quantum simulation. Indeed, we are studying a phase of matter that has been predicted to exist in condensed matter systems, but has never been observed in them. This situation is very different from, for example, the discoveries about superfluidity realized with atomic BECs, for which the observation of quantized vortices, persistent currents, or the Josephson effects, apart from their scientific importance, has always been an extension or a confirmation of analog phenomena observed in liquid helium or in superconductors.

For what concern the supersolid phase, we are at the same time simulating a physics that could exist also in real-world materials and realizing for the first time that kind of physics. That being said, the general aim of quantum simulation has still driven the research performed during my PhD. Recently, superfluid phases with a spontaneous spatial modulation have been observed in a variety of different systems, ranging from the aforementioned BEC systems to ^3He superfluids, from 2D crystal layers of ^4He to exotic pair density waves in superconductors. Nevertheless, connections with the supersolid phase are not always straightforward or haven't been clarified so far. I hope that the research conducted with the dipolar supersolid, which is the first system for which a large and diverse amount of evidence about supersolid behavior has been accumulated, can be stimulating and helpful for all the other systems. For this reason, chapter 1 of my thesis is a long and general introduction to the supersolid phase, where I dwell on the dipolar physics because it concerns the experimental system I studied, but I also discuss some recent results related to supersolidity in other systems.

Regarding the scientific results that I obtained during the PhD, I decided to follow a logical rather than chronological order. In chapter 2 I introduce the experimental system, the main tools to control the supersolid phase, and the techniques employed to get relevant information. I present the first original research results in chapter 3, which deals with the character of the quantum phase transition from the superfluid to the supersolid [15]. With a joint theoretical and experimental collaboration, we find a crossover from discontinuous to continuous phase transitions, which can be tuned with the atom number and the trap geometry. We give a dimensional explanation of the crossover: if the crystal structure develops in 2D, the transition is discontinuous, otherwise it is continuous. The ability to change experimentally the nature of the phase transition is a key tool to control the excitations and the formation process of the supersolid. From a fundamental point of view, the different kinds of phase transitions open up the possibility of exploring general mechanisms related to statistical physics in the supersolid phase [16, 17].

The central topic of the second half of the thesis is the concept of superfluid fraction. Broadly speaking, the superfluid fraction is the fraction of the system that has a superfluid-like response to external probes, like momentum or rotational kicks [18]. Usually, the superfluid fraction is discussed in terms of a two-fluid model, in which the system is split into two components: the superfluid and the normal part. The latter is populated by thermal excitations and becomes negligible lowering the temperature [3, 2]. The superfluid fraction f_s then becomes unity at $T = 0$, because the whole system is superfluid. As pointed out by Leggett [1], this is not true for the supersolid. The density modulation competes with superfluidity and lowers the superfluid response even at $T = 0$. Therefore, the supersolid has the exotic property of having $f_s < 1$ even at zero temperature. The sub-unity superfluid fraction doesn't rely on a two-fluid model (there is no normal part) and arises genuinely from the double nature of the supersolid. To investigate experimentally the superfluid fraction of the dipolar supersolid, together with my group we realized a rotational experiment, described in chapter 4, following the original proposal by Leggett and the experimental works performed with solid helium [8]. Despite the small size of our supersolid and its inhomogeneity, we were able to measure its moment of inertia and demonstrate that it is lower than the classical value, which was the first direct signature of

the superfluid response of a supersolid [19]. We could estimate a large superfluid fraction, compatible with 1, which arises from the cluster nature of the dipolar supersolid. However, the geometry of the system and the experimental technique employed didn't allow for a quantitative measurement of f_s . This project has an overlap with my master thesis [20], but I spent a large portion of my PhD finishing the paper and discussing its results (see [21] for an original presentation of Leggett's model and its relationship with our paper). We then designed a different kind of experiment intending to detect a sub-unity f_s , described in chapter 5. Instead of relying on rotations, for which our elongated geometry is not suitable, we focused on the transport of mass from one cluster to the other, which is directly sensitive to the superfluid flow across the weak link spontaneously induced by the crystal structure. Under appropriate conditions, this mass transport takes the form of Josephson oscillations between neighboring clusters. In our work, we point out the formal equivalence between the superfluid fraction defined in the context of rotations and in the Josephson effect, and we demonstrate experimentally that the supersolid, despite the absence of an external barrier, can display Josephson oscillations [22]. The dipolar supersolid is therefore the first example of a self-induced Josephson junction, in which the same atoms that take part in the superfluid flow are also responsible of the junction structure. From the observed Josephson oscillations, we finally deduce the decreasing f_s in the supersolid regime, which can be tuned from 1 to about 0.1, and represents the first observation of a sub-unity superfluid fraction in a supersolid.

The last chapter 6 deals with an ongoing project that occupied the last months of my PhD. The goal is to realize a supersolid in a ring geometry, that has the advantage of being a closed geometry with no finite-size effects. I describe the experimental progress to create a repulsive optical potential for dysprosium atoms with a ring shape and some outlook for future research directions. Again, a part of the discussion is focused on the superfluid fraction, which plays a fundamental role in the exotic behavior of the supersolid persistent currents in a ring.

Although most of the work reported in this thesis is experimental, I usually complement experimental results with simple numerical simulations or analytical models, which, I think, greatly help in getting an intuition about the fundamental aspects of the physics observed in the experiment. The relative easiness in the modeling of the dipolar supersolid reflects one of the most beautiful aspects of the research in this field: it is possible to investigate fundamental questions about the nature of an exotic quantum phase of matter in a relatively simple environment, a scenario probably unconceivable in other condensed matter systems.

List of publications

The research described in this thesis has been published in the following papers:

- Luca Tanzi, Julian G. Maloberti, Giulio Biagioni, Andrea Fioretti, Carlo Gabbanini, and Giovanni Modugno, Evidence of superfluidity in a dipolar supersolid from nonclassical rotational inertia. *Science*, **371**, 634 (2021).
- Giulio Biagioni, Evidence of superfluidity in a dipolar supersolid. *Il Nuovo Cimento C*, **44** (2021).
- Giulio Biagioni, Nicolò Antolini, Aitor Alaña, Michele Modugno, Andrea Fioretti, Carlo Gabbanini, Luca Tanzi and Giovanni Modugno, Dimensional crossover in the superfluid-supersolid quantum phase transition. *Phys. Rev. X*, **12**, 021019 (2022).
- Aitor Alaña, Nicolò Antolini, Giulio Biagioni, Iñigo L. Egusquiza, and Michele Modugno, Crossing the superfluid-supersolid transition of an elongated dipolar condensate. *Phys. Rev. A*, **106**, 043313 (2022).
- Giulio Biagioni, Nicolò Antolini, Beatrice Donelli, Luca Pezzé, Augusto Smerzi, Marco Fattori, Andrea Fioretti, Carlo Gabbanini, Massimo Inguscio, Luca Tanzi and Giovanni Modugno, Sub-unity superfluid fraction of a supersolid from self-induced Josephson effect. Submitted to *Nature* (2023). Preprint: [arxiv](#)
- Niccolò Preti, Nicolò Antolini, Giulio Biagioni, Andrea Fioretti, Giovanni Modugno, Luca Tanzi and Carlo Gabbanini, Blue light repulsive potentials for dysprosium atoms, in preparation (2023).

The supersolid phase of matter

In this introductory chapter, we give a global overview of state-of-the-art research on supersolids. We start with a general description of the supersolid phase, based on the original proposals of more than 50 years ago, and we highlight the differences with standard superfluids. We then briefly describe the research in bulk solid helium, the first experimental platform where supersolid physics has been investigated. In section 1.2, we review the basic features of dipolar physics and we describe the dipolar supersolid, the topic of this thesis. In section 1.3, we propose a list of recently discovered superfluids with some kind of spontaneous spatial modulation, which have been demonstrated to be supersolid, in some cases, or for which there are indications of possible connections with supersolidity, in others. Differences and similarities with the dipolar supersolid are also traced.

1.1 Superfluidity and supersolidity: first proposals and experiments

Quantum mechanics strongly affects the properties of matter at low temperatures. The most notable example is probably the liquid-superfluid transition which was first discovered by Kapitza [23] and Missner and Allen [24] in 1938 by cooling liquid ^4He below 2.17 K. In the superfluid state, helium atoms can flow without friction and show spectacular phenomena on a macroscopic scale, such as persistent currents or the fountain effect. The analog of superfluidity with charged particles, superconductivity, was discovered by Onnes in 1911, cooling down mercury. In superconductors, the frictionless flow of electrons is an electrical current running with zero resistance, whose comprehension led to enormous developments both in fundamental physics and technological applications. The history of superfluidity and superconductivity is so rich that it can be schematically summarized with a list of Nobel prizes. In addition to the cited Onnes and Kapitsa (Nobel prizes in 1913 and 1978, respectively), Bardeen, Cooper and Schrieffer were awarded the 1972 Nobel prize for the development of the BCS theory, which explains the onset of superconducting order through the condensation of loosely bound electron pairs, the Cooper pairs. Superfluidity of fermionic neutral particles, on the other side, was discovered by Osheroff, Gully, Richardson and Lee in 1973 in liquid ^3He (Nobel prize in 1996), at temperatures three orders of magnitude lower than that of the bosonic isotope ^4He . The exotic superfluid phase of ^3He , in which Cooper pairs have a non-trivial internal structure, has been extensively studied in the following years, leading to the 2002 Nobel prize to

A.J. Leggett (together with Abrikosov and Ginzburg, for their theoretical results about superconductivity), a scientist who gave also great contributions to the first ideas about supersolids and that will be extensively cited throughout this thesis. In the 90s, the development of techniques to cool down and trap gaseous samples of atoms to the nK regime opened the door to the field of quantum gases, in which Bose-Einstein condensates (BECs) have been explored as an ideal platform where to study superfluidity (see the Nobel prizes to Chu, Cohen-Tannoudji and Phillips in 1996 and to Cornell, Ketterle and Wieman in 2001). In fermionic ultracold gases, it is even possible to tune the superfluid order from the BEC type to the BCS type, across the famous BEC-BCS crossover [?].

Theoretically, superfluidity can be defined as a generalization of Bose-Einstein condensation [3]. In the superfluid phase, a macroscopic number of particles occupy a single state, described by the wave function $\psi_0(\mathbf{r}, t)$, while all other states are occupied by a number of particles of order 1. While in a classical fluid inter-particle interactions lead to scattering between particles and to a non-zero viscosity, the superfluid is composed of indistinguishable particles that behave as a single matter wave, moving coherently without friction. The number of particles in the condensate N_0 is less than the total number of particles N , due to the thermal population of excited states. Even at zero temperature, $N_0 < N$, and $(N - N_0)/N$, called quantum depletion, is the fraction of atoms scattered off from the condensate state due to interactions. In superfluid helium, which is a strongly interacting system, the condensate population is only 10 % of the total particles, while in dilute ultracold atom gases the condensate fraction can be near to 100 %. The superfluid dynamics is described by the hydrodynamic equations of a fluid with zero viscosity. The degrees of freedom of the superfluid are reduced compared to those of a classical fluid, and are encoded in the condensate wave function $\psi_0(\mathbf{r}, t) = \sqrt{n_c(\mathbf{r}, t)}e^{i\varphi(\mathbf{r}, t)}$, where $n_c(\mathbf{r}, t) = |\psi_0(\mathbf{r}, t)|^2$ is the condensate number density and $\varphi(\mathbf{r}, t)$ is the phase of the condensate. Crossing the liquid-superfluid transition, the condensate gets populated and a global phase φ is randomly chosen, spontaneously breaking the continuous $U(1)$ symmetry. The phase of the wave function sets the velocity of the superfluid through the relation

$$v_s(\mathbf{r}, t) = \frac{\hbar}{m} \nabla \varphi(\mathbf{r}, t), \quad (1.1)$$

with m the particle mass. Since it is the gradient of the phase, the superfluid velocity is always irrotational, $\nabla \wedge v_s = 0$. Eq. 1.1 lies at the heart of numerous dynamical phenomena peculiar to superfluids, such as the reduction of the moment of inertia, persistent currents, quantized vortices and the Josephson effect. I will discuss many of these phenomena and their generalization to the supersolid case in this thesis.

It is interesting to note how, in the case of superfluidity, experimental observations triggered the development of new ground-breaking theories, while in the case of supersolidity theoretical proposals brought forward by many years the first experimental results. The ideas that came out around 1970 have all in common the same general question: is it possible to have a superfluid state, with for example a coherent flow of mass, in a

solid, where atoms are localized in the sites of the crystal? Such a system would break simultaneously two continuous symmetries, the $U(1)$ symmetry of superfluids and the spatial translational symmetry of solids. The result is the so-called supersolid phase of matter, which is not fully superfluid nor fully solid, but the properties of the two phases mix together and give rise to new, exotic phenomena. One can imagine two possible routes for the formation of a supersolid phase. First, one could start from a classical solid and search for some kind of Bose-Einstein condensation of its constituent that preserves the crystal structure, while the wave function delocalizes over the whole crystal. This is the line of reasoning of the famous proposal by Andreev and Lifschitz [6] in 1969 (see also the work by Chester [5]), who considered a quantum crystal made of bosons in which, at low temperatures, the atoms arrange themselves in such a way to leave a small number of vacancies, i.e. empty sites. In other words, the number of atoms should be different from the number of sites. Such vacancies would obey Bose-Einstein statistics and at low temperatures could condense, realizing the supersolid phase. The other approach is to start from a fully superfluid system, described by a wavefunction with constant density $n_c = N/V$, with N the atom number and V the volume occupied by the superfluid. In 1957, Gross [4] pointed out that, depending on the shape of the inter-atomic interactions, there may be states with a periodic density modulation whose energy is lower than the uniform state, breaking the translational symmetry. The two different routes to supersolidity are sketched in Fig. 1.1. With a bit of over-simplification, we could say that the experiments about supersolids in the field of condensed matter physics naturally deal with the vacancy supersolid of Andreev and Lifschitz, while in the field of ultracold atoms, the starting point is usually a fully superfluid BEC, realizing the scenario proposed by Gross. Note that, while in the vacancy supersolid each lattice site is occupied by one atom, in the other case the 'lattice site' is a region of higher densities in the macroscopic wavefunction, which could be occupied by a huge number of atoms. In this case we talk about a cluster supersolid, which is what happens in dipolar BECs.

Another seminal work about supersolids came out in 1970, by A.J. Leggett [1]. Differently from the others, Leggett didn't investigate possible mechanisms for the supersolid formation, but made some crucial predictions about differences between standard superfluids and supersolids. Leggett considered a system in a ring geometry, with the container rotating at a small angular velocity. In this configuration, a superfluid can acquire angular momentum from the container only through the formation of quantized vortices, due to the irrotational condition $\nabla \wedge v_s = 0$. At low enough angular velocities, the formation of vortices is not energetically favorable and the superfluid doesn't move. The result is that a superfluid in a ring geometry has a moment of inertia equal to zero, $I = 0$. On the other hand, in the supersolid phase, the lattice sites with higher densities start moving quasi-classically, following the container, while the superfluid background moves in the opposite direction to preserve the irrotational motion. The moment of inertia increases compared to that of a superfluid, while staying below that of a classical solid. In equations

$$I = (1 - f_s)I_c, \quad (1.2)$$

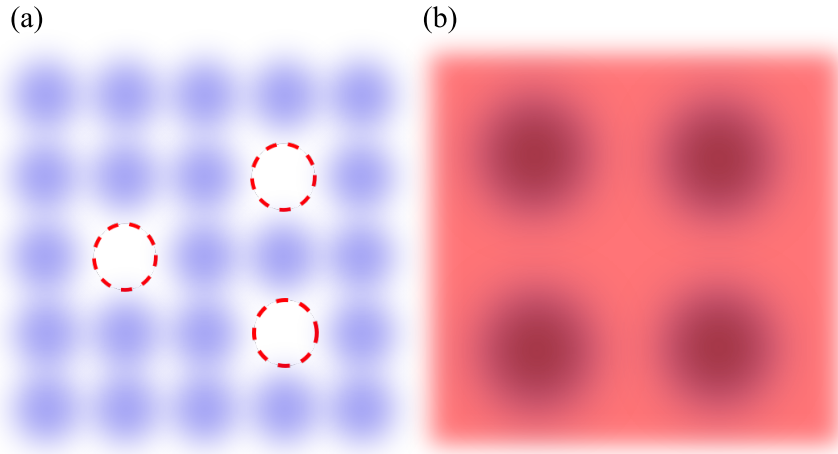


Figure 1.1: Seminal proposals of a supersolid phase. a) In the Andreev-Lifschitz scenario [6], a quantum crystal is supposed to spontaneously host vacancies even at zero temperature, indicated as dashed red lines. If the gas of vacancies becomes a Bose-Einstein condensate, superfluidity coexists with the crystal structure. b) In the proposal by Gross [4], a superfluid described by a wave function ψ_0 , indicated as a red homogeneous square, is supposed to spontaneously break the translational invariance forming regions of higher densities embedded in a superfluid background.

where I_c is the classical moment of inertia and f_s is the so-called superfluid fraction, which interpolates between the full superfluid, $f_s = 1$ and $I = 0$, and the classical solid, $f_s = 0$ and $I = I_c$. In Leggett's model, the upper bound to the superfluid fraction is

$$f_s \leq \left(\frac{1}{d} \int_{\text{cell}} \frac{dx}{\bar{n}(x)} \right)^{-1} \quad (1.3)$$

with $\bar{n}(x)$ is the normalized number density on the ring and the integral is performed on a unit cell with dimension d . Remarkably, as it is clear from the upper bound in Eq. 1.3, the sub-unity superfluid fraction of the supersolid comes only from the broken translational symmetry ($\bar{n}(x)$ is not a constant), and not from other effects, such as the population of thermal excitations. Leggett's model points out a quantitative difference between a standard superfluid and a supersolid, allowing experimentalists to search for a transition to a supersolid state. Either one searches for a drop in the moment of inertia, if the starting point is a classical solid as solid ^4He , or one searches for an increase in the moment of inertia, if the starting point is a superfluid such as a BEC, as in our dipolar quantum gas. The concept of superfluid fraction and Leggett's upper bound are central to this thesis. We will show in chapter 4 our measurement of the moment of inertia of the dipolar supersolids through rotations [19], and in chapter 5 another experiment where we introduce a novel technique to measure the superfluid fraction, based on the Josephson effect [22]. I also studied in detail Leggett's model and conceived an original interpretation [21], discussed in chapter 4. Finally, chapter 6 presents an outlook for future applications of Leggett's model in the original ring geometry.

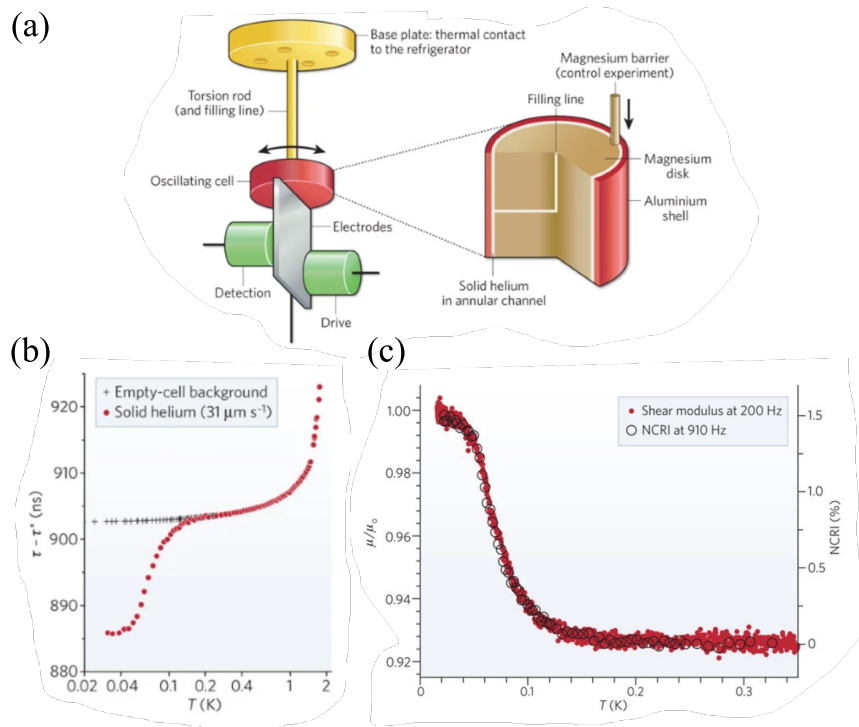


Figure 1.2: Experiments on solid helium, from [8]. (a) The torsional oscillator in Kim and Chan's experiments [25, 26] is composed of a torsion rod and an oscillating cell. Helium is introduced in the cell through a filling line and then occupies an annular channel. Electrodes are used to drive and detect the oscillation of the cell. (b) Period drop at about 0.1 K, compared with the measurement effectuated with the empty cell where no drop is detected. (c) Temperature dependence of the Non-Classical Inertia Fraction measured in the torsional oscillator experiments (empty circles) and the shear modulus variation (red circles), measured in [27].

The search in solid helium

Solid helium has been the first system to be experimentally investigated searching for a supersolid phase. Superfluidity, indeed, has been synonymous with helium for many years, since no other superfluid system was known. The first theoretical proposals of supersolidity were all about solid helium. Moreover, solid helium is the prototype of a quantum crystal. First, the light mass of helium atoms enhances quantum fluctuations around their equilibrium positions, whose kinetic energy is of the order $\hbar^2/(2m\Delta x^2)$, with Δx the quantum indetermination on the position of the helium atom. Second, the weak inter-particle interactions allow for a large overlap between the wavefunctions of different atoms, facilitating superfluid effects across different sites.

The first claim of the discovery of a supersolid phase in solid helium was made in 2004, in two papers by Kim and Chan [25, 26]. Their experimental approach to supersolidity was very close to Leggett's idea: the authors searched for anomalous behavior of the moment of inertia while lowering the temperature. The experimental set-up was a torsional oscillator, in which a cylindrical cell containing solid helium in an annular channel was suspended on

a torsion rod (see Fig. 1.1). At resonance, the period τ of the oscillator is given by

$$\tau = 2\pi\sqrt{\frac{I}{K}}, \quad (1.4)$$

where I is the moment of inertia of the whole system and K is the torsional spring constant.

Remarkably, they found a drop in the oscillation period below about 0.1 K, as depicted in Fig. 1.1(b). The measurements were consistent with the hypothesis of the formation of a supersolid, whose superfluid component should have stopped participating in the rotation, lowering the total moment of inertia I in Eq. 1.4. The authors found that the fraction of the mass that decoupled from the oscillation, which they called Non-Classical Rotational Inertia Fraction (NCRIF) and is related to the superfluid fraction f_s , was very small, of the order of 0.01. The same experiment was repeated with a sample of ^3He , and also with ^4He with different concentrations of ^3He , showing that the period drop was observable only if the concentration of ^3He was under a certain value, confirming that the phenomenon originated from the bosonic nature of the atoms.

A great effort, both theoretical and experimental, was made to understand the data and perform new experiments. For a review, see [28]. In 2007 it was discovered that solid helium has unexpected elastic properties at low temperatures [27]. Its shear modulus, which measures the resistance to transverse forces, increases exactly in the range of temperatures in which the rotational signal was observed, suggesting that most of the experiments could be explained in terms of changes of the elastic constant K , when the filling line containing helium passed also through the torsional rod, or in terms of a frequency-dependent moment of inertia, whose effects are different depending on the geometry of the cell. The change in shear modulus not only explained the temperature dependence of the observed signals, see Fig. 1.1 (c), but also the dependence on ^3He impurity, with a model based on the displacement of dislocations, which have effects in the elastic properties of the solid. The original experiment by Kim and Chan was repeated with a new apparatus designed to minimize the effect of the shear modulus anomaly, and indeed no period drop was found [29]. So far, there is no conclusive evidence of a supersolid region in the phase diagram of bulk solid helium.

1.2 Supersolidity in dipolar quantum gases

In this section, we give an introduction to dipolar quantum gases, the experimental system studied in this thesis. After a brief description of the dipolar interaction and the physics of dipolar BECs, we focus on the roton instability and the supersolid phase, whose characteristics are briefly outlined. Chapter 2 contains a more detailed description of the experimental realization of the dipolar supersolid, as well as its experimental characterization. For reviews about dipolar quantum gases and magnetic atoms, see [30, 31].

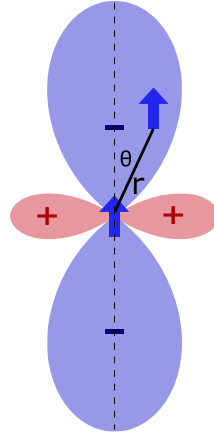


Figure 1.3: Anisotropy of the dipole-dipole interaction in Eq. 1.5. Two dipoles polarized along the same axis (shown as a dashed line) attract each other if they are in a head-to-tail configuration (blue regions) or repel each other if they are side by side (red regions).

Dipole-dipole interaction

We consider a system of magnetic dipoles polarized along the direction z , which, in the experimental realization, will be the vertical direction. The dipole-dipole interaction potential is

$$U_{dd}(\mathbf{r}) = \frac{\mu_0 \mu^2}{4\pi} \frac{1 - 3 \cos^2 \theta}{r^3}, \quad (1.5)$$

where μ is the magnetic moment of each atom, r is the modulus of the relative distance between the atoms and θ is the angle between the polarization axis and r , see Fig. 1.3. The dipolar interaction has two main features that strongly differ from the usual Van der Waals interactions between neutral atoms in quantum degenerate gases. First, it is anisotropic, with a d -wave symmetry given by the term $1 - 3 \cos^2 \theta$. Therefore, the interaction can be repulsive or attractive depending on the relative orientation between the atoms, as sketched in Fig. 1.3. Second, the dipolar interaction in three dimensions is long-range due to its dependence $\sim 1/r^3$. To see why, we consider the thermodynamic definition of long-range interactions. Given some generic inter-particle interaction energy $u(\mathbf{r})$, the interaction energy of a particle surrounded by a cloud of particles with homogeneous density n in d dimensions is $U = \sum_i u(\mathbf{r}_i) = n \int d\Omega \int_{r_0}^R u(\mathbf{r}) r^{d-1} dr$, where the integral is over the whole solid angle Ω and in between a hard core r_0 and an external radius R . A potential is short-range if the central particle only 'feels' the interaction of some neighboring particles. Mathematically, this condition means that the interaction energy U converges in the limit of an infinite cloud, $R \rightarrow \infty$, so that particles further and further away from the central one give a negligible contribution to the total energy. On the other side, the interaction is long-range if U diverges in the limit $R \rightarrow \infty$, which means that the contribution of the furthest particles is never negligible. Since the integral diverges if $u(\mathbf{r}) \sim 1/r^{d+\epsilon}$, with $\epsilon > 0$, the interaction u is long-range if it goes to zero with an exponent larger than d . The dipolar interaction in 3D is the marginal case in which $u(\mathbf{r}) \sim 1/r^d$ and the

energy U diverges logarithmically. For this reason, it is also called 'marginally long-range'. Interestingly, from a statistical mechanical point of view, a long-range interacting system doesn't favor a homogenous configuration in the thermodynamic limit, as it happens for short-range interactions [32]. If the interaction is attractive, as the system grows, the most energetically favorable configuration is the close-packing one, in which regions of higher density are separated by regions of lower density. A clear example of this scenario is a homogeneous gravitational system that fragments leading to, for example, the star formation process. On the other hand, if the interaction is repulsive, the particles get mashed at the edges of the space, as it happens in the classical electrostatic problem of electrons repelling through the Coulomb interaction inside a conductor. Even if the dipolar interaction doesn't fill in this simple schematization because it has both attractive and repulsive contributions, it is interesting to note that, indeed, in a trapped dipolar quantum gas both the close-packing configuration, corresponding to the supersolid formation, and the edge phase with atoms accumulated near the walls of a box [33] can happen.

The long-range nature of the dipolar interaction has implications for the scattering problem at ultralow temperatures. In the case of Van der Waals interactions decaying with distance as $1/r^6$, the centrifugal barrier prevents two particles from interacting in partial waves with relative angular momentum $l > 0$. The scattering phase shifts, indeed, go to zero very fast for low relative momenta k , and only the $l = 0$ phase shift is relevant, going linearly with k . Thanks to this property, the whole scattering process can be described in terms of a single parameter, the scattering length a_s , and the real interaction potential can be substituted with a delta-like and isotropic pseudopotential having the same value of the scattering length of the real one, i.e. $U_c(\mathbf{r}) = g\delta(\mathbf{r})$, with $g = 4\pi\hbar^2 a_s/m$ [3]. On the other hand, for the long-range dipolar interaction, the two colliding particles feel each other beyond the centrifugal barrier. All the scattering phase shifts contribute to the dynamics since they all behave linearly in k . No pseudopotential can be introduced for the dipolar interaction, and the full expression in Eq. 1.5 must be considered.

Dipolar BECs and roton instability

A weakly interacting dipolar BEC in the mean field approximation is described by the Gross-Pitaevskij equation (GPE) [3]

$$i\hbar\frac{\partial}{\partial t}\psi(\mathbf{r}, t) = \left(-\frac{\hbar^2}{2m}\nabla^2 + V_{trap}(\mathbf{r}) + g|\psi(\mathbf{r}, t)|^2 + \phi_{dd}(\mathbf{r}, t) \right)\psi(\mathbf{r}, t) \quad (1.6)$$

The mean field approximation consists in replacing the field operator $\hat{\psi}$ with the classical field ψ , neglecting completely the quantum fluctuations. The mean field approximation is justified by the presence of a condensate, whose population N_0 , in the case of weakly interacting quantum gases, is very close to the total atom number N . In this case, the operators relative to the condensed state are safely approximated with c-numbers $\hat{a}_0 \sim \hat{a}_0^\dagger \sim \sqrt{N_0}$, which corresponds to neglect their commutator (of order 1) compared to their expectation value (of order $\sqrt{N_0}$). On the right-hand side of the GPE equation, the first term is the kinetic energy, the second term is the trapping potential and the last

two terms are the contact and dipolar potentials, respectively. While the isotropic contact potential is simply proportional to the density of the condensate $n = |\psi(\mathbf{r}, t)|^2$, the dipolar potential is a non-local term

$$\phi_{dd}(\mathbf{r}, t) = \int d\mathbf{r}' U_{dd}(\mathbf{r} - \mathbf{r}') \psi(\mathbf{r}', t). \quad (1.7)$$

Finally, in the experiments described in this thesis, the trapping potential is usually harmonic $V_{trap}(\mathbf{r}) = 1/2m(\omega_x^2 x^2 + \omega_y^2 y^2 + \omega_z^2 z^2)$. The GPE equation is a non-linear Schrödinger equation for the macroscopic matter field $\psi(\mathbf{r}, t)$, where the non-linearities come from the interactions.

In the stationary case, the phase of the wavefunction evolves with the chemical potential μ , $\psi(\mathbf{r}, t) = \psi(\mathbf{r})e^{-i\mu t/\hbar}$. The GPE equation takes then its stationary form

$$\left(-\frac{\hbar^2}{2m}\nabla^2 + V_{trap}(\mathbf{r}) + g|\psi(\mathbf{r}, t)|^2 + \phi_{dd}(\mathbf{r}) - \mu \right) \psi(\mathbf{r}) = 0. \quad (1.8)$$

The chemical potential is fixed by the normalization condition $\int |\psi(\mathbf{r})|^2 d\mathbf{r} = N$. The solution of the stationary GPE equation with lower energy is the ground state of the system. In the case of contact interactions only, the ground state of a BEC in a harmonic potential is usually found neglecting the kinetic energy compared to the potential and interacting energies, the so-called Thomas-Fermi approximation. The solution is an inverted paraboloid of the form $n(\mathbf{r}) = n_0(1 - x^2/R_x^2 - y^2/R_y^2 - z^2/R_z^2)$, where R_i are the Thomas-Fermi radii and n_0 is the central density. Remarkably, the ground state of a dipolar BEC has the same parabolic shape, even if the solution is complicated by the dipolar energy term [?]. However, while in the pure contact case the aspect ratio of the atomic cloud is the same as the one of the harmonic potential, i.e. $R_i/R_j = \omega_j/\omega_i$, in the dipolar case the two aspect ratios are different. The atomic cloud gets elongated in the vertical direction due to the presence of the external magnetic field, which favors a head-to-tail configuration of the dipoles, an effect called magnetostriction.

We now turn to the problem of the stability of the dipolar gas. The attractive part of the dipolar interaction makes the stability issue much more subtle than the case of pure contact interactions, for which only the sign of the scattering length matters. First, we consider the simple case of a homogenous system with density n_0 . If the dipolar interaction is strong enough, we expect all the dipoles to arrange in a head-to-tail configuration, forming a long wire whose density would increase indefinitely, leading to the collapse. It is evident, therefore, that stability can be reached only with a repulsive contact interaction, i.e. $g > 0$, balancing the dipolar attraction. To quantitatively understand the stability conditions of the dipolar gas, one has to study the elementary excitations. The spectrum of the elementary excitations is obtained considering small density and velocity excitations with frequency ω and wavevector k around the equilibrium density n_0 [3]. Linearizing the time-dependent GPE 1.6 one obtains

$$\omega = k\sqrt{\frac{n_0}{m}\left[g + \mu_0\mu^2\left(\cos^2\alpha - \frac{1}{3}\right)\right] + \left(\frac{\hbar k}{2m}\right)^2}, \quad (1.9)$$

where the term in square brackets is the Fourier transform of the interaction potential, given by the sum of the contact and dipolar part. The dipolar interaction contributes with a dependence on the relative angle α between the wavevector k and the polarization axis. As in the case of pure contact interactions, the excitation spectrum has a phononic behavior for low k , where the excitations are collective, and a quadratic behavior for large k , where excitations are of single particle nature. In the dipolar case, however, many different phononic branches appear, depending on the angle α , each one with a different speed of sound. The most unstable branch is the one with $\alpha = \pi/2$, for which the direction of k , and hence of the density modulation, is perpendicular to the dipoles. In the region with higher density, the dipoles are in a head-to-tail configuration, so the energy is lower. The most stable branch is the one with $\alpha = 0$, for which the opposite happens: the modulation is in the direction of the dipoles, and in the high-density regions the interaction is mostly repulsive. The anisotropy in the dipolar excitation spectrum has been experimentally explored through Bragg scattering [34] and transport measurements [35]. The collapse happens when the mode with the lowest energy becomes imaginary for small k . From Eq. 1.9 with $\alpha = \pi/2$, the instability occurs when $\mu_0\mu^2/3 > g$. We define the interaction parameter ϵ_{dd} and the associated dipolar length a_{dd} as

$$a_{dd} = \frac{\mu_0\mu^2 m}{12\pi\hbar^2}, \quad \epsilon_{dd} = \frac{\mu_0\mu^2}{3g} = \frac{a_{dd}}{a_s}. \quad (1.10)$$

With these definitions, the dipolar collapse in the homogeneous case happens when $\epsilon_{dd} > 1$.

In the presence of a trap, the condition is modified. Intuitively, a harmonic trap in the vertical direction helps prevent the collapse, since the dipoles need to pay a potential energy cost to arrange themselves in a head-to-tail configuration. Generally, the collapse happens at values of ϵ_{dd} larger than 1. We consider a homogenous system in the xy plane and harmonic confinement in the z direction with frequency ω_z and harmonic oscillator length $l_z = \sqrt{\hbar/(m\omega_z)}$. The new length scale l_z modifies the energy spectrum and introduces an exciting novelty: the appearance of a minimum at finite momentum $k \sim 1/l_z$ [36], see Fig. 1.4. The minimum is called roton minimum, in analogy with superfluid liquid helium. For long wavelengths of the excitation (small k) the dipoles feel only the repulsive part of the interaction, and the spectrum is phononic. When the wavelength is of the order of l_z , the dipoles form local structures in which the attractive part of the interaction becomes relevant, decreasing the energy. For lower wavelengths (larger k), the kinetic energy of the excitation dominates and we enter the single-particle regime, where $\omega \sim k^2$. Close to the roton minimum, the quasi-particle energy has a parabolic shape of the form $(\hbar\omega)^2 = \Delta^2 + a(k - k_{rot}^2)$, where k_{rot} and Δ are the wavevector and the energy corresponding to the roton minimum, respectively. In superfluid helium, the roton minimum arises from the strong interparticle interactions and has a deep influence on the properties of the superfluid state. For example, it determines the Landau critical velocity setting the dissipation-free dynamics, which otherwise would be determined by the speed of sound [3]. In ultracold dipolar gases, the roton mode comes from the peculiar shape of the interaction, even if the system is very dilute and the interactions are small. The energy of the roton Δ

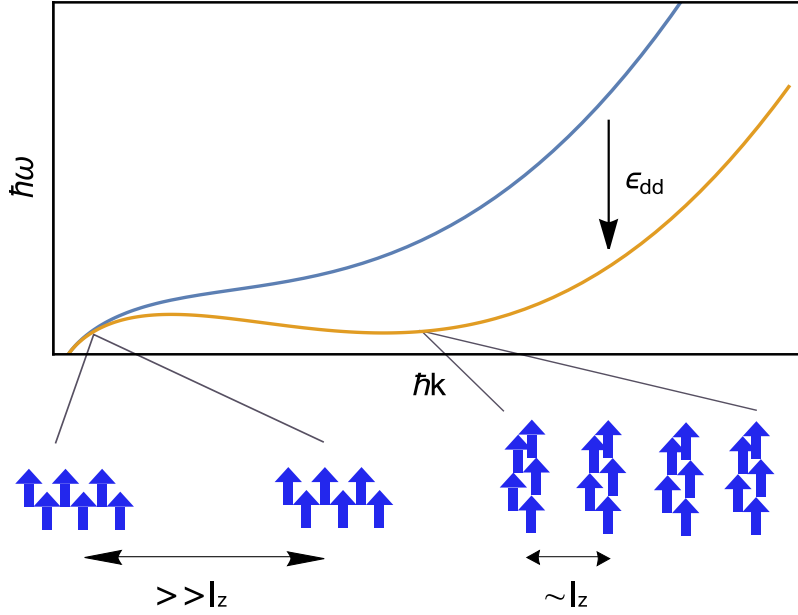


Figure 1.4: Sketch of the roton minimum in the excitation spectrum of trapped dipolar gases. In the phononic regime (low k) the wavelength of the excitation is much larger than the vertical harmonic oscillator length l_z , and the interaction is mainly repulsive. For wavevectors $k \sim 1/l_z$, the attractive part of the interaction becomes relevant and the dipoles reduce the energy of the excitation forming elongated structures. The roton minimum can be controlled with the interaction strength ϵ_{dd} .

can be easily tuned by changing ϵ_{dd} , as depicted in the sketch in Fig. 1.4. While the energy Δ decreases, the roton quasiparticles get more and more populated. The experimental observation of the roton minimum was reported by the Innsbruck group in [37]. In the experiment, the BEC was elongated along one direction, so that the minima appeared in two points $k = \pm k_{rot}$, and not on a whole annulus with radius k_{rot} as in the infinite case. The population of the roton mode, triggered by an interaction quench toward high values of ϵ_{dd} , was revealed in time of flight from the appearance of symmetric peaks at $\pm k_{rot}$.

Beyond mean-field stabilization and quantum droplets

The population of the roton mode is a precursor of crystallization. If the roton excitation could be populated more and more, the system would spontaneously form a density modulation with a period proportional to l_z . However, when the roton energy becomes imaginary, the mean-field theory predicts the collapse of the system, similar to the phononic collapse discussed previously for the homogeneous case. Instead of observing the collapse, experiments in the strongly dipolar regime reported the observation of a transition from the BEC to a stable state of separated liquid-like quantum droplets [38, 39, 9, 40], that can be also self-bound. The new crystal-like state was stabilized by the repulsion of quantum fluctuations, which was enough to prevent the attractive part of the mean-field interactions. To understand this beyond-mean field stabilization mechanism, which is crucial also for the existence of the supersolid phase, we consider a simple, single-particle, example [41].

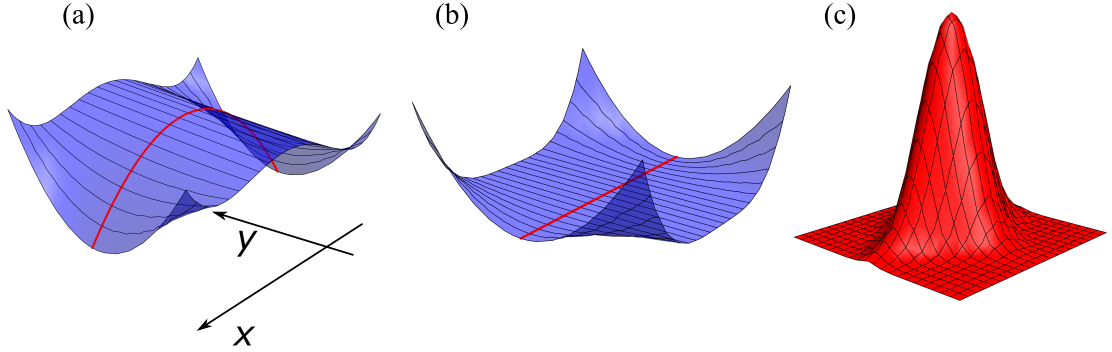


Figure 1.5: Sketch of the stabilization mechanism by quantum fluctuations. (a) The classical unstable potential of Eq. 1.11. The red line indicates one unstable classical trajectory. (b) The same potential stabilized by the quantum zero-point energy of the y degree of freedom. (c) Solution to the single-particle Schrödinger equation in the potential plotted in (a).

Let's take a classical potential for a particle with mass m of the form

$$U_{\text{classical}}(x, y) = -\frac{1}{2}mx^2 + \frac{1}{2}m\omega_y(x, y)^2y^2. \quad (1.11)$$

The potential is plotted in Fig. 1.5 for $\omega_y(x, y) = 1 + 6x^2 + 2x^4 + 2x^2y^2$. It has no minimum so the classical particle will roll down the negative valley and reach larger and larger x values. What happens if we switch on quantum mechanics? The zero-point energy of the harmonic oscillator is repulsive and equal to $\hbar\omega/2$. Since in the classical potential in Eq. 1.11 the frequency in the y direction increases as $|x|$ increases, also the quantum zero-point energy increases with $|x|$. If the increase is fast enough, it can compensate for the classical instability in the x direction. Indeed, the quantum potential considering quantum fluctuations, $U_{\text{quantum}}(x, y) = U_{\text{classical}}(x, y) + \hbar\omega_y(x, y)/2$, has a minimum in the origin, and the solution of the single-particle Schrödinger equation is localized at the center of the xy plane¹, see Fig. 1.5(b-c). This is an example of a classical unstable degree of freedom (x) stabilized by quantum fluctuations in another degree of freedom (y).

The same mechanism happens also in dipolar quantum gases. In this case, quantum fluctuations come from the fully quantum nature of the bosonic field operator, which can be expanded as $\hat{\psi}(\mathbf{r}) = \psi(\mathbf{r}) + \delta\hat{\psi}(\mathbf{r})$. The classical wavefunction $\psi(\mathbf{r})$ is the one relative to the condensed state, i.e. the one with $\mathbf{k} = 0$, and fulfills the GPE equation 1.6, while the quantum fluctuations term is a sum over all the other single-particle states, $\delta\hat{\psi}(\mathbf{r}) = \sum_{\mathbf{k} \neq 0} \phi_{\mathbf{k}} \hat{a}_{\mathbf{k}}$, where $\phi_{\mathbf{k}}$ and $\hat{a}_{\mathbf{k}}$ are the single particle wavefunction and the annihilation operator relative to the state \mathbf{k} , respectively. One can treat the quantum fluctuations term with different degrees of approximation. Usually, one takes all the quadratic terms with $\mathbf{k} \neq 0$, and the resulting Hamiltonian describes a gas of non-interacting quasiparticles following the Bogoliubov energy dispersion $E(\mathbf{k})$ [3]. Physically,

¹The solution is $\psi(x, y) \sim e^{-(1+x^2)}(1/2 + y^2)$.

there are two main consequences. First, the condensate state is not fully populated, but some particles are scattered into states with $\mathbf{k} \neq 0$, the so-called quantum depletion of the condensate. Second, the ground-state energy E_0 is modified by the population of higher-energy states. This additional zero-point energy is called Lee-Huan-Yang (LHY) correction. For a homogeneous system in a volume V with dipolar interactions, it reads [42]

$$E_{LHY} = \frac{gn^2V}{2} \frac{128}{15\sqrt{\pi}} \sqrt{na_s^3} \left(1 + \frac{3}{2}\epsilon_{dd}^2\right). \quad (1.12)$$

The two main features of the LHY correction are that it is isotropic and repulsive, also for dipolar interactions, and that it has a steeper dependence on the density n compared to the mean-field interactions: $\sim n^{5/2}$ instead of $\sim n^2$. However, the LHY correction scales as the gas parameter $\sqrt{na_s^3}$, which is very small in dilute ultracold gases. For this reason, quantum fluctuations are usually negligible compared to the mean-field energy. In dipolar gases, tuning the interaction parameter ϵ_{dd} , it is possible to reduce the mean-field interactions and eventually change their sign from positive to negative, at the mean-field critical point. While mean-field interactions decrease, they can become comparable in magnitude with the zero-point energy. In this regime, the LHY correction behaves as a stabilization mechanism, thanks to its fast dependence $\sim n^{5/2}$, which ensures the formation of a new ground state at higher densities, even if the mean-field part alone $\sim -n^2$ would predict the collapse. In analogy with the previous example of the quantum harmonic oscillator, the quantum fluctuations arising from higher energy modes (the 'fast' degree of freedom y) stabilize the low-energy instability of the mean-field theory (the 'slow' degree of freedom x).

The same stabilization mechanism happens also in binary Bose-Bose mixtures with pure contact interactions. In that case, the mean-field interactions are tuned by changing the attractive inter-species scattering length compared to the repulsive intra-species one. If the attraction prevails, the mean-field theory predicts the collapse. Again, since the critical point is in a region where two different mean-field interactions approximately compensate each other, quantum fluctuations provide an effective stabilization mechanism. The result is a single quantum droplet with liquid-like properties [43, 44], contrary to the dipolar case in which the long-range nature of the interaction leads to the formation of an array of multiple droplets [38, 39, 9].

The supersolid phase

In the previous paragraphs, we have seen that trapped dipolar quantum gases are a very promising system for the formation of a supersolid phase: starting from a fully coherent system, the BEC, the roton instability triggers a crystallization mechanism. However, the first observed arrays of dipolar droplets weren't supersolid. While displaying phase coherence inside each droplet as shown by interference fringes in time of flight, indeed, they didn't establish phase coherence across the array, preventing any superfluid motion from one cluster to the other [38]. In an experiment with a dipolar gas of dysprosium in 2019

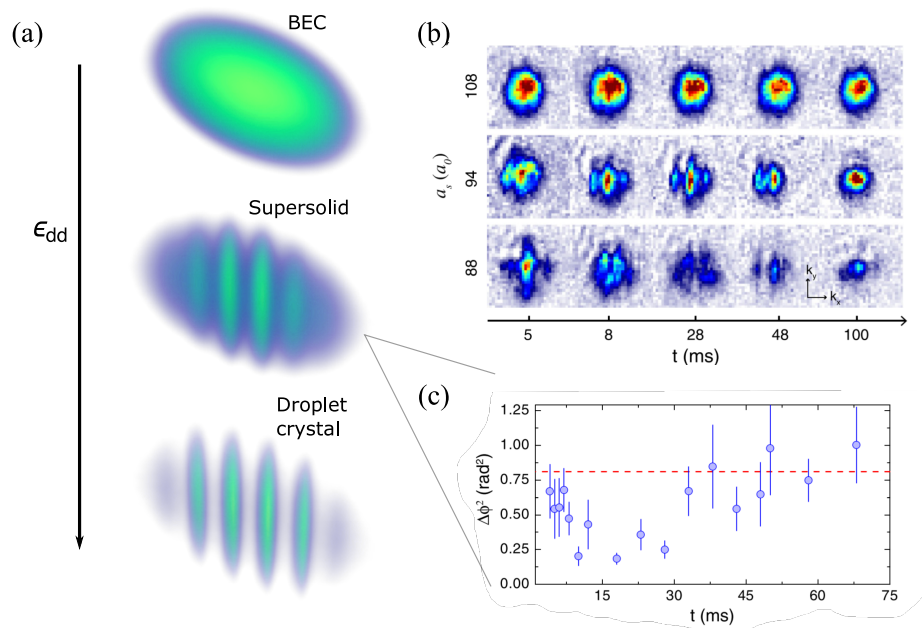


Figure 1.6: Experimental observation of the supersolid phase in a dipolar quantum gas [10]. (a) Sketch of the superfluid-supersolid phase transition in a cigar-shaped harmonic trap. The control parameter is the relative strength of dipolar over contact interactions, $\epsilon_{dd} = a_{dd}/a_s$, tuned with Feshbach resonances. The supersolid phase consists of an array of macroscopic clusters immersed in a superfluid background. For weaker dipolar interactions, the ground state is a BEC, while for stronger dipolar interactions it is an incoherent droplet crystal. (b) Observation of the three phases BEC, supersolid, and droplet crystal, from top to bottom, after a free expansion [10]. The horizontal axis is time. The supersolid phase is characterized by stable interference fringes. (c) Variance of the interference pattern phase in the supersolid regime as a function of time. In the first tens of ms phase coherence is maintained between different clusters. The red dashed line is the variance of a random variable, indicating the loss of global coherence.

[10], the group in Pisa found instead a small region of parameters in which the droplets overlap each other, maintaining the phase coherence across the whole array and hence combining the crystal and superfluid order. The BEC was trapped in a cigar-shaped trap, with the strongest confinement along the vertical direction, along which the dipoles were aligned. The elongated geometry favors the instability of the roton mode in the long-axis direction, forming a 1D array of few clusters, separated by a lattice period $d \sim l_z \sim 4\mu\text{m}$, see Fig. 1.6. The supersolid region lies in between the BEC side, where the system is superfluid but without a crystal structure, and the so-called droplet crystal side, where the array of droplets loses global phase coherence. The experimental signature of the supersolid formation was the appearance of an interference pattern in time of flight images, coming from the overlapping of the different matter waves forming each cluster of the supersolid, see Fig. 1.6(b). From the interference fringes, it is possible to extract the phase difference between neighboring clusters (see chapter 2). Crucially, the phase difference was constant over different repetitions of the experiment demonstrating the phase coherence between different clusters. On the other hand, when the superfluid background disappears and the density between different clusters goes to zero, phase coherence is suppressed and the measured phase distribution gets larger, reaching the incoherent droplet crystal regime. Similar results have been obtained also from the Stuttgart and Innsbruck groups, with dysprosium and erbium dipolar gases [11, 12].

The dipolar supersolid is of the cluster type since each lattice site hosts thousands of atoms, and can be reconduced to the first proposal by Gross, as opposed to the vacancy supersolid proposed by Andreev and Lifshitz, see Fig. 1.1. The cluster nature naturally enhances the superfluid properties, but, on the other hand, strongly limits the spatial extension of the crystal. Since the typical atom number in the BEC is of the order of a few ten thousand atoms, the number of clusters, i.e. of lattice sites, in the supersolid phase is of the order of a few units (typically from 4 to 8 clusters, see Fig. 1.6). Moreover, due to the presence of the trap, the population of the clusters is not homogeneous, with the central ones more populated than the lateral ones. On the other hand, the large period of the dipolar supersolid and the large dimensions of each cluster enable the study of the superfluid motion locally in each cell, as we will explain in this thesis, opening perspectives that would be very challenging in other condensed matter systems.

A significant limitation of the supersolid phase in dipolar gases is the limited lifetime due to three-body losses. Even if the system is very dilute, the probability for three particles to interact (instead of two) is not zero. The main three-particle interaction is inelastic, with two of the three particles that form a molecular state and the third one acquiring the remaining energy in the kinetic form. This three-body interaction leads to atom losses, scaling fast with the density $\dot{N}/N = -L_3 \langle n^2 \rangle$, where L_3 is the recombination constant and $\langle n^2 \rangle$ the mean squared density. In the supersolid regime, the peak density in the clusters is about 10 times larger than that of the BEC, so the lifetime is much shorter. Considering that three-body losses also decrease the phase coherence, the typical observation time in the supersolid regime is of the order of 100 ms. Nevertheless, it is enough to observe typical dynamical modes of the supersolid. Just after the first observations of the coherent density modulation, indeed, the Goldstone modes arising from the double symmetry breaking of the supersolid phase were observed [45, 46, 47], one related to the superfluid nature

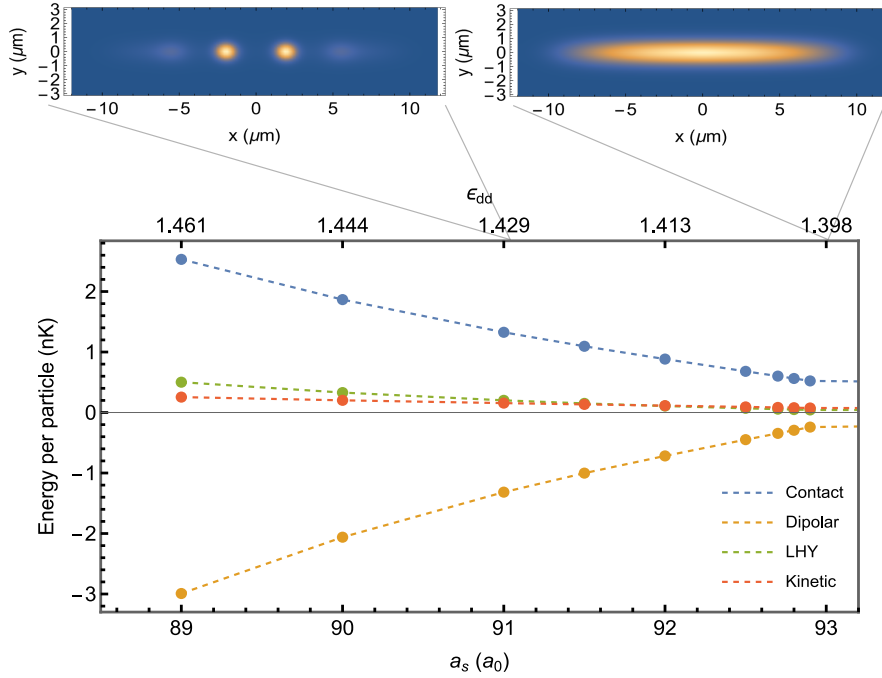


Figure 1.7: Energy terms in the ground-state solutions of the stationary eGPE (Eq. 1.13) across the BEC-supersolid phase transition, as a function of the scattering length a_s (lower axis) or of the dimensionless interaction parameter $\epsilon_{dd} = a_{dd}/a_s$. Insets show examples of the density $\rho(x, y)$ integrated in the vertical direction z in the BEC regime (right, $a_s = 93 a_0$) and in the supersolid regime (left, $a_s = 91 a_0$).

and the other to the crystal one. In particular, the low energy Goldstone mode [46] is associated with the broken continuous symmetry, and is the analog of the Goldstone mode observed in cavity supersolids [13], see next section. The presence of the harmonic trap in the dipolar case increases the energy of the mode, which is not zero, but it is much smaller than the trap frequencies and all the other modes. The higher energy Goldstone modes [45], instead, are related to phononic oscillations of the crystal structure, and demonstrate the elasticity of the crystal, necessary for full supersolid dynamics. To our knowledge, only in the dipolar supersolid there is experimental evidence of the coexistence of phase coherence, density modulation, and elastic solid behavior so far. Recently, also dipolar supersolids with 2D lattice structures have been realized [48, 49]. We note that, in addition to the quantum phase transition from the superfluid to the supersolid, crossed varying the interaction parameter ϵ_{dd} at low temperature, it is possible also to evaporate the thermal gas directly into the supersolid regime, crossing therefore a classical phase transition varying the temperature, as demonstrated in [50].

From a theoretical perspective, the ground state and the dynamics of the dipolar supersolid are simulated using an extension of the GPE equation that takes into account also the energy of quantum fluctuations through a local density approximation [51, 52]. The result is the so-called extended Gross-Pitaevskij equation (eGPE)

$$i\hbar\frac{\partial}{\partial t}\psi(\mathbf{r},t) = \left[-\frac{\hbar^2}{2m}\nabla^2 + V_{\text{trap}}(\mathbf{r}) + g|\psi(\mathbf{r},t)|^2 + \phi_{dd}(\mathbf{r},t) + \frac{32g\sqrt{a_s^3}}{3\pi} \left(1 + \frac{3}{2}\epsilon_{dd}^2\right) |\psi(\mathbf{r},t)|^3 \right] \psi(\mathbf{r},t). \quad (1.13)$$

The long-range dipolar potential ϕ_{dd} is the same as in Eq. 1.7, and the LHY term is the one proportional to $|\psi|^3$. As in the usual GPE, stationary solutions correspond to $\psi(\mathbf{r})e^{-i\mu t/\hbar}$. The eGPE equation can be numerically integrated to find the ground state in the stationary case, or to simulate the full dynamics of the system. The main novelty compared to calculations for non-dipolar condensates, apart from the LHY term, is the long-range dipolar potential ϕ_{dd} . Due to its non-local nature, it represents a huge complication for integrating the equation. It is usually treated in Fourier space, where it is conveniently computed with fast Fourier-transform algorithms [53, 54]. The interaction potential must also be regularized to avoid spurious boundary effects due to the long-range nature of the interaction. The main approximations of the eGPE simulations compared to experimental conditions are the absence of thermal effects, because all the dynamics is reduced to the wavefunction of the condensate, and the absence of dissipation mechanisms, mainly three-body losses which have a strong impact in the lifetime of the experimental samples. Nevertheless, eGPE simulations are quite accurate in describing the experimental systems, and usually the addition of phenomenological parameters like temperature and loss rates is not required to reproduce the experimental observations. The mean-field approach is supposed to break down in the independent droplet regime, where the system is no longer described by a global wavefunction, and the densities inside each cluster are larger, leading to stronger correlations. Reference [55] provides a comparison between experimental data, GPE equation, and quantum Monte Carlo simulations.

For our experiments in the supersolid regime, we compare to eGPE calculations. Most of the simulations performed in this thesis employ a code written by M. Modugno and A. Alañã, Bilbao University [15, 56].

Fig. 1.7 reports the evolution of the different energy terms appearing in the eGPE for the ground state of the dipolar system across the superfluid-supersolid transition, for typical experimental parameters: trap frequencies $(\omega_x, \omega_y, \omega_z) = 2\pi \times (20, 90, 100)$ Hz and atom number $N = 2 \times 10^4$. As discussed in the previous paragraphs, the dipolar energy becomes more and more negative lowering the scattering length a_s , and it is responsible for the development of the density modulation. When the energy cost of contact interactions and kinetic energy gets overcome by the dipolar energy gain, the transition from the superfluid to the supersolid happens. In the example of Fig. 1.7, the critical point is around $a_s = 92.9 a_0$. The contact repulsive energy then rapidly increases because of the increase in the peak density inside the clusters. Globally, the mean-field energy is negative, but the collapse is prevented by the repulsive LHY energy.

1.3 Spontaneously modulated superfluid phases in recent experiments

Recently, superfluid and superconducting phases with spontaneous density modulation have been discovered in a variety of different systems. Only for some of them a direct connection with the supersolid phase has been traced. Without attempting to be exhaustive, this section reports a brief overview of these systems. On one side, to our knowledge, a similar general discussion doesn't exist in the literature. On the other side, it is useful to get an idea of what happens in other fields to put the research on dipolar supersolids in perspective, and to trace useful connections between the results presented in this thesis and the other systems.

Excluding bulk solid helium, discussed in section 1.1, the most in-depth investigations of supersolid structures and properties come from ultracold atoms. As discussed in the previous section, the dipolar supersolid is probably the system for which the most striking evidence of supersolid behavior has been accumulated in the last years. The modulation is 100 % induced by inter-atomic interactions, the period is large and the cluster nature enhances the superfluid properties. Many of the key supersolid properties have been experimentally assessed: coexistence of density modulation and superfluidity, phononic crystal modes in the form of Goldstone modes and, in this thesis, we report on the superfluid behavior under rotation and the measurement of a sub-unity superfluid fraction at zero temperature. However, supersolid phases have been realized also in other ultracold atom platforms, with completely different physical mechanisms, which we discuss here: spin-orbit-coupled BECs and BECs in high-finesse optical cavities.

Moving from ultracold atoms to condensed matter systems, the energy and length scales, of course, change by order of magnitude: the lowest temperatures are of the order of the mK, and the spatial modulation is typically of the order of the lattice unit cell, a few nm or less. Supersolid-like phases have been investigated in 2D layers of solid ^4He and ^3He under confinement. The latter is an exception since the modulation is macroscopic, of the order of $1\ \mu\text{m}$, and shows some interesting parallelisms with the dipolar supersolid. We also briefly cite the elusive pair density wave phase in cuprate superconductors and more exotic phases, such as nuclear pasta in neutron stars. A comparison summary is presented in Table 1.1.

This overview is not for its own sake. The relative easiness, compared to other systems, of the experimental investigation and theoretical modeling makes the dipolar supersolid an ideal platform to study the fundamental properties of a new phase of matter, that, hopefully, will be assessed also in real-world condensed matter systems. Most of the research in this thesis has been performed with this goal in mind. Most of all, the measurement of a sub-unity superfluid fraction through the Josephson effect, discussed in chapter 5, could be of interest outside of the ultracold-atom community.

Spin-orbit-coupled BECS

Spin-orbit coupling (SOC) refers to the situation in which the spin degree of freedom is coupled to the orbital degree of freedom, namely the momentum of the particle. In

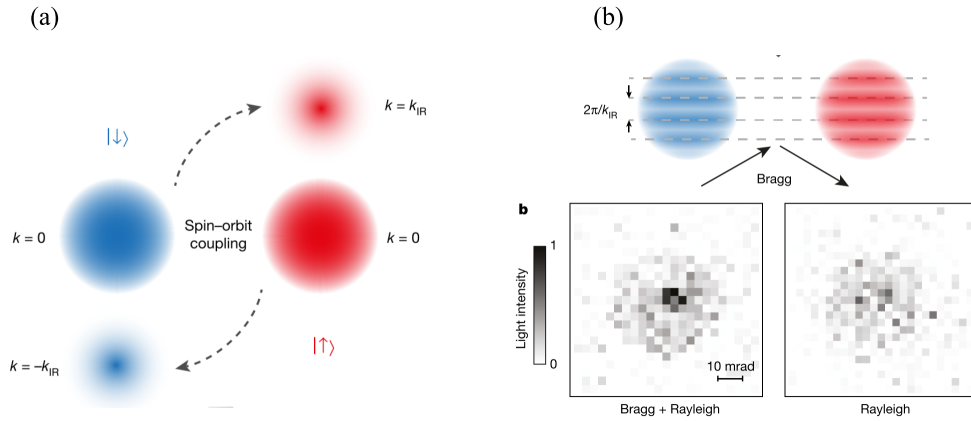


Figure 1.8: Stripe phase in SOC BECs from [14]. (a) SOC coupling induced by a two-photon Raman transition. The wavefunction has four components: two spin states at zero momentum and two spin states with plus and minus the momentum exchanged with the Raman beams. (b) The stripe phase emerges as a spatial interference between components of different momenta. The spatial modulation is detected through Bragg spectroscopy [14].

atomic physics, spin-orbit coupling arises due to the interaction of the electron with the magnetic field produced by the nucleus and is responsible for the fine-structure splitting. In condensed matter systems, the coupling between the electron spin and momentum is mediated by electromagnetic fields in the material. In ultracold atoms, spin-orbit coupling can be engineered by exploiting Raman transitions, in which a two-photon transition couples two hyperfine states (the two 'spin states') and is accompanied by a finite momentum transfer [57]. The phase diagram of SOC BECs is rich and can be explored by tuning the Raman coupling Ω , the detuning of the Raman transition δ and the density of the BEC [58, 3]. The interesting region hosting supersolid physics is the so-called stripe phase, which can be simply understood as a spatial interference within a wavefunction with four different components, as sketched in Fig. 1.8. The mixture of the two spin components, when SOC is present, has two additional components with momenta $\pm k_R$, the momentum acquired in a Raman transition. The interference between the $k = 0$ and $k = \pm k_R$ components in the same spin sector gives rise to the stripe phase, as sketched in Fig. 1.8(b). The period of the modulation is close to that of the Raman potential, but not equal because it gets modified by inter-particle interactions. The translational symmetry is thus spontaneously broken, because the period of the modulation was absent in the original Hamiltonian. Since the period is close to the Raman laser wavelength, it is usually $1 \mu\text{m}$ or smaller. Combined with a typical low contrast [59], the direct detection of the stripe phase with in situ imaging is challenging. The first experimental evidence of the stripe phase and its connection with supersolidity was pointed out in [14], where the density modulation was detected through Bragg spectroscopy, see Fig. 1.8(b). To favor the presence of the stripe phase in the phase diagram, one has to reduce the miscibility between the two spin species. This helps also in increasing the stripe contrast [60]. In standard

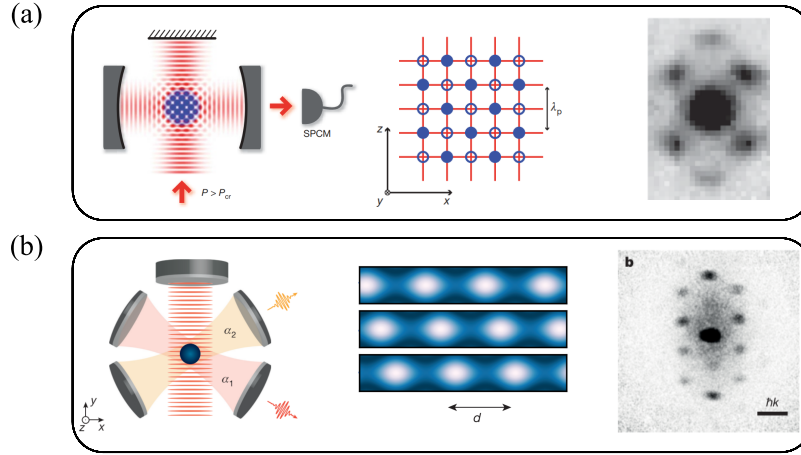


Figure 1.9: Supersolid phases of atoms in optical cavities. (a) Pump plus single cavity from [63], realizing a lattice supersolid that breaks a discrete spatial symmetry forming a checkerboard pattern (middle picture). The population of atomic momentum states with $\mathbf{k} \neq 0$ signals the onset of self-organization (right picture). (b) Pump plus two optical cavities from [13]. In this case, a continuous spatial symmetry is broken, and the density modulation forms with a spontaneously chosen spatial phase (middle picture). The supersolid phase forms when atoms are equally coupled to both cavities, as observed in the momentum populations (right image).

SOC experiments, the condensate is made of ^{87}Rb , for which the inter and intra-species interactions are very similar and the miscibility is high. The stripe phase lies at low Rabi frequencies Ω , in a region where magnetic field fluctuations are an experimental limiting factor. In the experiment [14], the two lowest eigenstates of a superlattice potential have been used as pseudospin states, for which the miscibility can be controlled by tuning the parameters of the superlattice. More recently, the stripe phase has been observed also in the originally proposed ^{87}Rb spin mixture [61], and the phase coherence of the stripe phase was also assessed. Theoretical works showed that the stripe phase possesses Goldstone modes associated with the double-symmetry breaking [62]. The supersolid lattice, therefore, is predicted to be deformable and to show phononic excitations, as in the dipolar supersolid. The experimental observation of the stripe dynamics is lacking, but the experiment on ^{39}K lead by L. Tarruell at ICFO, Spain, is promising for a direct detection of the density modulation. Exploiting Feshbach resonances, it is possible indeed to tune the miscibility of the spin states and to realize high-contrast stripes with observable supersolid effects.

BECs in optical cavities

Atoms inside high-finesse optical cavities are a source of rich and complex physics related to collective light-matter phenomena, in which long-range interactions and self-organization mechanisms can be engineered [64]. Supersolid phases have been experimentally explored in different cavities geometries, see Fig. 1.9. The basic platform consists of a BEC dispersively coupled to the photon fields of an optical cavity and a 1D transverse pump

lattice. The frequency of the pump laser is far red-detuned with respect to the atomic transition line but close detuned from a particular cavity mode. When the pump beam is perpendicular to the optical cavity, as in Fig. 1.9, the potential of the pump and cavity modes is a square lattice. By increasing the power of the pump beam, a quantum phase transition related to the Dicke model is crossed, and the atoms break the discrete symmetry of the lattice forming a checkerboard pattern [63]. The onset of this self-organization is monitored both through the occupation of atomic momenta states related to the scattering of photons between the pump and the cavity modes, see Fig. 1.9(a), and through the mean intracavity photon number. The resulting phase is a lattice supersolid, in which the broken continuous symmetry $U(1)$ is inherited by the BEC, and an additional discrete spatial symmetry is spontaneously broken.

A different geometry, consisting of two crossing optical cavities at an angle of 60° , enables the engineering of a continuous symmetry breaking along the direction perpendicular to the pump beam [13]. In this configuration, the atoms in the BEC scatter photons from the pump beam to one of the two cavity modes. By changing the coupling with the cavities, for example with the pump-cavities detunings Δ_1 and Δ_2 , one goes from a self-organization in a single cavity to a balanced coupling scheme in which the two cavity fields form a continuously degenerate manifold. In this configuration, atoms are self-organized in a modulated structure perpendicular to the pump beam, whose spatial phase is different in each experimental run, because it emerges from the spontaneous symmetry breaking. The period of the modulation for the experimental parameters of [13] is $d = \lambda_P / \cos 60^\circ$, with the pump wavelength $\lambda_P = 785$ nm. The dynamic of the modulation has been also studied, in relation to the Goldstone and Higgs modes of the supersolid phase [65]. Although the cavity supersolid displays a double-symmetry breaking, it doesn't possess higher energy Goldstone modes, related to phononic excitations of the crystal structure. In other words, the crystal is infinitely stiff because its period is fixed by the cavity fields. This is a major difference compared to the dipolar supersolid, for which the modulation is completely due to inter-atomic interactions and the lattice is deformable. Recently, a new cavity scheme that should be able to overcome this limitation has been implemented [66].

2D layer of solid ^4He

Bulk solid helium has been a candidate to host a supersolid phase at low temperatures for many years, as explained in section 1.1. While torsional oscillator results excluded the presence of a supersolid in 3D solid helium, promising research is going on in 2D layers of ^4He . The system consists of layers of bosonic helium adsorbed on graphite. While the first helium layer is strongly affected by the interactions with the graphite layer and forms a triangular lattice, the second helium layer is expected to show superfluid properties in some range of coverage densities, see Fig. 1.10. At low coverages, the layer is in a gas-liquid coexistence, while close to layer completion it forms a solid incommensurate with the previous layer. Two recent papers [67, 68] reported measurements of superfluid behavior in torsional oscillator experiments for intermediate coverages of the second layer around $n \sim 18$ atoms/nm², see Fig. 1.10(b-c). The technique is analog to that explained in section 1.1 about bulk solid helium. The temperature dependence of the superfluid

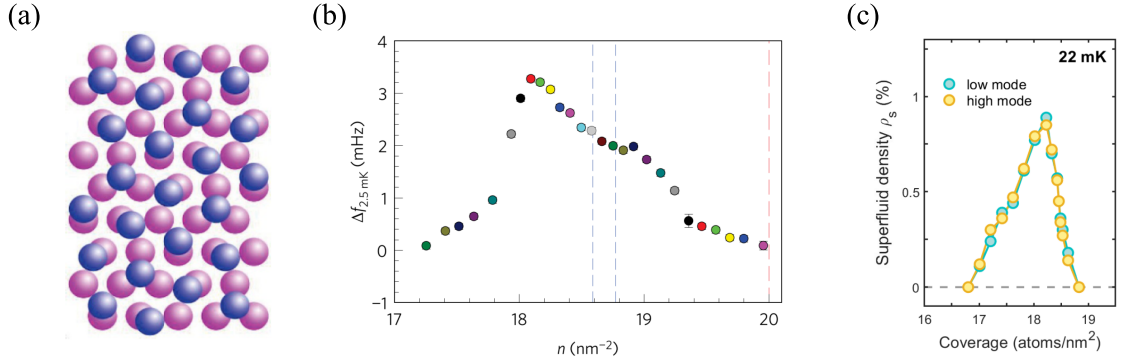


Figure 1.10: Superfluid phase in 2D solid ^4He from [67, 68]. (a) Two layers of ^4He adsorbed on graphite. The second layer (blue circles) shows superfluid properties for intermediate layer coverages. (b-c) Torsional oscillator frequency shift (b) and, analogously, superfluid fraction (c), as a function of the second layer coverage, from [67] and [68], respectively.

fraction isn't described by the usual BKT transition in 2D, and in [67] it is suggested that the reason could be the softening of roton modes and the formation of a density-wave order coexistent with superfluidity. In [68] a phase diagram with a possible supersolid region is proposed. As opposed to ultracold atom systems, the supposed supersolid in the second layer of ^4He on graphite probably belongs to the group of vacancies supersolids, namely a condensate of mobile vacancies immersed in a strongly correlated solid. The corresponding superfluid fraction should be lower than for cluster supersolids, see Fig. 1.10(b).

Superfluid ^3He under confinement

The fermionic isotope of helium, ^3He , becomes superfluid through the formation of Cooper pairs, in analogy to electrons in superconductors. In the absence of a lattice that mediates attractive interactions between the fermions, the attraction between ^3He atoms, needed for the formation of Cooper pairs, comes from the attractive part of the Van der Waals interaction. To avoid the strong hard-core repulsion, the pairs form with non-zero relative angular momentum, in a p -wave state, contrary to standard s -wave superconductors. For symmetry reasons, the spin part of the wavefunction must be a triplet state. The ^3He Cooper pair is, therefore, a very complex object, and the order parameter is a multi-dimensional tensor rather than a single complex wavefunction [2]. The superfluid phases exhibited by ^3He are very rich. The dominant superfluid phase is usually the B-phase, which has an isotropic energy gap in momentum space, as opposed to the A-phase. A typical phase diagram is shown in Fig. 1.11. The spontaneous breaking of translational symmetry can happen when the superfluid is confined in the vertical direction, as investigated in two recent works [69, 70]. For confinement dimensions D of the order of $1 \mu\text{m}$ or less, the gap in the B-phase gets distorted, and the A-phase gains space in the phase diagram. Correspondingly, a new phase appears at the boundary between the A and B phases,

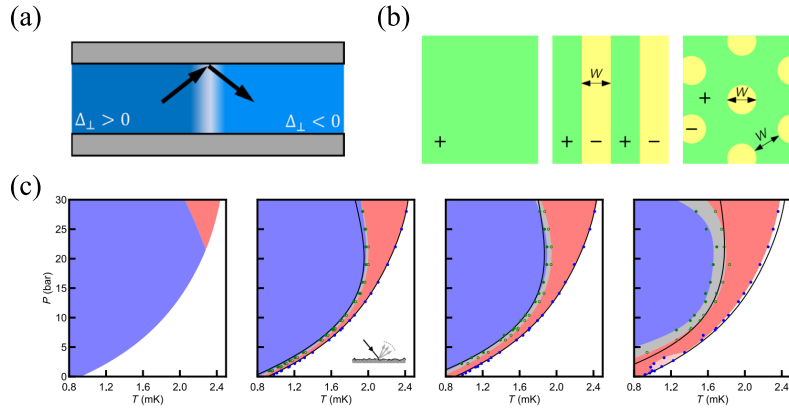


Figure 1.11: Pair density wave phase in confined ${}^3\text{He}$, from [69, 70]. (a) Sketch of the system. Domain walls separating regions with different signs of the gap Δ spontaneously form to suppress pair-breaking effects. (b) The gap modulation could be in the form of stripes (middle image) or in a 'polka dot' pattern (right image) [69]. (c) Phase diagram for vertical confinements D getting thinner from left to right. The blue region is the B-phase, the red region is the A-phase and the gray region is the pair density wave phase [70].

see Fig. 1.11. Such a phase has been experimentally explored through nuclear magnetic resonance [69] or through Helmholtz resonators [70], and it has been identified with a predicted pair density wave phase, in which the energy gap of the Cooper pairs Δ gets spatially modulated, as sketched in Fig. 1.11(a). The physical origin of the modulation lies in an energetic balance between pair-breaking effects near the confining walls and the formation of domain walls in the order parameter [71]. When a Cooper pair scatters from the surface, the sign of its momentum is reversed, and this favors the breaking of the pair. The creation of domain walls in which the energy gap changes sign, passing through zero, suppresses pair-breaking effects. For small confinements D , the energetic cost of creating a domain wall is compensated by the energetic gain of the suppression of pair-breakings, and a pair-density wave is predicted to be stable. The two experiments [69, 70] provide evidence of the modulated phase, although a direct observation of the modulation is lacking. Also, the consensus about the shape of the modulation is missing: it could be a 2D lattice, named 'polka dot' phase [69], or a stripe phase [70], see Fig. 1.11(c).

Interestingly, the pair density wave phase in ${}^3\text{He}$ has some strong similarities with the dipolar supersolid: it is mainly due to interactions and it requires a macroscopic vertical confinement of the order of $1\ \mu\text{m}$. The spatial period of the pair density wave is of the order of the vertical confinement so that it would belong to the group of cluster supersolids. Of course, the main difference is that the modulated quantity is not directly the density of the condensate, but the energy gap.

Pair density waves in high- T_c superconductors

High- T_c superconductors are among the most fascinating and complex condensed-matter systems. Cuprate superconductors, for example, have a rich and only partially understood

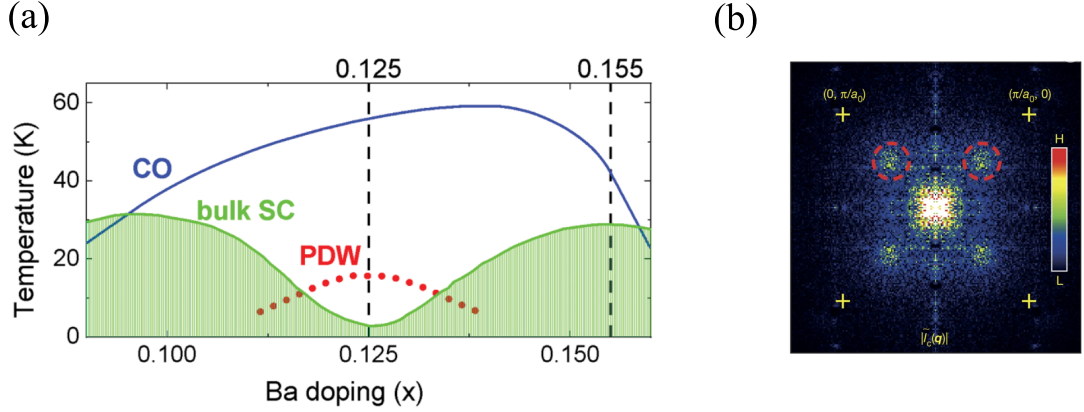


Figure 1.12: Pair density wave (PDW) phase in cuprates superconductors. (a) Phase diagram of the cuprate $\text{La}_{2-x}\text{Ba}_x\text{CuO}_4$. The green region is the superconducting phase. The blue line indicates the onset of the charge order. The PDW lies in the region of reduced critical temperature T_c . (b) Measurement of the spatial modulation of the Cooper pair density in Fourier space for the cuprate $\text{Bi}_2\text{Sr}_2\text{CaCu}_2\text{O}_{8+x}$ from [72], showing Fourier peaks corresponding to a periodic modulation equal to $8 a_0$ in real space.

phase diagram, featuring a d -wave superconducting phase but also many other ordered states, that could compete with superconductivity [73]. For what regards supersolid physics, a region of pair-density wave (PDW) phase inside the elusive 'pseudogap' regime is particularly interesting. The PDW is predicted to appear around a critical hole doping of $1/8$, and consists in a sinusoidal modulation of the energy gap Δ with a period $d = 8 a_0$, where a_0 is the dimension of the underlying lattice unit cell [74]. Also, the density of Cooper pairs should be modulated with half that period, $4 a_0$. The periodicity has its origin in the formation of Cooper pairs with finite momentum, which becomes the momentum of the spatial modulation. Without even trying to be exhaustive on the topic, we cite the first observation of the gap modulation [75] and of the Cooper pair density modulation [72]. Very recently, a PDW has been observed also in another class of high- T_c superconductors, the iron-based superconductors [76]. A phase related to PDWs, the so-called FFLO phase, is under study in unbalanced two-species ultracold Fermi gases [77]. The PDW exhibits global phase coherence in the form of superconductivity and also a spontaneous modulation of the order parameter, namely the energy gap. It has therefore all the characteristics to candidate for the group of supersolid phases of matter. However, the large literature about PDW in superconductors never mentions the possible relationship with supersolid physics. It is particularly interesting for the purposes of this thesis, that the PDW exists in a region of the phase diagram where the critical temperature for superconductivity has a dip, see Fig. 1.12. This effect suggests a competition between the spatial and superconducting order, and it is very tempting to associate it with a mechanism of reduced superfluidity quantified by the superfluid fraction, the main topic of chapters 4 and 5 of this thesis. There is indeed evidence that the superfluid stiffness of cuprate superconductors, quantifying their superfluid behavior, is particularly low and is

correlated with the critical temperature T_c for superconductivity [78, 79]. Any reference to the superfluid fraction or a similar quantity related to superconductors is however missing.

Neutron stars

As a last example, we cite an astrophysical object in which the extreme conditions of high density and low temperature make quantum effects important: the neutron star. It is widely believed that the core of neutron stars is composed of neutrons in a superfluid state, with densities of the order of the nuclear saturation density. The outer crust, instead, is expected to be a crystalline solid made of neutron-rich ions. In between the core and the outer crust, at intermediate densities, the superfluid smoothly connects to the crystal, possibly forming something similar to a supersolid phase. In this region, many theories point to the existence of the so-called 'pasta phases', in which neutrons are arranged in spatially-ordered structures of different geometries and dimensionalities [80]. Interestingly, the interaction between the superfluid and solid parts is often discussed in terms of an 'entrainment' mechanism, for which the free neutrons are entrained by the crystal structure [81]. The concept of entrainment has many similarities, also formally, with Leggett's model for a rotating supersolid and the concept of superfluid fraction, see section 4.1, and could be connected to the problem of the superfluid density of neutrons [82]. Recently, a theoretical paper proposed to simulate the phenomenon of glitches, namely the sudden increase of the rotational frequency of pulsars, with a dipolar supersolid, studying the analogy between the unpinning of vortices from the inner to the outer crust in a neutron star and the dynamics of vortices in the dipolar supersolid [83].

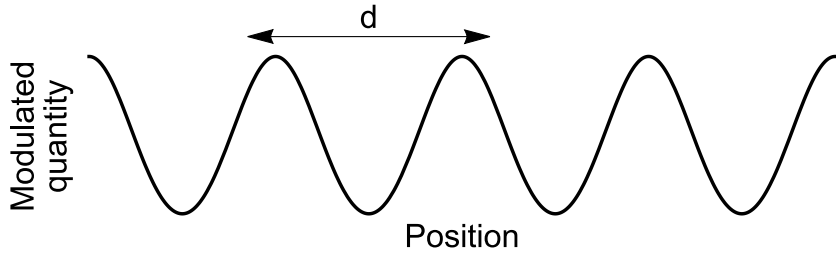
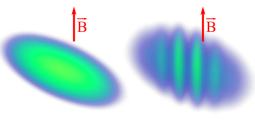
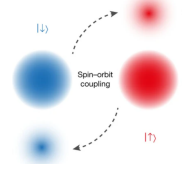
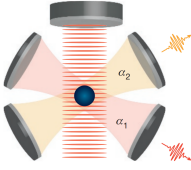
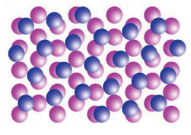
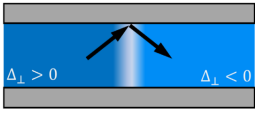
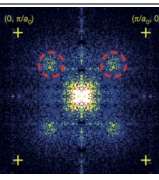
				
System	Modulated quantity	Lattice period d	Control parameter (at $T = 0$)	Dimensionality of the lattice
Dipolar BECs 	Number density	few $\mu\text{m} \sim l_z$ (harmonic vertical confinement)	$\epsilon_{dd} = a_{dd}/a_s$ (dipolar over contact)	1D or 2D
SOC BECs 	Number density	$\lesssim 1 \mu\text{m} \sim \lambda_R$ (Raman laser wavelength)	Ω_R (Raman coupling)	1D
BECS in cavities 	Number density	$\lambda_P / \cos 60^\circ \sim 1 \mu\text{m}$ (pump laser wavelength)	Ω_P (Rabi frequency of the pump laser) or pump-cavities detunings	1D
2D ^4He 	Number density	$< 1 \text{\AA}$	2^{nd} layer coverage	2D
Confined ^3He 	Energy gap	$\sim 1 \mu\text{m} \sim D$ (vertical confinement)	D (vertical confinement)	1D or 2D
PDWs in cuprates 	Energy gap and density of pairs	8 times the underlying lattice period (few nm)	Doping percentage	1D

Table 1.1: Modulated superfluid phases in recent experiments (see text). The images in the first column are from [15, 14, 13, 67, 70, 72] from top to bottom.

Experimental realization and detection of a dipolar supersolid

To realize dipolar supersolids, we work with bosonic dysprosium atoms cooled down to quantum degeneracy and trapped with optical methods. The key ingredient for the formation of the dipolar supersolid, the long-range and anisotropic dipolar interaction, arises due to the large permanent magnetic moment of dysprosium in its ground state, $\mu = 9.93 \mu_B$, about ten times larger than for alkali atoms, which means a dipolar interaction 100 times larger. According to the definition in Eq. 1.10, we quantify the strength of the dipolar interaction with the dipolar length, which for dysprosium is $a_{dd} = 130 a_0$, a large value that comes mainly from the large magnetic moment but also from the large mass. Therefore, to get into the strongly dipolar regime we need to tune the s -wave scattering length to values $a_s \sim 100 a_0$ and lower.

In this chapter, we describe the experimental setup for the production of the dysprosium BEC, the crossing of the supersolid phase transition tuning a_s and the imaging techniques to get information on the supersolid phase. Section 2.1 is a brief overview of the experimental sequence for the cooling of dysprosium to quantum degeneracy. Since this is not a specific topic of the thesis, we do not enter into details and we refer to [84, 85, 10] for further information on the experimental apparatus. In sections 2.2 and 2.3, we instead deepen the description of the imaging methods: the time of flight imaging after a free expansion and the in situ imaging, respectively. Note that the time of flight imaging is the standard technique that we employed in all the publications described in this thesis, while the in situ imaging was built appositely for the Josephson experiment, described in chapter 5, and is therefore absent in the other chapters.

2.1 Cooling and trapping Dy

Dysprosium is a rare-earth element belonging to the family of lanthanides (see the review [31] for a general description of the physics of ultracold lanthanides atoms). It has several abundant fermionic and bosonic isotopes. We work with the bosonic isotope ^{162}Dy , which has a relative abundance of 25.45 %. Some important properties of dysprosium are summarized in Tab. 2.1. The large magnetic moment of dysprosium arises from its peculiar submerged-shell electronic configuration, $[Xe]4f^{10}6s^2$, in which the higher energy orbital $6s$ is fully occupied, while the lower energy $4f$ orbital is populated by only 10 electrons. Among the 7 sublevels of the $4f$ orbital, 4 are populated by unpaired electrons which are

Table 2.1: Some key properties of the element ^{162}Dy .

μ (μ_B)	mass (amu)	a_{dd} a_0	T_{melting} ($^{\circ}\text{C}$)	T_{boiling} ($^{\circ}\text{C}$)	Ground state	Γ_{421} (MHz)	Γ_{626} (kHz)
9.93	161.93	130	1412	2560	5I_8	$2\pi \times 32.3$	$2\pi \times 136$

responsible for the high spin and orbital angular momentum quantum numbers, $S = 2$ and $L = 6$. The total angular momentum $\mathbf{J} = \mathbf{L} + \mathbf{S}$ has quantum number $J = 8$, which means a manifold of $2J + 1 = 17$ Zeeman sublevels. This large Zeeman space has been exploited to simulate bulk quantum Hall physics [86]. The spectroscopic notation for the ground state is 5I_8 . The bosonic isotopes of dysprosium (contrary to the fermionic ones) have an even number of protons and neutrons in the nucleus and hence they have zero nuclear magnetic moment \mathbf{I} . The hyperfine structure is, therefore, absent. Anyway, the excitation spectrum is very complex since excited states can be reached in many ways, both from the f - and s - electrons.

The melting point of dysprosium is $T_{\text{melting}} = 1412 \text{ }^{\circ}\text{C}$, so our source is heated up in an oven to produce an atomic beam. We typically work at $T = 1200^{\circ}\text{C}$, which is enough for the vapor pressure to produce a sufficient flux of Dy atoms. The critical condensation temperature, for our typical atom number and trap frequencies, is about $T_c \sim 60 \text{ nK}$. The main cooling stages to gap this 11 orders of magnitude in temperature are sketched in Fig. 2.1. We exploit two dysprosium resonances, both of them from the ground state $J = 8$ to an excited state $J' = 9$, involving the s -electrons. The first one is a strong transition at $\lambda = 421 \text{ nm}$ with a large linewidth $\Gamma_{421} = 2\pi \times 32.3 \text{ MHz}$, employed for the first stages of transverse and Zeeman cooling, but also for the imaging. The second one is at $\lambda = 626 \text{ nm}$ with a narrow linewidth of $\Gamma_{626} = 2\pi \times 136 \text{ kHz}$ and it is used for the Magneto Optical Trap (MOT).

Following the schematic sequence in Fig. 2.1, we start with a hot and fast atomic beam exiting from the oven. At $T = 1250 \text{ }^{\circ}\text{C}$, the mean velocity of the atoms is $v \sim 500 \text{ m/s}$. We employ a transverse cooling with two retroflected blue beams crossing perpendicularly with respect to the atomic beam (I), to cool down the transverse motional degree of freedom and limit the beam divergence. The atoms are then cooled in a spin-flip Zeeman slower (II) where the blue light counter propagates with respect to the atomic beam. The final velocity, at the position of the science cell, is of the order of 10 m/s . The third stage (III) consists of a 3D MOT on the narrow transition at 626 nm . We employ three retroflected beams with large waists and a quadrupole field generated by two coils in an anti-Helmholtz configuration. On one side, the small linewidth $\Gamma_{626} = 2\pi 136 \text{ kHz}$ ensures a small Doppler temperature $T_D = 3.3 \text{ } \mu\text{K}$, favorable for the subsequent optical trapping and evaporation. The downside of the narrow transition is that the capture velocity is low, about 5 m/s . Since atoms exiting from the Zeeman slower with a low velocity have also a large divergence, many of them can miss the MOT beams. To overcome this problem, we employ two different techniques. First, we frequency-modulate the MOT beams, effectively increasing the linewidth during the loading phase [87]. Second, we employ a final cooling

stage with the blue light, just before the MOT position, called angled slowing [88]. Two red detuned laser beams at 421 nm intersect in front of the MOT and exert a longitudinal force against the atoms, allowing for an increase of the final velocity at the end of the Zeeman slower and hence a reduced divergence of the cold beam. During the loading of the MOT, we polarize the sample in the ground state $m_J = -8$ with a magnetic field $B = 1.5$ G in the vertical direction. After the loading, we compress the MOT reducing the detuning and the intensity, to lower the temperature and increase the density. The typical final temperature is $T = 15$ μ K and the atom number is $N \sim 5 \times 10^7$.

From the MOT, we load the atoms in an optical trap realized by the standing wave pattern inside an in-vacuum optical resonator with finesse $\mathcal{F} \sim 1500$ (IV). The resonator is seeded by a single-mode laser at 1064 nm, which produces a deep trap of 200 μ K with a large waist of 300 μ m. This configuration ensures a large geometrical overlap with the MOT and an efficient loading into the optical trap with a limited input power (about 1 W) [89]. Inside the optical resonator, we perform a first stage of evaporative cooling and we load the atoms in an optical trap realized by two focused beams with $\lambda = 1064$ nm, ODT1 and ODT3, at a temperature $T \sim 3$ μ K (V). ODT1 has a waist of about 40 μ m, while ODT3 is elliptical with a horizontal waist of 80 μ m and a vertical one of 40 μ m. The two beams intersect at about 40°. We perform the final stage of evaporative cooling in the crossed dipole trap, in which the vertical trapping frequency is always larger than the average in-plane frequency, to avoid collapse due to the attractive part of the dipolar interaction. This is possible thanks to the ellipticity of the ODT3. We finally cross the thermal-BEC transition and form a BEC, for which the lowest detectable temperature, inferred from the thermal fraction in a free expansion, is 30 nK (VI) [85, 10]. The typical atom number can be adjusted between 2 and 5×10^4 atoms. As explained in section 1.2, the harmonic trapping has a cigar shape, with a weak confinement of about 20 Hz in one direction (x) and a tighter confinement in the vertical direction (z) of about 100 Hz. The transverse confinement (y) is variable by changing the relative power of the two trapping beams. In the experiment about the phase transition [15], described in chapter 3, we change the transverse confinement from 67 Hz to 100 Hz. In the experiment about the scissors mode [19], described in chapter 4, we instead work with the ODT3 plus another beam, ODT2, intersecting at an angle of 80°, see Fig. 2.1. This configuration produces smaller transverse frequencies, reducing the aspect ratio in the horizontal plane and favoring the excitation of the scissors mode, see chapter 4.

Tuning the interactions

We cross the BEC-supersolid phase transition by tuning the relative strength of dipolar and contact interactions, as explained in section 1.2. The dipolar length $a_{dd} = 130 a_0$ is fixed, and we tune the s -wave scattering length through Feshbach resonances. The relevant parameter for the phase diagram is $\epsilon_{dd} = a_{dd}/a_s$, and the critical value for the phase transition is around $\epsilon_{dd} \sim 1.4$, depending on the trap geometry and the atom number. We need therefore to tune the scattering length around the values 90-100 a_0 . Commonly to the other lanthanides atoms, dysprosium has a rich spectrum of Feshbach resonances [31]. We employ a set of two Feshbach resonances located around $B = 5.1$ G, characterized in

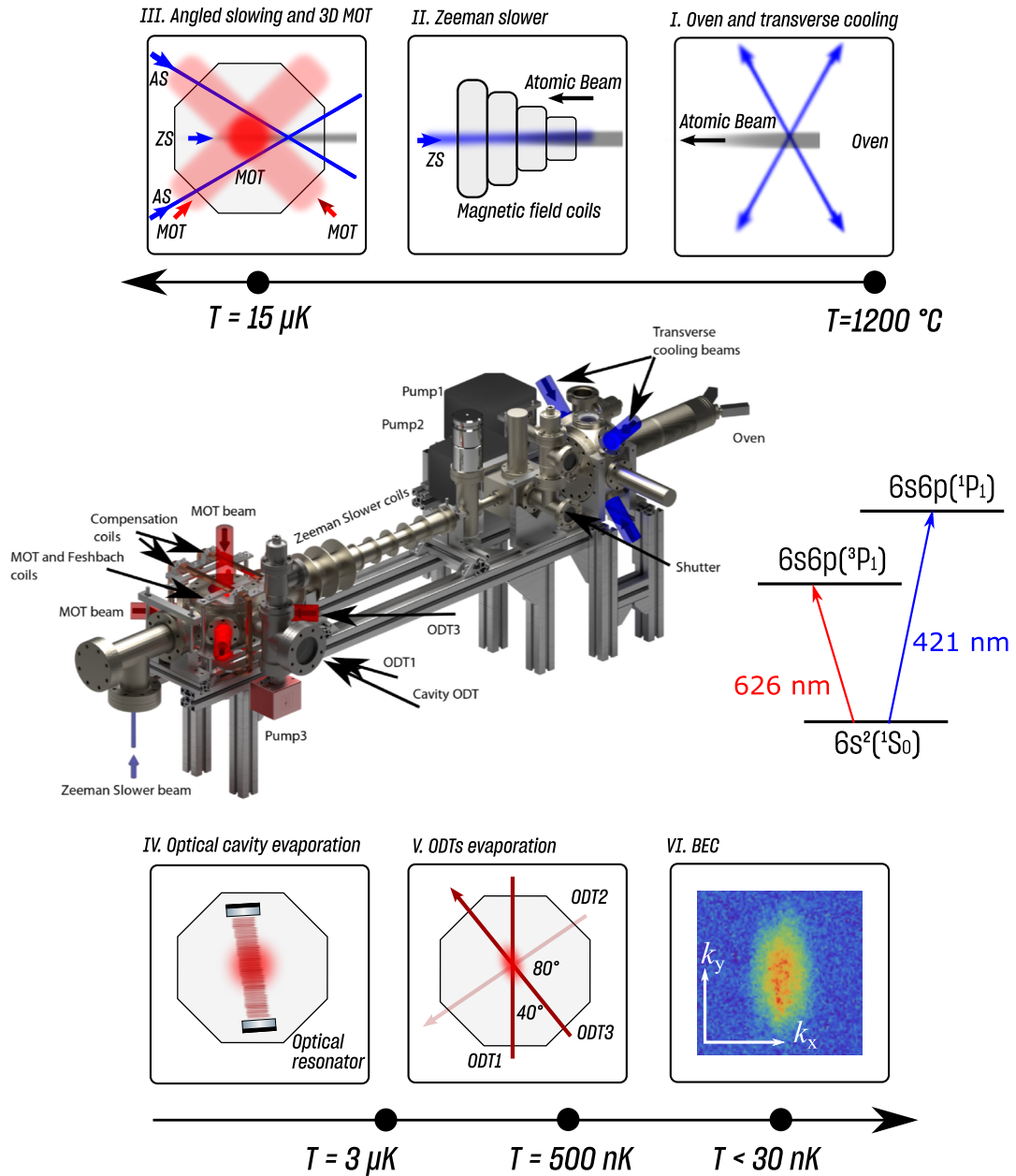


Figure 2.1: Experimental setup for the production of a dysprosium BEC [84, 85]. The two transitions employed for the cooling (421 nm and 626 nm) are highlighted. The insets show sketches of the main steps for the cooling and trapping on a temperature scale, from the production of the atomic beam in the oven (I) to the measured BEC density after a free expansion (VI). See text for a description.

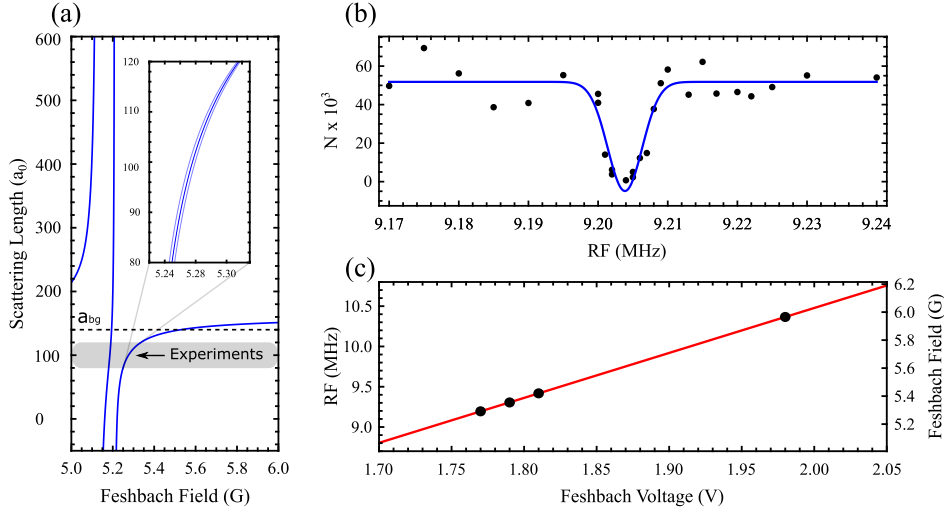


Figure 2.2: Tuning the interactions with Feshbach resonances. (a) Magnetic field B to scattering length a_s conversion in the region 5-6 G, where two resonances dominate [55]. The region in which we cross the BEC to supersolid transition and we perform the experiments reported in this thesis is shown in gray and corresponds to an interval of about 80-120 a_0 , highlighted in the inset. (b) Radiofrequency calibration of the Feshbach coils. The Zeeman resonance corresponding to a transition $m_J = -8 \rightarrow m_J = -7$ is detected through atom losses. (c) Finding the radiofrequency resonance at different values of the Feshbach coils' voltage, we calibrate the voltage to magnetic field conversion.

[55], with centers $B_1 = 5.126(1)$ G and $B_2 = 5.209(1)$ G and widths $\Delta B_1 = 35(1)$ mG and $\Delta B_2 = 12(1)$ mG plus a broader resonance at $B_3 = 21.95(5)$ G, with width $\Delta B_3 = 2.4(8)$ G, measured in [85]. The model for the B to a_s conversion is then

$$a_s(B) = a_{bg} \left(1 - \frac{\Delta B_1}{B - B_1}\right) \left(1 - \frac{\Delta B_2}{B - B_2}\right) \left(1 - \frac{\Delta B_3}{B - B_3}\right), \quad (2.1)$$

where $a_{bg} = (139 \pm 4) a_0$ is the background scattering length [55]. Eq. 2.1 is plotted in Fig. 2.2, where the relevant region for the experiments in the supersolid phase is highlighted. We typically produce the BEC around $a_s = 140 a_0$ and then lower the magnetic field to form the supersolid at the desired scattering length value. To calibrate the voltage of the Feshbach coils, we employ radio-frequency spectroscopy addressing the transition between the ground state $m_J = -8$ and the Zeeman level $m_J = -7$. The Zeeman splitting is

$$\Delta E_Z = \mu_B g_J B \quad (2.2)$$

where g_J is the Landè g -factor, which is 1.24 for the dysprosium ground state. When the radiofrequency energy $h\nu_{RF}$ matches the Zeeman splitting ΔE_Z , atoms are transferred in the excited Zeeman level and are lost due to inelastic dipolar scattering [31]. We scan the radiofrequency ν_{RF} at a fixed Feshbach voltage to find the resonance, shown in Fig. 2.2(b). Repeating the measurement for different Feshbach voltages, we calibrate the coefficients

in the conversion $B[G] = aFV[V] + b$, with $FV[V]$ the voltage of the Feshbach coils, as shown in Fig. 2.2(c). The width of the resonance is about 3 kHz, which translates into a 1 mG uncertainty in the calibration of the magnetic field. The magnetic field stability is 0.5 mG, resulting in an error in the scattering length of $0.3 a_0$. However, the background scattering length a_{bg} is known with quite a large error and dominates the error in the absolute scale of scattering lengths. Also with the latest and most precise measurement, performed through the critical atom number for the droplet formation [55], the error is 4 %, $a_{bg} = (139 \pm 4) a_0$, of the same order of the extension of the supersolid region ($\sim 6 a_0$ over $95 a_0$, 6 %). It is therefore very challenging to determine experimentally the critical scattering length. This is not a limitation, since in all the experiments in this thesis, we are not interested in the global scale of scattering lengths but only in relative changes. When we need to compare experimental and theoretical results, we identify a precise calibration of the absolute scale by comparing the critical point of the phase transition observed in the experiment and in the GPE numerical simulations [10, 15], as discussed in chapter 3.

2.2 Characterization of the supersolid phase: time of flight imaging

A very powerful technique in the field of ultracold quantum gases is the so-called time of flight imaging, which consists of switching off all the trapping potentials and letting the atomic gas expand in the gravitational field. After an expansion time t_{TOF} , we perform an absorption imaging at the resonant transition at 421 nm. In the ideal case of a non-interacting system, the real space density $\rho(\mathbf{r})$ is mapped, after a long enough expansion, in the momentum space density $\rho(\mathbf{k})$, related to the real space wavefunction by a Fourier transformation $\rho(\mathbf{k}) = |\text{FT}[\psi(\mathbf{r})]|^2$. In this simplified case, all the potential energy of the trap is transformed into kinetic energy. Since the spatial directions in which the gas is more strongly confined are the ones with more potential energy, the system acquires more kinetic energy along those directions. As a result, the aspect ratio of the atomic cloud gets inverted during the expansion: the smaller dimension in situ becomes the larger one after the time of flight. This technique is very useful, for example, to distinguish between a BEC and a thermal cloud. In the latter, many states with momentum $\mathbf{k} \neq 0$ are populated, and the expansion of the cloud is very fast: after a few ms it becomes too dilute to be detected with absorption imaging. In the BEC, on the other hand, the state with $\mathbf{k} = 0$ is macroscopically populated, and the expansion is much slower. For $t_{TOF} > 10$ ms, we observe a gaussian-shaped density distribution, centered around $\mathbf{k} = 0$. In the supersolid phase, instead, typical time of flight images in the $k_x - k_y$ plane are shown in Fig. 2.3. The density in momentum space shows an interference pattern, with typically three main interference fringes, corresponding to $k_x = 0$ and $k_x = \pm k_{rot}$. The interference comes from the overlap of the matter waves that form each cluster of the supersolid, each with its well-determined phase. The observed pattern comes mainly from next-neighboring clusters since coherences between more distant clusters would produce weaker peaks at smaller momenta [11]. The stripes are elongated along the k_y direction because in real

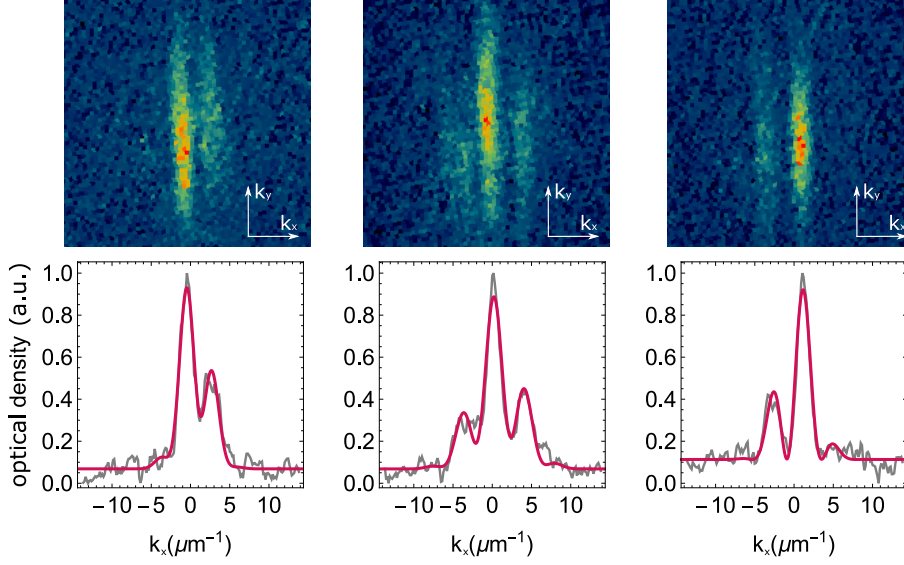


Figure 2.3: Time of flight images of the supersolid phase. Top row: absorption images of the momentum distribution in the $k_x - k_y$ plane after $t_{\text{TOF}} = 61$ ms. Lower row: integrated momentum distribution $\rho(k_x)$ and corresponding double slit fit (red lines) with the function in Eq. 2.4. The images show three typical situations with different phase differences, from left to right, $\varphi \sim 0.2\pi, 0.5\pi$ and 0.8π . The middle case corresponds to the ground state of the system.

space the system is more confined in the y than in the x direction. The relative amplitude of the interference peaks is determined by the relative phase φ between the clusters. The interference pattern is qualitatively similar to that of a coherent laser field diffracted by a rectangular double slit. In that case, the intensity recorded on a screen in the far field is

$$I(x) = I_0 \frac{\sin^2\left(\frac{\pi ax}{\lambda L}\right)}{\left(\frac{\pi ax}{\lambda L}\right)^2} \cos^2\left(\frac{\pi dx}{\lambda L} + \varphi\right). \quad (2.3)$$

The first factor is the diffraction pattern from the single slit, whose dimension is a and whose distance from the screen is L . The second factor is the interference between the two slits, whose separation is d . The phase difference of the electric field between the two slits is φ , and λ is the wavelength of light. The width of the envelope (the central diffraction peak) is proportional to the inverse of the single slit dimension a , while the period of the interference fringes to the inverse of the slit separation d , see Fig. 2.4. Analogously, in the supersolid interference pattern, the width of the envelope is of the order of one over the cluster's dimension, while the distance between the fringes is proportional to the inverse of the supersolid period d , $k_{\text{rot}} \sim 2\pi/d$. There are however some differences compared to the electromagnetic analogue, as sketched in Fig. 2.4(b). First, the density clusters do not have sharp edges like the rectangular slits, therefore we use a gaussian envelope instead of the cardinal sine. Second, we add a second gaussian with the same width of

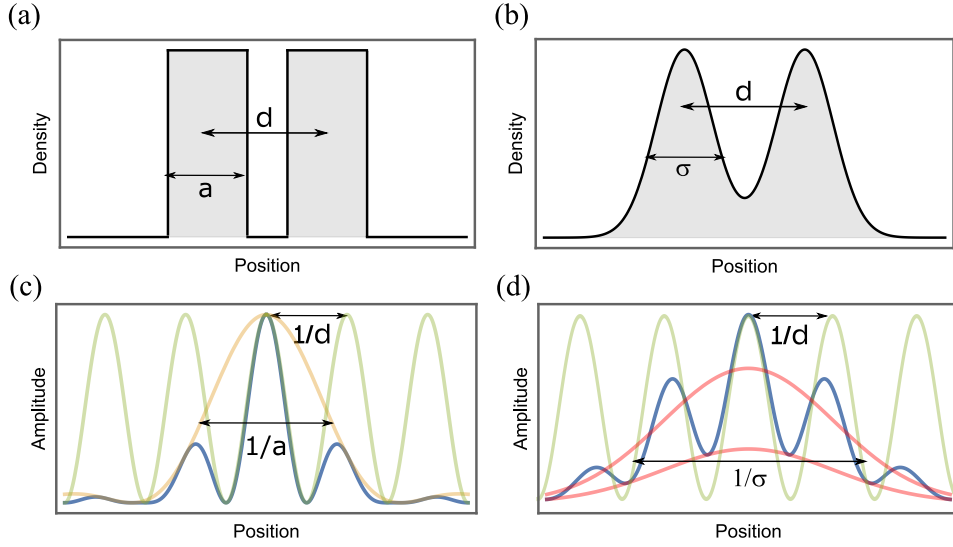


Figure 2.4: Sketch of the modelization of the interference pattern. In a double-slit (a) the interference pattern is given by Eq. 2.3, plotted in (b) as a blue line, together with the interference (green) and the envelope (yellow) terms. For the supersolid clusters (b) we modify the interference pattern as in Eq. 2.4, plotted in (d) as a blue line, together with the interference (green) and gaussian (red) terms.

the envelope to take into account the finite contrast of the interference. The contrast is less than one for two reasons: the optical resolution of the imaging system is finite, about $0.2 \mu\text{m}^{-1}$ in momentum space ($1/e$ gaussian width) [10], and the clusters have a finite overlap, depending on the amplitude of the density modulation, and hence on the value of the interaction parameter ϵ_{dd} . The resulting double slit fitting model is

$$\rho(k_x) = A e^{-\frac{(k_x - k_0)^2}{2\sigma_k^2}} \left[1 + A_1 \cos^2 \left(\frac{\pi}{k_{rot}} (k_x - k_0) + \varphi \right) \right], \quad (2.4)$$

where σ_k is the width of the envelope and k_0 is the center of the interference pattern. In Fig. 2.3 three examples of time of flight images are depicted with the corresponding integrated density distribution $\rho(k_x)$ and the fitted model of Eq. 2.4.

Time of flight images are needed to get information on the relative phase φ , which is not measurable in situ. On the other hand, in situ imaging is preferable for measuring quantities related to the real-space density, such as the period or the amplitude of the density modulation. However, an optical microscope with a good enough spatial resolution is required to image the density modulation in situ, which wasn't available in the experiment at the beginning of my PhD. In the next section, we will describe an implementation of such a microscope. Nevertheless, it is possible to get information on the density modulation also from the time of flight images. The task would be very simple if the hypothesis of the absence of interactions during the expansion were correct. In that case, the real space and momentum space densities would be linked just by a Fourier transform, and

from a measurement of the latter would be possible to quantitatively trace it back to the real space density. Unfortunately, interactions play a relevant role in the expansion. Both contact and dipolar interactions affect the expansion of the atomic cloud in the first milliseconds, while they get transformed into kinetic energy. Afterwards, the gas becomes much more dilute and the expansion is effectively interaction-free. While the Fourier transform still gives qualitative information about the observed time of flight images (for example the order of magnitude of the period, $d \sim 2\pi/k_{rot}$) it is difficult to extract more precise information. The role of contact interactions in the interference of multiple BECs is relatively well understood [90, 91], but the more complex dipolar interaction is much more difficult to model. The role of the dipolar interaction has been measured in the expansion of a chromium BEC through the modification of its aspect ratio [92], and some simulations studied the interference fringes produced by the expansion of two separated dipolar BECs [93], but there is no work on the expansion of the supersolid phase. In the experiment, to mitigate the role of dipolar interactions in the expansion dynamics, we ramp the scattering length to $a_s = 140 a_0$ about 200 μs before the release of the atoms from the trap.

We developed an empirical analysis to quantitatively measure the formation of the density modulation in the superfluid-supersolid transition from the time of flight images [15]. The idea is that the relative amplitude between the lateral and central peaks of the interference pattern is proportional to the density contrast between minima and maxima in the real space density. On the BEC side, it is zero because there are no lateral peaks, and it starts increasing entering the supersolid region, where the lateral peaks become more and more visible. We therefore define a contrast $\tilde{C} = \max^L / \max^C$ as depicted in Fig. 2.5. There are two technical problems with this definition. The first is that the amplitude of the lateral peaks is not always symmetric, but it changes for different values of the relative phase φ . Since we do not want to take into account the phase degree of freedom, but only the density modulation, we first shift the fitted momentum density $\rho(k_x)$ imposing $\varphi = \pi/2$, to get the symmetric configuration plotted with a red line in Fig. 2.5. The second problem is that we would like an observable capable of distinguishing between the BEC and supersolid phase. As a matter of fact, the contrast \tilde{C} is not always zero on the BEC side, because the double slit fit sometimes finds a fictitious lateral peak due to fluctuations in the shape of the gaussian profile. To overcome this problem, we define a second observable taking into account also the minimum between the two peaks, $\tilde{C}_{control} = (\max^L - \min) / (\max^L + \min)$, which is indeed zero on the BEC side, because eventual fictitious lateral peaks practically coincide with their relative minimum. We use $\tilde{C}_{control}$ as a control parameter: if $\tilde{C}_{control} = 0$, we set $\tilde{C} = 0$. We do not use $\tilde{C}_{control}$ to quantify the density modulation on the supersolid side because we found that it is much more sensitive to the atom number than \tilde{C} . Typically, as a function of ϵ_{dd} , $\tilde{C}_{control}$ has a maximum in the supersolid region and then starts decreasing, because the atom number decreases approaching the droplet crystal.

Fig. 2.6 summarizes the information we get from a time of flight experiment, as a function of ϵ_{dd} . The contrast \tilde{C} increases from zero on the BEC side up to about 0.6 in the supersolid, then saturates. The point in which \tilde{C} becomes larger than zero sets the experimental transition point. The complementary observable, φ , has a narrow distribution

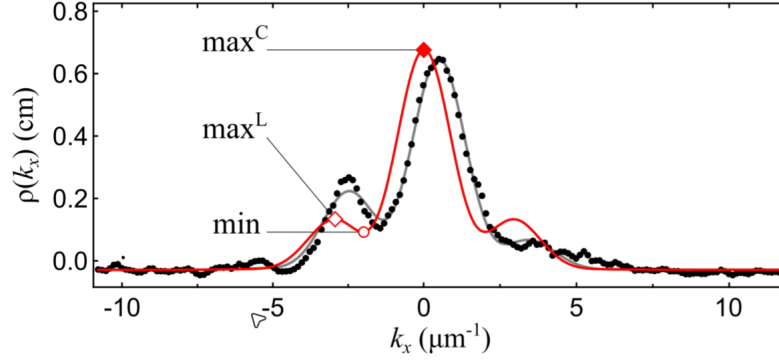


Figure 2.5: Definition of the momentum space contrast \tilde{C} . Black points are the measured momentum space density $\rho(k_x)$ in a time of flight experiment, in the supersolid regime. The gray solid line is the double slit fit in Eq. 2.4. The red solid line is the result of the fit shifted such that $\varphi = \pi/2$. Markers indicate the points employed in the definition of \tilde{C} and $\tilde{C}_{\text{control}}$: the central and lateral maxima max^C and max^L , and the relative minimum min .

in the middle of the supersolid phase and gets larger approaching the droplet crystal phase. Contrary to the BEC-supersolid transition, we are not able to detect a clear transition from the supersolid to the droplet crystal phase.

2.3 Characterization of the supersolid phase: in situ imaging

Although from time of flight images we can get information on both the phase coherence and the density modulation of the supersolid phase, there are observables that we can only measure in situ. One major example is the relative population between the clusters, a key quantity to understand the Josephson effect, as discussed in chapter 5. During my PhD, we built an optical microscope to measure the density of the supersolid in real space. This section deals with the optical setup and the experimental techniques employed to get real space images of our system.

Test of the imaging system

The geometry configuration of our vacuum cell combined with the actual cooling and trapping schemes, which determine the final position of the atomic cloud, limits the minimum atom-lens distance to be about 50 mm. It is not possible, therefore, to reach a high numerical aperture and a sub-micron resolution, as in modern quantum gas microscopes. However, our goal is to resolve relatively large structures, because the lattice period of the supersolid is of the order of 4 μm . To successfully resolve the population of the different clusters, we need an imaging system with a resolution smaller than this value. We developed a very simple optical scheme, with a commercial lens¹ with a focal

¹Achromatic doublet AC508-075-A, Thorlabs.

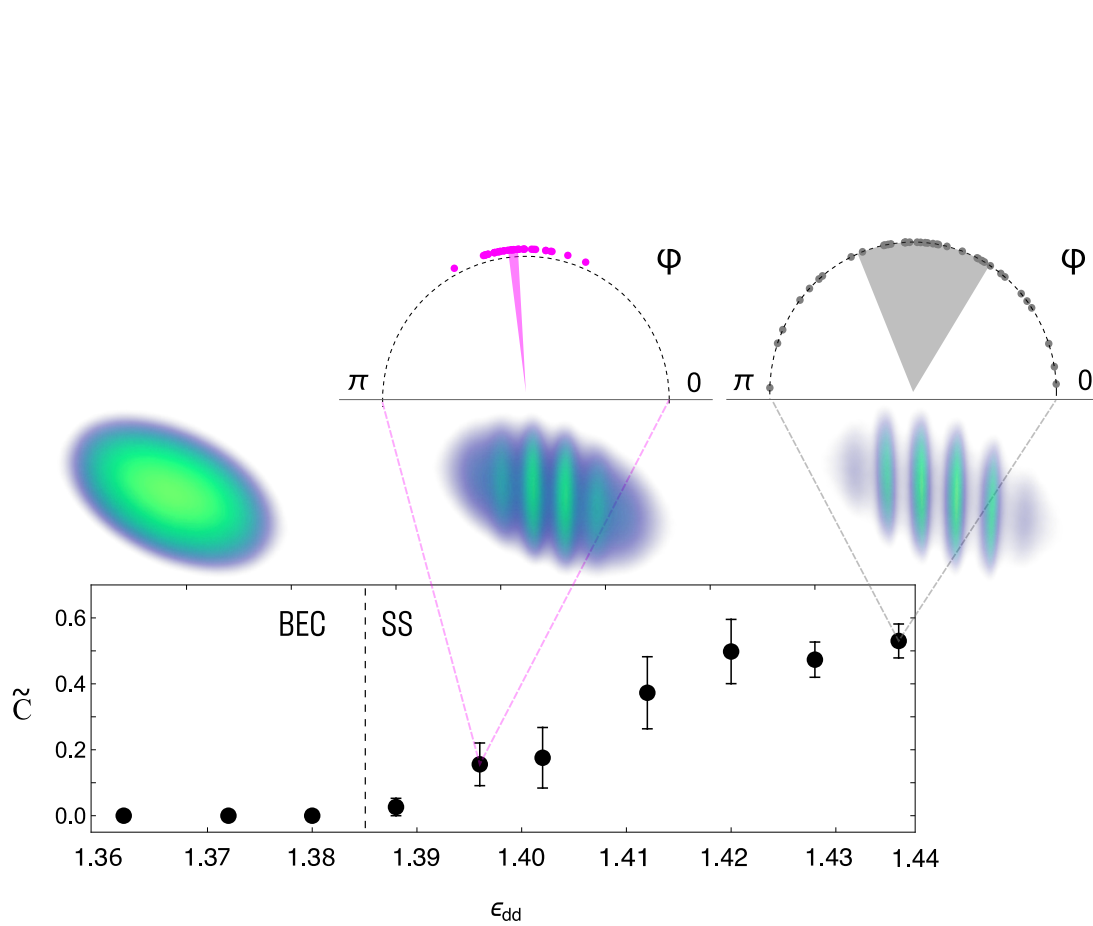


Figure 2.6: Supersolid formation in time of flight images. Lower row: contrast in momentum space \tilde{C} as a function of ϵ_{dd} in the same experimental configuration as in Fig. 2.3. The vertical dashed line indicates the BEC-supersolid transition. Middle row: 3D sketches of the real space density in the three phases BEC, supersolid, and droplet crystal, from left to right, respectively. Upper row: phase φ distributions for about 30 different experimental shots at the center of the supersolid regime at $\epsilon_{dd} = 1.396$ (pink data) and close to the droplet crystal regime $\epsilon_{dd} = 1.436$ (gray data).

length of 75 mm (f_1) and a second lens with a focal length of 500 mm (f_2) to focus the image of the atoms on a camera. The sketch of the scheme and some measurements to test the objective are shown in Fig. 2.7. To get an estimate of the optical resolution, we took images of a standard USAF target², composed by many groups of three black lines with different dimensions. In Fig. 2.7(c) the element with spacing 3.48 μm , similar to the period of the supersolid, is shown. We select a portion of the image, integrate it in the vertical direction and obtain a 1D profile, where the steps of the target are blunt by the finite resolution. We fit the 1D profile with the convolution of a sum of step functions, representing the target, and the point spread function of the optical system, approximated by a gaussian with width σ

$$f(x) = A \sum_{i=1}^3 \int \text{Step}(y - id) e^{-(x-y)^2/(2\sigma^2)} dy, \quad (2.5)$$

where $\text{Step}(x) = 1$ if $|x| \leq d/4$ and 0 otherwise. The width σ is related to the optical resolution by $\text{res} = \sigma/0.35$. We repeated the measurement for different positions in the vertical direction of the first lens, which was mounted on a translational stage. The results are plotted in Fig. 2.7(d). We obtain a minimum around $\text{res} = 2 \mu\text{m}$.

Phase-contrast imaging

The technique of absorption imaging, that we use for the time of flight images, is not suitable for detecting the real space density. Especially in the supersolid regime, the sample is much more dense than in the BEC, and the absorption tends to saturate. For this reason, we employ phase-contrast imaging on the 421 nm transition line, which relies on the dispersive phase shift introduced by the atoms on the light field at large detunings from resonance. This technique has been introduced for the imaging of lithium BECS [94], and more recently has been employed in an experiment on dysprosium quantum droplets [9].

Since the absorptive and dispersive parts of the atomic polarizability scale with the detuning Δ and the linewidth Γ as $(\Gamma/\Delta)^2$ and Γ/Δ , respectively, at large detunings the dispersive interaction prevails over the absorption. A sketch of the implementation of phase-contrast imaging in our system is shown in Fig. 2.8. The physical mechanism is based on an interferometric measurement. We employ light with linear polarization, propagating in the vertical direction so that the electric field is perpendicular to the polarizing magnetic field. The linear polarization can be thought of as a superposition of two opposite circular polarizations, with complex versors \hat{e}_+ and \hat{e}_- . The atoms are in the ground state with $m_J = -8$. The two circular polarization components drive the transition to the excited states $m_{J'} = -7$ and $m_{J'} = -9$, respectively. However, the first transition is suppressed compared to the second one by a factor of 150, due to the difference in Clebsch-Gordan coefficients. Practically, the atoms interact only with the σ_- polarization. After interacting with the atoms, the two components of the electric field take a relative phase β

²1951 USAF Test Target, Thorlabs

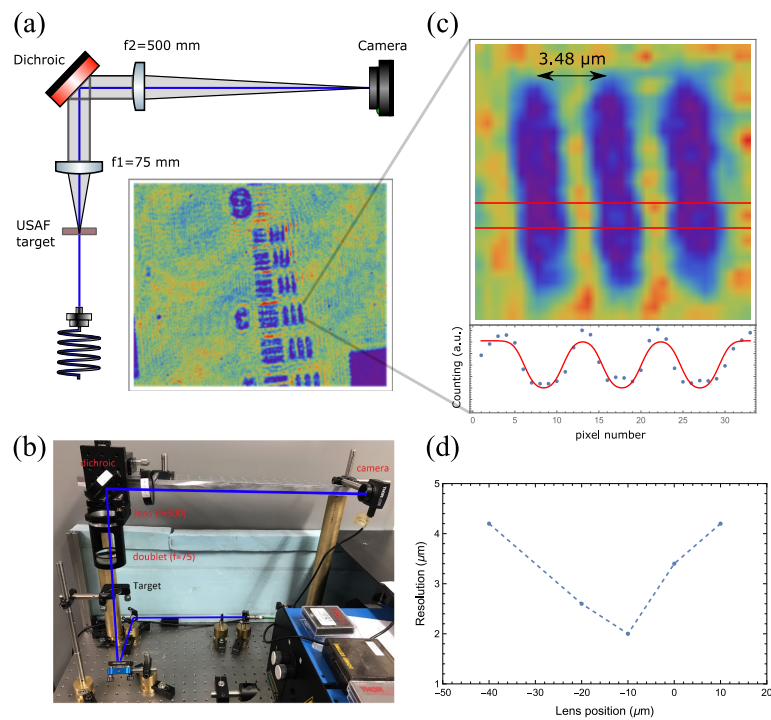


Figure 2.7: Test of the in situ imaging system. (a) Sketch of the optical scheme. Collimated blu light (421 nm) goes through a USAF target and is collected by a commercial lens f_1 . After the reflection from a dichroic, the image is focused by a second lens f_2 on a camera. The inset shows a typical image of the group of the target. (b) Photograph of the test setup. (c) Image of element 2, group 7, of the USAF target, with period $3.48 \mu\text{m}$, similar to the supersolid one. Red lines indicate the selected area for the estimation of the resolution. In the inset, the integrated 1D profile is fitted with Eq. 2.5, shown as a red line. (d) Fitted resolution as a function of the vertical position of the first lens f_1 , displaying a minimum at $\text{res} = 2 \mu\text{m}$.

$$\mathbf{E} = \frac{E_0}{\sqrt{2}}(\hat{e}_+ + \hat{e}_-) \rightarrow \mathbf{E} = \frac{E_0}{\sqrt{2}}(\hat{e}_+ + e^{i\beta}\hat{e}_-). \quad (2.6)$$

The dispersive phase β is proportional to the optical density OD , hence to the real space density, $\beta \propto \rho(x, y)(\Gamma/\Delta)$. To gain spatial information from the phase β , we combine the two components with a $\lambda/2$ waveplate and a polarizing beamsplitter, which select a polarization axis forming an angle θ with the original light polarization. The observed intensity is $I = I_0 \cos^2(\theta - \beta/2)$. In the absence of atoms ($\beta = 0$), no light is detected if $\theta = \pi/2$, while all the light is detected if $\theta = 0$. The first case is called 'dark-field' imaging, and one can show that the signal goes as β^2 for small β . At $\theta = \pi/4$, instead, the signal is linear in β . Changing θ , therefore, one can adjust the signal-to-noise ratio. Since the strength of the atom-light interaction depends on Γ/Δ , the total signal depends also on the detuning. Increasing the detuning suppresses the absorption and heating of the sample, but also decreases the dispersive signal, for a fixed power. In our case, we found a good compromise with $\Delta = 5\Gamma$ and $\theta = 60^\circ$.

The final image is acquired by an Andor camera. Assuming a linear camera response, the intensity recorded I_c is proportional to the real one I , $I_c = AI + B$. To get a signal independent of the camera parameters, we take three images. The first one I_1 is taken with both the imaging light and the atoms and contains the relevant information on the density. The second one I_2 is taken with the imaging light but without the atoms ($\beta=0$). The last one I_3 is a picture of the background, without the imaging light ($I_3 = B$). Extracting the angle β from the intensity $I = I_0 \cos^2(\theta - \beta/2)$, we get a signal proportional to the real space density ρ

$$\rho \propto \frac{\Delta}{\Gamma} \left[\theta - \arccos \left(\sqrt{\frac{I_1 - I_3}{I_2 - I_3}} \cos \theta \right) \right]. \quad (2.7)$$

Compared to the test setup in Fig. 2.7, we added a third lens with $f_3 = 75$ mm which focuses the primary image into the camera, to increase the total magnification. We measured the magnification with a large-period optical lattice (employed for the Josephson experiment, see Chapter 5). After loading the BEC in a deep lattice, we measured the period from time of flight images, for which the magnification of the imaging system was known. Then, from in situ images we calibrated the total magnification, which results in $M = 67(2)$.

In situ imaging of the supersolid phase

In order to search for the optimal position of the first lens f_1 , we loaded the BEC in our 1D optical lattice with period $8 \mu\text{m}$, used also for the measurement of the magnification. When the lattice potential is high, i.e. larger than about 100 nK, the BEC is well separated into typically three sites, without tunneling between them. We changed the position of f_1 , mounted on a 3D translational stage, searching for the configuration in which the three sites of the BEC were best resolved. A typical image of the supersolid phase in our best configuration is shown in Fig. 2.9. Although the period is similar to the one of

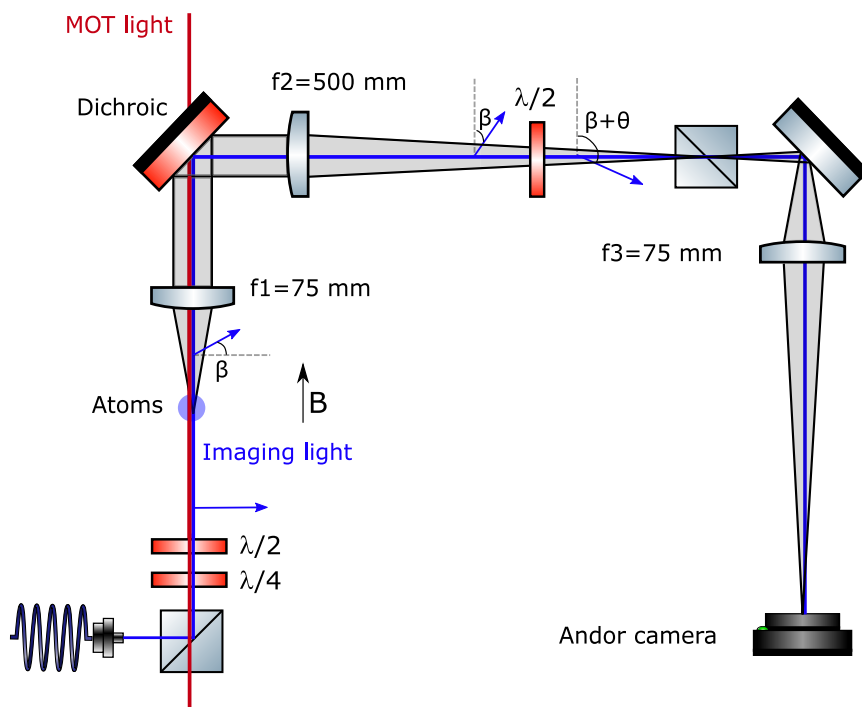


Figure 2.8: Optical scheme of the phase-contrast imaging. We employ linearly polarized light at 421 nm (blue line) detuned by $\Delta = 5\Gamma$ from the transition. After the interaction with the atoms, the σ_+ and σ_- components of the electric field take a relative phase β , proportional to the real space density. A $\lambda/2$ waveplate has its axis rotated by an angle θ to the original polarization, which determines how much light is transmitted by a polarizing beamsplitter. The image is magnified by an objective composed of three lenses and recorded by an Andor camera. We employ a dichroic mirror above the atoms to separate the imaging light at 421 nm from the MOT light at 626 nm (red line).

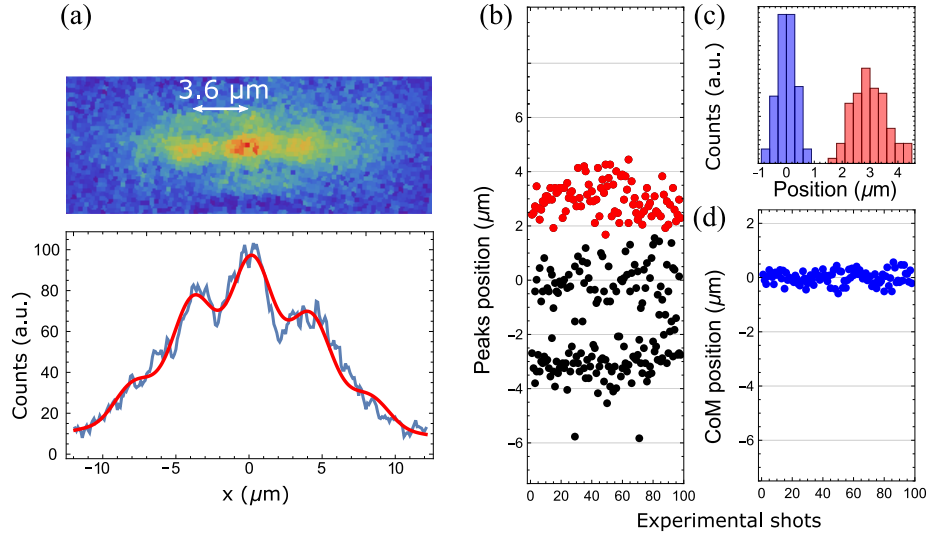


Figure 2.9: In situ imaging of the supersolid phase. (a) Supersolid with about $N \sim 3 \times 10^4$ atoms, at $\epsilon_{dd} = 1.42$, in the xy plane. The 1D density $\rho(x)$ is fitted with the function in Eq. 2.4 (red line) to extract the period and positions of the peaks. (b-d) Observation of the low-energy Goldstone mode. Positions of the three supersolid clusters (b) and of the center of mass in the x direction (d) for about 100 experimental runs, together with the histograms of the position of one of the supersolid clusters (red) and the center of mass (blue) (c). The standard deviations are $\sigma_{cluster} \sim 1 \mu\text{m}$ and $\sigma_{com} \sim 0.4 \mu\text{m}$, respectively.

the USAF target in Fig. 2.7, the imaging of the supersolid phase is much more difficult, because the density contrast can be much smaller than 1, and strongly depends on the atom number, possible thermal backgrounds, and the interaction parameter ϵ_{dd} . Moreover, the window of the science cell introduces aberrations. We found, indeed, that the best configuration is the one in which we reduce the numerical aperture of the lens with an iris, losing in resolution but eliminating aberrations and globally increasing the quality of the images. Although we don't have a quantitative measurement of the resolution in the final configuration, comparisons with numerical simulations suggest that it is about 3 μm, instead of 2 μm as measured in the test setup. In Fig. 2.9(a) we resolve three clusters, separated by $d = 3.6 \mu\text{m}$. Depending on the final atom number, we can have also two- and four-cluster configurations.

As a first in situ measurement, we report in Fig. 2.9(b-d) the positions of the three supersolid clusters for different repetitions of the experiment. We observe that the single peaks always form in slightly different positions, while the center of mass is much more stable. This is a clear signature of the low-energy Goldstone mode, arising due to the broken translational symmetry. In an infinite, homogeneous system, the Goldstone mode would have zero energy, and all the possible positions of the lattice would be equally favorable. In our case, the presence of the harmonic trap fixes the position of the main clusters in the middle, and the Goldstone mode reveals itself in oscillations around this position, with an energy much lower than the trap frequency. The change in the position of the lattice comes with a superfluid flow which keeps the center of mass fixed. The presence of the low-energy Goldstone mode was first demonstrated by the Stuttgart group

[46]. The analog Goldstone modes with higher energy were observed by the Pisa group studying the splitting of collective modes in time of flight images [45]. The presence of the low-energy Goldstone mode has implications for the physics of the self-induced Josephson junction, discussed in chapter 5.

The superfluid-supersolid quantum phase transition

Classical phase transitions from a liquid to a solid state are usually of the first order, meaning that the order parameter itself, and not only its derivatives, has a discontinuity at the critical point [17]. The dipolar supersolid is, however, very different from a classical solid. First, each lattice site is a macroscopic cluster of thousands of atoms and second, the inter-particle interactions have Van der Waals, dipolar, and purely quantum (LHY term) contributions. It is not possible, therefore, to make predictions about the nature of the superfluid-supersolid phase transition based on its classical counterpart. As an example of the supersolid counterintuitive behavior, it was recently shown [95] that increasing the temperature on the superfluid side induces a classical transition to the supersolid phase, exactly the opposite of what happens for classical solids.

Moreover, in our experiment, we cross the phase transition at the lowest temperature we can achieve, well below the condensation temperature. In a classical phase transition, the temperature is changed and thermal fluctuations are responsible for the formation of a new phase. In our case, the control parameter is another parameter of the hamiltonian, namely the magnetic field which controls the strength of contact interactions between atoms. In this configuration, we expect quantum fluctuations, rather than thermal fluctuations, to be driving the phase transition. We therefore deal with a quantum, rather than classical, phase transition [96].

The knowledge of the order of the phase transition has a twofold importance. From a fundamental point of view, first- and second-order transitions share some very general phenomenology, regardless of the system in which the transition actually takes place. For example, the discontinuous nature of a phase transition involves the existence of metastable states near the critical point, linked to hysteresis and the release of latent heat [17]. In continuous phase transitions, the Kibble-Zurek theory is widely employed to describe the emergence of the ordered phase after quenches across the critical point [97]. On the other hand, the nature of the transition has deep implications in the experimental realization of the ordered phase. Realizing the supersolid with a discontinuous phase transition unavoidably produces excitations, which can disturb the experimental measurements [45, 19], while in a continuous transition, it is in principle possible to adiabatically prepare the ground state of the system.

Even if in the last few years numerous theoretical and experimental investigations on the dipolar supersolid phase have been carried out, there was no general consensus about the order of the superfluid-supersolid quantum transition, and the literature offered a quite

complex scenario. For infinite systems in the thermodynamic limit, the situation is simpler, with some general models predicting a discontinuous transition in 2D [98, 99, 100] and a continuous one in 1D [101]. In trapped systems, the finite size and the inhomogeneity introduced by the harmonic confinement considerably complicate the problem. Theoretical simulations predicted both continuous and discontinuous phase transitions to a plethora of supersolid states, from 1D arrays in infinite tubes [102, 103] to triangular, honeycomb and labyrinthic phases in oblate trapping geometries [104, 105]. In simulations performed in current experimental conditions, the transition was predicted to be discontinuous in 2D [106, 48]. On the experimental side, there were partial indications of both a discontinuous [19, 10, 11, 45, 9] and a continuous transition [107].

In this chapter, we discuss a systematic study of the quantum phase transition in our elongated trapping geometry. The results are published in the main paper [15] and in a theoretical follow-up [56]. We find clear signatures of both continuous and discontinuous transitions, depending if the crystal structure has a 1D or a 2D nature. The resulting scenario is a dimensional crossover in which the order of the transition can be tuned through the geometry of the system. We interpret our results on the basis of the general Landau theory, connecting our observations in the small, trapped systems to general results in the thermodynamic limit. The peculiarities of our dipolar supersolid emerge clearly. First, the shape of the crossover from continuous to discontinuous transition is determined by the high compressibility of the supersolid, which can accommodate a 2D structure in the density background. Second, the crystallization in macroscopic clusters allows us to observe the character of the phase transition even in our lattice made of a few sites, limiting the impact of finite-size effects. Finally, we explain some observations with the presence of the unusual LHY energy contribution.

The structure of this chapter follows a line of increasing complexity. In the first section 3.1, we develop the Landau theory for a crystallization phase transition in an infinite dipolar system, both in 1D and 2D. The Landau theory only deals with the ground state of the system and neglects dynamical effects and fluctuations, but it gives the basis of our dimensional interpretation of the order of the phase transition. In the second section 3.2, we focus on the experimental trapped system. We therefore introduce the inhomogeneity of the harmonic trap and finite size effects. However, we study only ground-state simulations, neglecting again dynamical effects and fluctuations. In the third section 3.3, we discuss the experimental observations of both continuous and discontinuous transitions and the validation of the dimensional interpretation. In the experiment, the dynamics, the excitation of collective modes and the fluctuations are important, and we discuss them in detail.

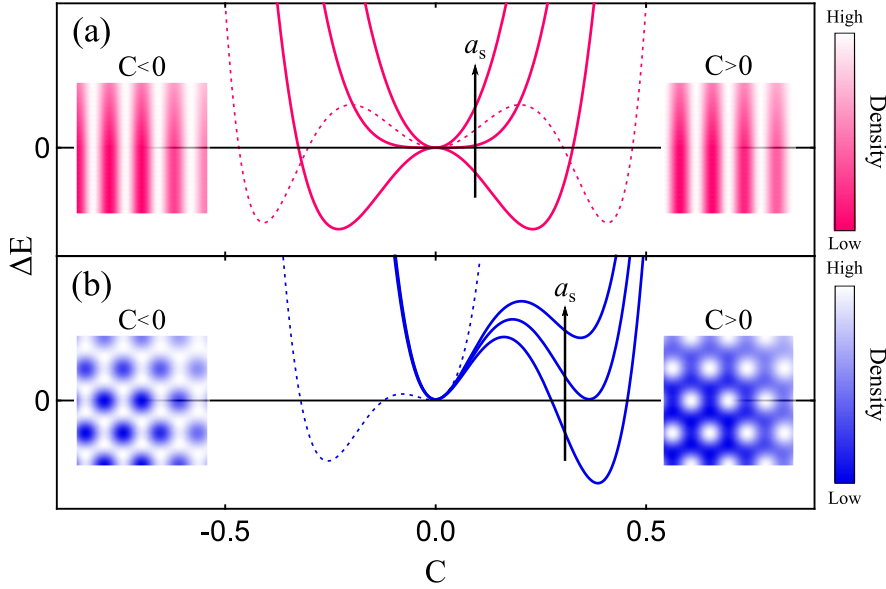


Figure 3.1: Sketch of the Landau theory for the superfluid-supersolid quantum phase transitions. (a-b) Energy difference ΔE between homogeneous and modulated states as a function of the contrast C . The transition happens when the energy develops an absolute minimum with $C \neq 0$. (a) 1D lattice. In 1D the energy is an even function of C and leads to a second-order phase transition. Two states differing only for the sign of C are sketched in the insets and are physically equivalent. The dashed line shows the LHY-induced first-order transition, see text. (b) 2D lattice. The energy is an odd function of C and develops a barrier between the minimum in $C = 0$ and the one in $C \neq 0$, leading to a first-order phase transition. Insets: density modulations with $C > 0$ (triangular lattice) and with $C < 0$ (honeycomb lattice), physically different. The dashed line is the LHY-induced transition to the honeycomb lattice, see text.

3.1 Landau theory for the superfluid-supersolid transition

Here we develop a simple model based on the Landau theory of phase transitions, for an infinite system undergoing the superfluid-supersolid quantum phase transition. The model, even if very different from the actual physical realization, simply catches the main effect of dimensionality in the order of the transition, and it is very helpful in getting an intuition about the phenomena observed in the real trapped system. Moreover, even if our model is not quantitative, it is able to predict some qualitative features we observe in numerical simulations, and even, to some extent, the role of the trapping confinement.

In the Landau theory, the behavior of a system near a phase transition is described by the so-called order parameter, which is zero on one side of the transition and different from zero on the other side. For symmetry-breaking phase transitions, the order parameter is zero in the disordered phase and becomes different from zero in the ordered phase. Famous examples are the ferromagnetic phase transition, in which the order parameter is the magnetization (zero in the paramagnetic state and different from zero in the ferromagnetic

state), or the superfluid phase transition, in which the order parameter is the complex wavefunction of the condensate [16]. For crystallization phase transitions, breaking the continuous translational symmetry of space, a possible order parameter is the density contrast C between the maxima and the minima in the density. The contrast is zero in the liquid-like phase (uniform density) and larger than zero in the crystal phase. In Landau's theory, the energy of the system is expanded in powers of the order parameter when it is close enough to the transition point, hence when the order parameter is small

$$\Delta E = aC + bC^2 + cC^3 + dC^4 + .. \quad (3.1)$$

where ΔE is the energy difference between the ordered state ($C = 0$) and the symmetry-broken one ($C \neq 0$). When ΔE is negative, the ground state of the system changes and the phase transition happens. For classical phase transitions, ΔE refers to the free-energy difference, which takes into account also the temperature. The coefficients of the expansion $a, b, c, d..$ depend on the temperature, which is typically the control parameter. In the superfluid-supersolid quantum phase transition, the control parameter is the scattering length a_s and we consider zero temperature $T = 0$, so that ΔE is directly the energy difference.

To model our dipolar system close to the transition point, a commonly employed ansatz for the density is a sinusoidal one

$$\rho(\mathbf{r}) = \rho_0 \left[1 + C \sum_i \cos(\mathbf{k}_i \cdot \mathbf{r}) \right], \quad (3.2)$$

where ρ_0 is the average density and \mathbf{k}_i the lattice wavevectors determining the dimensionality. The coordinate \mathbf{r} refers to the xy plane, $\mathbf{r} = (x, y)$. We integrate out the vertical coordinate z , and the vertical dimensions are absorbed in the averaged density ρ_0 . We will refer to 1D or 2D supersolids depending on the breaking of translational invariance happening along one or two dimensions, even if the system is always 3D from a collisional point of view.

As usual in the context of Landau's theory, we can gain information on the nature of the phase transition from the symmetries of the order parameter, as sketched in Fig. 3.1. For 1D lattices, the density ansatz in Eq. 3.2 describes a stripe state that is symmetrical with respect to the operation $C \rightarrow -C$, which produces only a global shift of the stripes. Due to this symmetry, the energy ΔE must be unchanged when $C \rightarrow -C$, hence all the odd terms in the energy expansion must disappear $a = c = .. = 0$. The remaining even terms lead to a second-order phase transition, depicted in Fig. 3.1(a). When the scattering length is lowered, the density-modulated state gains energy until it becomes the ground state. The transition is smooth, because the new minimum appears for arbitrary small values of C . On the other hand, 2D lattices don't have the symmetry in the sign of the contrast. When $C > 0$, the system self-organizes in a triangular lattice, which is the closest-packing configuration in a plane. When $C < 0$, instead, the same ansatz 3.2 describes a triangular lattice of holes, i.e. a honeycomb lattice. The two configurations have different energies so the energy ΔE contains also odd terms in the order parameter. In particular, the combination $b > 0, c < 0$ and $d > 0$ leads to the typical scenario of

first-order phase transitions depicted in Fig. 3.1(b). The energy develops a minimum at $C \neq 0$ already before crossing the phase transition. When the ground state changes, the contrast jumps from zero to a value larger than zero, and all the intermediate points are not accessible. The metastable state leads to typical phenomena of first-order transitions, such as hysteresis and the release of latent heat [17].

Symmetries of the order parameter simply predict the change in the order of the transition depending on the dimensionality of the lattice. We will find that this result is true also in the small and inhomogeneous experimental system. We note that, in principle, the modulated state is not described only by the contrast C but also by a phase ϕ which determines the position of the lattice. In infinite systems, all the lattices with different phases have the same energy, and ϕ plays no role in the transition. The energy landscape, instead of the 1D plots in Fig. 3.1, has the famous shape of a mexican hat, in which all the infinite equivalent minima correspond to different ϕ . When we introduce the trap, there are some lattice configurations favorable compared to others and the mexican hat should be deformed to take into account energy variations for different ϕ . However, the degree of freedom associated to the position of the lattice, i.e. the Goldstone mode of the system, has much lower energy than the amplitude mode [45]. We therefore continue neglecting the phase ϕ and consider only the contrast C .

Before turning to the numerical simulations and the experimental realization, we describe in more detail the Landau theory for the dipolar system, showing some original results that are confirmed in the numerical simulations of our system.

1D lattice

For a 1D lattice there is only one wavevector $k_1 = k$ and Eq. 3.2 becomes $\rho(x) = \rho_0(1 + C \cos kx)$. The Landau energy expansion ΔE is found calculating the total energy of the dipolar system with our ansatz and expanding in powers of the contrast C . The various energy terms are the ones appearing in the eGPE 1.13, with $\rho = |\psi|^2$

$$E[\psi] = E_{kin} + E_{cont} + E_{dip} + E_{trap} + E_{LHY}. \quad (3.3)$$

The kinetic energy is $E_{kin} = \hbar^2/2m \int |\nabla\psi|^2 dV$, the mean field interaction energies are the contact one, $E_{cont} = g/2 \int \rho^2 dV$, and the dipolar one $E_{dip} = 1/2 \int \int U_{dd}(r - r')\rho(r)\rho(r')dVdV'$, the trap energy is $E_{trap} = m/2 \int (\omega_x^2 x^2 + \omega_y^2 y^2)\rho dV$ and the LHY energy is $E_{LHY} = g_{LHY} \int \rho^{5/2} dV$, with g_{LHY} the LHY coefficient [15]. In the infinite case, $E_{trap} = 0$ and all the odd terms in the energy expansion correctly disappear. The contact and dipolar interactions contribute only to the quadratic coefficient b_{1D} , while the kinetic and LHY energies contribute to all orders. The behavior of the energy terms as a function of a_s is plotted in the previous section in Fig. 1.7. While lowering a_s , the dipolar energy decreases and becomes negative, changing the sign to the coefficient b_{1D} . To form the modulated state, the energy gain of the dipolar term must overcome the energy cost of the contact, kinetic, and LHY terms. The fourth-order coefficient d_{1D} is determined by the kinetic and LHY energies

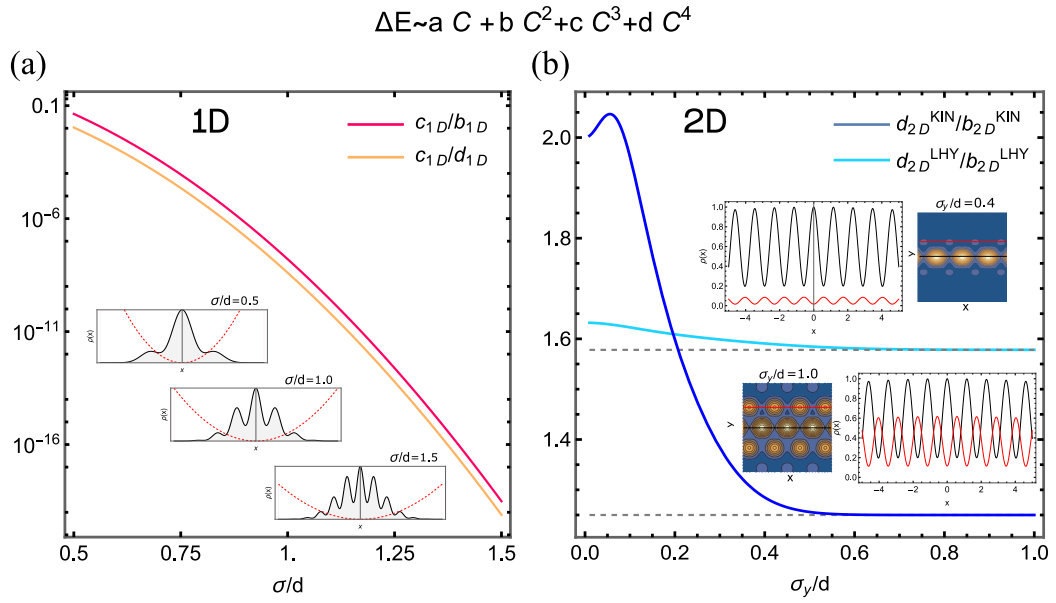


Figure 3.2: Effect of the trapping potentials in the Landau expansion of the energy. (a) 1D lattice with a confinement in the x direction, simulated by a gaussian envelope $g(x)$ with width σ . The plot shows c_{1D}/b_{1D} (red line) and c_{1D}/d_{1D} (orange line), as a function of the width of the envelope σ over the lattice period d . The odd coefficient c_{1D} is well under 1% for all values $\sigma/d > 0.5$, corresponding to systems that have at least two lateral clusters, as shown in the insets. Red lines in the insets are the energy profiles of the harmonic trapping potential. (b) 2D lattice with a confinement in the y direction, simulated by a gaussian envelope $g(y)$ with width σ_y . The blue (light blue) line shows the ratio of the even coefficients d_{2D}/b_{2D} for the kinetic (LHY) energy, versus the ratio σ_y/d . Dashed lines are the prediction of the infinite model [99]. The kinetic energy coefficients are shifted vertically for clarity. Insets show density cuts along x for $y = 0$ (black line, corresponding to the central row of clusters) and for $y = \sqrt{3}/2d$ (red line, corresponding to the first lateral row of clusters) for $\sigma_y/d = 0.4$ and 1, respectively. The deviation from the infinite case happens around $\sigma_y/d \sim 0.4$, when the lateral clusters are suppressed at a level about 10% of the central ones.

$$d_{1D} = \frac{\hbar^2}{2m} \frac{\rho_0 \pi^2}{8d} - g_{LHY} \frac{15\rho_0^{5/2} d}{1024}, \quad (3.4)$$

where d is the lattice period, $k = 2\pi/d$. With the typical densities of the experiments, the kinetic contribution dominates over the LHY one, and $d_{1D} > 0$, ensuring the stability of the system at large values of the contrast. The transition is then of second order, and the shape of ΔE follows the sketch in Fig. 3.1(a). However, also in the 1D case, the Landau theory predicts a first-order transition under particular conditions. For very high densities, the LHY contribution reverses the sign of d_{1D} . In this case, the energy would become more and more negative increasing the contrast, and no stable ground state would exist. To get a new ground state, we have to consider the next term in the expansion, $\sim e_{1D}C^6$. The coefficient e_{1D} is again given by a competition between kinetic and LHY energies

$$e_{1D} = \frac{\hbar^2}{2m} \frac{\rho_0 \pi^2}{16d} - g_{LHY} \frac{25\rho_0^{5/2} d}{16384} \quad (3.5)$$

but in the region where d_{1D} is negative, e_{1D} is positive, ensuring the presence of a new minimum in the energy. In this regime, when the ground state has $C \neq 0$, the combination of the coefficients is $b_{1D} > 0$, $d_{1D} < 0$ and $e_{1D} > 0$. The resulting energy curve, plotted in Fig. 3.1(a) as a dashed line, resembles that of a first-order transition, with an energy barrier between the minimum at $C = 0$ and that at $C > 0$.

We also partially investigated the effect of the confinement in the 1D system. To model the presence of the harmonic trap, we modify the ansatz 3.2 adding a gaussian envelope $g(x)$ with width σ , $\rho(x) = \rho_0(1 + C \cos kx)g(x)$. The presence of the envelope breaks the symmetry of the energy for $C \rightarrow -C$, so in principle the odd terms in the energy expansion should differ from zero. However, we find that they are negligible compared to the even terms also for quite strong confinements. In Fig. 3.2 we plot the ratios c_{1D}/b_{1D} and c_{1D}/d_{1D} for different values of σ/d . The odd term is well under 1 % of the even terms until one single macro droplet survives to the confinement, see the insets in Fig. 3.2(a). Therefore, even for small systems like the experimental ones, the effect of the trap in the long direction doesn't change the thermodynamic prediction that the odd term must vanish and hence the transition must be continuous.

2D lattice

In 2D the Landau theory has been developed in [99]. The authors employed the same ansatz as in Eq. 3.2, with three wavevectors of equal length satisfying $\mathbf{k}_1 + \mathbf{k}_2 + \mathbf{k}_3 = 0$. The density modulation has a triangular structure, see insets in Fig. 3.1(b). Contrary to the 1D case, the third order coefficient c_{2D} is different from zero and is determined by the competition of kinetic and LHY energies. At low enough densities, the kinetic energy dominates, similar to what happens to the even terms in 1D, giving $c_{2D} < 0$. The presence of a negative cubic term produces a first-order phase transition while lowering b_{2D} , see Fig. 3.1(b). This is the general prototype of crystallization phase transitions, usually of the

first order [17]. However, the LHY energy, specific to our dipolar system, can change this established result. Increasing the density, the LHY term compensates the kinetic energy one and $c_{2D} = 0$, giving a second-order transition in one single point of the phase diagram. Increasing more the density, the LHY term dominates and $c_{2D} > 0$, producing a first-order transition but towards a modulated state with $C < 0$, i.e. a honeycomb lattice, depicted in Fig. 3.1(b).

Also in 2D, we investigated the effects of harmonic confinement. We added a gaussian envelope $g(y)$ in the y direction with width σ_y . Depending on the ratio between the width and the lattice period σ_y/d , the lateral rows of clusters experience different levels of suppression. We want to explore to which extent the results in the thermodynamic limit apply also to a trapped system. The results are shown in Fig. 3.2(b). We plot the ratio of the coefficients d_{2D}/b_{2D} for the kinetic and LHY energy, as a function of σ_y/d . We observe deviations from the predictions of the infinite system only when $\sigma_y/d \sim 0.4$, corresponding to a configuration in which the density of the first lateral clusters row is about 10 % of the central row, see the insets. This observation means that even a tiny 2D modulation gives results very similar to the infinite system.

3.2 Phase diagram from ground-state simulations

We now turn to a quantitative analysis of the phase transition in the trapped system. In the experimental configuration, many approximations of the previous simplified model based on the Landau theory must be released. First, the system is not in the thermodynamic limit but it is very small, with few lattice sites. Second, the inhomogeneity introduced by the trap can mix different phases, depending on the local value of the density. We should, therefore, replace the thermodynamic concepts of first- and second-order phase transitions with continuous and discontinuous phase transitions, empirically distinguished depending on the behavior of the order parameter at the critical point and on the amount of energy the system gets in the form of excitations when crossing the phase transition. In principle, it is even possible that finite-size effects completely mix continuous and discontinuous transitions, canceling any difference between the two. Remarkably, we discover that, even in our small system, it is possible to clearly distinguish between the two kinds of transition.

In this section, we present a study based on numerical simulations of the ground state of the system. We therefore exclude dynamical effects, which are discussed in the experimental section. In the simulations, we fix the trapping frequency in the x and z directions to typical values $\nu_x = 20$ Hz and $\nu_z = 80$ Hz. The polarization axis is along z , as usual. We explore a phase diagram of the transition by changing the transverse confinement ν_y and the atom number N . For each configuration, we solve the eGPE 1.13 in its stationary form to find the ground state and we explore how it evolves as a function of the scattering length a_s . To quantify the density modulation, instead of the real-space contrast C , we define a momentum-space contrast \tilde{C} , in analogy to the experimental observable discussed in section 2.2, as the relative amplitude of the Fourier peak of the density modulation

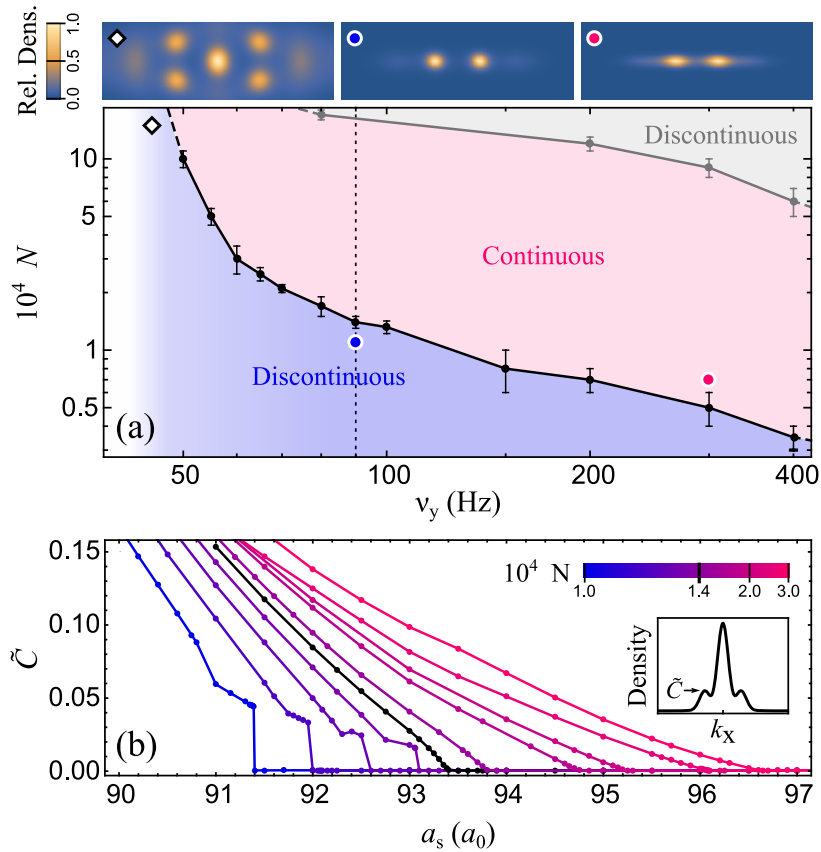


Figure 3.3: Crossover from discontinuous to continuous transitions in ground state simulations. (a) Character of the superfluid-supersolid transition as a function of the transverse trapping frequency ν_y and the atom number N . Black dots mark the boundary between the continuous and discontinuous regimes and the corresponding error bars are the atom number resolution in the simulations. The gray region indicates the discontinuous transition induced by the LHY term in the 1D configurations at high densities. Insets show examples of the density distribution of the supersolid at different points of the diagram. (b) Contrast \tilde{C} versus scattering length a_s for $\nu_y = 90$ Hz and variable atom number, corresponding to the vertical dashed line in (a). The black curve represents the transition at the continuous-discontinuous boundary. Inset: definition of the contrast \tilde{C} in the momentum distribution.

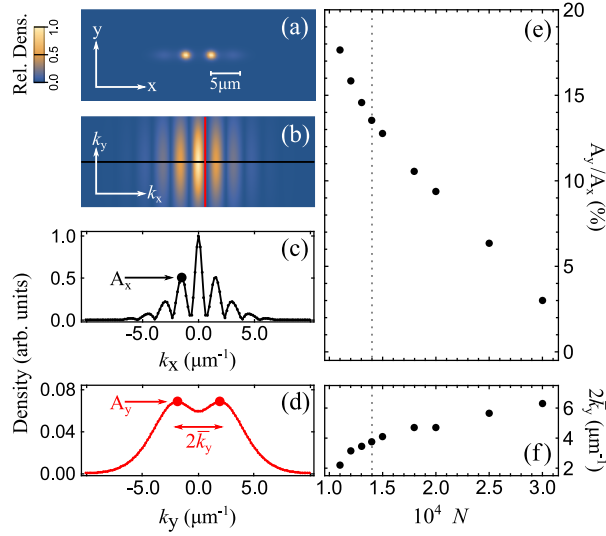


Figure 3.4: Dimensional nature of the continuous-discontinuous crossover. Real space (a) and Fourier space (b) density of a supersolid with $N = 1.4 \times 10^4$ atoms and $\nu_y = 90$ Hz, at the continuous-discontinuous boundary. (c) 1D cut of the Fourier space density in (b) along the black line ($k_y = 0$). (d) 1D cut along the red line ($k_x = \pi/d$), revealing the presence of peaks along the k_y axis in a triangular geometry. (e) Amplitude A_y of the lateral peaks along k_y relative to that of the first lateral peak along k_x , A_x , as a function of N for $\nu_y = 90$ Hz and $\tilde{C} \sim 0.04$ [same simulations as in Fig. 3.3(b)]. (f) Period $2\tilde{k}_y$ of the modulation along k_y as a function of N .

at the momentum $k = 2\pi/d$, with d the lattice period. In the limit of small contrasts, the two observables are related by $\tilde{C} = C^2/16$. Fig. 3.3 summarizes the results of the simulations. Since most of the configurations we explored are strongly elongated in the x direction, the density modulation develops mainly in that direction. One would, therefore, naturally associate such configurations with the continuous phase transition of the 1D infinite system discussed before. Instead, we observe both continuous and discontinuous phase transitions, in agreement with other simulations in an infinite tube [103]. At low atom numbers and low trapping frequencies, the discontinuous transition is favored, while we reach continuous transitions increasing N or ν_y . We arbitrarily choose a boundary between the two kinds of transitions as the smallest value of N that gives a jump in \tilde{C} smaller than 0.001, for fixed ν_y . Such a boundary is plotted in Fig. 3.3(a) as a black line. The behavior of \tilde{C} versus a_s for different atom numbers across the boundary is shown in Fig. 3.3(b).

We interpret this crossover between continuous and discontinuous transitions as a dimensionality effect, in analogy with the Landau theory. An analysis of the Fourier transform of the density distributions, indeed, reveals the presence of a triangular structure of the background for the configurations with a discontinuous transition. An example of such analysis for a specific simulation is shown in Fig. 3.4. Cutting the Fourier transform along k_y , we find small peaks with amplitude A_y , much smaller than the amplitude A_x of the

peaks in the x direction, and tunable with N and ν_y . Fig. 3.4(e) shows the decreasing of the triangular structure, quantified with the ratio A_y/A_x , while increasing the atom number N for a fixed ν_y . Interpreting these results in the light of the Landau theory, we conclude that increasing the atom number or the transverse frequency reduces the cubic coefficient in the energy expansion, producing a smooth crossover from discontinuous transitions, with a 2D lattice, to continuous transitions, with a 1D lattice. The boundary between the two regimes is around $A_y/A_x \sim 10\%$. Remarkably, this observation is in qualitative agreement with our Landau model of the 2D trapped system in Fig. 3.2(b), and demonstrates that even a tiny density modulation with a 2D structure is enough to modify the nature of the phase transition.

The peculiar shape of the crossover in Fig. 3.3 comes from the compressibility of the cluster supersolid. Contrary to a solid with one atom per lattice site, indeed, in the dipolar supersolid the dimensions and shape of each cluster can be modified by the external harmonic trapping and the total atom number. For low atom numbers, it is easier for the system to accommodate a triangular structure in the density background, and the discontinuous transition is favored. For weak confinements ν_y , the critical atom number to cross the boundary becomes higher, since the system has to pay less potential energy cost to form a triangular background. The deformability of the dipolar supersolid is shown in Fig. 3.5, where we focus on the transitions at the boundary of the crossover (indicated as a black line in Fig. 3.3). We observe that, in most of the phase transitions, the width of the supersolid σ_y is very close to the dimension of a non-interacting system in the harmonic trap, $l_y/\sqrt{2}$, with l_y the harmonic length in the y direction. This is consistent with the expectation that, at the critical point, contact and dipolar interactions tend to cancel each other. On the other hand, for small confinements, the width σ_y strongly increases. This happens together with an elongation of the single clusters along y , as captured by the behavior of the deformation parameter $\beta_{ss} = \langle x^2 - y^2 \rangle / \langle x^2 + y^2 \rangle$, which at large ν_y is positive (clusters elongated along x) and becomes negative at small ν_y (clusters elongated along y), see Fig. 3.5(b). We explain this behavior as an effect of the repulsive LHY energy. Since the boundary of the crossover happens at high atom number N for small ν_y , also the peak density is higher, see Fig. 3.5(c). To lower the LHY energy, scaling as $\sim \rho^{5/2}$, the system limits the increase in peak density elongating the clusters in the y direction. This 'stripe' phase has been reported also in other numerical studies [104, 105].

Finally, in the phase diagram in Fig. 3.3, we observe a second region of discontinuous transitions at high atom numbers, hence at high densities (gray region). In this region, the lattice is 1D, since the transverse confinement ν_y is strong. We interpret this additional boundary as the finite-size analog of the first-order transition induced by the LHY energy in 1D (section 3.1), reversing the sign of the fourth order coefficient d_{1D} . We think that such a mechanism could explain the presence of both continuous and discontinuous transitions in the infinite tube numerically investigated in [103]. Remarkably, our Landau model in the infinite system captures quite well this discontinuous region in the phase diagram. From the expressions of the fourth- and sixth-order coefficients d_{1D} and e_{1D} of the energy expansion in 1D, Eq. 3.4 and 3.5, we get that the conditions $d_{1D} < 0$ and $e_{1D} > 0$ are

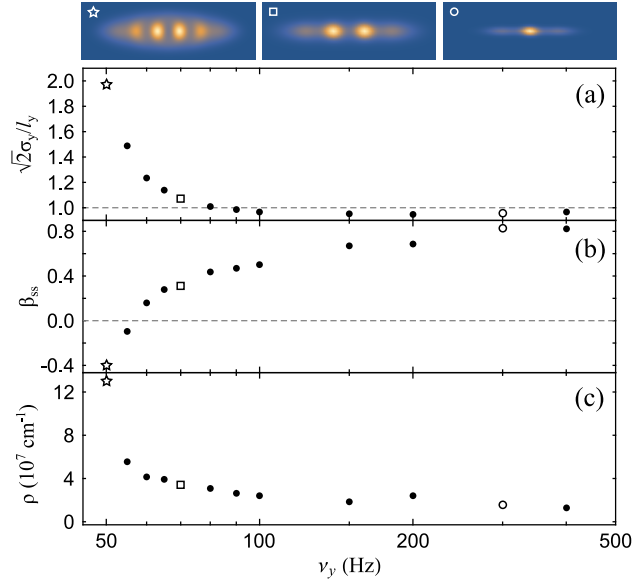


Figure 3.5: Supersolid structure for the phase transitions at the boundary of the dimensional crossover (black line in Fig. 3.3), as a function of the transverse confinement ν_y . (a) Transverse width σ_y normalized to the width of a non-interacting system $l_y/\sqrt{2}$ (l_y is the harmonic length). (b) Deformation parameter $\beta_{ss} = \langle x^2 - y^2 \rangle / \langle x^2 + y^2 \rangle$ of the central clusters. (c) Peak density of the central clusters. Insets show examples of the supersolid density distributions in the xy plane.

obtained simultaneously around a mean density $\rho_0 \sim 8 \times 10^{20}$ atoms/m³. Considering a lattice period $d \sim 4 \mu\text{m}$ and realistic transverse dimensions $L_y \sim 4 \mu\text{m}$, $L_z \sim 8 \mu\text{m}$, the critical atom number is $N_c = \rho_0 d L_x L_y \sim 10^5$ for each lattice cell. Therefore, for a 4-clusters configuration, the model predicts a LHY-induced first-order transition in 1D at around $N \sim 4 \times 10^5$. This result is of the same order of magnitude as the numerical one in Fig. 3.3.

3.3 Experimental evidence of continuous and discontinuous phase transitions

Experimentally, we tested the theoretical predictions for two trapping geometries, with different aspect ratios in the yz plane: potential V_C , with frequencies $(\nu_x, \nu_y, \nu_z) = [15.0(0.7), 101.0(0.3), 93.9(0.6)]$ Hz, and potential V_D , with frequencies $[21.8(1.0), 67(0.8), 102.0(0.7)]$ Hz. The atom number in both configurations is about $N = 3 \times 10^4$ atoms. From ground-state numerical simulations, the transition to the supersolid state is discontinuous for potential V_D , with a jump of about 0.02 in the contrast \tilde{C} at the critical point, and continuous for potential V_C , which has a stronger confinement in the y direction.

Contrary to the stationary simulations, in the experiment the dynamic has a relevant role. The experimental dynamical sequence is sketched in Fig. 3.6. We start from the BEC

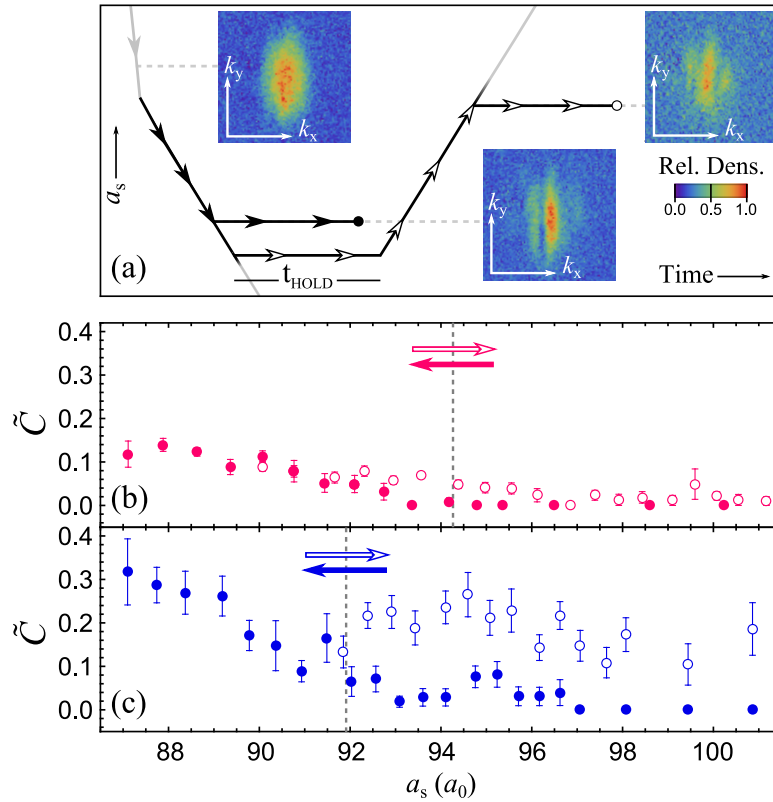


Figure 3.6: Experimental characterization of continuous and discontinuous phase transitions. (a) Experimental time sequence. We cross the superfluid-supersolid phase transition with a ramp in the scattering length a_s . We wait for $t_{\text{hold}} = 15$ ms at a variable scattering length in the supersolid regime. At the end of this in-going ramp, we take a time of flight image (full arrows) or we ramp back the scattering length, cross again the phase transition and take an image after waiting at the final a_s for t_{hold} (empty arrows). Insets: examples of time of flight images in different points of the protocol. (b-c) Contrast in momentum space \tilde{C} as a function of the scattering length a_s in the in-going ramp (full circles) and in the out-going ramp (empty circles) for potential V_C (b) and V_D (c). Vertical dashed lines indicate the position of the transition in the ground-state simulations.

at high a_s , then we ramp linearly to the supersolid regime. In principle, the ramp speed should be as slow as possible to cross adiabatically the phase transition. However, we are limited by unavoidable three-body losses, which scale as ρ^2 and lower the lifetime of the system in the supersolid regime, so that our observation time is limited to about 100 ms¹. We employ a ramp speed $\dot{a}_s = 0.5 a_0/\text{ms}$, which allows us to cross the transition in potential V_C almost adiabatically. At the end of the ramp, we wait for a holding time $t_{\text{hold}} = 20$ ms, larger than the formation time of the supersolid. We then characterize the supersolid state by measuring the contrast in momentum space \tilde{C} from time of flight images, as explained in section 2.2. The measured \tilde{C} as a function of the scattering length is plotted with full circles in Fig. 3.6(b-c) for trap V_C and V_D , respectively. Following this in-going ramp to the supersolid regime, we also perform an out-going ramp, from the supersolid back to the superfluid regime, crossing for the second time the phase transition. After the out-going ramp, we wait again $t_{\text{hold}} = 20$ ms and we measure the contrast \tilde{C} . The results are plotted in Fig. 3.6(b-c) as empty circles. These measurements show some key features that reveal the different nature of the phase transition in the two potentials. The most apparent difference is the contrast in the out-going ramps. In potential V_C we are able to follow the ground state of the system, recovering an unmodulated state with $\tilde{C} = 0$ on the BEC side. On the other hand, in potential V_D the system is highly excited and preserves a strong density modulation after the out-going ramp, up to at least 10 a_0 in the superfluid regime. Another important difference is that in potential V_D , before crossing the phase transition, we observe strong fluctuations in \tilde{C} , which are instead absent in potential V_C . All these observations are consistent with a different nature of the phase transition in the two potentials: discontinuous for V_D and continuous for V_C .

We checked that these differences persist for different ramp speeds, repeating the same experiment with $\dot{a}_s = 0.25 a_0/\text{ms}$ and with $\dot{a}_s = 1 a_0/\text{ms}$. We enter by 2 a_0 inside the supersolid regime, wait for the hold time t_{hold} , and then we cross again the phase transition ending at 4 a_0 inside the superfluid regime. The results are plotted in Fig. 3.7 as empty circles. Each data point is the average of different waiting times 10, 20, and 20 ms in the superfluid regime. The contrast \tilde{C} , which quantifies the degree of excitation, is always larger for potential V_D than for V_C . However, for both potentials, we observe a linear increase of the final \tilde{C} with the ramp speed. This dependence comes from the finite formation time of the supersolid, about 15 ms, which is not much lower than the total duration of the ramps [56]. We cannot, therefore, cross completely adiabatically the transition, since longer ramps become comparable with the lifetime of the supersolid. Extrapolating the linear fit in the limit of infinitely long ramp ($\dot{a}_s \rightarrow 0$), the intercept for potential V_D is larger than for potential V_C . We attribute the finite value of the latter to atom losses, which lead to a loss of adiabaticity in the long-time limit. In a different

¹As described in the rest of the chapter, the observation time is limited both by atom losses and by a decoherence process that increases the fluctuations of the relative phase between the clusters. Three body losses are responsible for the decreasing atom number in the supersolid regime, and they also introduce noise in the phase distribution. Their effect is similar in the two traps, since the geometry and the scattering length scales are quite similar, see Fig. 3.8(c-d). Decoherence is however induced also by the excitation of high-amplitude collective modes. This effect is much more pronounced after crossing the discontinuous phase transition, see Fig. 3.12.

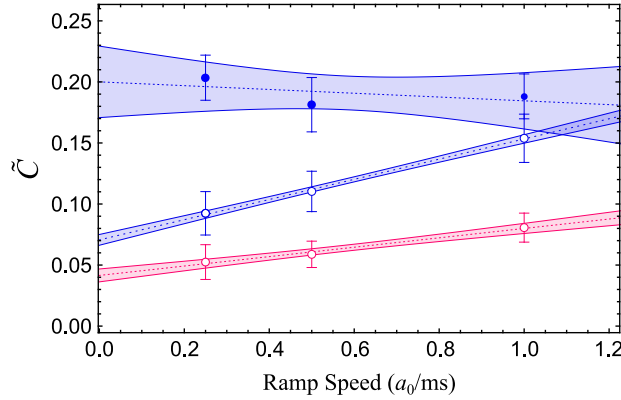


Figure 3.7: Effect of the ramp speed. Contrast \tilde{C} after the in-going ramp (full circles) and the out-going ramp (empty circles) for potential V_D (blue) and V_C (magenta) for different ramp speeds. The case $\dot{a}_s = 0.5 a_0/\text{ms}$ is the one of Fig. 3.6. Dashed lines are linear fits and colored bands are the confidence intervals at one standard deviation.

kind of experiment, we studied the contrast \tilde{C} after the in-going ramp in potential V_D , in the region of strong fluctuations just before the transition (around $92.5 a_0$). For all the ramp speeds, we observe the same contrast \tilde{C} , once we exclude the shots in which $\tilde{C} = 0$ (see full circles in Fig. 3.7). This is consistent with what we expect in a discontinuous transition, for which two minima, one with $\tilde{C} = 0$ and one with $\tilde{C} \neq 0$ exist near the critical point. More information about fluctuations is in the last paragraph of this section. As it is evident from the measurements in Fig. 3.7, with the available ramp speeds, limited by the lifetime of the supersolid, we are not able to follow the ground state during the dynamics, and the system is driven out of equilibrium. Therefore, we do not interpret the high values of the contrast in the outgoing ramp in potential V_D as a hysteresis, which would be expected in a first-order phase transition but is an equilibrium concept. We prefer to explain the behavior in the out-going ramp in terms of excitations of collective modes, which is more appropriate for our out-of-equilibrium system. In the hypothetical equilibrium case, numerical simulations show a small hysteresis which appears in a shift of about $0.5 a_0$ of the critical point depending on the direction in which the transition is crossed [15].

Excitation of collective modes

Crossing the discontinuous transition in potential V_D excites many different collective modes of the supersolid. To quantify the degree of excitation of the system and compare with potential V_C , we study the kinetic energy from the measured momentum distribution $\rho(k_x, k_y)$, as shown in Fig. 3.8. In addition to the energy of the collective modes, the kinetic energy after the expansion contains also the contributions from the interaction

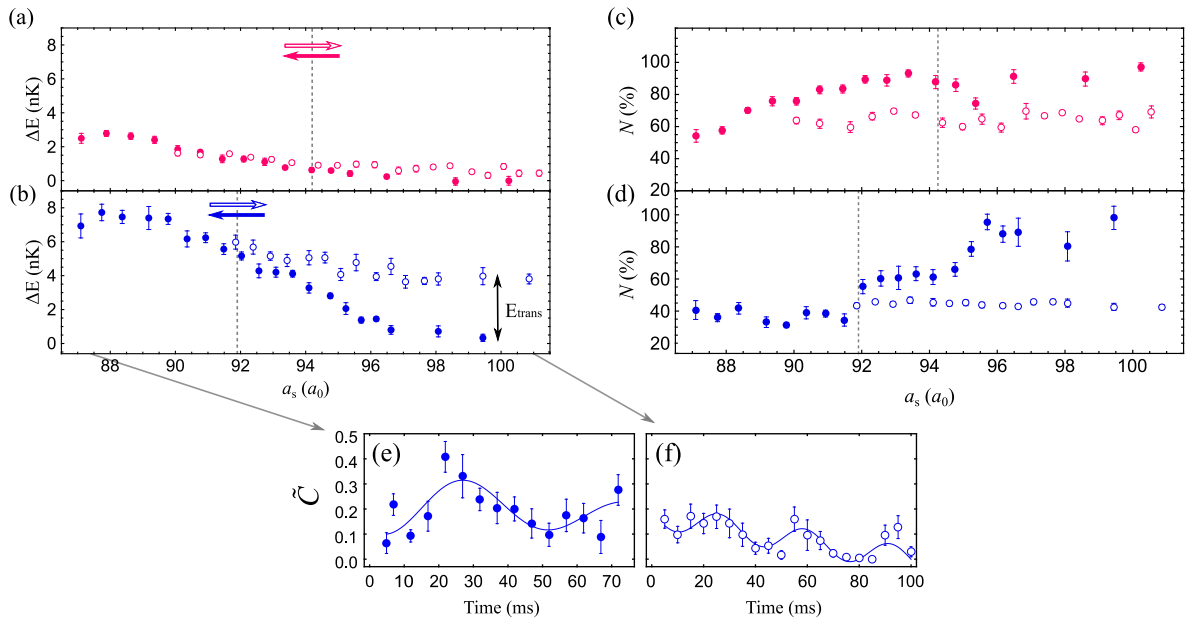


Figure 3.8: Excitation of collective modes. (a-b) Released energy ΔE (see text for the definition) after the in-going and out-going ramps for potential V_C (a) and V_D (b). The energy acquired by crossing back and forth the transition is much larger for potential V_D , $E_{\text{trans}} \sim 4$ nK, than for potential V_C , $E_{\text{trans}} \sim 0.5$ nK. (c-d) Atom number in the in-going and out-going ramps for potential V_C (c) and V_D (d). In both potentials, N is reduced to about 40 % of the initial atom number due to three-body losses. The variation of N is considered to normalize the energy ΔE in panels (a-b), see text. The jump in atom number at the critical point in V_D is used to calibrate the magnetic field-scattering length conversion. (e-f) Excitation of the order parameter \tilde{C} in potential V_D after the in-going ramp at $87.3 a_0$ (e) and after the out-going ramp at $100.3 a_0$ (f).

energies. For each potential, we thus subtract the average of all the images $\langle \rho \rangle$, computing $\delta\rho = \rho - \langle \rho \rangle$. The energy 'in excess', due to the collective modes, is given by

$$E_{\text{exp}} = \frac{\hbar^2}{2m} \int \delta\rho(k_x, k_y)(k_x^2 + k_y^2) dk_x dk_y. \quad (3.6)$$

Since we use normalized momentum distributions, $\int \rho(k_x, k_y) dk_x dk_y = 1$, E_{exp} is the energy per particle. However, due to the contribution of the interaction energies, scaling as N^2 (or $N^{3/2}$), E_{exp} depends on the actual atom number N , which strongly varies across the phase transitions, as depicted in Fig. 3.8(c-d). Due to three-body losses, we lose about 60% of the atoms by going from the BEC to the supersolid with lowest a_s , in both traps². Losses are described by $\dot{N} = -L_3\rho^2$, where L_3 stays approximately constant during our ramps and the increased losses in the supersolid are due to the increase in the peak density ρ . On the out-going ramp, instead, N is quite constant, because the density already decreased during the permanence on the supersolid side and losses are less effective. We do not observe substantial heating associated with atom losses. In all the supersolid regime, we do not observe the appearance of a thermal fraction, meaning that the temperature stays below our sensitivity to thermal components, which we estimate to be about 10 nK. This is consistent with reference [10], in which heating above 10 nK was observed only in the independent droplets regime.

To take into account variations in the atom number for the energy calculation, we rescale E_{exp} using a linear regression $E_{\text{exp}} \rightarrow E_{\text{exp}} - \gamma_i(N - \bar{N})$, where \bar{N} is the average atom number on the BEC side and the coefficients γ_i are independently determined in each subject i of images with similar atom number [15]. In this way, the energy in the images with low atom number $N < \bar{N}$ is increased, while in those images with high atom number $N \sim \bar{N}$ it is unaffected. In Fig. 3.8(a-b) we plot the energy difference ΔE , obtained subtracting to E_{exp} the energy of the superfluid with largest a_s . Also in this analysis, the larger excitation of the supersolid in potential V_D , compared to potential V_C , is apparent. It is difficult to extract quantitative information from ΔE measured in the in-going ramp, because we cannot compare our results to the energy of the ground state, which we can't reach adiabatically in the experiment. However, we can make a quantitative measurement of the excitation energy in the out-going ramp, since in this regime we can compare the excited state to the BEC ground state of the in-going ramp. As shown in Fig. 3.8(a-b), in potential V_C the energy released after crossing back and forth the transition is $E_{\text{trans}} \sim 0.5$ nK, while in potential V_D it is much larger, $E_{\text{trans}} \sim 4$ nK.

In Fig. 3.8(e-f) we show the effect of the released energy on the contrast \tilde{C} in potential V_D . We observe oscillations as a function of time both after the in-going and after the out-going ramps. However, the two oscillations reveal the different nature of the excited states on the two sides of the transition. In the supersolid regime, the contrast \tilde{C} oscillates around a mean value different from zero and shows a damping due probably to

²Note that the critical transition point in potential V_D is detected as a jump in the atom number, see Fig. 3.8(b), associated with a sudden increase of the peak density in situ. We employ this jump to experimentally identify the critical point and to calibrate the global scale of scattering length, as explained in section 2.1: we apply a global shift ($6.7 a_0$) to match the observed jump with the critical point of ground-state simulations. We apply the same shift also for potential V_C .

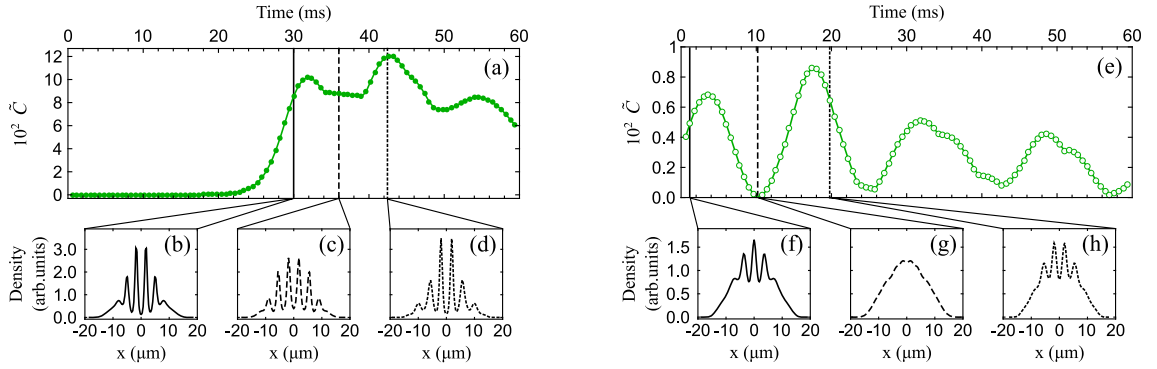


Figure 3.9: Nature of the excited systems after the in-going and out-going ramps from numerical simulations for potential V_C . Contrast \tilde{C} versus time after the in-going ramp from $95 a_0$ to $93 a_0$ (a) and the out-going ramp from $90 a_0$ to $95 a_0$ (e). Panels (b-d) and (f-h) show snapshots of the real space density distribution along x for selected times.

three-body losses. The fitted frequency $\nu = 21(3)$ Hz is consistent with the so-called amplitude mode of the supersolid [45]. In the out-going ramp, instead, the oscillation touches zero and has a larger frequency. We interpret the excited mode after the in-going ramp as a collective mode of the supersolid, for which the real-space contrast C (proportional to \tilde{C}) oscillates around the equilibrium value, while the excitation after the out-going ramp is an excited mode of the superfluid, with the density modulation oscillating around $C = 0$. Such a mode is related to the roton mode but in the large amplitude regime.

These conclusions are corroborated by dynamical numerical simulations, performed by M. Mougno and A. Alana, at Bilbao University [15]. In the simulations, the time-dependent eGPE 1.13 is integrated with a time-dependent scattering length $a_s(t)$, which simulates the experimental protocol. The simulated system is a simplification of the real one because it doesn't take into account losses and thermal effects. However, it is useful for a qualitative comparison with the experiment, without introducing phenomenological parameters such as the temperature and the loss rate. Due to the absence of dissipation, the phase transition in potential V_C is crossed quasi-adiabatically, as in the experiment, only with a ramp speed one order of magnitude lower than the experimental one, $\dot{a}_s = 0.05 a_0/\text{ms}$. In this configuration, in potential V_D , numerous collective modes are excited and mixed together, and the single-frequency oscillations of \tilde{C} observed in the experiment are not reproduced. In Fig. 3.9, instead, we show the small-amplitude (see the scale in the vertical axes) collective modes excited in potential V_C , which are in qualitative agreement with the experimental observations. After the in-going ramp, Fig. 3.9(a), the contrast increases and then oscillates around a finite mean value. This mode produces an oscillation in the amplitude of the clusters, as shown in the real space densities snapshots in Fig. 3.9(b-d). On the other hand, for the excited mode on the superfluid side, \tilde{C} touches periodically zero, and the real space density periodically recovers the shape of the BEC.

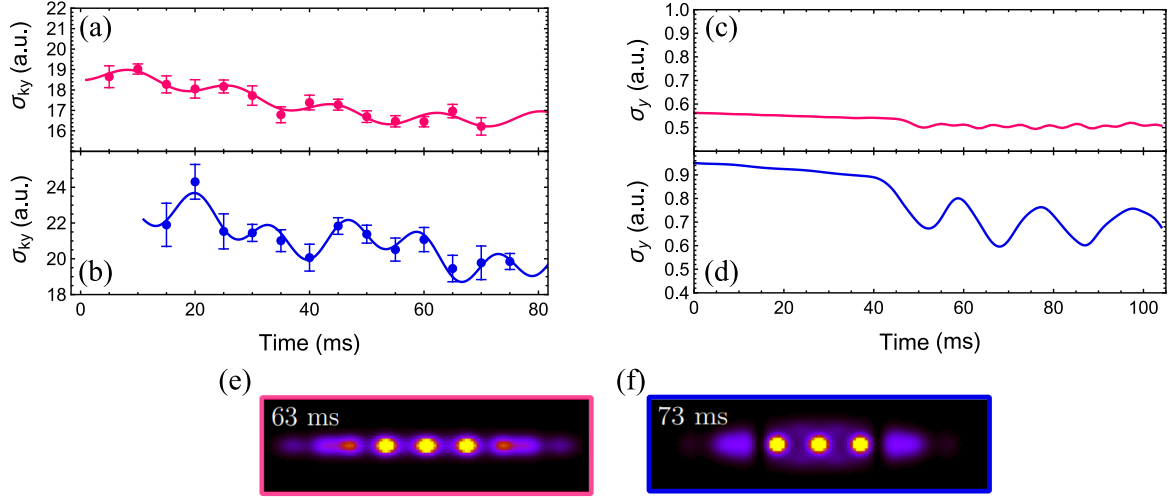


Figure 3.10: Transverse collective modes. (a-b) Time evolution of the y -width σ_{ky} in time of flight images for potential V_C (a) and V_D (b), after crossing the phase transition at $92.9 a_0$ and $90.9 a_0$, respectively. Thick lines are a single-frequency fit for V_C and a double-frequency fit for V_D (see text). (c-d) Time evolution of the transverse width σ_y for potential V_C (c) and V_D (d) in the numerical simulations. A transverse collective mode is activated only in the discontinuous transition, in agreement with the dimensional interpretation of the crossover. Time $t = 0$ ms corresponds to the crossing of the critical scattering length. In the simulations, the formation time of the supersolid is longer than in the experiment, probably due to the absence of dissipation [56]. (e-f) Snapshots of the simulations for potential V_C at $t = 63$ ms (e) and V_D at $t = 73$ ms (f).

The same dynamical simulations are also in qualitative agreement with our measurements in Fig. 3.8 of the energy released after crossing the phase transition. Starting from the ground state in the BEC and after the in-going ramp, the energy is $E_{\text{trans}} = 0.2$ nK for trap V_C and 1 nK for trap V_D .

Transverse collective modes

In a theoretical follow-up paper [56], we explored in more detail the effects of the continuous and discontinuous transitions in the formation dynamics of the supersolid. Here, we discuss an interesting observation that supports the dimensional nature of the crossover from continuous to discontinuous transitions. We focus on the transverse collective mode excited during the formation of the supersolid. In Fig. 3.10, we plot the time evolution of the transverse width σ_y of the system following the in-going ramps, with speed $0.5 a_0/\text{ms}$ in the experiment and $0.05 a_0/\text{ms}$ in the simulations. Remarkably, in the simulations we observe a transverse collective mode only in potential V_D , detected by the oscillation of σ_y at a high frequency $\nu \sim 60$ Hz. This transverse oscillation is associated with the formation of a 2D pattern in the density background, reminiscent of the triangular lattice

expected in the infinite 2D case. In the experiment, we observe a similar fast oscillation in the transverse width in momentum space, σ_{ky} , in potential V_D , and a much weaker oscillations in potential V_C , see Fig. 3.10(a-b). We fit the oscillation in V_D with a sum of two frequencies, $\nu_1 = 76(3)$ Hz and $\nu_2 = 30(4)$ Hz. The fast frequency component has a 5 % amplitude. In V_C , we fit a single frequency $\nu = 56(5)$ Hz with a 1 % amplitude. The excitation of a collective mode in the transverse direction y in potential V_D , both in the experiment and in the theory, is a consequence of the enlarged dimensionality of the supersolid formed in the discontinuous transition. This evidence, coming from the formation dynamics, completes the analysis of the triangular structure in the ground state density in Fig. 3.4 and strengthens the dimensional interpretation of the crossover.

Fluctuations and Landau energy

Fluctuations have an important role in phase transitions and are enhanced near the critical point. Density fluctuations evaluated in situ allowed for the experimental measurement of the static structure factor and the excitation spectrum across the superfluid-supersolid phase transition [108]. In our case, the fluctuations properties of the order parameter \tilde{C} provide further evidence for the different nature of the transitions in potentials V_C and V_D . In the experimental system, fluctuations have both a fundamental origin, due to the finite temperature and quantum indeterminacy, and a technical origin, due mainly to shot-to-shot fluctuations in the atom number, which in turn determine shot-to-shot fluctuations in the critical scattering length. In Fig. 3.11 we show histograms with the fluctuation spectra of the contrast \tilde{C} in different regions of the phase diagram for both potentials. Region I is on the superfluid side, well before crossing the transition. We therefore observe always $\tilde{C} = 0$. Region II and III are just before and after the critical point, respectively. Region IV is well inside the supersolid regime, near to the droplet crystal. The main difference between the two potentials is in region II. Here, in potential V_C we observe a smooth broadening of the spectrum, with values slightly larger than zero being populated. On the other hand, in potential V_D the spectrum is well separated in a peak at $\tilde{C} = 0$ and one at $\tilde{C} \neq 0$. In region III, the peak in potential V_C is shifted to non-zero values, while in potential V_D it keeps the double-peak structures, but becomes more noisy. Finally, in region IV both spectra are very broad, probably because three-body losses strongly affect the density distribution, depending on the details of the actual formation process.

We interpret these results with the different shapes of the Landau free energy in the two transitions, as explained by our model in section 3.1. In the continuous transition, the energy has always a single minimum, that smoothly moves from $\tilde{C} = 0$ to $\tilde{C} \neq 0$. In the discontinuous case, near to the critical point, two different minima compete, and due to the experimental fluctuations, we populate one or the other from shot to shot. This interpretation is validated by a calculation of the free energy of the system as a function of \tilde{C} , shown in Fig. 3.11(c-d). We consider an ansatz similar to Eq. 3.2, but modified to take into account the effect of the trapping potential

$$\rho(\mathbf{r}) = A \left[1 + C e^{-\frac{x^2}{2w_x^2}} \sum_i \cos(\mathbf{k}_i \cdot \mathbf{r}') \right] \left(1 - \frac{x^2}{R_x^2} \right) e^{-\frac{y^2}{2\sigma_y^2}} \left(1 - \frac{z^2}{R_z^2} \right). \quad (3.7)$$

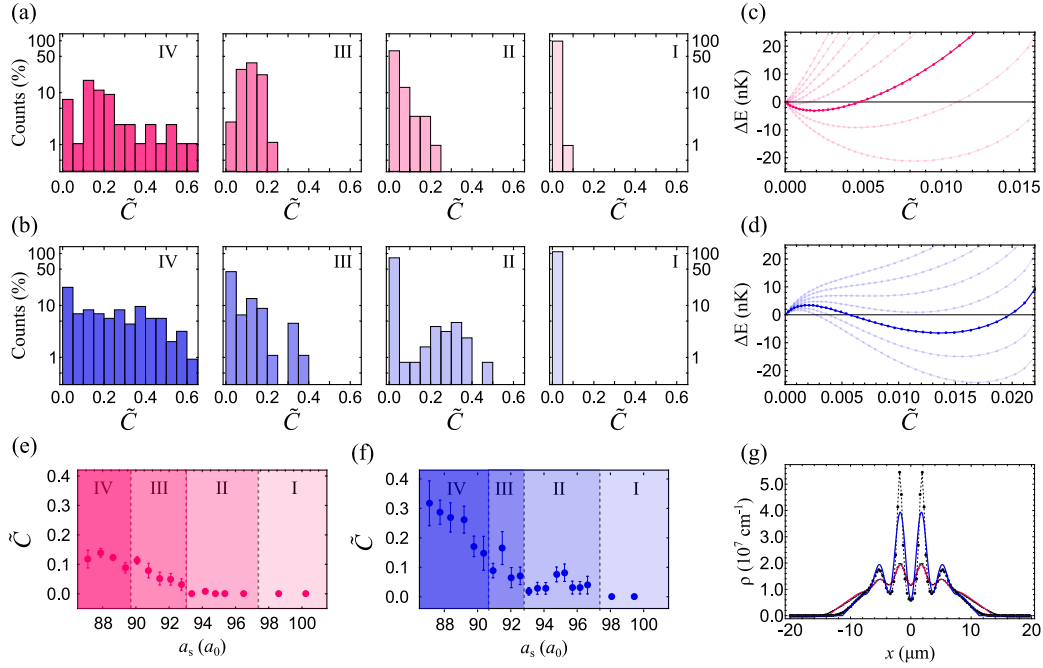


Figure 3.11: Fluctuations of the order parameter and Landau free energy. (a-b) Histograms of the contrast \tilde{C} divided into four different regions of scattering lengths: well before (I), just before (II), just after (III), and well after (IV) the phase transition, for potential V_C (a) and V_D (b). The different regions in scattering lengths are highlighted in (e-f). (c-d) Free energy ΔE of the system as a function of \tilde{C} calculated with the ansatz 3.7 for potential V_C (c) and V_D (d). The different curves correspond to different values of a_s , spaced by $1 a_0$ ($0.25 a_0$) around the central one at $94 a_0$ ($90 a_0$), for potential V_C (V_D). Thick lines are the first curves after the critical point, to be compared with the fluctuations of regions II in (a-b). (e-f) Four regions I, II, III and IV in panels (a-b) highlighted in the \tilde{C} versus a_s plots, for potential V_C (e) and V_D (f). (g) Ansatz 3.7, used for the numerical calculation of the free energy in (c-d). Black points are a 1D cut along the x direction of the numerical simulations of the ground state, just after the transition ($94.25 a_0$ for V_C and $91.94 a_0$ for V_D). Thick lines are fits using the ansatz 3.7 (blue for V_D and magenta for V_C). To calculate the free energy, the parameters of the fit are fixed and only the contrast C is varied.

Here, the lattice wavevectors are $\mathbf{k}_1 = 2\pi/\lambda(0, 1, 0)$, $\mathbf{k}_2 = -2\pi/\lambda(\sqrt{3}/2, 1/2, 0)$ and $\mathbf{k}_3 = 2\pi/\lambda(\sqrt{3}/2, -1/2, 0)$, $\sqrt{3}\lambda$ is the lattice period, $\mathbf{r}' = (x - \sqrt{3}\lambda, y, 0)$, C is the contrast and A a normalization constant. The effect of the trap is encoded in the gaussian envelope along y with width σ_y and in the Thomas-Fermi profiles along x (z) with radii R_x (R_z). We also add a gaussian envelope along x for the sinusoidal modulation, with width w_x . We set all the parameters characterizing the ansatz 3.7 to realistic values obtained from fits of the simulated ground states in potentials V_C and V_D [15], see Fig. 3.11(g). We then numerically calculate the energy of the system Eq. 3.3 using ansatz 3.7 as a function of the contrast C only. The results are plotted in Fig. 3.11(c-d) for potentials V_C and V_D , respectively, for different values of the scattering length a_s . For a direct comparison with the experimental results, we plot the energy as a function of \tilde{C} , obtained from the Fourier transform of the wavefunction, as in the simulations. We correctly reproduce the same energy shapes of continuous and discontinuous transitions of the Landau model, see Fig. 3.1. The critical regions of the model, highlighted by the thick lines in Fig. 3.11(c-d), are in qualitative agreement with the experimental fluctuations spectra of region II. Our simple model captures quite well also the critical scattering lengths, equal to $96 a_0$ ($90 a_0$) for potential V_C (V_D) against $94 a_0$ ($91.9 a_0$) obtained from the numerical simulations. The qualitative success of the model in explaining the observations validates the choice of the contrast \tilde{C} as the order parameter of the transition, since its variation alone across the critical point is enough to capture the main features of the fluctuation spectra. Overall, the analysis of the order parameter fluctuations, together with the numerical Landau energies, is clear evidence of the different nature of the two phase transitions.

In addition to amplitude excitations, related to the contrast \tilde{C} , we also studied the fluctuations of the phase difference φ between the main clusters, extracted from time of flight images, see section 2.2. The phase fluctuations must be small in both potential V_C and V_D , otherwise the distinctive phase coherence of the supersolid phase is lost. Results are shown in Fig. 3.12. Note that in our fitting function in Eq. 2.4, the ground state corresponds to $\varphi = \pi/2$, consisting of a central peak and two symmetric lateral ones. In potential V_C , we observe a very high degree of coherence, with a variance $\sigma_\varphi^2 = 0.035$ considering all the images in the interval 89-93 a_0 . In potential V_D , the variance is one order of magnitude larger, $\sigma_\varphi^2 = 0.17$, in the interval 90-92 a_0 . Both values are safely lower than the variance of a uniform distribution, $\sigma_\varphi^2 = \pi^2/12 \sim 0.8$, as expected in the supersolid phase. However, it is clear that in the discontinuous phase transition also collective modes related to the phase φ are excited, and the supersolid in potential V_C is much nearer to the ground state than in potential V_D . For lower scattering length regions, in both potentials the phase distribution gets broader, probably due to three-body losses. In potential V_C (V_D), $\sigma_\varphi^2 = 0.055$ ($\sigma_\varphi^2 = 0.48$) in the interval 86-89 a_0 (88-90 a_0).

Some remarks about phase transitions in finite systems

In this paragraph, I want to report some objections that I received, mainly from theorists, presenting at international conferences the work about phase transitions. The first objection is that we can't speak about crystals in 1D and 2D, since stable crystals at finite temperature exists only in 3D. The first answer is that our system is intrinsically 3D,

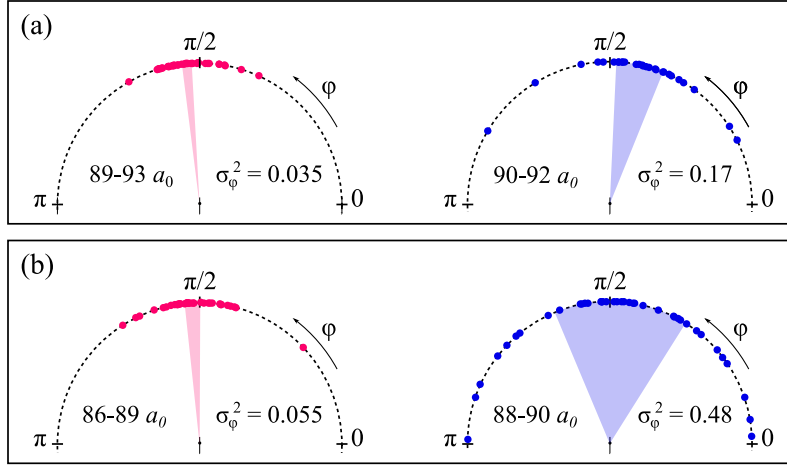


Figure 3.12: Phase fluctuations. (a) Phase ϕ from all the images just after the transition for potential V_C (left) and V_D (right). The intervals in scattering length are 89-93 a_0 and 90-92 a_0 , respectively. (b) Same phase fluctuations as in (a), but deeper in the supersolid regime: 86-89 a_0 for V_C and 88-90 a_0 for V_D . In both panels, the shaded areas indicate the interval $\bar{\phi} \pm \sigma_\phi^2$, with $\bar{\phi}$ and σ_ϕ^2 the mean and variance of the distributions, respectively.

but the translational symmetry breaking happens along one or two dimensions. However, considering in detail the objection, I found that the reason for which 1D and 2D crystals aren't stable is that they are destroyed by long-wavelength fluctuations. Considering a lattice of harmonic oscillators, one can calculate the mean fluctuation δ of the position of the single lattice site due to the temperature T . Of course, the solid can't be stable if δ is larger than the lattice period. The result is that δ goes as $k_B T / m \int k^{d-3} dk$, where d is the dimensionality of the system and the integral is over the wave vector k [109]. If $d = 3$, δ is finite, but if $d = 2$ ($d = 1$), δ diverges as $\ln k$ ($1/k$) when k goes to zero.

However, it actually diverges only if the system is infinite. In a finite system with dimension L there is a minimum wave vector $\bar{k} = 2\pi/L$, so that the solid is stable provided that $\delta < a$, with a lattice period. This is why 2D crystals such as graphene can exist also at finite temperatures. Since our dipolar supersolid is of the cluster type, the mass of each lattice site is $\sim 5 \times 10^3 m$, with m the mass of each atom, so that the fluctuations of the single-site position are strongly suppressed. Moreover, the lattice period is $a = 4 \mu\text{m}$, which means that the stability is much more robust. Putting the numbers, we find that at $T = 50 \text{ nK}$, in $d = 1$ (where the divergence is more dramatic), supersolids up to 5×10^4 droplets are stable against thermal fluctuations³. A similar reasoning applies also to quantum fluctuations.

The second objection is that we can't speak about phase transitions if the system has

³The model consists of a chain of harmonic oscillators. The stability condition requires that the number of lattice sites s should be much lower than $\sqrt{\frac{2\pi^2 M \omega^2 a^2}{k_B T}}$. To estimate the frequency ω , we take the typical frequency of phononic excitations of the supersolid, $\omega \sim 2\pi \times 20 \text{ Hz}$ [45]

only a few lattice sites, of the order of 4-5: finite size effects are too strong and all the thermodynamic functions are broadened. Nevertheless, the presence of a sharp transition from the BEC to the supersolid is supported by experimental evidence, as demonstrated in this chapter. The explanation of this observation is again related to the cluster nature of the dipolar supersolid, and relies on the fact that finite size effects depend on the atom number N : the broadening of the critical region of a first-order phase transition goes as $\Delta T_C/T_C \sim 1/N$, see for example [110]. The atom number usually coincides with the number of sites, but not in the cluster supersolid, where N is about 10^4 times the number of sites. Regarding finite size effects, therefore, the cluster supersolid with 4 lattice sites should be considered as a chain with 4×10^4 sites with one atom per site.

Chapter 4 Supersolidity and rotations

Some of the most striking differences between superfluids and classical fluids emerge in the rotational properties. The reason at the core of the anomalous rotational behavior of superfluids is the existence of the macroscopic wavefunction and the connection between its phase and the velocity of the superfluid, $\mathbf{v} = \hbar/m\nabla\varphi$. Since the velocity is the gradient of the phase, the velocity field must be irrotational, $\nabla \wedge \mathbf{v} = 0$. This condition is a striking difference compared to classical systems and limits the possible dynamics of the superfluid. The effects of the irrotational condition are enhanced in circular geometries. When the container of the superfluid is rotated (a physical container for superfluid helium, or the optical harmonic trap for atomic BECs and Fermi gases) the superfluid can't acquire angular momentum in the form of a rotational motion, meaning that its moment of inertia is zero. This effect, in the context of superfluid helium, is called the Hess-Fairbank effect [2]. For larger angular velocities, vortices can form. They correspond to a rotation of the superfluid with a quantized angular momentum in multiples of \hbar per atom, related to a phase jump along a closed path with amplitude equal to an integer multiple of 2π [3], and a vanishing density at the center of the vortex. Pioneering experiments explored rotational anomalies in superfluid ^4He (the Hess-Fairbank experiment) [111], in superfluid ^3He [112], in BECs [113], and in Fermi gases across the BEC-BCS crossover [114]. The analog effect in superconductors is the so-called Meissner effect, namely the expulsion of magnetic fields from the superconducting region, equivalent to the expulsion of rotational fields from superfluids [2].

In this chapter, we investigate the general question of how a supersolid rotates, sticking to the low-velocity regime in which vortices are not excited. What are the analogies and differences with standard superfluids? Being described by a macroscopic wavefunction, the fundamental relationship $\mathbf{v} = \hbar/m\nabla\varphi$ holds also for supersolids, but the presence of a density modulation brings on important novelties, which highlight the intermediate nature of the supersolid between superfluids and crystals. We start in section 4.1 with a detailed description of the seminal Leggett's model, cited in the first chapter 1.1, for which we propose an original interpretation [21]. We then discuss in sections 4.2 and 4.3 our measurement of the moment of inertia of the dipolar supersolid through the scissors mode [19], a collective mode previously employed to measure the moment of inertia of standard BECs [115, 116]. The moment of inertia of the supersolid results lower than the classical value, demonstrating its superfluid properties under rotation. The differences relative to the BEC phase are connected to the concept of superfluid fraction f_s , which emerges clearly in the Leggett model as the quantity that determines the role of the density

modulation in the rotation, interpolating between the fully superfluid and the classical moments of inertia. In section 4.4, we deal with the role of the superfluid fraction in our experiment, which we estimate to be of order 1.

We note that the superfluid fraction discussed here is different from the usual f_s of superfluids at finite temperatures. In that case, a two-fluid model depicts the system as separated into a normal part, made of thermal excitations, and a superfluid part, described by a macroscopic wavefunction [3]. The superfluid fraction then naturally goes to 1 when thermal excitations are absent. For supersolids at zero temperature, the superfluid fraction instead arises genuinely from the breaking of translational invariance and doesn't rely on a two-fluid model [1, 117]. The sub-unity superfluid fraction at zero temperature is, therefore, a peculiarity of the supersolid phase.

We remark that the concept of superfluid fraction is also different from that of condensed fraction f_c . The latter quantifies the population of the macroscopic wavefunction, while the first is the fraction of the system with a superfluid response to external probes. In strongly interacting systems, such as superfluid helium or ultracold Fermi gases, it is evident that the two quantities are different because the condensate depletion is high at low temperatures (hence f_c is less than one), but $f_s = 1$ at $T = 0$ [18]. Even if accurate measurements of f_c in the supersolid phase are missing¹, the general agreement of experiments with the mean-field GPE simulations points toward a large condensed fraction $f_c \sim 1$, while f_s can be much less than 1, a situation similar to that of zero-temperature Bose systems with disorder [118].

Even if the discussion in this chapter about f_s only concerns the physics of rotations, in the next chapter 5 we give a broader definition, from which we draw out a new measurement technique enabling us to assess the sub-unity and tunable superfluid fraction of the supersolid.

4.1 Leggett model for a rotating supersolid

The seminal model by Leggett [1] considers a system confined in a ring with radius R and with thickness small enough to neglect all the degrees of freedom in the transverse directions. We therefore consider a 1D numerical density $n(x)$, which is known and describes the ground state of the system at rest. The spatial coordinate x runs over the ring and takes values from 0 to $D = 2\pi R$. The total atom number is $N = \int_0^D n(x) dx$. The ring rotates at constant angular velocity ω , and we want to calculate the moment of inertia I of the system through the definition $I = \lim_{\omega \rightarrow 0} \langle L \rangle / \omega$, where $\langle L \rangle$ is the total angular momentum the system takes from the container and the operation $\langle \cdot \rangle$ is an average

¹Generally, for weakly interacting BECs, the quantum depletion η at zero temperature, namely the fraction of the atoms coherently scattered out of the condensate ($\eta = 1 - f_c$), is calculated in the framework of the Bogoliubov theory and depends on the small gas parameter $\sqrt{na_s^3}$. For dipolar BECs, the quantum depletion is $\eta = \frac{8}{3\sqrt{\pi}} \sqrt{na_s^3} (1 + 3/10\epsilon_{dd}^2)$ [42]. In our experiment, on the BEC side, near to the transition, we have $n \sim 10^{14} \text{ cm}^{-3}$, $a_s \sim 100 a_0$ and $\epsilon_{dd} \sim 1$, giving $\eta_{BEC} \sim 0.7 \%$. It is not clear to what extent the Bogoliubov theory for a homogeneous superfluid applies also to the supersolid ground state. However, taking the peak density $n \sim 10^{15} \text{ cm}^{-3}$, $a_s \sim 90 a_0$ and $\epsilon_{dd} \sim 1.5$, we get $\eta_{SS} \sim 2.4 \%$.

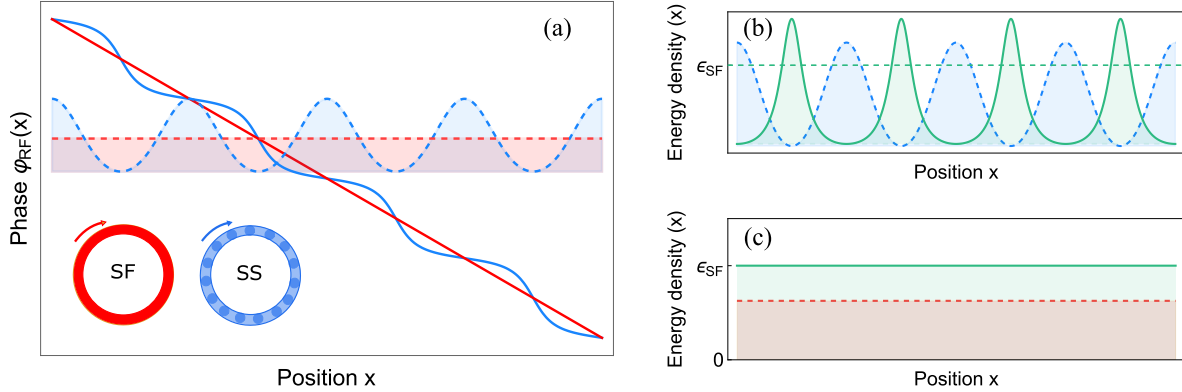


Figure 4.1: Leggett model for a rotating supersolid in the rotating frame. (a) Phase profile $\varphi_{RF}(x)$ that minimizes the kinetic energy 4.2 for a homogeneous superfluid (red) and a supersolid (blue). Dashed lines indicate the density profiles in the two cases. Insets: sketches of the density of the system in the rotating ring. (b-c) Kinetic energy densities associated with the phase profiles in (a) for a supersolid (b) and a homogeneous superfluid (c). Thick green lines are the kinetic energy densities, while dashed lines are the density profiles for the supersolid (blue) and the homogeneous superfluid (red). The superfluid fraction is the ratio between the areas under the green lines in the two panels, according to Eq. 4.7.

over the density $n(x)$. We consider small angular velocities ω so that we don't excite any vortex in the system, i.e. $\omega < \omega_c$ with ω_c the critical angular velocity for the nucleation of a vortex [3]. We know that for a classical system in equilibrium with the container, the velocity field is $v_c = \omega R$ and the moment of inertia is the classical one, $I = I_c = NmR^2$. For a homogeneous superfluid with $n(x) = \bar{n} = N/D$, like a BEC in a ring potential, the irrotational condition of superfluid hydrodynamics $\nabla \wedge \mathbf{v} = 0$ prohibits the classical velocity field, and no angular momentum can go from the container to the system. The irrotational condition, in terms of the phase φ of the wavefunction, means that the wavefunction must be single-valued when going back to the same position along the ring, $\varphi(0) = \varphi(L)$. The velocity is zero everywhere and the moment of inertia vanishes, $I = 0$.

We want to understand what happens to a supersolid, that has to fulfill the irrotational condition but also has a spatially varying density $n(x)$. The density is periodic in space with period d , $n(x+d) = n(x)$. We tackle the problem by asking what is the state with minimum energy, compatible with the rotation of the ring and the condition $\varphi(0) = \varphi(D)$. We would be tempted to answer that such a state is the one with zero velocity, as in the superfluid case. However, the subtle point is that in the lab frame, the confining potential is time-dependent, and to minimize the energy we must move into the time-independent frame corotating with the ring (if we don't do so, the minimum energy state also for a classical system would be the one at rest). In the rotating frame, the wavefunction takes on a Galileian phase, $\psi' = \psi \text{Exp}[-i(mVx + mV^2t/2)/\hbar]$ [3], with $V = \omega R$ the velocity of the moving frame. Since the phase transforms as $\varphi \rightarrow \varphi_{RF} = \varphi - (mVx + mV^2t/2)/\hbar$, the single-valuedness boundary condition $\varphi(0) = \varphi(L)$ becomes

$$\varphi_{RF}(D) - \varphi_{RF}(0) = \Delta\varphi = -\frac{m\omega RD}{\hbar}. \quad (4.1)$$

The effect of the rotation is therefore to impose a phase twist $\Delta\varphi$ proportional to the angular velocity ω . We can then minimize the kinetic energy due to the rotation

$$E_{kin} = \frac{\hbar^2}{2m} \int_0^D n(x) |\nabla\varphi|^2 dx \quad (4.2)$$

with the boundary condition 4.1. The density profile $n(x)$ is fixed and we search for the phase profile $\varphi(x)$ which minimizes the energy. Since the problem is 1D, $\nabla\varphi(x) = \varphi'(x)$. The kinetic energy in Eq. 4.2 has the form of a classical action $S = \int \mathcal{L} dx$ with the lagrangian $\mathcal{L}(\varphi, \varphi') = n(x)\varphi'^2$. The minimum of the action S , and hence of the kinetic energy E_{kin} , is given by the Euler-Lagrange equation of motion of classical mechanics $\frac{d}{dx} \frac{\partial}{\partial \varphi'} \mathcal{L} - \frac{\partial}{\partial \varphi} \mathcal{L} = 0$. In our case, it reduces to

$$\frac{d}{dx} \left(n(x)\varphi'(x) \right) = 0. \quad (4.3)$$

This expression is nothing but the continuity equation for the superfluid in the rotating frame, if one assumes a stationary flow $\frac{\partial}{\partial t} n = 0$ [119]. By integration and multiplying by \hbar/m we obtain that the current density in the rotating frame is a constant, $n(x)\frac{\hbar}{m}\varphi'(x) = J$, to be determined imposing the boundary condition 4.1. The result is $J = -\omega R\bar{n}f_s^u$, with

$$f_s^u = \left(\frac{1}{d} \int_0^d \frac{dx}{n(x)/\bar{n}} \right)^{-1}. \quad (4.4)$$

The expression for f_s^u is the upper limit for the superfluid fraction in Leggett's model, as it will be clear in a moment. Note that in Eq. 4.4 the lattice period d can be replaced by the length of the ring D due to the periodicity of the density $n(x)$. The phase in the rotating frame is

$$\varphi_{RF}(x) = \frac{m}{\hbar} J \int_0^x \frac{dx'}{n(x')} \quad (4.5)$$

The phase is plotted in Fig. 4.1 for a homogeneous superfluid and for a supersolid with $f_s^u \sim 0.5$. In the superfluid, with $n = \bar{n}$ we get $f_s^u = 1$, $J = -\omega R\bar{n}$ and $\varphi_{RF} = -\frac{m}{\hbar}\omega Rx$. The phase profile is linear. In the supersolid, the phase variation is faster in the density minima and slower in the density maxima. We can understand this behavior by noticing that it is the most efficient way to minimize the kinetic energy, given a fixed phase twist $\Delta\varphi$. Indeed, the faster variation in the phase is compensated by the low density, and the integrand in Eq. 4.2 is lower. In Fig. 4.1(b-c) we plot the density of kinetic energy $\frac{\hbar^2}{2m}n(x)\varphi'_{RF}(x)^2$ using the phase we found before in Eq. 4.5. The kinetic energy is lower for the supersolid than for the superfluid. In this sense the supersolid is 'less superfluid' than the homogeneous superfluid: it pays less energy to accommodate a given phase twist $\Delta\varphi$. Writing down the kinetic energy obtained from our variational approach, we get

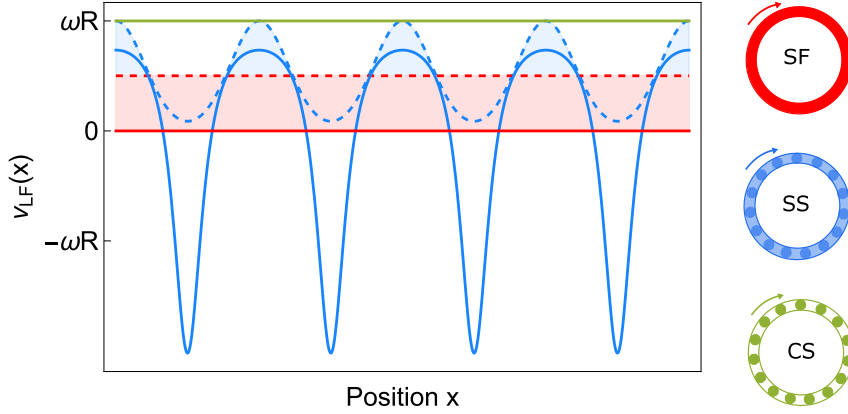


Figure 4.2: Leggett model for a rotating supersolid in the lab frame. Thick lines are the velocity fields along the ring for a homogeneous superfluid (red), a supersolid (blue), and a classical solid (green). In the first two cases, the velocity field is irrotational ($\int v dx = 0$), while in the third case, it is the classical rotational velocity ($\int v dx = 2\pi\omega R^2$). The velocity field determines the moment of inertia in Eq. 4.9. Shaded areas delimited by dashed lines are the density distribution of the homogeneous superfluid (red) and the supersolid (blue). Insets: sketches of the density distribution in the rotating ring for a homogeneous superfluid (red), a supersolid (blue) and a classical solid (green).

$$E_{kin}^{var} = \frac{N\hbar^2}{2mD^2} f_s^u \Delta\varphi^2. \quad (4.6)$$

The superfluid fraction f_s^u has the role of an elastic constant for the phase deformation. The stiffer the system is to phase deformations, the more superfluid it is. Noting that in the homogeneous case the kinetic energy cost for the twist $\Delta\varphi$ is $E_{kin}^{hom} = \frac{N\hbar^2}{2mD^2} \Delta\varphi^2$, because the phase slope is constant and equal to $\Delta\varphi/D$, an equivalent definition of the superfluid fraction is

$$f_s = \frac{E_{kin}}{E_{kin}^{hom}}, \quad (4.7)$$

namely the ratio of the kinetic energies due to a fixed phase twist in the modulated and homogeneous case. This definition of f_s will be the starting point of the Josephson experiment described in the next chapter.

Going back to the rotating ring, we can find the velocity field in the lab frame and calculate the moment of inertia of the supersolid. The velocity field in the lab frame is given by $v_{LF} = \omega R + v_{RF}$ and it is [21]

$$v_{LF}(x) = \omega R \left(1 - \frac{\bar{n}}{n(x)} f_s^u \right). \quad (4.8)$$

This function is plotted in Fig. 4.2. When $n = \bar{n}$, the superfluid fraction is 1 and we correctly get $v_{LF} = 0$. For a classical solid, instead, $f_s^u = 0$ and $v_{LF} = \omega R$. For the intermediate supersolid case, the velocity of the clusters tends to be near the classical

value, while the superfluid background moves in the opposite direction. We can interpret this motion as a combination of the crystal structure which is dragged by the classical rotation and of the superfluid background that preserves the irrotational condition (indeed $\int_0^D v_{LF}(x)dx = 0$). Calculating the angular momentum $\langle L \rangle = \int_0^D n(x)mv_{LF}(x)Rdx$ we get the moment of inertia

$$I = (1 - f_s^u)I_c \quad (4.9)$$

with $I_c = NmR^2$ the classical moment of inertia. This expression shows that f_s^u is indeed the superfluid fraction of the system, also from a rotational point of view. However, since we employed a variational approach to calculate the kinetic energy, what we found is an upper bound of the real superfluid fraction f_s , $f_s \leq f_s^u$. Remarkably, the simple expression in Eq. 4.4 for f_s^u depends only on the ground state density, and it is particularly sensitive to the density depletion between one cluster and the other. When $f_s^u < 1$, the superfluid fraction is restricted to be lower than one. The sub-unity superfluid fraction of the supersolid arises purely from the spontaneous symmetry breaking of the ground state, and not from more familiar thermal effects that deplete the population of the condensate. Leggett's model, therefore, predicts the peculiar property of supersolids of having a sub-unity superfluid fraction even at $T = 0$, tunable with the amplitude of the density modulation.

Starting from the expression of the kinetic energy in 3D, with the full density $n(x, y, z)$, Leggett found also a lower bound [117]

$$f_s^l = \int dydz \left(\frac{1}{d} \int_0^d \frac{1}{n(x, y, z)/\bar{n}} dx \right)^{-1}, \quad (4.10)$$

where this time \bar{n} is the average 3D density. The upper and lower bound coincide if the density is separable in the transverse coordinates y and z , i.e. $n(x, y, z) = f(x)g(y, z)$. For example, if the density modulation is in one dimension only (stripes), the density is separable $n(x, y, z) = Af(x)$. In this case $f_s = f_s^u = f_s^l$ and the expression in Eq. 4.4 is exact.

Finally, we note that the model we developed in this section is analog to a classical problem, namely finding the capacitance C of a capacitor with a fixed potential difference ΔV and a spatially varying dielectric constant $\epsilon(x)$ [120]. Since the electrostatic energy is $E_{el} = \epsilon_0/2 \int \epsilon(x)|\nabla V|^2 dx$, the problem is equivalent to that of the rotating supersolid with $\varphi \rightarrow V$ and $n \rightarrow \epsilon$. The energy can be written as $E_{el} = C\Delta V^2/2$, so the capacitance C has the role of the superfluid fraction. Indeed, it quantifies how much energy can be stored in the capacitor (supersolid) for a given applied voltage ΔV (phase twist $\Delta\varphi$).

4.2 The scissors mode

From a conceptual point of view, the most simple geometry to study rotations is the ring, as explicated by the Leggett model of the previous section. Also on the experimental side, many measurements about the rotation of superfluids have been performed in ring-shaped

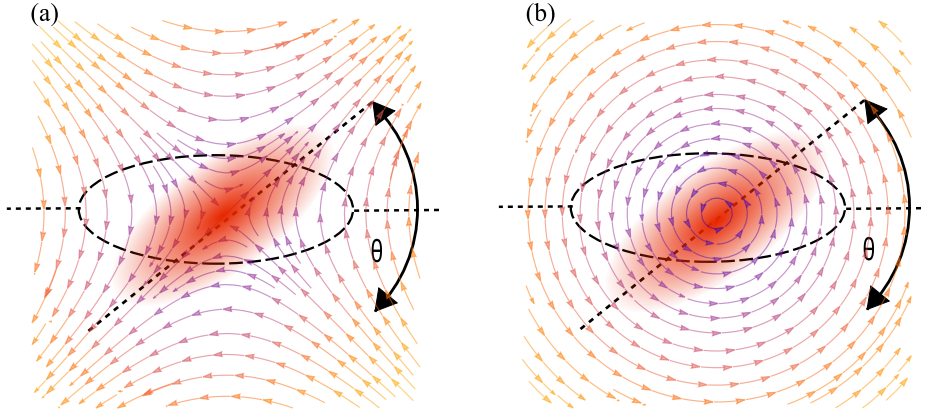


Figure 4.3: Superfluid versus classical rotation. (a) Velocity field of the scissors mode Eq. 4.12 in the xy plane. The velocity field has a quadrupole character and is irrotational: the velocity circulation along any closed path is zero. In the presence of the harmonic trap and in the limit of small oscillations, the motion is shape-preserving and the atomic cloud (red region) oscillates back and forth around the equilibrium position. The angle θ individuated by the main axis shows sinusoidal oscillations with frequency ω_{sc} . (b) Classical rotational velocity field. Globally, the motion is a rotation of the main cloud axis, as in the scissors case, but the velocity field in this case is rotational and the circulation along a closed path is different from zero.

potentials. However, superfluidity affects the dynamics also in anisotropic potentials, as the cigar-shaped trap of our dipolar supersolid. In this case, the most sensitive probe to superfluidity is the so-called scissors mode, a collective mode that consists of an oscillation of the atomic cloud around its main axis, as sketched in Fig. 4.3. The scissors mode bears its name from nuclear physics, where it corresponds to an out-of-phase oscillation of the neutron and proton clouds which resembles the movement of the blades of a pair of scissors [121]. It has then been employed to measure the moment of inertia of BECs [115, 116] and studied also in Fermi gases [122] and dipolar crystals of independent droplets [123]. The motion of the atomic clouds during the scissors oscillation is very similar to the dynamics of a sample oscillating in a torsional pendulum. In the latter case, the oscillation frequency of the pendulum is determined by the moment of inertia of the sample, $I = K/\omega_{tp}^2$, where K is the elastic constant of the rod of the pendulum. A measurement of ω_{tp} gives, therefore, a measurement of I . The torsional pendulum has been employed in solid helium experiments to search for a superfluid quenching of the moment of inertia, as explained in section 1.1, following the proposal suggested by Leggett. The scissors oscillation is the equivalent, for quantum gases, of the torsional pendulum in condensed matter, with the difference that the whole harmonic trap applies the torque needed to maintain the oscillation, instead of a single rod. Each atom, therefore, feels a different restoring force depending on its position in the trap. The frequency of the scissors oscillation ω_{sc} , as in the torsional pendulum, is directly related to the moment of inertia of the quantum gas through the following relationship, independent of the shape of the density distribution (BEC or supersolid) [124, 125]

$$\frac{I}{I_c} = \alpha\beta \frac{\omega_x^2 + \omega_y^2}{\omega_{sc}^2}, \quad (4.11)$$

where $\alpha = (\omega_y^2 - \omega_x^2)/(\omega_y^2 + \omega_x^2)$ and $\beta = \langle x^2 - y^2 \rangle / \langle x^2 + y^2 \rangle$ are geometric factors quantifying the deviation of the trapping potential and the density distribution from cylindrical symmetry, respectively. The numerator in Eq. 4.11 has the role of the elastic constant K . To highlight completely the relationship with the torsional pendulum, we derive Eq. 4.11 exploiting this analogy [126]. In the harmonic trap, the force applied on one atom at position (x, y) is $\mathbf{F}_{ho} = -\nabla V_{ho} = -m(\omega_x^2 x \hat{x} + \omega_y^2 y \hat{y})$. The torque in the vertical z direction is $\tau = xF_y - yF_x = -mxy(\omega_y^2 - \omega_x^2)$. During the oscillation, the spatial coordinates rotate, in the small angle limit, as $x \rightarrow x - \theta y$ and $y \rightarrow y + \theta x$. The effective elastic constant is $K = -\partial\tau/\partial\theta = m(y\partial x/\partial\theta + x\partial y/\partial\theta)(\omega_y^2 - \omega_x^2) = m(x^2 - y^2)(\omega_y^2 - \omega_x^2)$. Averaging over the whole density distribution and remembering that $I_c = \langle x^2 + y^2 \rangle$, we get Eq. 4.11 in the form $I = K/\omega_{sc}^2$.

For the BEC, it is possible to derive the scissors mode from the hydrodynamic equations moving in a frame rotating at constant angular velocity Ω [124, 125, 127]. The frequency of the mode results to be $\omega_{sc} = \frac{\alpha}{\beta} \sqrt{\omega_y^2 + \omega_x^2}$ and the associated velocity field is

$$\mathbf{v}_{sc} = \Omega\beta(y, x). \quad (4.12)$$

The scissors velocity field is plotted in Fig. 4.3(a). While in the small angle limit the motion of the cloud is shape-preserving and resembles a classical rotation, the velocity field is very different from the classical one, plotted for comparison in Fig. 4.3(b). The scissors field has a quadrupole character and satisfies the irrotational condition $\nabla \wedge \mathbf{v} = 0$, while the classical field is $\mathbf{v}_c = \Omega(-y, x)$ and it is rotational, $\nabla \wedge \mathbf{v}_c \neq 0$. The possibility for the superfluid to rotate with a finite angular momentum in the anisotropic trap means that its moment of inertia is larger than zero, differently from what happens in the cylindrical case. The angular momentum associated with the scissors field has a quadrupole character $L = |\langle \mathbf{r} \wedge \mathbf{v}_{sc} \rangle| = \Omega\beta \langle x^2 - y^2 \rangle = \Omega\beta^2 I_c$. The moment of inertia of the BEC is therefore

$$I_{BEC} = \beta^2 I_c. \quad (4.13)$$

We can obtain the same result from the general formula in Eq. 4.11 using the expression for the scissors frequency of the BEC. Since $\beta < 1$, the moment of inertia of the BEC is quenched compared to the classical one, but it is indeed larger than zero, a limit that we recover in the cylindrical case with $\beta = 0$. In the opposite limit of $\beta = 1$, corresponding to a 1D line, the behavior is completely dominated by the geometry and the scissors and classical fields are undistinguishable, resulting in $I = I_c$. To employ the scissors mode as a probe of superfluidity, the aspect ratio of the cloud should be neither too small (the scissors oscillation is difficult to detect because the geometry is nearly circular and $\mathbf{v}_{sc} \rightarrow 0$) nor too large (superfluid effects are suppressed). In the non-dipolar case, we have the simplification that the aspect ratio of the atomic cloud is completely determined by the trap and $\alpha = \beta$. In the dipolar case, instead, the cloud is elongated in the vertical direction due to the polarizing magnetic field (magnetostriction effect), and the aspect

ratio in the xy plane deviates from that of the trap [127]. The parameter β is, therefore, different from α and varies with the interaction parameter, $\beta = \beta(\epsilon_{dd})$.

The simple relationship in Eq. 4.11 between the scissors frequency ω_{sc} and the moment of inertia I is formally derived using a sum-rule approach [128, 129]. The frequency appearing in the equation is actually an upper bound for the frequency of the lowest energy state excited by the angular momentum operator. In a more general treatment, one has to study the response of the many-body system to a sudden rotation of the trap. Since the rotation of the harmonic trap by a small angle θ produces a perturbation in the potential $\mathcal{H}_{per} \propto xy$, the dynamics is induced by the quadrupole operator $Q = xy$. The moment of inertia is then determined by the frequency response of the quadrupole operator Q through the relation

$$\frac{I}{I_c} = \alpha\beta(\omega_x^2 + \omega_y^2) \frac{\int d\omega S_{QQ}(\omega)/\omega^3}{\int d\omega S_{QQ}(\omega)/\omega} \quad (4.14)$$

where $S_{QQ}(\omega)$ is the dynamical structure factor relative to the quadrupole operator Q [129]. In this more general framework, the response of the system to the perturbation in the whole frequency domain contributes to the moment of inertia. In the case of single-frequency response, as for the BEC for which the scissors mode is a normal mode, $S_{QQ}(\omega)/\omega = A\delta(\omega - \omega_{sc})$ and we get the sum-rule prediction 4.11. The simplest case of a multi-frequency response is that of a thermal gas. After the rotation of the trap, the gas oscillates with two frequencies $\omega_{\pm} = \omega_y \pm \omega_x$, with the same amplitude [124]. Using $S_{QQ}(\omega)/\omega = A\delta(\omega - \omega_+) + A\delta(\omega - \omega_-)$ in 4.14 we get $I = I_c$, as we expect for a thermal gas above the critical temperature for condensation.

4.3 Moment of inertia of the supersolid

In the experimental system, we excite the scissors mode and study its oscillation frequency across the BEC-supersolid phase transition [19]. We collaborated with the theory group of S. Stringari and A. Recati from Trento University. Their numerical simulations show that the scissors mode indeed is well defined also in the supersolid regime, and its frequency dominates the response of our system [128]. The sum-rule relationship 4.11 gives therefore direct access to the moment of inertia.

The experimental configuration of the scissors experiment consists of a supersolid trapped in a cigar-shaped harmonic trap with frequencies $(\omega_x, \omega_y, \omega_z) = 2\pi \times (23, 46, 90)$ Hz, realized by two crossed off-resonant optical beams at an angle of about 80° ². With a typical atom number of $N = 2 \times 10^4$ atoms, the critical point is at about $\epsilon_{dd} = 1.42$, and the supersolid is formed by two main clusters along the x axis. The transverse confinement along y is quite weak and the transition is well in the discontinuous regime of the phase diagram in Fig. 3.3 of section 3.2. The aspect ratio of the trap, however, is not too large, $\alpha = 0.6$, and favors superfluid effects in the scissors oscillation. Crossing the discontinuous transition

²ODT2 and ODT3 in the sketch of the experimental apparatus in Fig. 2.1.

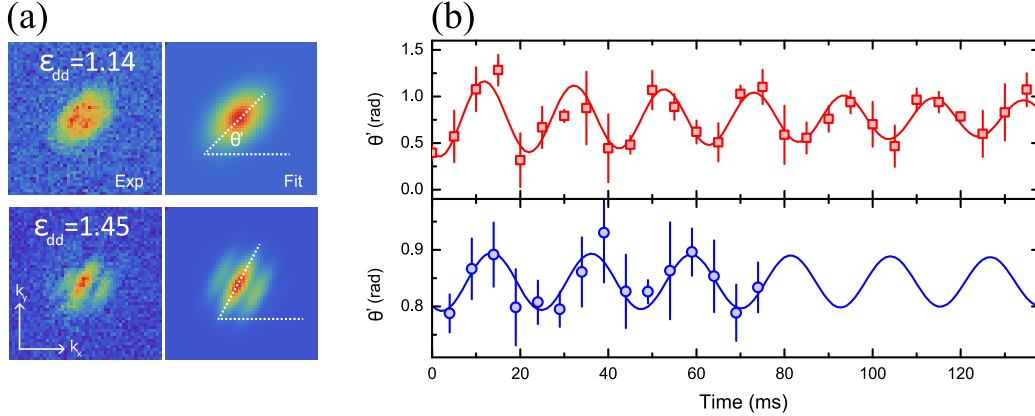


Figure 4.4: Scissors oscillation of the trapped supersolid. (a) Experimental images of the BEC at $\epsilon_{dd} = 1.14$ (up) and of the supersolid at $\epsilon_{dd} = 1.45$ (down) after a time of flight expansion and corresponding 2D fitting functions to measure the tilting angle θ' . (b) Single frequency oscillations of the tilting angle $\theta'(t)$ for the BEC (red) and the supersolid (blue). Thick lines are sinusoidal fits to extract the scissors frequency ω_{sc} .

from the superfluid to the supersolid excites a combination of different modes, as discussed in Section 3.3. Due to the cigar-shaped geometry of the trap, the strongest excited mode is the breathing mode, consisting of an oscillation of the x -width of the supersolid [45]. One of the main technical challenges in measuring the scissors oscillation, indeed, has been the development of a method to excite deterministically the scissors oscillation and avoid a strong coupling with the unavoidable breathing mode³. We, therefore, developed two different techniques. The first one consists of switching on for a short time a third off-resonant optical beam, in addition to the two beams forming the trapping potential. The angle of the main trap axis changes and the atoms start the scissor oscillation. This method, however, also changes the trap frequencies and excites other modes, mainly the axial breathing mode in the x direction. Both the resulting scissors and breathing amplitude are quite large, about 0.3 rad in the first case and 20 % of the equilibrium x -width in the second case. We employ this method on the BEC side, where the breathing and scissors modes are normal modes of the system and don't mix. The second method consists of changing slightly the power in the two crossed beams that form the optical trap. This method rotates the main axis of the trap without significantly modifying the trap frequencies. As a result, the breathing mode is less excited (amplitude about 10 %, coming mainly from the crossing of the phase transition), but the scissors mode also has a lower amplitude of about 50 mrad. We employ the second method in the supersolid regime, where with the first method we observe a mixing of breathing and scissors mode that increases the scissors frequency.

The single-frequency oscillations of the BEC and the supersolid are shown in Fig. 4.4. In addition to the small amplitude, the precision in determining the scissor frequency in the

³We first performed the scissors experiment and later we characterized the phase transition, as explained in chapter 3. Indeed, the excitations we observed in the scissors experiment after crossing the transition have been a strong motivation for searching for a continuous phase transition.

supersolid is also limited by the shorter lifetime. To measure the tilting angle θ of the atomic cloud, we take time of flight images and we fit with a 2D gaussian for the BEC and with the 2D version of the double slit fit in Eq. 2.4, as shown in Fig. 4.4(a) [19]. After the time of flight, we observe a tilting angle θ' different from the angle θ in situ. Even if the two angles are not easily connected, due to the complicated dynamics during the expansion, the oscillation frequency is the same [130]. We observe a single frequency oscillations ω_{sc} for all the interaction regimes we investigate. We measure the frequency ω_{sc} with a sinusoidal fit of the points $\theta'(t)$, see Fig. 4.4(b). In Fig. 4.5, we plot ω_{sc} as a function of ϵ_{dd} , normalized to the theoretical scissors frequency of a non-dipolar BEC, $\sqrt{\omega_x^2 + \omega_y^2}$. On the BEC side, ω_{sc} slowly decreases, consistently with the expected slow variation in the deformation parameter $\beta(\epsilon_{dd})$. Crossing the transition to the supersolid regime, we observe a sharper decrease in the frequency, signaling the onset of the transition, in agreement with the numerical simulations [128].

To translate the frequency measurements in the moment of inertia, we employ Eq. 4.11, where the deformation parameter β is taken from the numerical simulation of our system [128]. In Fig. 4.5(b) we plot I/I_c versus ϵ_{dd} . The moment of inertia of the BEC agrees with the prediction of superfluid hydrodynamics $I = \beta^2 I_c$, which gives $I \sim 0.5 I_c$ for our parameters. The moment of inertia of the supersolid is larger than that of the BEC but, at least for the point at $\epsilon_{dd} = 1.45$, well below the classical value. Our observation demonstrates that, even if the formation of the crystal structure increases the moment of inertia, the system is still superfluid. This is the first evidence of the superfluid behavior of the supersolid phase under rotation. The following point at $\epsilon_{dd} = 1.5$, closer to the droplet crystal, has instead a moment of inertia consistent with the classical one.

We also studied the effect of the temperature on the scissors oscillations, repeating the same experiment on the BEC side for different temperatures below and above the critical temperature T_c for Bose-Einstein condensation ($T_c \sim 60$ nK). The results are shown in Fig. 4.6. Below T_c , we measure the scissors oscillation for the condensed part, while we determine the temperature with an independent measurement of the thermal fraction with a lower expansion time (25 ms). We always observe a single-frequency oscillation, with a slight reduction compared to the zero-temperature limit for $T/T_c \sim 0.8$, probably due to interactions between the condensate and the thermal component. This measurement shows that, at the low temperatures at which we perform the experiment, $T/T_c < 0.4$, thermal effects are negligible. For $T > T_c$, we observe a scissors oscillation of the thermal cloud, shown in Fig. 4.6(a). The behavior is very different from that of the condensate: the angle θ' oscillates with two frequencies, near the hydrodynamics prediction for a collisionless gas, $\omega_+ = \omega_x + \omega_y$ and $\omega_- = \omega_x - \omega_y$ [124]. This observation demonstrates that our weakly interacting Bose gas is indeed in the collisionless regime. Even if not surprising, it is an important check because classical systems in the strongly interacting regime (the so-called hydrodynamic limit) can have a behavior very similar to superfluids, for example showing a single-frequency scissors oscillation. This is the reason why in strongly-interacting Fermi gases the scissors mode is not a good probe of superfluidity. In our case, instead, the observed scissors dynamics is a genuine consequence of superfluidity.

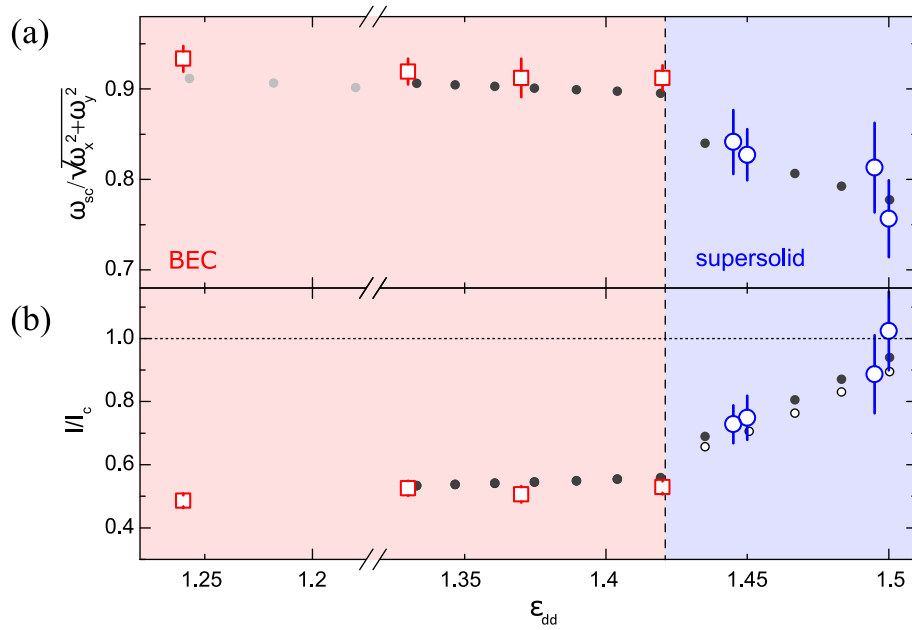


Figure 4.5: Scissors frequencies and moment of inertia. (a) Scissors frequency ω_{sc} as a function of ϵ_{dd} across the BEC-supersolid phase transition. The vertical dotted line is the theoretical critical point. Red points are in the BEC regime, while blue points are in the supersolid regime. Black points are the results of numerical simulations with the experimental parameters reported in [128]. Gray points are numerical simulations without the LHY energy term. Error bars correspond to one standard deviation. (b) Moment of inertia calculated from the measured scissors frequency and the numerical deformation parameter β , according to Eq. 4.11. Black points are the numerical results [128]. White points in the supersolid regime are the prediction for a fully superfluid system ($f_s = 1$) with the same β of the supersolid, namely $I = \beta^2 I_c$. The dashed horizontal line is the classical moment of inertia, $I = I_c$.

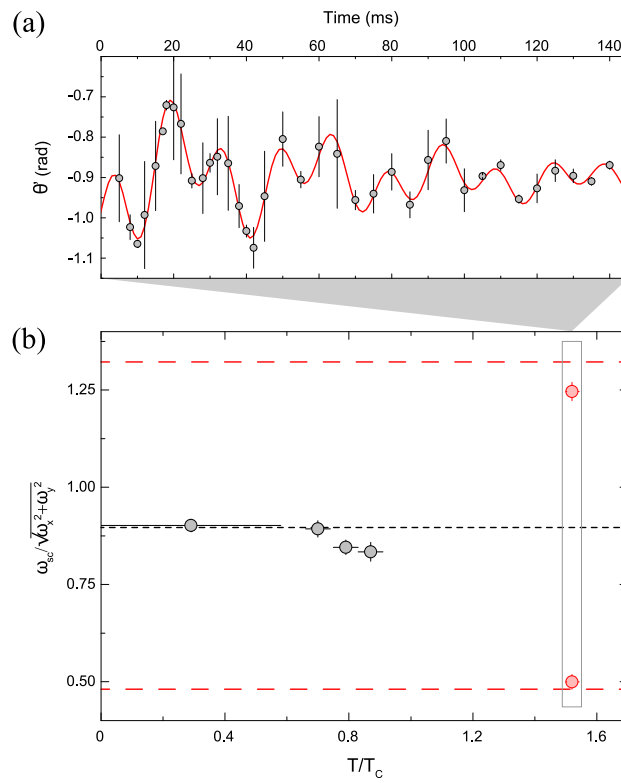


Figure 4.6: Scissors oscillations of the BEC at finite temperature. (a) Scissors oscillation $\theta'(t)$ for a thermal sample at $T > T_c$, showing a two-frequency oscillation. (b) Scissors frequency as a function of T/T_c . Red points are the frequencies measured on the thermal sample shown in (a). Dashed horizontal lines are the prediction for a thermal gas in the collisionless regime [124]. Gray points are the frequencies measured on the condensate for $T < T_c$. The first point with the large horizontal error bar corresponds to the final temperature of the experiment, when no thermal fraction is detected.

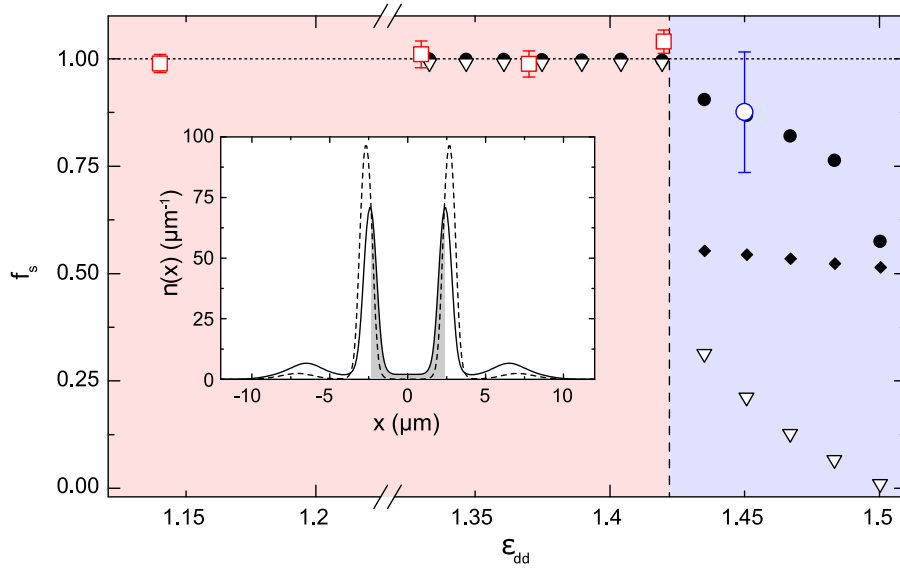


Figure 4.7: Superfluid fraction in the scissors experiment. The superfluid fraction is calculated from the measured moment of inertia I/I_c and the numerical β according to Eq. 4.15. Black points are the result of the same calculation with the numerical moment of inertia of [128]. The data point in the supersolid regime is the weighted average of the two data points at $\epsilon_{dd} = 1.45$ in Fig. 4.5. Open triangles are Leggett upper bound f_s^u in Eq. 4.4 calculated on the numerical ground state. Black diamonds are the estimation for the superfluidity of the single cluster f_{sID} , according to the ‘independent-droplet’ model in Eq. 4.17. Inset: numerical ground state density $n(x)$ employed for the calculation of Leggett upper bound at $\epsilon_{dd} = 1.45$ (continuous line) and at $\epsilon_{dd} = 1.5$ (dashed line). The integral in Eq. 4.4 is performed on the central cell between the two maxima (gray region).

4.4 Discussion about the superfluid fraction

The increase in the moment of inertia from the BEC to the supersolid has two causes. The first and dominant one is a geometrical change in the density distribution, encoded in the change of β . With the formation of the crystal structure, the system shrinks in the y direction and β increases. In Fig. 4.5(b), on the supersolid side we plot, as open dots, the moment of inertia $I = \beta^2 I_c$ of a hypothetical fully superfluid system ($f_s = 1$) with the same β as the supersolid. The remaining discrepancy with the observed moment of inertia is due to the decreased superfluid fraction of the supersolid, which physically implies a deformed velocity field compared to the scissors field $\mathbf{v}_{sc} \propto (y, x)$ of the standard BEC. As we see from the comparison between the results of the numerical simulations (black dots) and the open dots, the difference is present but very small. With the experimental errors, we are unable to appreciate the effect of the decreased superfluid fraction. Moreover, as one moves towards larger ϵ_{dd} , the region between full superfluidity ($I = \beta^2 I_c$) and classical rotation ($I = I_c$) shrinks, because β increases and the motion is dominated by geometrical effects.

To translate these considerations in terms of a superfluid fraction, we modify the general definition in circular geometries $I = (1 - f_s)I_c$ to include the effects of our anisotropic

trapping potential. We search for an empirical formula in which the superfluid fraction should interpolate between the classical result I_c and the full superfluid result in the cigar-shaped trap, $I = \beta^2 I_c$. We write⁴

$$I = (1 - f_s)I_c + f_s\beta^2 I_c, \quad (4.15)$$

which correctly reduces to the general definition in the cylindrical case, $\beta = 0$. From the measured I/I_c and the numerical β , we extract f_s as defined in Eq. 4.15. The results are plotted in Fig. 4.7. We obtain correctly $f_s = 1$ in the whole BEC regime, a result that supports the absence of thermal effects at the lowest temperatures achievable in the experiment, as already discussed in Fig. 4.6. A residual thermal fraction would indeed interact with the BEC and lower the scissors frequency, resulting in a lower superfluid fraction. For the datapoints in the supersolid regime at $\epsilon_{dd} = 1.45$, we get $f_s = 0.88 \pm 0.14$, a large value compatible with 1 under the experimental error. This result confirms the expectation of a large superfluid component in the dipolar supersolid, due to its cluster nature that enhances superfluid effects and coherence between different clusters. In this regard, the dipolar supersolid is strikingly different from other condensed matter systems. For example, in 2D ^4He and confined ^3He the superfluid fraction seems to be of the order of a few % [67, 68, 70], while in bulk solid helium, the first measurements indicated $f_s \sim 1\%$ [25, 26] (although they were then attributed to the elastic properties of ^4He , as explained in section 1.1). This large difference is not surprising: it arises from the cluster nature of the dipolar supersolid, which favors superfluid effects, as opposed to the vacancy supersolid, with one atom per lattice site, expected in the strongly-interacting regime of solid helium. We also compare our results with Leggett's upper bound for the ring geometry, Eq. 4.4. We calculate f_s^u from the numerical simulation of the ground state at $\epsilon_{dd} = 1.45$. We integrate the 3D density distribution along the y and z direction to obtain $n(x)$, shown in the inset in Fig. 4.7. To exclude the role of inhomogeneity, we calculate the Leggett formula only in the unit cell at the center of the trap, in the region highlighted in the inset. We also use the same interval to calculate f_s in the BEC regime. With this choice, we correctly get $f_s^u = 1$ for the BEC, and $f_s^u \sim 0.3$ for the first point in the supersolid. For larger ϵ_{dd} , f_s^u goes to zero because the overlap between the clusters vanishes. Leggett prediction is definitely lower than our measurement, but it accounts only for the dynamics between different clusters, which dominate in the ring geometry. Our case is very different since the scissors oscillation involves complicated dynamics in the whole xy plane. Indeed, the results of the numerical simulations, in which we calculate f_s with the same procedure as in the experiment, tend to saturate at $f_s \sim 0.5$ towards the droplet crystal regime, while Leggett's formula goes to 0.

We explain this behavior considering that a large contribution to f_s should come from the single cluster's rotational motion around the trap's center. Since the single cluster is a superfluid itself, its moment of inertia should be reduced compared to the classical value. The single cluster rotating around the trap's center, therefore, should contribute to

⁴In some successive papers [129] the superfluid fraction introduced here is called Non-Classical Rotational Inertia Fraction and indicated as f_{NCRI} , to distinguish it from the superfluid fraction f_s defined in the cylindrical geometry.

the superfluid fraction of the system, independently from the mass flow between different clusters. To estimate this contribution, which we expect to be quite large since the single cluster occupies a significant fraction of the whole system, we develop a simple classical model, depicted in Fig. 4.8. For a homogeneous disk of radius R and mass M rotating around an axis at a distance d from its center, classical mechanics predicts $I_c = I_{CM} + Md^2$, where the first term accounts for the rotation of the disk around its own center of mass, $I_{CM} = MR^2/2$, and the term Md^2 accounts for the rotation of the center of mass around the central point. This result is known as the Huygens-Steiner theorem. For the superfluid cluster, the rotation around its own center of mass is zero, due to its cylindrical symmetry, $I_{CM} = 0$. Therefore, the actual moment of inertia for this 'independent droplet' is $I_{ID} = Md^2$. Dynamically, the difference between I_c and I_{ID} could be explained with the shape of the velocity field: circular lines centered in the origin with magnitude $v = \omega r$ in the first case, and straight lines with the same magnitude $v = \omega d$ inside the same cluster in the second case, see Fig. 4.8. To quantify the contribution to f_s of the single cluster, we write Eq. 4.15 in the form

$$f_s = \frac{1 - I/I_c}{1 - \beta^2}. \quad (4.16)$$

To estimate β for the single cluster, we apply the same reasoning of the Huygens-Steiner theorem, considering a cluster with its center on the x axis at distance d from the origin. Recalling $\beta = \langle x^2 - y^2 \rangle / \langle x^2 + y^2 \rangle$, we calculate the numerator in this equation moving to the reference frame $x'y'$ centered on the droplet at coordinates $(x, y) = (d, 0)$. It becomes $\langle (x' + d)^2 - y'^2 \rangle = \langle x'^2 - y'^2 \rangle + \langle d^2 \rangle + 2d\langle x' \rangle$. The first and last terms vanish due to the cylindrical symmetry of the cluster. Calculating the average over the mass distribution, the result is $\langle x^2 - y^2 \rangle = Md^2 = I_{ID}$. The denominator $\langle x^2 + y^2 \rangle$ is instead equal to I_c . We therefore conclude that, for an independent droplet, $\beta = I_{ID}/I_c$. Using the expression for f_s in Eq. 4.16, we find

$$f_{sID} = \frac{1}{1 + \beta}. \quad (4.17)$$

Note that this estimation of f_{sID} is unaffected by the number of clusters forming the supersolid, as soon as they are all aligned in a 1D lattice. Indeed, for a system with n clusters, both I and I_c are multiplied by n and the ratio I/I_c doesn't change. From the numerical calculated β , we plot f_{sID} in Fig. 4.7 as black diamonds. The dependence on ϵ_{dd} is weak and we get $f_{sID} \sim 0.5$, which explains the saturation towards the droplet crystal regime, where only the contribution coming from the 'independent-droplet' model survives.

To conclude, we interpret the large value of f_s that we estimate in our system as a combination of the rotational motion of the single cluster around the center of the trap (f_{sID}) and the superfluid motion from one cluster to the other, estimated by Leggett formula (f_s^u). This interpretation is visualized in Fig. 4.9, where we plot two snapshots of numerical simulations during the scissors dynamics. While in the BEC case the velocity field has exactly a quadrupole shape, as predicted by Eq. 4.12, in the supersolid it gets

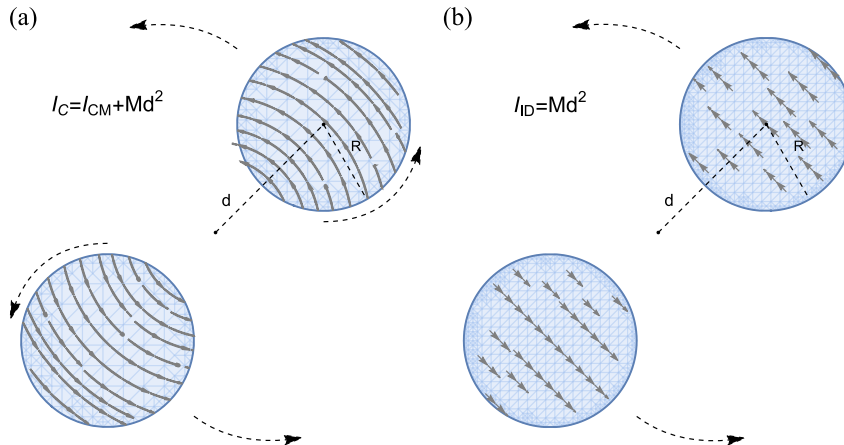


Figure 4.8: Model for the rotation of independent droplets around the center of the trap. (a) Classical droplets are approximated as disks with radius R rotating around an axis at a distance d from their center. The classical moment of inertia is $I_C = I_{CM} + Md^2$ according to the Huygens-Steiner theorem. Velocity field lines are circles around the rotation center, accounting for both the rotation of the center of mass around the trap center and of the single droplet around its center of mass (black arrows). (b) Superfluid droplets have a vanishing I_{CM} because of their cylindrical symmetry. Only the rotation of their center of mass around the trap center contributes to the moment of inertia, $I = Md^2$. The velocity field lines consistent with this picture are straight lines instead of circular lines. The reduced moment of inertia contributes to the total superfluid fraction of the system according to Eq. 4.17.

modified. The clusters are dragged by the rotational motion, and have a nearly constant velocity distribution that resembles that of the independent-cluster model. On top of that, there is a flow of atoms between the smaller lateral clusters across the weak links in the density background (since the aspect ratio of the trap is quite large, small lateral clusters appear also in the transverse direction). Even if this interpretation is largely qualitative, it is the first attempt to probe the rotational properties of the supersolid phase, and more generally the problem of superfluidity in a crystal, with the benchmark model by Leggett.

Comparison with larger systems

A natural improvement of our measurement would be to reproduce the same experiment in a configuration in which the role of the single clusters is reduced, so that other contributions to the superfluid fraction could emerge. A promising candidate is a supersolid with a more 2D crystal structure, in which the deformation parameter β is lower and hence geometrical effects are reduced. Numerical simulations show, indeed, that in a 2D configuration made up of two rows of clusters, rather than one single row as in our case, f_s calculated from the moment of inertia as in Eq. 4.16 correctly goes to zero in the independent droplets regime [129]. The scissors experiment has been performed by the Innsbruck group in the 'zig-zag' configuration consisting of a two-row supersolid [126]. However, they found out that the measured scissors frequency is unaffected by the density modulation and doesn't probe the decreasing superfluid fraction. The reason is that, in the more complex

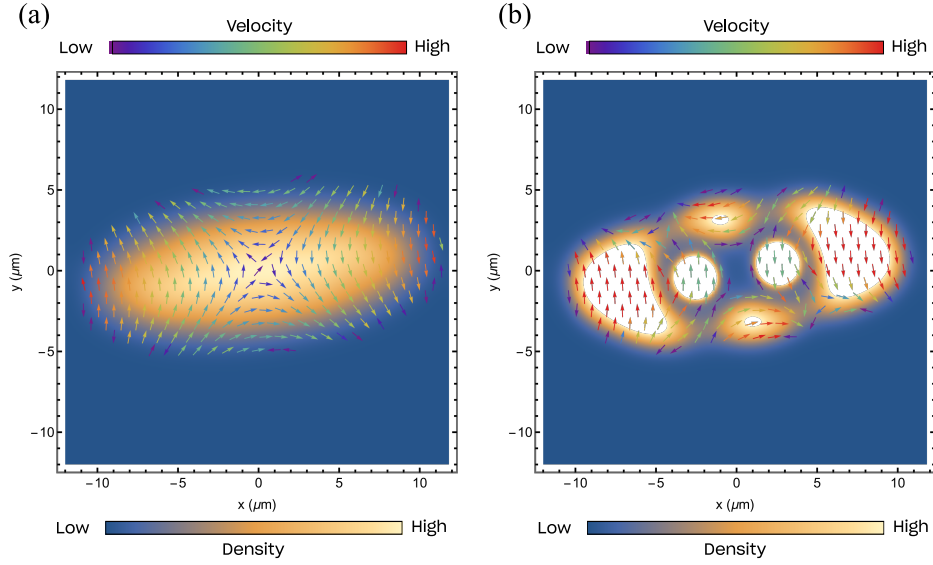


Figure 4.9: Snapshots from numerical simulations of the scissors oscillation. (a) Density of the BEC in the xy plane together with the velocity field (colored arrows). The velocity field has the quadrupole shape predicted for the scissors oscillation Eq. 4.12. (b) Density of the supersolid in the xy plane saturated to make visible also the density modulation in the background. The velocity field is modified compared to the BEC in (a). The differences of the velocity fields in (a) and (b) are the microscopic counterparts of the differences between the moment of inertia of the supersolid and that of a fully superfluid system.

2D system, the simple connection between ω_{sc} and the moment of inertia, namely Eq. 4.11, doesn't hold anymore because the response of the system becomes multi-mode. One should then rely on the more general Eq. 4.14 involving the whole frequency response of the quadrupole operator Q . The subtle point is that the moment of inertia is determined by the quadrupole structure factor S_{QQ} weighted by the inverse of the mode frequencies, see Eq. 4.14. Therefore, the weakest and slowest frequencies can make a huge contribution to the moment of inertia, despite being negligible in the real-space dynamic of the atomic cloud. As a matter of fact, the scissors oscillation detected experimentally still shows a single-frequency response, but that frequency alone is not enough to correctly trace back to the moment of inertia [126]. One should increase the interrogation time to measure the slower frequency contributions, but this appears to be difficult also in the numerical simulations [129], and practically impossible in the experiments. Therefore, the scissors technique is limited to small and single-row systems, like the one we investigated, in which the frequency response is saturated by a single component and Eq. 4.11 applies.

Sub-unity superfluid fraction from self-induced Josephson effect

In the previous chapter, we discussed how the anomalous superfluid properties of the supersolid affect its rotational response. The superfluid fraction f_s was pointed out as the quantity which determines the departure of the supersolid behavior from that of a fully superfluid system, through the modification of its moment of inertia. For the dipolar supersolid, the measurement of this quantity through rotations is challenging. On one side, in small linear systems, a simple relationship between the scissors mode and the moment of inertia exists, but the superfluid rotation is strongly influenced by the behavior of the single (big) clusters, rather than by the global motion from one cluster to the other. On the other side, in larger and 2D systems, the relationship between scissors mode and moment of inertia gets complicated and requires prohibitive experimental conditions to be probed.

In this chapter, we present a novel approach to the problem. We discuss the superfluid fraction in a more general framework than rotations, relating f_s to the so-called superfluid stiffness, namely the energy cost required to twist the wavefunction phase of a superfluid. Within this approach, the superfluid fraction quantifies how much the superfluid stiffness is reduced by the presence of the competing crystal-like order. Inspired by this new point of view, we develop a new method for the measurement of the superfluid fraction, based on the Josephson effect between different clusters of the supersolid. The Josephson effect is peculiar to superfluids and superconductors and it is usually observed when two superfluid baths are separated by an external potential barrier, forming a so-called Josephson junction. The idea itself of a supersolid phase is very similar to a Josephson junction array: when a superfluid develops a crystal structure, the different clusters are connected by a weak link. However, in the supersolid, the barrier between different clusters is self-induced by interactions between the same atoms that form the junction and is not externally imposed. It is not clear a priori, therefore, if the supersolid can sustain Josephson oscillations between its clusters.

In our work [22], we develop a method to excite Josephson oscillations in the supersolid, and we observe coherent phase-population oscillations in perfect agreement with the Josephson junction physics. We observe a progressive slowing down of Josephson oscillations by increasing the density modulation of the supersolid, and from our measurements we quantitatively assess a sub-unity superfluid fraction, which is tunable from 1 to about 0.1.

Our method allows for a local measurement of the superfluid fraction, since in prin-

principle it involves only the dynamics inside the unit cell, as opposed to rotational kicks which involve measurements of global quantities, such as the moment of inertia. Regarding the specific case of dipolar supersolids, the Josephson method solves many problems related to rotational probes: it is directly sensitive to the motion across the weak link between clusters, and its local nature allows for eliminating the complications introduced by the inhomogeneity of the density distribution. But, even more important, the generality of the Josephson method could also be of interest for other systems, as the modulated states in condensed matter superfluids, for which measurements of the superfluid fraction have been performed only through rotational or similar probes [67, 68, 70] or in which the concept of the superfluid fraction is not discussed at all, as in the pair density wave phases in superconductors [72, 76]. As discussed in section 1.3, there is evidence of a reduced superfluid stiffness in cuprate superconductors, associated with a competition between spatial and superconductive orders [73], which is correlated with the critical temperature for superconduction [78, 79]. Also in superconductors, the superfluid stiffness is measured with a global probe, namely the penetration depth of magnetic fields. The superfluid fraction, thanks to its generality, is a candidate for a universal system-independent quantity, useful to compare supersolid-like phases in different fields of physics.

In section 5.1 we discuss the connection between the superfluid fraction and the Josephson dynamic. In sections 5.2 and 5.3 we describe the experimental protocol to excite and measure Josephson oscillations in the supersolid. In section 5.4 we illustrate the modelization of the supersolid as a Josephson junction and, finally, in section 5.5 we present the results for the measured superfluid fraction, together with a discussion of interesting phenomena, related to the sub-unity superfluid fraction, to be investigated in the future. Finally, in section 5.6, we give an outlook on the possible role of the low-energy Goldstone mode, related to the peculiar dynamics of the junction barrier.

5.1 Superfluid fraction and Josephson oscillations

One of the most striking differences between a solid and a liquid is that the first is able to sustain shear stress, while the second is not. In other words, the solid is rigid and the liquid is fully deformable. The changing degree of rigidity going from one state to the other can be captured by a single parameter, such as the shear modulus, which is zero for a liquid and different from zero for a solid. The emergence of rigidity is not a peculiarity of the solid phase, but it is a general feature of symmetry-breaking phase transitions [16]. The ordered phase, which forms when the symmetry is broken, possesses some kind of emergent rigidity that was absent in the disordered phase, when the symmetry wasn't broken. Another example is the so-called spin stiffness, which quantifies the energy cost of modifying locally the spin direction in a ferromagnet, creating a spin wave. Generally, for a transition with some order parameter θ , the generalized stiffness S quantifies the energy cost of transverse spatial variations, namely in the direction perpendicular to θ

$$\delta F = \frac{S}{2} \Delta\theta_{\perp}^2. \quad (5.1)$$

The concept of emergent rigidity applies also to superfluids and superconductors. In this case, the order parameter is the modulus of the wavefunction $|\psi|^2$, and the emergent rigidity is the energy scale relative to the deformation in the perpendicular direction. Thinking about the mexican hat Landau's potential, the perpendicular direction to $|\psi|^2$ is the space of the wavefunction phase, $\theta_{\perp} = \varphi$. The superfluid stiffness, therefore, quantifies the energy cost of phase variations, which are in the form of kinetic energy. The existence of a finite superfluid stiffness is at the heart of most of the peculiar superfluid behavior, such as supercurrents, quantized vortices and the Josephson effect. In superconductors, the superfluid stiffness is an energy scale competing with the energy gap of the Cooper pair Δ . The first is the energy scale of phase fluctuations that can destroy the coherence of the superconductor, the second one is the binding energy of the Cooper pair. While in standard superconductors, described by the BCS theory, Δ is the only relevant energy scale $\Delta \ll S$, in more exotic superconductors they can be comparable, and phase fluctuations are responsible for new phenomena [74]. A notable example is the group of cuprate superconductors, for which the superfluid stiffness is particularly low [73]. In our work [22], we show that the superfluid fraction f_s is a measurement of the reduced superfluid stiffness of the supersolid due to the competing crystal order. The basic idea of our approach is shown in Fig. 5.1 and is related to the discussion of the Leggett model in section 4.1. We consider a 1D superfluid system described by a number density $n(x)$ and we apply a phase twist $\Delta\varphi$ over some distance D . The phase variation has a kinetic energy cost

$$E_{kin} = \frac{\hbar^2}{2m} \int_0^D n(x) |\nabla\varphi(x)|^2 dx. \quad (5.2)$$

We then search for the phase profile $\varphi(x)$ which minimizes the kinetic energy. Since the supersolid can accommodate most of the phase variations in the minima of the density, the applied phase twist has less energy cost for the supersolid than for the superfluid, see Fig. 5.1. The superfluid fraction is defined as the ratio between the two kinetic energies, for the same phase twist

$$f_s = \frac{E_{kin}}{E_{kin}^{hom}}. \quad (5.3)$$

In the Leggett model in section 4.1, the energies are calculated in the rotating frame and the phase twist is a consequence of the rotating ring. For a homogeneous superfluid, $n(x) = \bar{n}$, the phase profile is linear and the energy cost is $E_{kin}^{hom} = N\hbar^2\Delta\varphi^2/(2mD^2)$. The superfluid stiffness, according to the definition in Eq. 5.1, is simply dependent on the atom number N and the spatial dimension D . For the supersolid, Leggett's variational result is $E_{kin} = \frac{N\hbar^2}{2mD^2} f_s^u \Delta\varphi^2$, where it is evident that the superfluid fraction quantifies the reduction of the superfluid stiffness in the supersolid and has the role of an elastic constant for the phase deformation. Leggett's upper bound f_s^u clarifies also that the reduction is directly connected to the extent of the density modulation

$$f_s^u = \left(\frac{1}{D} \int_0^D \frac{dx}{n(x)/\bar{n}} \right)^{-1}. \quad (5.4)$$

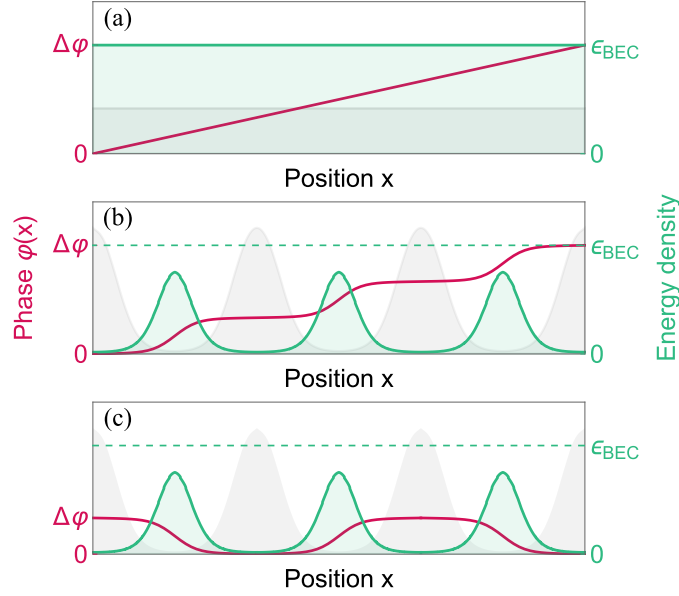


Figure 5.1: Sketch of the definition of the superfluid fraction at $T = 0$ in rotations and Josephson oscillations. (a) Applied phase twist $\Delta\varphi$ on a homogeneous superfluid. The red line is the phase profile minimizing the kinetic energy 5.2. The green line is the corresponding kinetic energy density, $\epsilon(x)$. The gray line is the density $n(x)$. (b) Same applied twist $\Delta\varphi$ to a supersolid. The kinetic energy cost is minimized accommodating most of the phase variation in the minima of the density, as discussed in Leggett model in section 4.1. The superfluid fraction is the ratio between the green areas in (b) and (a), according to Eq. 5.3. The dynamics described by the phase $\varphi(x)$ is a global flow of atoms, which, in the ring geometry, corresponds to a rotation. (c) Alternating phase twists $\Delta\varphi$ from one cell to the other. The phase profile is the same as in (b), but with a changing slope from cell to cell. The kinetic energy cost is the same, as well as the definition of f_s . However, the resulting dynamics is a Josephson oscillation of phase and population difference.

When the phase twist is applied globally on the whole system, the resulting dynamics is a global superfluid motion that, if the geometry is closed in a ring shape, coincides with the rotation discussed in the previous chapter. Here we change approach and we propose an alternative method to measure the superfluid fraction. Instead of applying a global phase twist, we apply local twists from cell to cell, with the same amplitude but with different alternating signs. The situation is sketched in Fig. 5.1(c). The kinetic energy cost supported by the supersolid is the same as the global phase twist of the panel (b), because the kinetic energy is insensitive on the sign of the slope of $\varphi(x)$. The definition of f_s is, therefore, unchanged. However, the dynamic produced by $\varphi(x)$ is very different. The alternating phase variations from one cell to the other produce a situation equivalent to an array of Josephson junctions, in which the atom current induced by the phase variation produces a population imbalance between the cells, which then oscillates back in a phase difference, and so on. The resulting dynamics, instead of being a global flow of mass, is a Josephson oscillation of the two variables characterizing each junction: the phase and

population differences, $\Delta\varphi$ and Z , of two adjacent clusters [131].

In this framework, we can calculate the kinetic energy relative to the twist $\Delta\varphi$ using the Josephson Hamiltonian. Restricting ourselves to a single Josephson junction, the energy is

$$H = N^2 U \frac{z^2}{2} - 2NK(1 - \cos \Delta\varphi), \quad (5.5)$$

where the first term is the interaction energy inside each cluster, quantified by the interaction parameter U , and the second term is the kinetic energy associated with the phase variation, quantified by the tunneling energy K . Their combination determines the behavior of the junction, and for small excitations, when the system is equivalent to a simple pendulum, they set the frequency of the oscillation $\hbar\omega_J = 2K\sqrt{1 + NU/(2K)}$. For small twists $\Delta\varphi$, the kinetic energy in the Hamiltonian 5.5 is $E_{kin} = NK\Delta\varphi^2$. Using the definition 5.3 and the energy for the homogeneous superfluid on a distance equal to the unit cell d , we get an expression for the superfluid fraction

$$f_s = \frac{K}{\hbar^2/(2md^2)}, \quad (5.6)$$

showing a direct relationship between f_s and the tunneling energy of the junction K . We note that Leggett discussed an expression similar to his upper bound f_s^u in the context of a single Josephson junction [120], to quantify the tunneling energy K , but with no connection with the superfluid fraction. The relationship 5.6 is thus an original result of our work.

We have shifted the problem of measuring the superfluid fraction to the problem of detecting Josephson oscillations between the clusters of the supersolid and measuring the coupling energy. This is not an easy task, since the supersolid has a self-induced structure, and no external barrier guarantees that it can sustain stable Josephson oscillations. In the next sections, we describe the experimental implementation of this program.

5.2 Excitation of Josephson oscillations: phase imprinting

For the Josephson experiment, the supersolid is produced in the usual cigar-shaped optical trap, with frequencies $(\omega_x, \omega_y, \omega_z) = 2\pi[18(1), 97(1), 102(2)]$ Hz, similar to the potential V_C in chapter 3. The superfluid-supersolid phase transition is continuous, and we cross it adiabatically enough to minimize the spontaneous excitation of collective modes [15]. The quasi-adiabatic preparation of the supersolid helps in preventing the coupling of the mode we are interested in with other modes, as it happened in the scissors experiment in chapter 4. To excite Josephson oscillations in our supersolid, we employ a long-wavelength optical lattice realized with off-resonant light at $\lambda = 1064$ nm. The characterization of the optical lattice and of the excitation method is summarized in Fig. 5.2. With an atom number $N = (2.8 \pm 0.3) \times 10^4$, the ground state in the supersolid phase is formed by two main clusters symmetric with respect to the trap center and two couples of smaller lateral

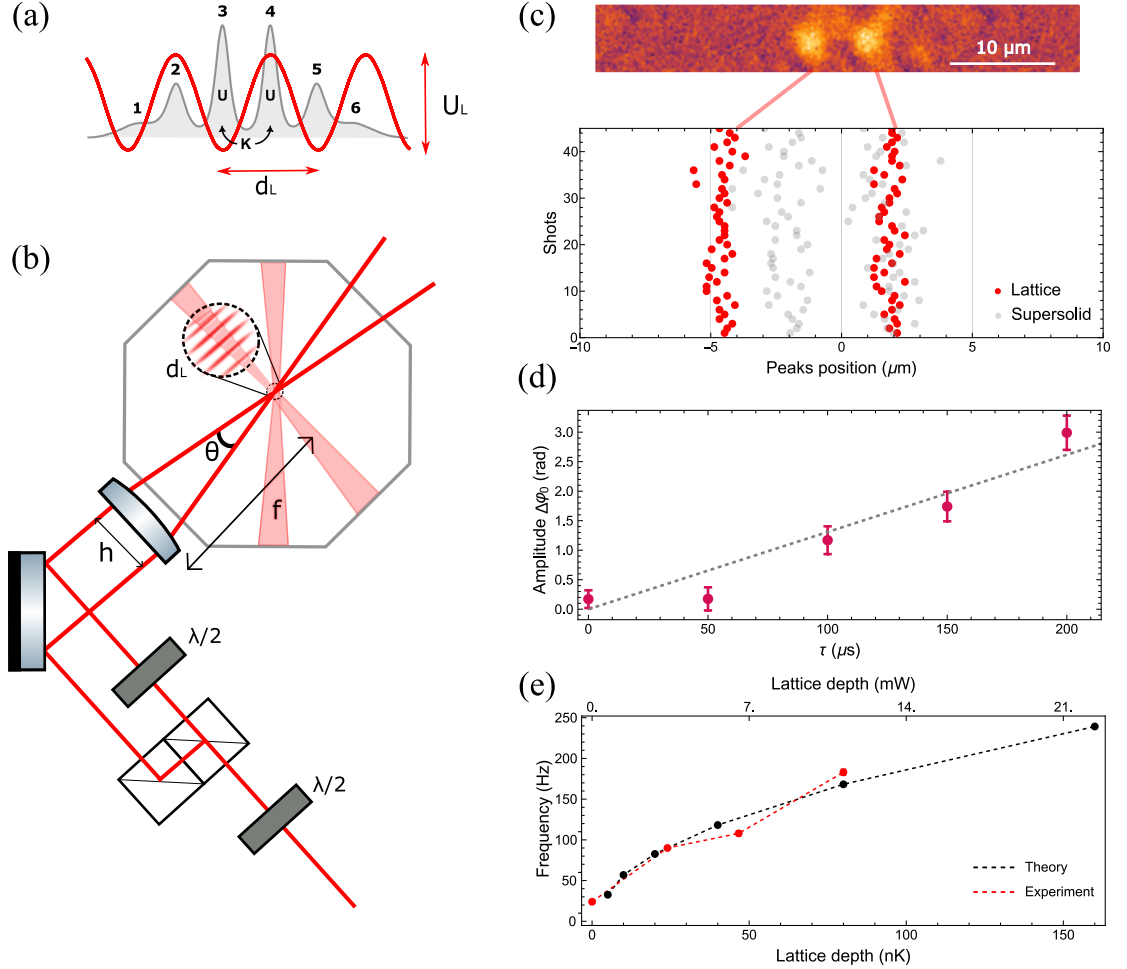


Figure 5.2: Excitation of the Josephson oscillations. (a) Sketch of the method. We imprint on the supersolid wavefunction a phase with the spatial profile of an optical lattice with a period d_L about two times that of the supersolid. The dynamic starts with an alternating phase twist between adjacent clusters, as in Fig. 5.1(c). (b) Optical scheme of the lattice. Two beams are separated by two polarizing beamsplitters and then focused on the atoms by a lens. The two crossed beams forming the cigar-shaped harmonic trap are also indicated inside the octagonal science cell. The lattice develops approximately in the direction of the supersolid modulation. (c) Position of the lattice (red points) and of the supersolid (gray points) in situ in different experimental shots. Inset: the position of the lattice is determined by loading a BEC in a deep lattice. (d) Phase difference $\Delta\phi_0$ imprinted between the main clusters with a lattice depth $U_L = 100$ nK, for different pulse depths τ . The phase is measured in time of flight. The dotted line is the theoretical prediction $\Delta\phi_0 = U_L \tau / \hbar$. (e) Calibration of the lattice depth. Oscillation frequency in a single well of the lattice in the experiment (red dots) and from a non-interacting Schrödinger equation (black dots), as a function of the lattice depth in nK (bottom) and in power of the lattice beams (top).

clusters, see Fig. 5.2(a). To imprint on odd excitation, we build an optical lattice with a period two times that of the supersolid, so that adjacent clusters experience a maximum and a minimum of the potential, respectively. The optical lattice is formed by two beams separated by a couple of polarizing beamsplitters and then focused by a single lens on the atoms, as shown in Fig. 5.2(b). Since the two beamsplitters are mounted together, we find that this configuration minimizes fluctuations in the phase of the lattice. In a test setup, we estimate these fluctuations to have a standard deviation of $\sigma \sim 0.05$ rad, over about one hour of measurements [20]. The separation between the two beams at the lens position is $h = 25.4$ mm, and the focusing lens has $f = 200$ mm. Since the period of the lattice is $d_L = \lambda/(2 \sin \theta/2) = \lambda f/h$, we get approximately two times the period of the supersolid, $d_L \sim 8$ μm . The geometry of the beams is such that the stripes of the optical lattice form approximately in the long direction of the cigar-shaped trap, along which the clusters of the supersolid are aligned. We thus consider a 1D potential of the form $V_L(x) = U_L \sin^2(\pi x/d_L)$, shown in Fig. 5.2(a).

To measure the position of the lattice on the atoms, we switch on the lattice at high power ($U_L > 100$ nK) and we observe in situ the localization of the atoms in the single sites of the lattice, as shown in Fig. 5.2(c), employing the objective characterized in section 2.3. We populate mainly two or three lattice sites, depending on the relative alignment of the lattice and the atoms. The lattice period is¹ $d_L = (7.9 \pm 0.3)$ μm and the standard deviation of the fluctuations of the single site position is about 10 % of the period. The lattice is more stable than the supersolid, as shown in Fig. 5.2(c). The reason is the low-energy Goldstone mode, which is thermally excited even at the lowest temperatures of the experiment [46], as already explained in connection with the in situ imaging in section 2.3. The Goldstone mode, associated with the spontaneous breaking of the translational symmetry, consists in a slow oscillation of the supersolid peaks, associated with a superfluid current in the opposite direction. Since the Goldstone mode is thermally, rather than deterministically, excited, it has a different phase in each experimental shot. This is the reason for the fluctuations in the supersolid peak positions shown in Fig. 5.2(c). The presence of the harmonic trap, however, limits the possible range of fluctuations, and the two central peaks always form near the center of the trap (in a homogeneous system, all the different phases of the solid lattice would be equivalent, as discussed in the Landau model in section 3.1). The standard deviation of the fluctuations in the peak positions is about 25 % of the supersolid period. Moving the last mirror of the optical lattice, we can adjust its position with respect to the supersolid. Despite the Goldstone excitation, we can position one maximum of the lattice on a supersolid peak and maintain this configuration for the total duration of a measurement, as shown in Fig. 5.2(c).

To excite the Josephson oscillation, we phase imprint the spatial profile of the optical lattice on the atoms. Switching on the lattice potential for a short time τ , the wavefunction evolves as

¹Actually, the period of the lattice is measured in time of flight and then used to measure the magnification of the in situ imaging, as explained in chapter 2.

$$\psi(\tau) = \psi_0 e^{-iV_L(x)\tau/\hbar}. \quad (5.7)$$

If the time τ is much shorter than the typical dynamical timescales of the system, the density stays constant and the only effect is to imprint the phase $\varphi(x) = V_L(x)\tau/\hbar = U_L \sin^2(\pi x/d_L)\tau/\hbar$ on the wavefunction. The resulting phase profile consists of alternating phase twists between neighboring clusters, as in Fig. 5.1(c). We measure the imprinted phase difference between the main clusters $\Delta\varphi_0$ by measuring the phase in time of flight. Fig. 5.2(d) reports the imprinted phase $\Delta\varphi_0$ for $U_L = 100$ nK and different time pulses τ . To calibrate the depth of the lattice, we load a BEC in a deep lattice and we measure the oscillation frequency inside a single lattice site. The measurement is compared with the solution of a non-interacting Schrödinger equation that calculates the eigenvalues in the lattice potential. From the comparison, we derive the conversion between the power of the lattice beams and the lattice depth. An example of this calibration is shown in Fig. 5.2(e).

5.3 Detection of Josephson oscillations: phase and imbalance

The hallmark of the Josephson effect is the oscillation of both the phase difference $\Delta\varphi$ and the population difference Z with the same frequency and with a $\pi/2$ phase shift. The two conjugate observables behave, indeed, as the angle and velocity, respectively, of a simple pendulum [131]. In quantum gases systems, the Josephson effect has been observed both in BECs [132, 133, 134] and in Fermi gases [135] trapped in double-well potentials. The oscillations of $\Delta\varphi$ and Z are the equivalent, in condensed matter physics, of the Josephson alternating current when a constant voltage is applied (the so-called AC Josephson effect), which was the original proposal by Josephson [136]. Recently, a Josephson array model has been employed to describe the re-phasing dynamics of the supersolid after an interaction quench [137], however without any connection to the possibility of observing Josephson oscillations or to the superfluid fraction.

Our excitation protocol imprints an initial phase difference $\Delta\varphi_0$ between the central clusters, while the initial population difference is zero, $Z_0 = 0$. In the pendulum analogy, this excitation corresponds to tilting the angle of the pendulum and starting the dynamic with zero velocity. We measure the phase difference $\Delta\varphi$ with the time of flight imaging, while the population imbalance is measured with in situ imaging, employing the objective characterized in section 2.3, in a different experimental shot. Remarkably, we observe single-frequency oscillations of both the observables in the whole supersolid regime, in excellent agreement with the expected dynamic of a Josephson junction, as well as with numerical solutions of the eGPE simulating the same experimental protocol. An example of such oscillations is shown in Fig. 5.3 for the supersolid at $\epsilon_{dd} = 1.428$. The measured Josephson frequencies from both population and phase oscillations are shown in Fig. 5.4 as a function of ϵ_{dd} . They decrease going towards the droplet crystal phase, signaling a slowing down of the Josephson dynamic which is connected to the decreasing of the tunneling energy and hence of the superfluid fraction. Our measurements not only demonstrate

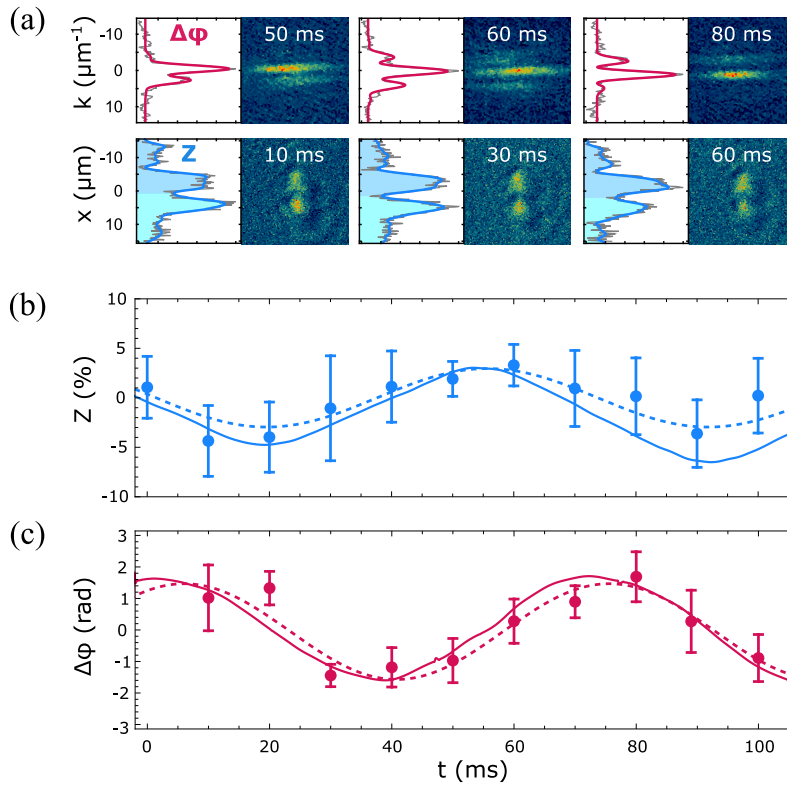


Figure 5.3: Josephson oscillations in the supersolid. (a) Experimental snapshots and corresponding integrated 1D profiles. Upper row: interference patterns after a free expansion. Red lines are double slit fits used to extract the phase difference $\Delta\phi$. Lower row: in-situ images. Shaded areas indicate the populations of the left and right halves of the supersolid used to extract the population imbalance Z , according to Eq. 5.8. (b) Oscillation of Z for the supersolid at $\epsilon_{dd} = 1.428$. The thick line is the numerical simulation for the same experimental parameters. The dashed line is the sinusoidal fit to the data used to extract the Josephson frequency ω_J . Error bars are the standard deviation of the mean for about 20-30 measurements. (c) Same for $\Delta\phi$.

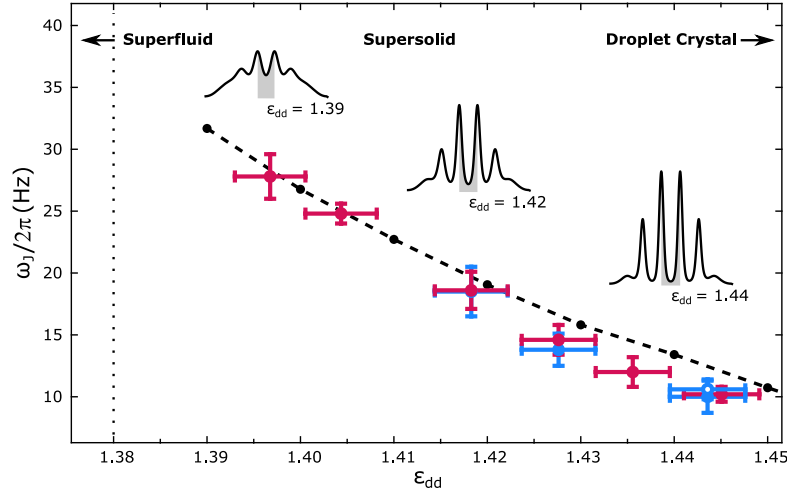


Figure 5.4: Josephson frequencies as a function of the interaction parameter ϵ_{dd} . Red points are the results of phase measurements, while blue points are the results of population imbalance measurements. Full and open blue dots refer to measurements of Z with and without the optical separation technique, respectively. Black points are the results of numerical simulations, while the dashed line is a guide for the eye. Vertical error bars correspond to the error of the sinusoidal fit, while horizontal error bars indicate the stability of the magnetic field, as explained in section 2.1. Insets show density profiles for different values of ϵ_{dd} . The vertical dashed line indicates the critical point of the superfluid-supersolid phase transition.

that the supersolid can sustain robust Josephson oscillations, despite the absence of an external barrier, but also that they are a normal mode of the system, since they have a single-frequency in all the interaction regimes we explored.

Before investigating further the analysis of the supersolid Josephson oscillations and their connection with the superfluid fraction, we discuss in more detail the measurement of the observables $\Delta\varphi$ and Z , which is far from trivial due to the peculiarities of the supersolid structure. Our supersolid, indeed, is different from a simple Josephson junction formed by two superfluid baths separated by a barrier. The ground state has more than two clusters, as shown in Fig. 5.2(a), although the two central ones have a density more than two times larger than the lateral ones. In the experiment, we cannot detect independently the population and phase of each cluster forming the supersolid. We have access only to the phase difference $\Delta\varphi$ that we measure in time of flight with a double-slit model (see section 2.2), and to the populations that we are able to resolve in situ.

Imbalance Z

Due to our limited optical resolution $\text{res} \sim 2 - 3 \mu\text{m}$ (see section 2.3), and the overlap between different clusters, we can resolve only the two central clusters, while the lateral ones are hidden below the tails of the central ones or under the image noise. We therefore define a global population imbalance as the difference between the right and left halves of

the density distribution

$$Z = \frac{N_1 + N_2 + N_3 - N_4 - N_5 - N_6}{N}, \quad (5.8)$$

where the indices of the clusters are defined in Fig. 5.2(a). To measure Z , we integrate the in situ density $\rho(x, y)$ along the transverse y direction and we detect the two main peaks in the 1D density $\rho(x)$. We then integrate the signal to the left and to the right of the minimum between the main peaks, obtaining $N_1 + N_2 + N_3$ and $N_4 + N_5 + N_6$, respectively. We finally compute Z . An example of this analysis on the experimental images is shown in Fig. 5.3(a). Even this global observable is difficult to evaluate in situ, depending on the value of ϵ_{dd} . Near to the BEC, indeed, the density modulation is very low and we don't resolve the different clusters (remember that we are probing a continuous phase transition, so the modulation smoothly develops starting from the BEC). Therefore, the first two points in Fig. 5.4 are only from phase measurements. For $\epsilon_{dd} > 1.415$, we distinguish the two main peaks, but the overlap is too large to correctly extract the imbalance Z . We therefore employ an optical separation technique to increase the distance between the clusters. We switch on the same optical lattice used for the excitation 5 ms before the image acquisition, with $U_L = 5$ nK. The presence of the additional potential pushes the clusters into the minima of the lattice, increasing their distance. After 5 ms they are distant enough to resolve the different populations. Although the optical lattice doesn't have the optimal spatial phase to separate the clusters, since it has a maximum on the position of one cluster and a minimum on the other, we checked with numerical simulations that the only effect on the imbalance Z is the addition of a constant offset, as shown in Fig. 5.5. The efficiency of the optical separation, despite the unfavorable relative position between the clusters and the lattice, can be explained by the fact that the atoms that suddenly feel the potential maximum prefer to tunnel in the empty lattice site, rather than mix with the other cluster, due to the dipolar repulsion between clusters (see the snapshots of numerical simulations in Fig. 5.5). For the datapoint at $\epsilon_{dd} = 1.444$, instead, where the density modulation is deeper, we resolve the main clusters without the need for optical separation. In Fig. 5.4, we compare the measured frequency with and without applying the optical separation. The two frequencies are consistent under the experimental error, corresponding to one standard deviation.

Phase difference $\Delta\varphi$

The phase difference $\Delta\varphi$ measured in time of flight is the result of the expansion of at least four clusters, each with its own well-defined phase. The typical Josephson situation in situ is sketched in Fig. 5.6, with an alternating phase φ from one cluster to the other. A combination of different factors leads to the conclusion that $\Delta\varphi$ extracted from a double-slit fit of the interference pattern coincides with the phase difference between the two central clusters, within a good enough approximation (the maximum error is about 0.6 rad, comparable with the typical standard deviation of a phase measurement, see Fig. 5.3). Here we describe a model of the expansion of four clusters, approximated by four gaussians of width σ , separated by a distance d and with central populations two times the lateral

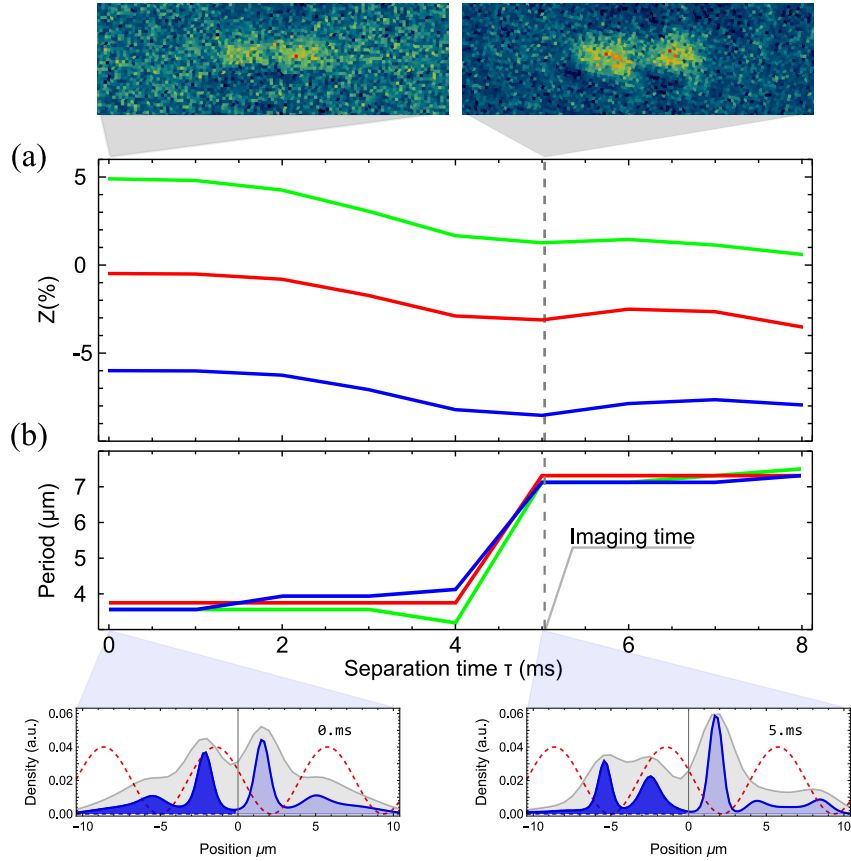


Figure 5.5: Optical separation method. Due to the limited optical resolution, when the density modulation is weaker we need to artificially increase the distance between the clusters to measure Z . (a) Numerical simulations of the dynamic after switching on the lattice potential with $U_L = 5$ nK, for different initial imbalances $Z = 5\%$ (green), $Z = 0\%$ (red) and $Z = -5\%$ (blue). The time $\tau = 0$ ms corresponds to the switch-on of the lattice. The experimental image is taken at $\tau = 5$ ms. Despite the non-optimal spatial phase of the lattice, the only effect on Z is the addition of a constant offset, which doesn't alter the Josephson frequency. Insets: experimental snapshots of the supersolid before (left) and after (right) the application of the optical separation. (b) Period between the clusters as a function of time τ . Insets: numerical snapshots of the density $\rho(x)$ at $\tau = 0$ ms (left) and $\tau = 5$ ms (right) for the negative imbalance case (blue). The gray region indicates the convolution with a point spread function with $\text{res} = 3 \mu\text{m}$. The red dashed line is the profile of the optical lattice.

ones, $N_2 = N_3 = 2N_1 = 2N_4$, see Fig. 5.6. We consider an interaction-free expansion so that the momentum distribution $\rho(k_x)$ after a long time of flight is the Fourier transform of the in situ wavefunction $\rho(k_x) = |\text{FT}[\psi(x)]|^2$. In the case of only two clusters at distance d , the phase difference $\Delta\varphi$ appears directly in the interference term $\cos(ak_x + \Delta\varphi)$, and the period of the modulation is $2\pi/d$. With larger systems, we have more couples of clusters that interfere, and the phase of the interference pattern gets contributions from all of them. In the case of four clusters, we expect interference terms related to neighboring clusters, with period $2\pi/d$, to second-neighboring clusters, with smaller period $2\pi/(2d)$, and to third-neighboring clusters, with period $2\pi/(3d)$ [11]. Due to the finite resolution of our time of flight imaging ($0.2 \mu\text{m}^{-1}$, $1/e$ gaussian width [10]), we resolve only the contribution of neighboring clusters, as depicted in Fig. 5.6(b). This contribution comes from three different couples of clusters. In the typical Josephson configuration shown in Fig. 5.6(a), two of them have a phase difference $-\varphi$, and the central one has a phase difference φ . Taking into account the different populations, the three interference terms have the form $\sqrt{N_1 N_2} \cos(ak_x - \varphi) + \sqrt{N_2 N_3} \cos(ak_x + \varphi) + \sqrt{N_3 N_4} \cos(ak_x - \varphi)$. They can be expressed as a single cosine $A \cos(ak_x + \Delta\varphi_{TOF})$, where the phase $\Delta\varphi_{TOF}$ is the one measured with the double-slit fit. It is related to the physical phase difference between the central clusters $\Delta\varphi = \varphi$ by

$$\tan \Delta\varphi_{TOF} = \frac{\sqrt{N_2} - 2\sqrt{N_1}}{\sqrt{N_2} + 2\sqrt{N_1}} \tan \Delta\varphi. \quad (5.9)$$

In the case of equal populations $N_1 = N_2$, we get $\tan \Delta\varphi_{TOF} = -(\tan \Delta\varphi)/3$, which is the average of the tangents of the three angles. Note that, since two couples contribute with a negative phase, the final phase is negative. If $N_1 = 0$, instead, we get $\Delta\varphi_{TOF} = \Delta\varphi$. In Fig. 5.6(c) we compare the in situ phase $\Delta\varphi$ with the phase $\Delta\varphi_{TOF}$ extracted from a double slit fit of the calculated momentum distribution $\rho(k_x)$, convolved with the point spread function of the imaging system. The result is well described by the formula 5.9. The first observation is that we estimate $-\Delta\varphi$ instead of $\Delta\varphi$. We take into account this minus sign when plotting $\Delta\varphi(t)$ together with $Z(t)$ as in Fig. 5.3. Second, the error is very small near 0 and $\pm\pi/2$, which are approximately the extrema of our Josephson oscillations. This means that we can safely measure the Josephson frequency and also the amplitude of the phase oscillations. Moreover, as anticipated at the beginning of the paragraph, the maximum error, around $\Delta\varphi = \pm\pi/4$, is about 0.6 rad, which is similar to the standard deviation of a phase measurement. We conclude that the observable $\Delta\varphi_{TOF}$ is a good measurement of the phase difference $\Delta\varphi$ between the central clusters. This conclusion is also confirmed by the measured phase twist in Fig. 5.2(d), which is in agreement with the expected applied twist between the central clusters, $\Delta\varphi_0 = U_L\tau/\hbar$.

High amplitudes

In the experiment, we detect clear Josephson oscillations only if the initial imprinted phase is $\Delta\varphi_0 > 1$ rad. The need for such large amplitudes is probably due to the presence of the Goldstone mode, which introduces an unavoidable noise, with smaller amplitude,

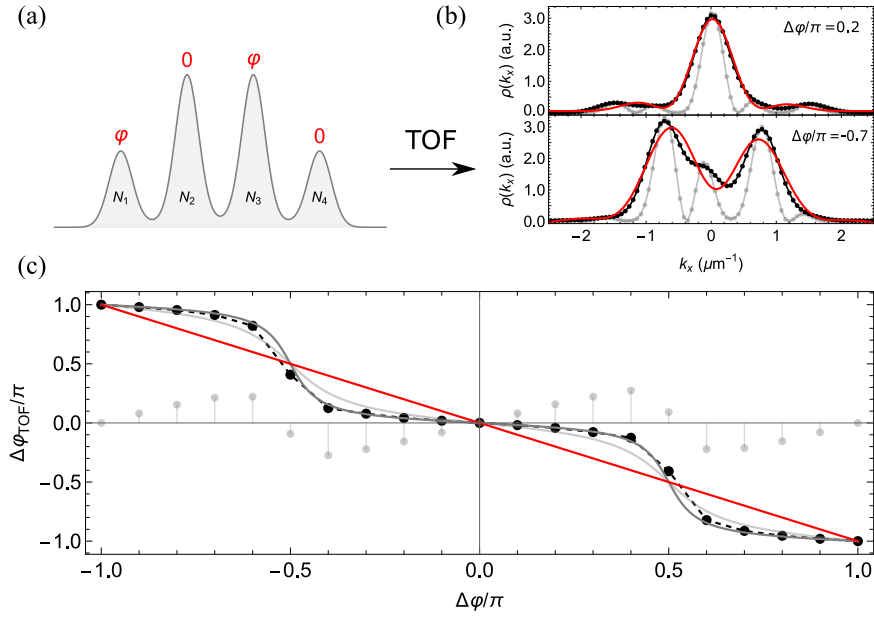


Figure 5.6: Relationship between the physical phase difference $\Delta\varphi$ of the central clusters and the phase difference $\Delta\varphi_{TOF}$ extracted in time of flight. (a) Model of the in situ wavefunction. Four Gaussians with different populations ($N_2 = 2N_1$) have an alternating phase, as in a typical Josephson oscillation. (b) We simulate the time of flight (TOF) expansion calculating the momentum distribution $\rho(k_x) = |\text{FT}[\psi(x)]|^2$ (gray dots). The limited optical resolution of the imaging system (black dots) washes out the small-period contributions of next-nearest neighbor clusters. The resulting momentum distribution is fitted with a double slit function (red line) to extract $\Delta\varphi_{TOF}$. Upper panel: $\Delta\varphi = 0.2\pi$. Lower panel: $\Delta\varphi = -0.7\pi$. (c) $\Delta\varphi_{TOF}$ versus $\Delta\varphi$. Black dots are the result of the fit of $\rho(k_x)$. Gray lines are the prediction of Eq. 5.9 for $N_2 = 2N_1$ (dark gray) and $N_2 = N_1$ (light gray). The red line $\Delta\varphi_{TOF} = -\Delta\varphi$ is for comparison. Light gray points are the residual between $\Delta\varphi_{TOF}$ and $-\Delta\varphi$.

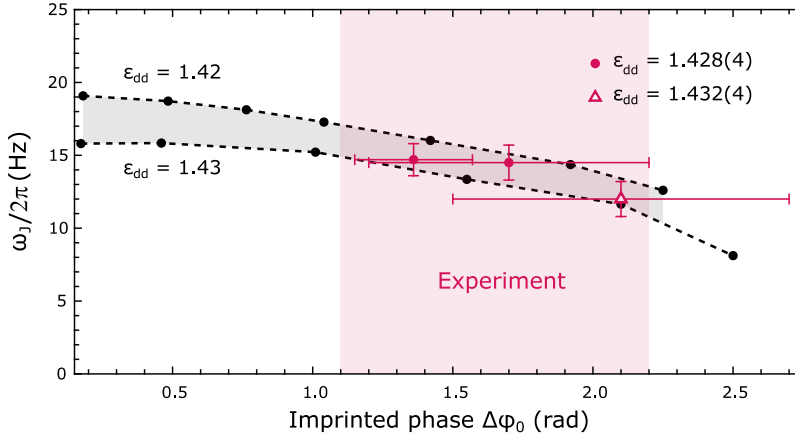


Figure 5.7: Josephson frequencies versus the amplitude of the phase oscillation. Black dots are the result of numerical simulations for $\epsilon_{dd} = 1.42$ and $\epsilon_{dd} = 1.43$. Red points are experimental results for $\epsilon_{dd} = 1.428$ (circles) and $\epsilon_{dd} = 1.432$ (open triangle). The Josephson oscillations studied experimentally lie in the pink region, between 1.1 rad and 2.2 rad.

in the observables $\Delta\varphi$ and Z . We typically employ a lattice depth $U_L = 100$ nK and a pulse time $\tau = 100$ μ s, giving a phase amplitude of about $\pi/2$. In Fig. 5.7, we study the dependence of the Josephson frequencies of phase oscillations on the amplitude $\Delta\varphi_0$. In the numerical simulations, we observe single-frequency oscillations in all the regimes we explored, with a decreasing frequency for larger amplitudes. In the experiment, we varied the range of phase amplitudes from 1.1 rad to about 2.2 rad. We observe, in agreement with the simulations, a 15 % decrease in the Josephson frequencies, which can explain the slight disagreement between simulations performed in the small-amplitude limit and the experiment in Fig. 5.4 at larger ϵ_{dd} .

5.4 The supersolid as an array of Josephson junctions: a model

The experimental measurements presented so far demonstrate that the supersolid can oscillate as a Josephson junction even without an external barrier. To derive information on the superfluid fraction, however, we need a model of our system to extract the tunneling energy K from the observed Josephson oscillations. Our model neglects the movement of the barrier and considers an array of fixed Josephson junctions, with different populations due to the inhomogeneity. In the case of a single Josephson junction, the equations of motion can be derived from the Hamiltonian 5.5. The imbalance $Z = N_2 - N_1$ and the phase difference $\varphi_{21} = \varphi_2 - \varphi_1$ satisfy

$$\begin{aligned}\dot{Z} &= -2K \sin \varphi_{21} \\ \dot{\varphi}_{21} &= UNZ,\end{aligned}\tag{5.10}$$

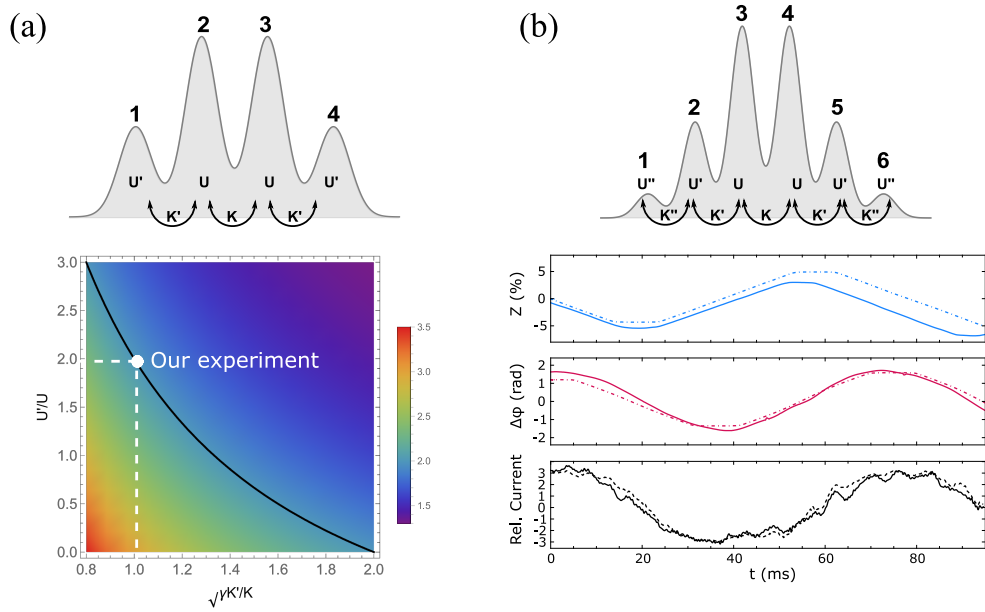


Figure 5.8: Models of the supersolid as an array of Josephson junctions. (a) Four-modes model. Sketch of the four clusters with the parameters characterizing the junction (upper panel) and function $f(U'/U, \sqrt{\gamma}K'/K)$ entering the eigenvector 5.19 of the four-modes dynamic (lower panel). The black line indicates the validity of the relation 5.14 between the Josephson currents, necessary to have a Josephson normal mode. The white point indicates the parameters of our experiment. (b) Six modes model, developed in [22]. Comparison between the oscillations of Z (blue) and $\Delta\varphi$ (red) in the numerical solutions of the eGPE (thick lines) and in the model (dashed lines). Lowest panel: relative currents between the central and lateral clusters appearing in the six-mode analog of Eq. 5.14, from eGPE simulations. The solid line is $(\dot{N}_3 - \dot{N}_2)/2$ and the dashed line is $\dot{N}_6 + \dot{N}_5 - \dot{N}_2 - \dot{N}_1$.

where we assume the interaction energy is much larger than the tunneling, namely $NU/2K \gg 1$. This condition is known as the Josephson regime [138, 133] and is well realized in the supersolid, as discussed below. We also assume small imbalances $Z \ll 1$. The coupled equations 5.10 predict sinusoidal oscillations in the small-angle limit, $\varphi_{21} \ll 1$, with frequency $\hbar\omega_J = \sqrt{2NUK}$. The same equations can also be written in terms of the single populations

$$\begin{aligned}\dot{N}_1 &= -\dot{N}_2 = -2K\sqrt{N_1N_2}\sin\varphi_{21} \\ \dot{\varphi}_{21} &= U(N_2 - N_1),\end{aligned}\tag{5.11}$$

where the condition $Z \ll 1$ gives $\sqrt{N_1N_2} \sim N/2$.

We start from Eq. 5.11 to extend the model to an array of Josephson junctions. We discuss the case of 4 clusters, but the model can be generalized to more clusters. We introduce two symmetric lateral tunneling energies K' and interaction energies U' , and the trapping energy E_0 experienced by the lateral clusters, see Fig. 5.8. The initial populations are symmetric $N_1^0 = N_4^0$ and $N_2^0 = N_3^0 = N^0$, and the lateral ones are smaller, $N_1^0 = \gamma N^0$, $\gamma < 1$. The central clusters exchange two currents this time, one for each neighboring cluster. In the same approximation of small Z , which in this case means $\sqrt{N_1N_2} \sim \sqrt{\gamma}N^0$ and $\sqrt{N_2N_3} \sim N^0$, the equations for the populations are

$$\begin{aligned}\dot{N}_1 &= -2K'\sqrt{\gamma}N^0\sin\varphi_{21} \\ \dot{N}_2 &= 2K'\sqrt{\gamma}N^0\sin\varphi_{21} - 2KN^0\sin\varphi_{32} \\ \dot{N}_3 &= 2KN^0\sin\varphi_{32} - 2K'\sqrt{\gamma}N^0\sin\varphi_{34} \\ \dot{N}_4 &= 2K'\sqrt{\gamma}N^0\sin\varphi_{34},\end{aligned}\tag{5.12}$$

and are coupled to the three equations for the phase differences

$$\begin{aligned}\dot{\varphi}_{12} &= E_0 + U'N_1 - UN_2 \\ \dot{\varphi}_{32} &= U(N_2 - N_3) \\ \dot{\varphi}_{43} &= -E_0 + UN_3 - U'N_4.\end{aligned}\tag{5.13}$$

Even in the small-angle regime, the sets of equations for the 4 clusters predict a multi-frequencies dynamic for both the populations and the phases. Harmonic single-frequency oscillations with a $\pi/2$ shift between populations and relative phases are recovered with an additional constraint on the Josephson currents

$$\dot{N}_3 - \dot{N}_2 = 2(\dot{N}_1 - \dot{N}_4).\tag{5.14}$$

Remarkably, this relation between the different currents is very well satisfied in our experimental conditions, as verified in the solutions of the eGPE, shown in Fig. 5.8. The relationship 5.14 allows us to decouple the dynamical variables of the central clusters from

the others. Putting together the populations 5.12, the phases 5.13 and the condition 5.14, we finally obtain Josephson-like equations for the current between the central clusters

$$\begin{aligned}\dot{N}_2 - \dot{N}_3 &= -4K(N_3^0 + N_2^0) \sin \varphi_{23} \\ \dot{\varphi}_{23} &= U(N_2 - N_3).\end{aligned}\quad (5.15)$$

The only difference with the equations 5.10 for the single junction is a factor 2. The condition 5.14 allows us also to write the Josephson equations in terms of the experimental observables. In the four-modes model, the experimental global imbalance 5.8 takes the form $Z = (N_1 + N_2 - N_3 - N_4)/N$, and it satisfies $N_2 - N_3 = 2NZ$. The equations for the observables Z and $\Delta\varphi = \varphi_{23}$ are then

$$\begin{aligned}\dot{Z} &= -2K \frac{N_{23}}{N} \sin \varphi_{23} \\ \dot{\varphi}_{23} &= 2UNZ,\end{aligned}\quad (5.16)$$

where $N_{23} = N_3^0 + N_2^0$. In the small angle limit, the Josephson frequency is

$$\omega_J = \sqrt{4N_{23}UK}. \quad (5.17)$$

We will use both 5.16 and 5.17 in the next section to extract the superfluid fraction from the Josephson measurements.

We could wonder where the relationship 5.14 comes from, apart from the numerical evidence. It can be recast, indeed, in terms of relationships between the parameters of the supersolid junction. Combining Eq. 5.12 and 5.13, we can write the whole dynamic of the array as

$$\begin{pmatrix} \ddot{N}_1 \\ \ddot{N}_2 \\ \ddot{N}_3 \\ \ddot{N}_4 \end{pmatrix} = 2KN^0U \begin{pmatrix} -\frac{U'}{U} \frac{K'}{K} \sqrt{\gamma} & \frac{K'}{K} \sqrt{\gamma} & 0 & 0 \\ \frac{U'}{U} \frac{K'}{K} \sqrt{\gamma} & -\left(\frac{K'}{K} \sqrt{\gamma} + 1\right) & 1 & 0 \\ 0 & 1 & -\left(\frac{K'}{K} \sqrt{\gamma} + 1\right) & \frac{U'}{U} \frac{K'}{K} \sqrt{\gamma} \\ 0 & 0 & \frac{K'}{K} \sqrt{\gamma} & -\frac{U'}{U} \frac{K'}{K} \sqrt{\gamma} \end{pmatrix} \begin{pmatrix} N_1 \\ N_2 \\ N_3 \\ N_4 \end{pmatrix} + const. \quad (5.18)$$

The normal modes of the system are given by the diagonalization of this matrix. Among the four eigenvectors, two have the correct form to describe an alternate dynamic from cell to cell, realizing the Josephson mode, namely $\mathbf{v} \sim (-a, b, -b, a)$. They look

$$\mathbf{v} \propto \begin{pmatrix} -1 \\ f(U'/U, \sqrt{\gamma}K'/K) \\ -f(U'/U, \sqrt{\gamma}K'/K) \\ 1 \end{pmatrix}, \quad (5.19)$$

where $f(x)$ is a function of the junction's parameters, plotted in Fig. 5.8(a). The

existence of the Josephson normal mode, related to the condition $N_3 - N_2 = 2(N_1 - N_4)$, requires that the eigenvector should be in the form $\mathbf{v} \propto (-1, 2, -2, 1)$, namely the parameters should satisfy the condition $f(U'/U, K'/K\sqrt{\gamma}) = 2$. Fitting the numerical solutions of the eGPE to the Josephson model 5.12 and 5.13, we find for our system $U'/U \sim 2$ and $\sqrt{\gamma}K'/K \sim 1$, which satisfy indeed $f(U'/U, K'/K\sqrt{\gamma}) = 2$, as depicted in Fig. 5.8(a). Interestingly, we can estimate the ratio K'/K also from the Leggett formula. From our expression of the superfluid fraction 5.6, we have $K'/K = f'_s/f_s$, where f'_s is the superfluid fraction calculated between clusters 1 and 2. Calculating Leggett's upper bound 5.4 between these two clusters in the ground-state numerical simulations, we find the same result $\sqrt{\gamma}K'/K \sim 1$, with very small fluctuations of a few % with ϵ_{dd} .

Our theoretical collaborators in the group of A. Smerzi performed a more refined analysis, modelizing the system as an array of 6 clusters. The two models are qualitatively similar, and the results for the experimental observables 5.16 and 5.17 are the same provided that we replace the indices as $N_{23} \rightarrow N_{34}$ and $\varphi_{23} \rightarrow \varphi_{34}$. In Fig. 5.8(b) we plot the comparison between the six-mode model and the simulated dynamic. The analog of the current relationship 5.14, namely $\dot{N}_3 - \dot{N}_4 = 2(\dot{N}_6 - \dot{N}_1 + \dot{N}_5 - \dot{N}_2)$, is well satisfied. The model confirms also that the supersolid is in the Josephson regime, since $N_{34}U/2K > 35$ for all the values of ϵ_{dd} .

5.5 Sub-unity superfluid fraction

Combining the experimental Josephson oscillations and the model discussed in the previous section, we are in the position to extract the superfluid fraction. The simplest analysis consists of finding the tunneling energy K from the measured Josephson frequency ω_J , employing Eq. 5.17, namely $K = \omega_J^2/(4N_{34}U)$. We then extract the superfluid fraction from Eq. 5.6, $f_s = 2md^2K/\hbar^2$, where the supersolid period $d = (3.7 \pm 0.1) \mu\text{m}$ is measured in situ. This method allows us to measure the superfluid fraction in all the supersolid regime, also near to the BEC where we have only phase measurements. However, we need to calculate the interaction energy $N_{34}U$ from numerical simulations. The results are plotted in Fig. 5.9 as black dots. To take into account the effect of the relatively large amplitudes in the experiment, we add a 15 % upper error bar due to the underestimation of the Josephson frequencies, as explained in Fig. 5.7.

In the region of larger ϵ_{dd} , where we have combined Z and $\Delta\varphi$ measurements, we employ also a different method that exploits the full Josephson oscillations. We fit the linear dependence of \dot{Z} and $\sin \Delta\varphi$ to extract K , according to the current-phase equation 5.16, $\dot{Z} = -2K(N_{34}/N)\sin \Delta\varphi$. Plots of \dot{Z} versus $\sin \Delta\varphi$ are shown in Fig. 5.9(b) for both the experiment and the numerical simulations, together with the corresponding linear fit. The resulting superfluid fraction is indicated as pink circles in Fig. 5.9(a) and is in agreement with the results from the Josephson frequencies. The pink circles demonstrate the sub-unity superfluid fraction without any theoretical input of the interaction energy U . However, we still compute the fraction of atoms in the central cluster N_{34}/N from numerical simulations to isolate the tunneling K in the slope of the current-phase relation.

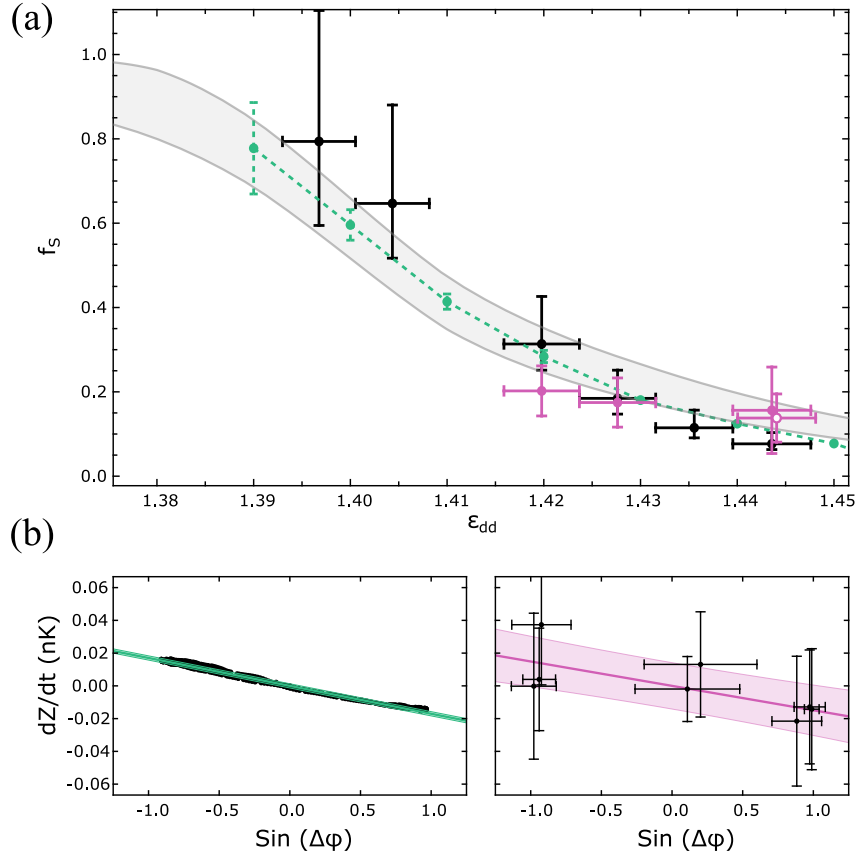


Figure 5.9: Superfluid fraction from Josephson oscillations. (a) Superfluid fraction as a function of ϵ_{dd} . Black dots indicate f_s derived from the Josephson frequencies, while pink dots indicate f_s derived from the current-phase relation 5.16. Closed and open pink dots refer to measurements of Z with and without the optical separation technique, respectively. Green dots are the results of numerical simulations, employing the current-phase relation 5.16. The gray region indicates Leggett's upper and lower bounds, $f_s^l \leq f_s \leq f_s^u$, calculated on ground-state simulations. (b) Current-phase relation 5.16 employed to extract the tunneling energy K in numerical simulations (left) and in the experiment (right) for the supersolid at $\epsilon_{dd} = 1.444$. Green and pink lines are linear fits to the data and the shaded areas are the confidence bands for one standard deviation.

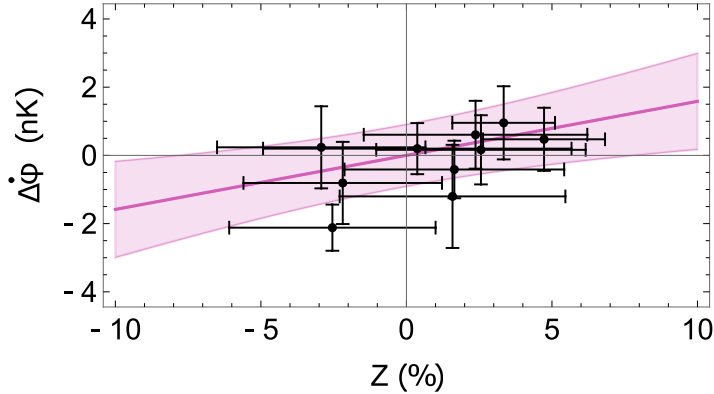


Figure 5.10: Experiment-simulations check of the interaction parameter. Example of linear correlation between $d\Delta\varphi/dt$ and Z for the Josephson oscillation at $\epsilon_{dd} = 1.428$. From the fitted slope $2NU$ we extract the interaction parameter $NU = (8 \pm 5)$ nK, consistent with the value of 12 nK from numerical simulations.

As an additional check, we extract the interaction energy $N_{34}U$ from the experimental data employing the second Josephson equation, $\Delta\varphi = 2NUZ$, finding values consistent with the theory. An example of this analysis is shown in Fig. 5.10 for $\epsilon_{dd} = 1.428$.

Overall, the experimental data of the superfluid fraction are in good agreement with the eGPE simulations, in which the same linear fit to the current-phase relation is employed to compute K , as for the experimental pink data. The tunneling energy K decreases from 0.1 nK to about 0.01 nK, while the interaction energy weakly depends on ϵ_{dd} . Correspondingly, the superfluid fraction shows a progressive decrease as the modulation depth increases and can be tuned from 1 to about 0.1 with the inter-atomic interactions.

Since we extract the superfluid fraction from the tunneling energy K between the central clusters, thanks to the modelization explained in section 5.4, our measurement is local and probes the superfluid fraction in the central region of the system. For this reason, it is not affected by inhomogeneity effects and coincides with the superfluid fraction of a hypothetical homogeneous supersolid, composed of cells identical to our central one, like the one in the ring geometry of Leggett model.

We also compute Leggett upper and lower bounds f_s^u and f_s^l (Eqs. 4.4 and 4.10) from ground-state simulations. The region between the two bounds is indicated in gray in Fig. 5.9(a). The bounds reduce to an equality when the density is separable in the transverse coordinates y and z . Since our system develops a 1D modulation because the transition is continuous [15], the two bounds are close each other. Remarkably, our results well agree with Leggett's prediction. The experimental error bars are too large to claim that the measurements satisfy Leggett's bound, but the numerical calculations lie between the two bounds in the whole regime we investigated. This agreement is significant because Leggett's model is not directly related to the Josephson oscillations: it is an important and independent check of the Josephson probe to measure the superfluid fraction.

As explained in the introduction of the chapter, the superfluid fraction quantifies the

reduction of superfluid stiffness due to the density modulation. This connection is well exemplified in Fig. 5.9(a) by the agreement between Josephson data and Leggett's bounds. The physical origin of the density modulation, however, has no role in the definition of the superfluid fraction. Recently, indeed, a sub-unity superfluid fraction has been measured also in BECs in which the translational symmetry is externally broken by a 1D optical lattice [119]. In this case, it is natural to associate the superfluid fraction with the effective mass m^* of the atoms in the lattice, which quantifies the curvature of the energy band for small quasi-momenta. The superfluid fraction can be expressed as $f_s = m/m^*$. Since the effective mass fixes the speed of sound in the condensate, $c^2 = (\kappa m^*)^{-1}$, through the compressibility κ , a measurement of the speed of sound gives access to the superfluid fraction. In the experimental configurations of [119], the lattice is 1D, so the superfluid fraction in the direction x of the modulation is measured by the ratio of the sound speeds parallel and perpendicular to the density modulation, $f_{sx} = c_x^2/c_y^2$. Such a measurement is consistent with a direct measurement of the density modulation and the associated Leggett's upper bound [119]. The application of this method to the dipolar supersolid is not feasible because the excitation spectrum is more complex than that of a BEC, and a simple connection between f_s and the speed of sound doesn't exist.

Our results are, instead, the first observation of a sub-unity superfluid fraction in a system with spontaneously broken translational symmetry. The absence of an external potential, which constrains the dynamic of the system, is crucial, and totally new phenomena peculiar to the supersolid phase and associated with the sub-unity superfluid fraction are expected. Some examples are the persistent currents with counter-propagating components as discussed concerning the Leggett model in section 4.1: one semi-classical associated with the density peaks and one fully superfluid associated with the background [21]. The angular momentum transported by these persistent currents in a ring geometry should be partially quantized, meaning that each atom should have less than \hbar angular momentum [139]. Similar predictions in circular harmonic traps, instead of ring potentials, point out the existence of partially quantized vortex states in the supersolid, linked to the sub-unity superfluid fraction [140, 141]. We can understand the anomalous behavior of persistent currents in the supersolid by adding together the results presented in the current and previous chapters, namely that the moment of inertia of the supersolid is less than the classical value but finite, even in a circular trap, and that the superfluid fraction is less than one. The thought experiment consists of asking what is the angular momentum L of the system as a function of the rotating frequency of the container Ω . A standard superfluid shows a step-like function, see Fig. 5.11, corresponding to the excitation of a vortex state ($L = N\hbar$) at the critical angular velocity Ω_c [3]. On the other hand, a supersolid has a finite moment of inertia $I = (1 - f_s)I_c$ so that its angular momentum increases also before the excitation of a vortex, as $L = (1 - f_s)I_c\Omega$. When the vortex is excited, therefore, the jump in angular momentum must be less than $N\hbar$. In the limit of a classical system, there is no jump and the angular momentum linearly increases as $L = I_c\Omega$. Looking at the plot in Fig. 5.11, it is easy to conclude that the jump at Ω_c is $\delta = f_s N\hbar$. The superfluid fraction, therefore, is responsible for the partial quantized nature of a vortex in the supersolid phase. This intuitive picture is confirmed by theoretical

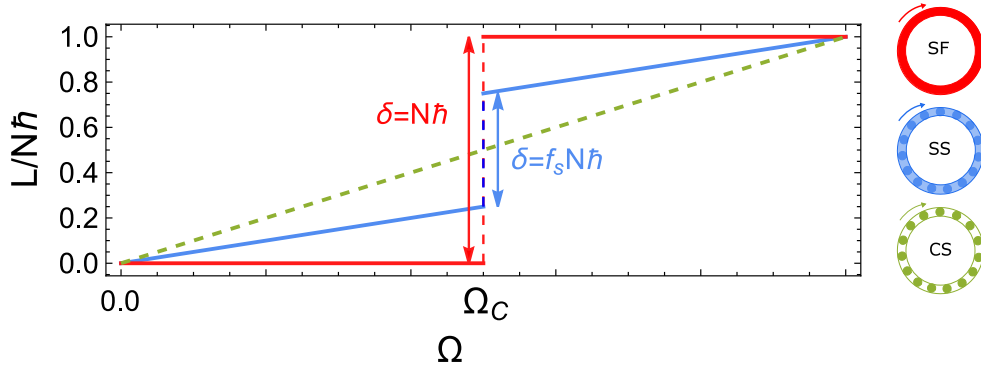


Figure 5.11: Sketch of the role of the sub-unity superfluid fraction in a quantized vortex. Angular momentum L versus angular velocity Ω of a rotating circular trap. For a standard superfluid (red) a vortex is energetically favorable above a critical velocity Ω_c , and the angular momentum has a jump $\delta = N\hbar$. In a supersolid (blue), angular momentum enters the system also before Ω_c , because the moment of inertia is different from zero, $L = (1 - f_s)I_c\Omega$. The jump at the critical velocity is lower and proportional to the superfluid fraction, $\delta = f_s N\hbar$. For a classical system (green) there is no jump and the angular momentum grows linearly, $L = I_c\Omega$.

calculations [140, 139].

Our measurements of a large and tunable superfluid fraction, with values ranging from 1 to 0.1, open the possibility of observing such exotic superfluid phenomena at a macroscopic level. In order to make progress in this direction, however, we should change the geometry of the system from the cigar-shaped harmonic traps discussed so far to a circular geometry, favorable for experiments related to rotations. This is the topic of the last chapter of the thesis.

5.6 A self-induced Josephson junction: the Goldstone mode

The observation of Josephson oscillations in Fig. 5.3 demonstrates that the supersolid can behave as a self-induced Josephson junction, without any external barrier separating the two superfluid clusters. Since the effective barrier is completely induced by the inter-atomic interactions, its position is not fixed a priori but is an additional degree of freedom of the system. In other terms, since the junction structure arises from the spontaneous breaking of the translation symmetry, there is an additional degree of freedom consisting in the Goldstone mode, an oscillation of the barrier position coupled with an oscillation of the population imbalance due to the harmonic trap [46]. As explained in section 5.2, the experimental signature of the low-energy Goldstone mode is the shot-to-shot fluctuation of the supersolid peaks position. A deterministic observation of the mode would be challenging due to its low energy (much lower than the trapping frequency $\hbar\omega_x$). When we excite the higher-energy Josephson mode with the phase imprinting protocol, we do

not observe a coupling with the Goldstone mode. In the simulations, the movement of the barrier is negligible and the dynamic is dominated by the standard Josephson oscillations. The same is true in the experiment since we measure single-frequency oscillations of Z and $\Delta\varphi$ that agree with the theory. The effect of the Goldstone mode in the experiment is to introduce a noise in the oscillations, because the relative position between the optical lattice and the supersolid changes from shot to shot, see Fig. 5.2(c), leading to fluctuations in the imprinted phase that contribute to the error bars in Fig. 5.3.

To estimate the energy of the Goldstone mode, we perform simulations in which we excite the Josephson dynamic with a different technique. Instead of triggering the oscillation with an initial phase difference, we prepare the ground state of the supersolid in the lattice potential, which has a population imbalance between the clusters. We then remove the lattice and let the system evolve in the harmonic trap. The results are shown in Fig. 5.12 for $\epsilon_{dd} = 1.41$. The initial ground state, due to the presence of the lattice, has the central density minimum in a position δ_0 displaced from the center of the trap. In the following dynamic, we observe two frequencies in the oscillations of both Z and $\Delta\varphi$: the usual Josephson frequency $\omega_J = 2\pi \times (23.85 \pm 0.03)$ Hz, and the smaller Goldstone frequency $\omega_G = 2\pi \times (3.56 \pm 0.08)$ Hz. The latter dominates the oscillation of the weak link position δ , see Fig. 5.12(a). The Josephson frequency ω_J is the same as the one observed with the phase imprinting method, hence without exciting the Goldstone mode, demonstrating the absence of coupling between the two modes. We propose a suggestive mechanical analogy to interpret the two-frequency dynamics. The standard Josephson dynamics can be mapped into that of a simple pendulum, where the phase difference $\Delta\varphi$ is the angle that the pendulum forms with the vertical direction and the population imbalance Z is the pendulum velocity. In the self-induced Josephson junction, the simple pendulum acquires an additional lower frequency, resembling a double pendulum with one length (the Goldstone one) larger than the other (the Josephson one), $l_G \ll l_J$, see Fig. 5.12(d).

Regarding possible applications of the Goldstone mode in the actual junction, we think that it could affect the fluctuation properties. In a standard Josephson junction, Z and $\Delta\varphi$ display fluctuations of both quantum and thermal origin. Focusing on the relative phase $\Delta\varphi$, the variance of the quantum fluctuations in the two-mode approximation is $\sigma_{\varphi-Q}^2 = \sqrt{U/(2NK)}$ [142], while for thermal fluctuations it is $\sigma_{\varphi-T}^2 = k_B T / (2NK)$ [143]. With our parameters, the quantum fluctuations are small because of the large atom number N , and we consider only thermal fluctuations. We know from the measurements performed on the phase transition, that the variance of the supersolid phase just after its formation is $\sigma_{\varphi-T}^2 \sim 0.035$, see Fig. 3.12. From this value and the estimated junction parameters of this chapter, we can extract the system temperature, exploiting the phase fluctuations as a thermometer [144]. We recast the phase variance in terms of the Josephson frequency $\omega_J = \sqrt{4N_{34}UK}$, obtaining $\sigma_{\varphi-T}^2 = k_B T \frac{2U}{(\hbar\omega_J)^2}$. The estimated temperature is therefore

$$k_B T = \sigma_{\varphi-T}^2 \frac{(\hbar\omega_J)^2}{2U}. \quad (5.20)$$

Using $\hbar\omega_J = 1$ nK (corresponding to the measured $\omega_J \sim 2\pi \times 20$ Hz) and $N_{34}U = 6$ nK,

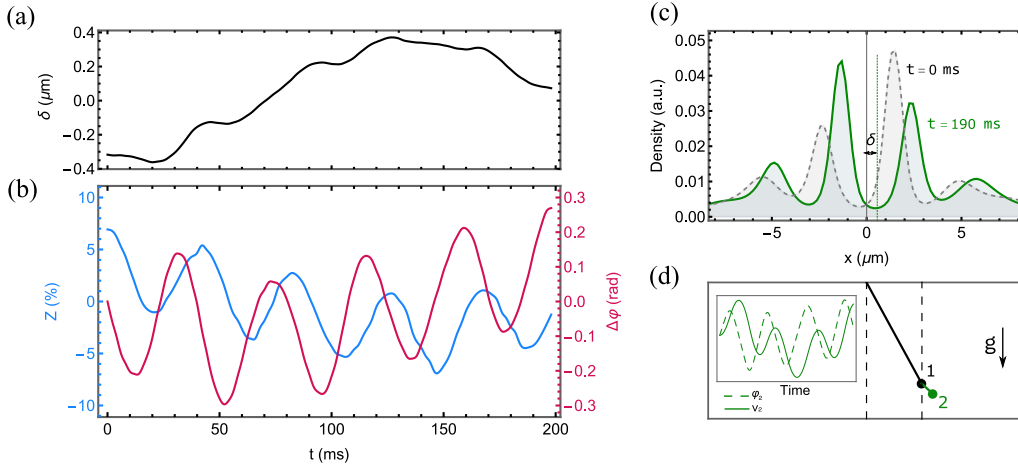


Figure 5.12: Goldstone and Josephson oscillations in numerical simulations. (a-b) We start the Josephson dynamics from the ground state in the presence of the lattice potential, instead of employing the phase imprinting protocol as in the experiment. Doing so, the weak-link position δ is displaced from the center of the trap and the Goldstone mode is also excited. We measure its low frequency (~ 3 Hz) from the oscillation of the weak-link position (a). The same low frequency appears also in Z and $\Delta\phi$, on top of the faster Josephson oscillation (b). (c) Snapshots of the dynamical simulations at $t = 0$ ms (gray) and at $t = 190$ ms (green), showing the different positions δ of the weak link. (d) Mechanical analogy with a double pendulum, for which one length (the Goldstone, black) is much larger than the other (the Josephson, green). Inset: the time evolution of the angle and velocity of the second pendulum is the sum of a fast and slow frequency, similar to what happens in the self-induced Josephson junction (b).

we get $k_B T \sim 60$ nK, a quite large value of the order of the condensation temperature. On the other hand, from time of flight measurements, we know that the thermal component of the BEC is small, and when it is no longer detectable the temperature is very likely to be less than 10 nK [10]. It is interesting to note that we can recover a result of this order of magnitude ($k_B T \sim 1$ nK) if we substitute the energy scale of the Josephson oscillations $\hbar\omega_J \sim 1$ nK with the energy scale of the Goldstone mode, $\hbar\omega_G \sim 0.15$ nK. This is just a rough estimation, which employs the standard two-mode approximation of Josephson junctions, but the intuition at the basis of the reasoning is that the lower energy scale of the Goldstone mode could strongly affect the fluctuation properties of the junction, revealing its self-induced nature.

Towards a supersolid in a ring

All the experiments described so far have been performed in a cigar-shaped trap. This geometry favors the softening of the roton mode along the weak direction of the trap and has been a key factor in the discovery of the supersolid phase. However, for future developments, the cigar-shaped geometry has several limitations. The inhomogeneity is strongly enhanced because the clusters are less and less populated while moving towards the edges of the trap. This complicates the analysis of the superfluid-supersolid phase transition, as discussed in chapter 3, and modifies the excitation spectrum. In chapter 4 we have seen that the anisotropy of the trap plays a relevant role in the rotational dynamics, and can hide peculiar supersolid properties, such as the sub-unity superfluid fraction. The problem is complicated by the long-range nature of the dipolar interaction, which makes homogeneous potentials impractical due to strong edge effects: the atoms get stacked at the boundary of the box [33].

On one side, a possible route toward homogeneous systems consists of forming larger supersolids in circular traps. In this regard, the recent realization of supersolids with 2D lattices opens the door to exciting research directions [48, 49]. However, the long-term goal of realizing a supersolid dominated by the bulk and with negligible edge effects, as in real solids, is far away, as it requires a large number of atoms or a different mechanism for supersolidity. To get an order of magnitude, we can think about a square lattice with L clusters per side, containing in total L^2 clusters. We naively estimate the transition to bulk-dominated physics when the number of clusters on the edge of the square is much less than the number in the bulk, namely $4L \ll L^2$. This is realized with $L \sim 10$, meaning $L^2 \sim 100$ clusters, a number beyond current experimental possibilities.

A different approach consists of eliminating the edges, by realizing a closed geometry. In this chapter, we describe recent experimental steps toward the realization of a supersolid in a ring geometry. The ring doesn't suffer from finite size effects and inhomogeneity, and it resembles a 1D infinite system. The scientific motivations are numerous and some of them are sketched in Fig. 6.1. The natural continuation of the results discussed in this thesis is the study of persistent currents. In the ring geometry, we can excite persistent currents using a phase imprinting technique as the one described in chapter 5 for the Josephson experiment. We will investigate the anomalous quantization properties of the supersolid currents [139], as discussed at the end of the previous chapter. We expect the shape of the phase profile and the velocity field to be in the form predicted by Leggett's model, with two counter-propagating currents, one semiclassical associated with the clusters and the other associated with the superfluid background, see section 4.1.

Regarding phase transitions, we know from chapter 3 that the transition will be continuous

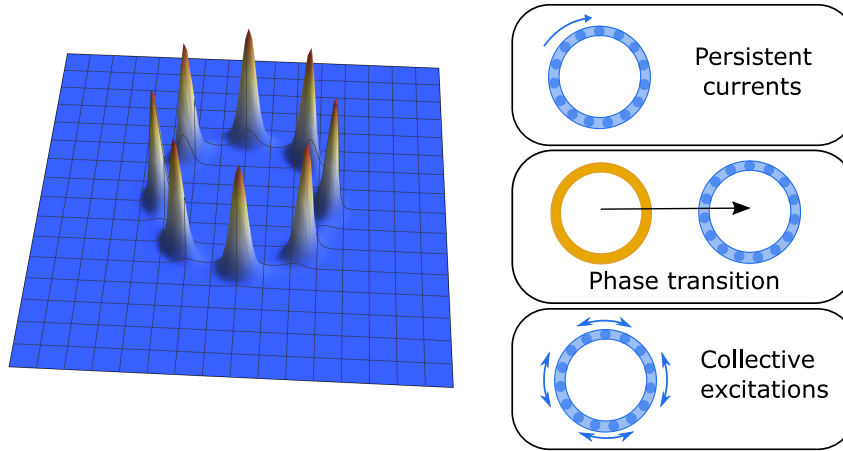


Figure 6.1: Scientific motivations for realizing a dipolar supersolid confined in a ring geometry. Left: density of an 8-cluster supersolid state in a ring. Right: possible research directions, including the study of persistent currents; the superfluid-supersolid phase transition and Kibble-Zurek mechanism; collective excitations and connection to supersolid hydrodynamics.

if the width of the ring is small enough. An interesting question is the role of the Kibble-Zurek mechanism across the continuous superfluid-supersolid phase transition. Originally introduced in cosmology, the Kibble-Zurek mechanism has been studied in the BEC transition in annular geometries [145] as well as in homogeneous potentials [97]. When the phase transition is crossed with a quench, the symmetry can be broken differently in spatial regions that don't have the time to exchange information. In the superfluid case, this leads to disconnected superfluid islands, each with its own phase. A persistent current can appear depending on the pattern of the spontaneously chosen phases. This is a stochastic process, whose statistics give information about the critical exponents of the transition. We expect that the Kibble-Zurek mechanism applies also to the superfluid-supersolid phase transition, but what is the nature of the resulting stochastic excitations is unknown and is an exciting open question. Probably, the crystal structure would form with different spatial phases, producing defects in the crystal and a stochastic dynamic exhibiting a mixed superfluid and solid nature.

Finally, we cite the possibility of studying collective excitations in a homogeneous potential, which, in contrast to the harmonic case, allows for a more direct connection to hydrodynamic quantities, such as the speed of sounds. In a recent theoretical proposal [146], Goldstone modes are excited in a ring geometry with our experimental parameters, and connections with other general quantities as the superfluid fraction are discussed. An interesting peculiarity of the ring configuration is that the low-energy Goldstone mode of the harmonic trap (see section 5.6) reduces to exactly zero energy. This means that in every experimental realization, the spatial phase of the supersolid lattice should be different since they have all the same energy.

Most of the results reported in this chapter are preliminary. In section 6.1 we describe the

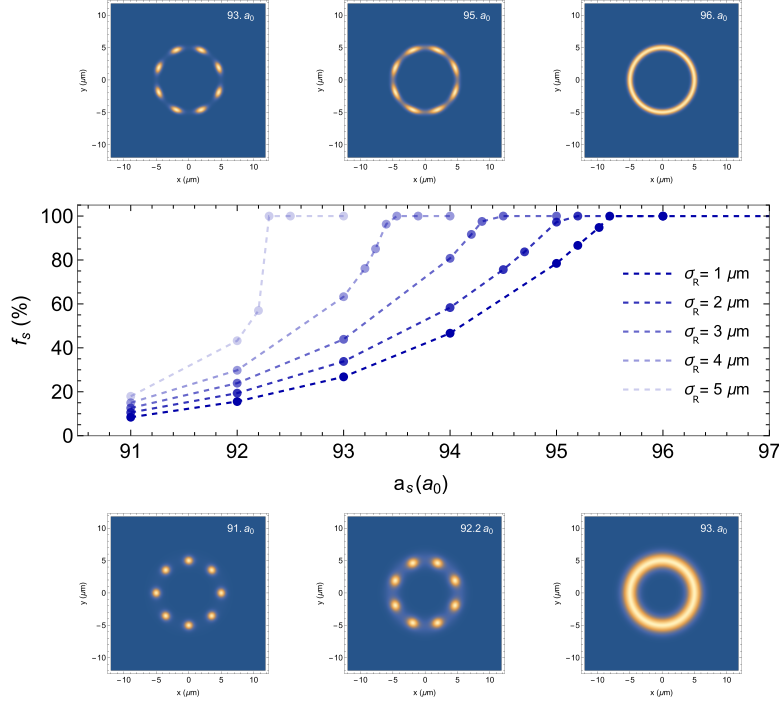


Figure 6.2: Ground-state simulations of the supersolid state in a ring-shaped potential, as described by Eq. 6.1, with radius $R = 5 \mu\text{m}$ and $N = 5 \times 10^4$ atoms. Superfluid fraction f_s calculated along the ring as a function of the scattering length a_s , for various ring thicknesses σ_R . The transitions are continuous for thin rings and discontinuous for thick rings. Insets: density distribution in the xy plane for $\sigma_R = 1 \mu\text{m}$ (upper row) and for $\sigma_R = 5 \mu\text{m}$ (lower row), for different scattering lengths. The supersolid forms with 8 clusters.

optical setup planned to realize the ring potential, through a Digital Micromirror Device (DMD), which we characterized but is currently being mounted in the lab. In sections 6.2 and 6.3 we show the characterization of the repulsive potential that will form the ring geometry, both for what regards the laser source and the dysprosium polarizability at $\lambda = 404 \text{ nm}$, which was unknown. Some of these results will be published in a paper in preparation [147]. Finally, in section 6.4, we discuss some preliminary numerical simulations about the excitation of persistent currents in the supersolid regime.

6.1 Optical scheme for a ring-shaped potential

To estimate some realistic parameters for the ring potential, we perform ground-state simulations in a harmonic trap with frequencies $(\omega_x, \omega_y, \omega_z) = 2\pi \times (20, 20, 100) \text{ Hz}$ plus the potential

$$U_R(x, y) = -U_R \text{Exp}[-(r - R)^2 / (2\sigma_R^2)] \quad (6.1)$$

where $r = \sqrt{x^2 + y^2}$, R is the ring radius, U_R the depth of the ring potential and σ_R the thickness of the ring. The resulting 3D potential is a torus, whose projection in the xy plane is a ring. In principle, one could consider a steeper potential instead of a gaussian, but as we will see the available optical resolution will smear out the potential walls, so the expression 6.1 is a good approximation of the experimental configuration. The size of the ring is determined by our vertical trapping frequency $\omega_z = 2\pi \times 100$ Hz, which gives a supersolid period $d \sim 4 \mu\text{m}$, and by the atom number. Considering an atom number inside each cluster of $N_c = 5 \times 10^3$, for a given radius R we need $N = N_c 2\pi R/d \sim 3 \times 10^4 R/d$ atoms. From this estimation, we conclude that the radius R should be of the order of the supersolid period d . We therefore set as a target a ring with radius $R = 5 \mu\text{m}$, for which we get supersolid states with a realistic atom number $N = 5 \times 10^4$. We checked with simulations that for larger rings, for example $R = 8 \mu\text{m}$, we need $N > 8 \times 10^4$ atoms to fill the ring, while for smaller N , the ground state is an array of distant independent clusters. Fig. 6.2 shows the results of ground-state numerical simulations with $R = 5 \mu\text{m}$, $N = 5 \times 10^4$ atoms and a ring potential depth of $U_R = 100$ nK. We plot the superfluid fraction f_s calculated through Leggett's upper bound 5.4 as a function of the scattering length a_s , for different ring thicknesses σ_R . Moving from thinner to larger rings the transition from continuous becomes discontinuous, as evident from the appearance of a jump in the superfluid fraction. This is the analog of the dimensional crossover in the cigar-shaped trap, the topic of chapter 3: when the system gets enough 'space' in the transverse direction, the transition becomes discontinuous [15]. Since we plan to work with a continuous transition, to minimize excitations in the supersolid, we will employ thin rings, $\sigma_R \sim 1 - 2 \mu\text{m}$.

The DMD

To create a ring-shaped optical beam to trap the atoms, we will employ a Digital Micromirror Device (DMD), an optical element consisting of an array of micrometer-sized mirrors, individually controllable. The mirrors can take two different positions ('on' or 'off'), differing by the tilting angle with respect to the surface of the DMD. Our model¹ is an array of 2560×1600 mirrors, where the 'on' ('off') state consists of a mirror tilted by 12° (-12°). The DMD takes in input a 2D binary matrix, which is translated into a specific mirror configuration. When a laser beam is diffracted by the DMD, the spatial shape of the mirror array gets imprinted on the intensity profile of all the diffraction orders. Therefore, the DMD allows the generation of arbitrary-shaped optical potentials.

To perform rotational experiments like the ones proposed in the previous section, a crucial prerequisite is that any defect in the ring potential should be as small as possible. Fluctuations or distortion of the ring geometry would break the rotational symmetry and would severely influence the dynamic of the system, for example inhibiting the flow of persistent currents. Therefore, we performed a careful characterization of the optical ring produced with the DMD in a test setup, shown in Fig. 6.3. We employ a laser beam with wavelength $\lambda = 404$ nm, on the blue side of a dysprosium resonance, see next section.

¹DMD [DLP9000X](#) Texas Instrument, controlled by the module Superspeed Vialux [V-900-12](#). Mirror size = $7.56 \mu\text{m}$.

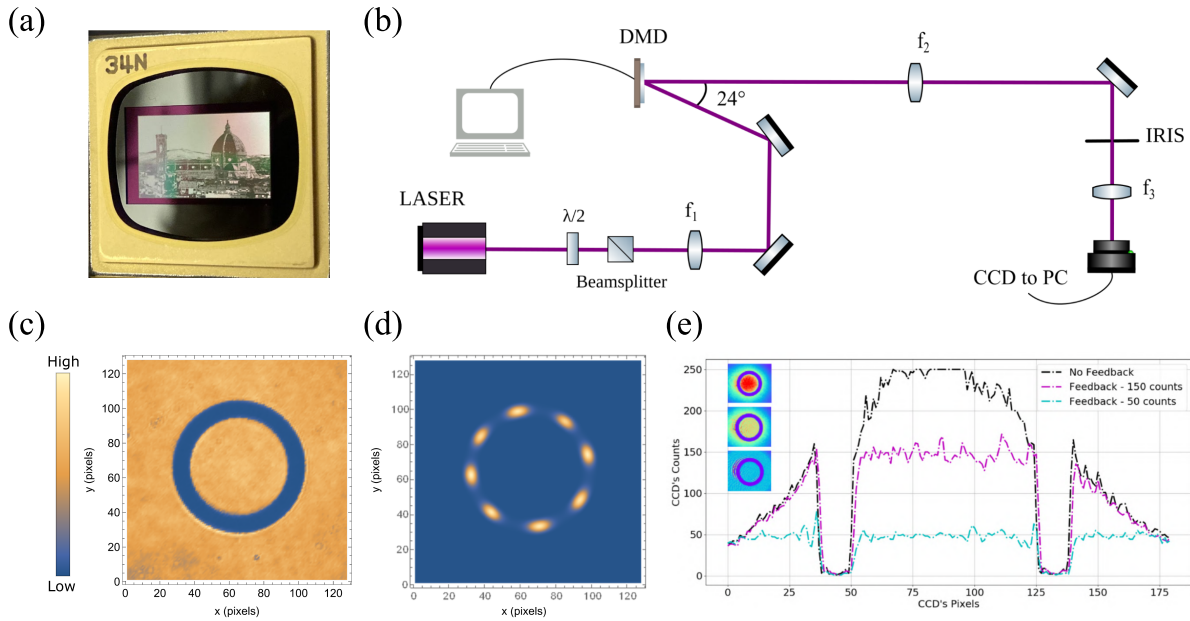


Figure 6.3: Characterization of the optical ring profile created with a DMD. (a) Photo of the DMD's programmable array. (b) Optical setup for the test of the DMD. A laser at 404 nm impinges on the DMD with an incident angle of 24° . The main diffraction order is selected, demagnified by a factor of 5 with a telescope and focused on a CCD camera. An iris in the focal plane inside the telescope eliminates high-frequency components of the image. (c) Intensity profile acquired with the CCD camera displaying the annular dark region (d) Ground-state simulation in the supersolid phase with the CCD image in (c) injected in the GPE equation as an external potential in the xy plane, to simulate the effects of the potential imperfections on the atoms. (e) Feedback protocol to eliminate the gaussian shape of the beam. 1D cuts in the x direction without feedback (black) and with feedback with two different targets (magenta and cyan). The insets show the corresponding 2D images.

The motivation for employing a repulsive potential is related to the need to minimize imperfections: any fluctuation in the light field will have a minimal effect on the atoms if they are trapped in the dark regions. The spatial profile imprinted into the laser beam by the DMD is, therefore, a dark annular region. The light diffracted by the DMD is focused on a CCD camera after a demagnification of a factor 5. Since the DMD is a blazed diffraction grating, the maximum of the diffracted power isn't in the 0^{th} order, but in a different order that depends on the incident angle. As shown in Fig. 6.3(b), we decided to work with a 24° incident angle. In this configuration, we get a good diffraction efficiency of about 50 %, and the reflected beam is perpendicular to the DMD surface. This geometry minimizes aberration on the final image, because all the DMD's mirrors are at the same distance from the focal plane. We tested the quality of the ring produced with the DMD by injecting into the eGPE equation the image acquired with the CCD camera as an external potential in the xy plane and calculating the ground-state of the system. This is done after mapping the spatial scale of the camera to the grid of the simulation in such a way that the ring potential has a radius $R = 5 \mu\text{m}$, and mapping the intensity

recorded by the camera into a temperature scale, such that the depth of the ring potential is between 100 and 200 nK. The external potential is completed with a vertical harmonic trap with frequency $\omega_z = 2\pi \times 100$ Hz. All the fluctuations and aberrations of the optical ring are then reflected in distortions of the calculated ground-state density distribution. An example of this procedure is shown in Fig. 6.3(c-d), where for a given ring recorded by the camera (panel c) we obtain a supersolid ground state (panel d) similar to the ones calculated in the analytical potential, see Fig. 6.2, with only small modifications of the lattice period along the ring. The optimization of the optical ring consists mainly of a careful alignment of the optical path, the aforementioned choice of the incident angle on the DMD, and the introduction of an iris in the focal plane inside the microscope, which acts as a bandpass filter cutting high-frequencies in the Fourier space of the image. We also implemented a feedback procedure that allows us to create nearly homogenous potential and to get rid of the gaussian shape of the beam. The feedback consists of a Python code that compares the camera image with a target image and corrects the DMD pattern to minimize the error between the two images [148, 149]. The feedback is fast (a few seconds) and it converges after about 5 iterations. An example of the feedback program on the ring potential is shown in Fig. 6.3(e). The potential displayed in Fig. 6.3(c) has been obtained after 5 iterations of the feedback program.

Optical trap and imaging

The beam diffracted by the DMD will propagate in the vertical direction z , providing the ring-shaped confinement in the xy plane. The additional confinement in the vertical direction is given by two attractive beams at 532 nm, shown in Fig. 6.4. The first one is a light sheet propagating in the x direction with waists $w_y = 190$ μm and $w_z = 20$ μm . The strong confinement in the z direction balances gravity and gives a harmonic frequency between $2\pi \times 100$ Hz and $2\pi \times 150$ Hz, depending on the power. Up to 2 W are available for the light sheet. However, despite the large aspect ratio, we found that the light sheet produces also a harmonic confinement of about $2\pi \times 30$ Hz in the y direction, while the confinement is negligible in the propagation direction (x). This configuration is anisotropic in the xy plane, and it would result in a localization of the atoms along the ring. To correct for the anisotropy, we add a second attractive beam at 532 nm, propagating in the vertical direction z and with a similar aspect ratio: $w_x = 37$ μm and $w_y = 300$ μm . The strong-confining direction of this second light sheet is in the x direction and can thus compensate for the anisotropy. Changing the power of the second beam, we found an approximately circular trap with frequencies $(\omega_x, \omega_y) = 2\pi \times [32.6(8), 30.1(3)]$ Hz. We produce the BEC in the infrared optical trap discussed in the rest of the thesis and we load it in the green trap at the end of the evaporation process, see Fig. 5.5(b). This is the starting point for the loading of the ring potential, which is the next goal of the experiment.

To correctly focus the optical potential imprinted by the DMD on the atoms, we also need an objective with a good enough resolution. Our current objective has a resolution between 2 and 3 μm , as described in chapters 2 and 4. The limited optical resolution has been one of the main challenges in the Josephson experiment. Since we want to create

a ring potential with radius $R = 5 \mu\text{m}$ and width σ_R around $2 \mu\text{m}$, and we want also to detect the in situ density distribution of the supersolid, we designed a new microscope. The imaging scheme is exactly the same: we will employ dispersive phase-contrast imaging as described in chapter 2, but we will use a diffraction-limited aspheric lens² as the first lens of the microscope. Even if its focal length is larger than the previous one, $f = 100 \text{ mm}$ instead of 75 mm , we should achieve a diffraction-limited resolution of $\text{res} \sim 1.5 \mu\text{m}$ due to the better performance of the lens. We confirmed this value with a test on the USAF target exactly as described in Fig. 2.7 in chapter 2. Particularly, since the new lens is aspheric, we should be able to use the full numerical aperture without incurring detrimental aberrations, contrary to the previous achromat lens. Finally, the larger focal length increases the depth of focus ($15 \mu\text{m}$) so that the alignment procedure of the objective should be easier than the previous one.

The project combining the imaging and DMD paths is shown in Fig. 6.5. The imaging light at 421 nm comes from the atoms and focalizes the image either in the Stringray camera, for the time of flight imaging (with a magnification $M_{\text{TOF}} \sim 2.5$), or in the Andor camera, for the in situ imaging (magnification $M_{\text{in situ}} \sim 50$). The DMD light at 404 nm comes from the DMD and is focalized on the atoms through the same microscope, with a total de-magnification of $M_{\text{DMD}} \sim 35$. The ring on the DMD should, therefore, have a radius $R_{\text{DMD}} = M_{\text{DMD}} \times 5 \mu\text{m} \sim 175 \mu\text{m}$. The building of this scheme is currently ongoing in the lab.

6.2 A laser source at 404 nm for repulsive optical potentials

To generate the repulsive optical potential, we work on the blue side of a strong dysprosium resonance at $\lambda = 404.7 \text{ nm}$ [150], shown in Fig. 6.6, with a linewidth $\Gamma_{405} = 2\pi \times 33 \text{ MHz}$, similar to the 421 nm transition used for the cooling (section 2.1). The choice of this wavelength is motivated by the possibility of achieving a better resolution compared to larger wavelengths, and by the proximity of our imaging light (421 nm) so that we can employ the same objective for the in situ imaging and the focalization of the optical potentials. We employ a continuous wave multimode laser diode³ emitting around $\lambda = 404 \text{ nm}$. The output power of the diode is about $P = 120 \text{ mW}$, with a broad spectrum in a free-running configuration shown in Fig. 6.6. The emission of the diode is very close to the resonance and is more than 1 nm wide. The envelope of the emission can be tuned, for example, with the temperature of the diode. Even at the lowest temperature, however, the emitted light has some frequency component at resonance and gets absorbed by the atoms, severely limiting the lifetime of the sample. Frequency filtering of the laser diode is therefore required to make the light available for optical trapping. The positive drawback of working with such a small detuning is that the polarizability of the atom is huge, as shown in the next section, and even a moderate power of the laser beam produces deep

²Aspheric lens [AL50100G-A](#), Thorlabs

³Nichia [NDV4313](#)

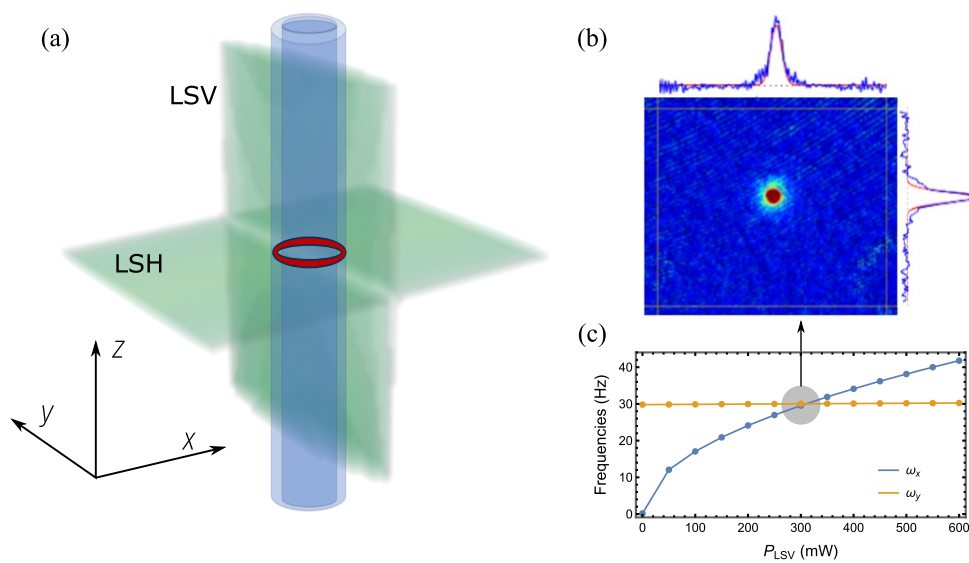


Figure 6.4: Geometry of the optical potential for the ring trap. (a) Sketch of the two attractive light sheets at 532 nm that form a disk trap. The horizontal light sheet (LSH) gives vertical confinement and has a power between 1 W and 2 W. The vertical light sheet (LSV) has a similar aspect ratio but produces the strongest confinement in the x direction, to compensate for the anisotropy of the first light sheet. The blue ring-shaped beam will propagate vertically. (b) Time of flight imaging of the BEC trapped in the green trap, with frequencies in the plane $(\omega_x, \omega_y) = 2\pi \times [32.6(8), 30.1(3)]$ Hz. (c) Simulations of the green potential showing the method to obtain a disk-shaped trap. The two frequencies in the plane ω_x and ω_y are equal for a given power of the vertical light sheet, P_{LSV} , while the other beam has $P_{LSH} = 1.5$ W.

optical potentials.

To filter the laser diode, we mounted a diffraction grating with 3600 grooves/mm and we operated the diode in the Littrow extended cavity configuration (ECDL). The external grating reflects back into the diode the first diffraction order and selects the emission of a single mode, while the output beam is collected from the zeroth order of the grating. The ECDL allows for a narrow spectral emission and a suppression by orders of magnitude of the power at resonance, at the cost of a reduced output power. In our case, we get $P = 20$ mW in the ECDL configuration. The wavelength of the emission peak can be tuned to about 1 nm changing the angle of the grating.

To test the performance of the laser diode in single-mode operation, we focalize the blue laser onto the BEC, while it is trapped in the cigar-shaped infrared trap, and we measure the lifetime. The optical setup is shown in Fig. 6.7. To monitor the spectral profile of the diode, we couple the light to a scanning Fabry-Perot cavity, from which we can control if the emission is multimode or single mode. Even with the ECDL, we observe a huge reduction in the BEC lifetime, which is as low as 160 ms even at low power $P = 2$ mW. This is probably due to residual amplified spontaneous emission light, with a fraction on resonance with the atoms. We therefore further clean the laser spectrum with a second diffraction grating, which spatially separates the different frequency components so that the resonant ones don't impinge on the atoms. The setup shown in Fig. 6.7 allows for the simultaneous alignment of the 1st and 0th diffraction orders on the atoms, so that we can compare the effect of the two beams in the same conditions. With the clean 1st diffraction order we observe a relevant increase in the lifetime, $\tau = 2.5$ s, which becomes comparable to that in the infrared trap, of the order of a few seconds. In Fig. 6.7(b) the lifetimes of the BEC with the two diffraction orders are compared. We can also estimate the lifetime from theoretical calculations. Considering a detuning $\Delta = -1.1$ nm, a power $P = 2$ mW and the predicted polarizability $\alpha = -8000$ a.u. (atomic units), we expect a lifetime $\tau \sim 500$ ms (in the next section we experimentally confirm the theoretical prediction for α). The observed lifetime of 2.5 s is due to the repulsive nature of the potential: the atoms are pushed away from the high-intensity regions, and experience a lower intensity. Given the ratio between the measured and theoretical lifetimes $2.5 \text{ s}/0.5 \text{ s} = 5$, we estimate that the equilibrium position of the atoms in the infrared plus blue potential should be distant about 1 waist of the blue beam from the maximum intensity. This is consistent with a modelization of the trapping potential [147]. The measured lifetime is a lower limit for the experimental conditions since the atoms in the ring potential will be trapped in the dark region and will experience an even lower intensity of the blue laser.

The lifetime increase comes at the cost of reduced power. The second diffraction grating reduces by about 50 % the power of the beam so that we only have 10 mW left. To increase the available power, we mounted an alternative configuration without diffraction grating [149], shown in Fig. 6.8. We employ two diodes in a master-slave configuration. The first one is in the ECDL configuration, while the second is free-running. The single-mode light of the first diode is injected into the second, which works as an amplifier. It is forced to emit at the frequency selected by the master diode. To further clean the spectrum, we

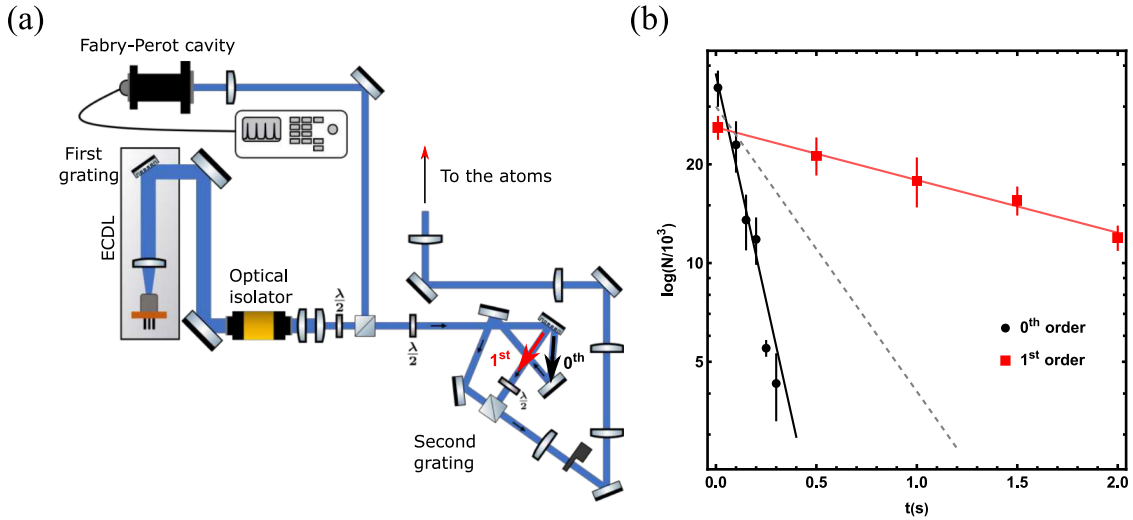


Figure 6.7: BEC lifetime with and without the second diffraction grating. (a) Optical setup. The single-mode ECDL light is diffracted by a holographic grating. The 1st diffraction order is cleaned from the residual light on resonance with the atoms, contrary to the 0th order, thanks to the large distance from the atoms. Both orders are focused on the atoms so that we can measure the lifetime with the two kinds of light in the same conditions. A Fabry-Perot cavity is employed to monitor the emission of the ECDL and control that it is single-mode. (b) Atom number N of the BEC as a function of time in the infrared attractive potential plus the repulsive blue potential ($P = 2$ mW, $\lambda = 403.6$ nm) coming from the 0th (black points) or the 1st (red points) orders of the second diffraction grating. In the first case the lifetime is $\tau = 160$ ms, while in the second case it is $\tau = 2.5$ s. The dashed gray line is the estimated lifetime assuming the maximum intensity of the blue beam (see text).

employ a narrow filter⁴ whose tilting angle can be tuned to cut by six orders of magnitude the light on resonance with the atoms. The light reflected by the filter shows a sudden drop when the amplifier gets injection-locked, and can in principle be used in a feedback loop to stabilize the locking of the two diodes. The design is based on [151]. We then add an AOM and a fiber which cleans the spatial mode. With this configuration, we obtain about 40 mW of blue light after the optical isolator, and about 15 mW after the fiber. The lifetime is similar to the one with the diffraction grating shown in Fig. 6.7(b).

6.3 Dysprosium polarizability at 404 nm

The depth of an optical dipole trap is determined by the intensity of the laser beam and by the dynamic polarizability of the atom $\tilde{\alpha}(\omega)$, through

$$U_{\text{dip}}(\mathbf{r}) = -\frac{1}{2\epsilon_0 c} \text{Re}(\tilde{\alpha}) I(\mathbf{r}). \quad (6.2)$$

The polarizability quantifies the induced electric moment on a neutral atom due to an

⁴Semrock laser clean-up filter LL01-405.

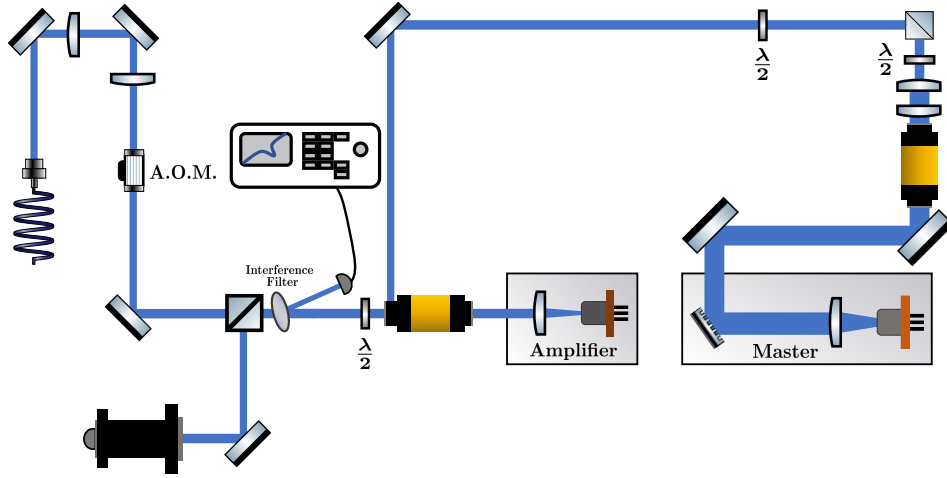


Figure 6.8: Injection locking of the diode laser. Optical setup for the operation of two diodes in a master-slave configuration. The single-mode light emitted from the ECDL (master) is injected into a second free-running diode (amplifier) through an optical isolator. The light is forced to emit the same single mode of the master. The light is further cleaned with an interference filter. A Fabry-Perot cavity monitors the spectrum of the emitted light. The light is then coupled to an AOM and an optical fiber.

external electric field. It is a complex quantity: the real part is related to the dispersive interaction of the atom with the radiation and determines the conservative dipole potential in Eq. 6.2, while the imaginary part is related to the absorptive part and determines the scattering rate [152]. In the previous section, we characterized the laser source at $\lambda = 404$ nm and we got an idea of the available power, and hence the intensity, for the trapping potential. To estimate the achievable potential depths, we need a measurement of the polarizability. For dysprosium, the dynamic polarizability has been measured for the ground state at larger wavelengths [153, 154, 155], but there are no experimental results around 404 nm. The real part of the polarizability, which we call $\alpha = \mathcal{R}e(\tilde{\alpha})$ from now on, has scalar, vectorial and tensorial contributions. We consider the case of linearly polarized light so that the vectorial part is zero. While for alkali atoms the tensorial polarizability is usually negligible compared to the scalar one, for lanthanide atoms it is much larger and makes the atom-light interaction anisotropic [31]. Recently, the tensorial part of the polarizability of dysprosium atoms has been exploited to produce an array of ultracold atoms at sub-50 nm separation [156]. In our case of a stretched ground state ($J = 8$ and $m_J = -J = -8$) the polarizability is

$$\alpha(\omega) = \alpha_s(\omega) + \frac{3 \cos^2 \theta - 1}{2} \alpha_t(\omega), \quad (6.3)$$

where α_s and α_t are the scalar and tensorial part, respectively, and θ is the angle between the light polarization and the quantization axis, defined by the external magnetic field (in our case, the z axis). While in spectral regions far away from resonances the tensorial

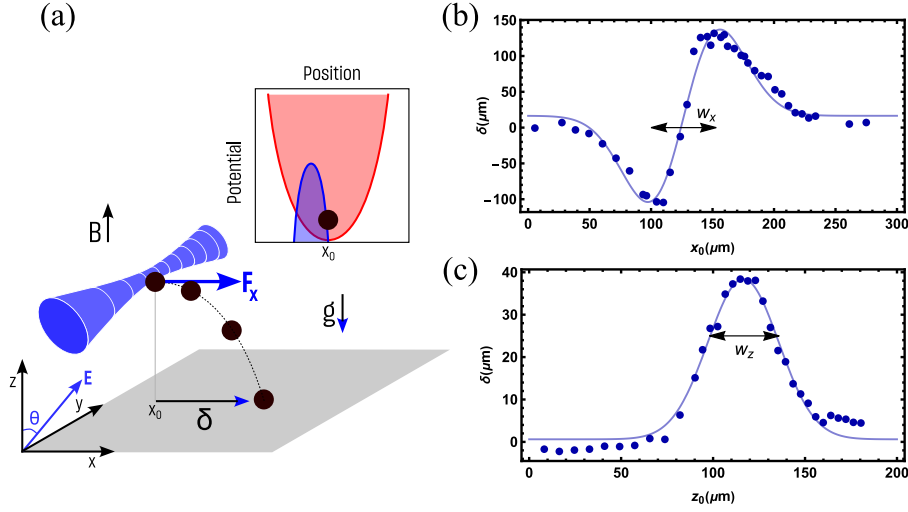


Figure 6.9: Measurement of the polarizability at 404 nm with a momentum kick. (a) Sketch of the method. A focused laser beam with variable λ , around 404 nm, is switched on for a small time δt . The atoms (black circle), initially trapped in the infrared optical trap, get a momentum kick due to the dipole force in the direction perpendicular to the beam propagation. We measure the displacement of the atomic cloud δ in the xy plane after a free expansion in time of flight. The final displacement depends on the polarizability and on the relative position between the beam and the atoms. The electric field of the light forms an angle θ with the z axis. Inset: sketch of the potential during the kick. Atoms are trapped in the attractive infrared potential and feel the repulsive potential of the blue beam. (b) Displacement δ as a function of the beam position x_0 along the x axis. The shape is the derivative of a gaussian, see Eq. 6.4. To measure the polarizability, we place the beam in the position of maximum force. The distance between the two maxima is the waist w_x . (c) Displacement δ as a function of the beam position z_0 along the z axis. The shape is a gaussian, from which we fit the waist w_z . In (b) and (c), thick lines are fits to the data.

part is much lower than the scalar part, as it happens for example at $\lambda = 1064$ nm, in our case, due to the proximity of the 404.7 nm resonance, we expect α_s and α_t to be similar.

Because our potential is repulsive, we cannot rely on the usual method of extracting the polarizability from the trapping frequencies [154]. Therefore, we develop a technique that relies on the momentum kick imparted by the dipole force during a pulse of the repulsive potential. A sketch of the method is shown in Fig. 6.9. A laser beam with a tunable wavelength around 404 nm is focused on the BEC, which is trapped in the attractive infrared potential. After switching on the repulsive blue potential for a small time δt , the atoms get a momentum kick $\delta \mathbf{p} = \mathbf{F}_{\text{dip}} \delta t$, where the dipole force is $\mathbf{F} = -\nabla U_{\text{dip}}$. The dipole force has two main components: one in the vertical z direction and one in the x direction transverse to the beam propagation. We measure the position δ of the BEC in the xy plane switching off all the laser beams just after the application of the kick, and letting the BEC expand for $t_{\text{TOF}} = 25$ ms. We are thus sensitive to the momentum kick imparted by the x component of the dipole force, $F_{\text{dip},x} = -\frac{\partial}{\partial x} U_{\text{dip}}$. Using Eq. 6.2 for U_{dip} and the expression of the light intensity $I = 2P/(\pi w_x w_z) \text{Exp}[-2x^2/w_x^2 - 2z^2/w_z^2]$ the dipole force is

$$F_{\text{dip},x}(x, z) = \frac{4\alpha P}{\epsilon_0 c \pi w_x^3 w_z} x e^{-2x^2/w_x^2} e^{-2z^2/w_z^2}. \quad (6.4)$$

From the ballistic expansion $\delta = t_{\text{TOF}} \delta p / m$, we get an expression linking the observable δ to the polarizability

$$\delta = \frac{F_{\text{dip},x} \delta t}{m} t_{\text{TOF}}. \quad (6.5)$$

The maximum displacement δ corresponds to the largest module of the force $F_{\text{dip},x}$, exerted for $x = w_x/2$ and $y = 0$, where the slope of the potential is maximum. To precisely align the laser beam such that the center of mass of the BEC is located in the position in which the force is the strongest, we employ a motorized mirror that changes the angle of the beam on the last lens, changing therefore the position of the beam in the atomic plane. We can scan the motorized beam in the x or z direction and measure the resulting displacement δ in time of flight. The results are plotted in Fig. 6.9(b-c). Along the x direction we observe an odd profile corresponding to the derivative of a gaussian, as in Eq. 6.4. We can clearly place the beam in one of the two maxima. The same measurement with a scan of the mirror in the z direction produces instead a gaussian, as shown in Fig. 6.9(c). With an iteration of this process, we can find the global maximum of the force. This kind of measurement gives also direct access to the waists of the beam on the atomic plane. In the first case, we can fit the horizontal waist $w_x = (58 \pm 7) \mu\text{m}$, which is the distance between the two peaks, while in the second case, we fit $w_z = (38 \pm 3) \mu\text{m}$ which is the waist of the observed gaussian. The errors come both from the fitting procedure and the uncertainties in the mirror calibration.

Using the expression for the force 6.4 in $x = w_x/2$ and $y = 0$, we get the relationship between the displacement and the polarizability

$$\delta = \frac{2\alpha(\omega) P t_{\text{TOF}} \delta t}{\epsilon_0 c \pi \sqrt{e m w_x^2 w_z}}. \quad (6.6)$$

To extract α_s and α_t , we do two kinds of measurement, shown in Fig. 6.10. First, for a fixed interaction time δt , we vary the angle θ of the light polarization and we observe the displacement δ . The polarizability changes according to Eq. 6.3, and we observe indeed sinusoidal oscillations of δ , see Fig. 6.10(a). From these oscillations, we can fit the ratio α_s/α_t . Remembering that α_s is negative, because the potential is repulsive, but α_t is positive, the minimum displacement is obtained for $\theta = 0$, when $\alpha = \alpha_s + \alpha_t$. From Fig. 6.10(a) we see that $|\alpha_s|/\alpha_t \sim 1$, because the minimum displacement is near zero, meaning that the two components nearly cancel each other. Then, we set the angle $\theta = \pi/2$ giving the maximum displacement, corresponding to $\alpha_s - \alpha_t/2$, and we measure δ as a function of the interaction time δt , see Fig. 6.10(b). We observe a linear correlation as predicted by Eq. 6.6, and from the fitted slope we extract the absolute value of $\alpha_s - \alpha_t/2$. Combining the two measurements, we obtain α_s and α_t . We repeat the same procedure for different values of λ , varied by changing the tilting angle of the diffraction grating in the ECDL. In Fig. 6.11 we plot the results for α_s , α_t and $\alpha_{\text{max}} = \alpha_s - \alpha_t/2$ in atomic units (1 a.u.

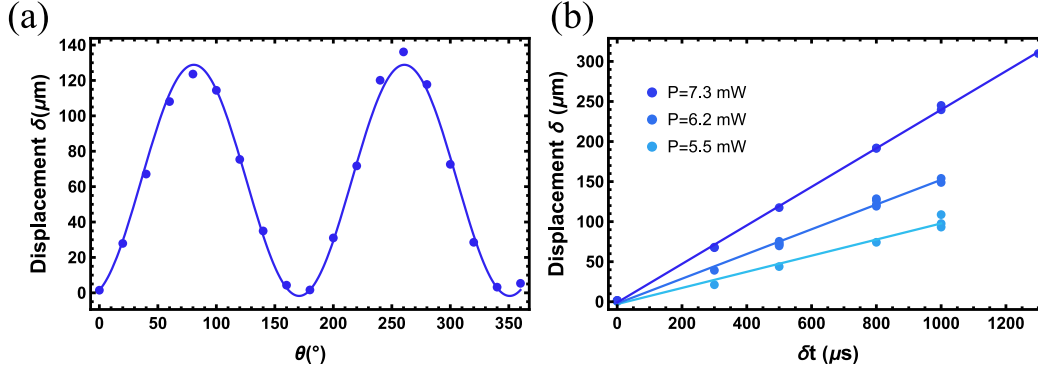


Figure 6.10: Measurement of α_s and α_t at $\lambda = 403.6$ nm. (a) For a fixed interaction time δt , we measure the displacement δ changing the angle θ of the light polarization. The resulting oscillation comes from the anisotropic light-atom interaction, see Eq. 6.3. From the fitted oscillation (thick line) we extract the ratio α_s/α_t . (b) With the angle $\theta = \pi/2$, corresponding to the maximum displacement δ , we measure δ as a function of the interaction time δt . From the fitted slope (thick lines) we extract $\alpha_s - \alpha_t/2$. The three lines correspond to three different powers of the beam.

$= 4\pi\epsilon_0 a_0^3$), together with theoretical calculations employing the models in [157, 158]. As expected due to the proximity of the resonance, we obtain huge polarizabilities up to about $\alpha_{\text{max}} \sim -13000$ a.u. for $\lambda = 404.1$ nm. We do not explore the region closer to the resonance because we observe a reduction in the lifetime. The experimental results are in agreement with the theoretical calculations under the error bars, which are about 30 % of the mean value. The main contribution to the experimental error comes from the uncertainty in the waists, as usual in polarizability measurements which cannot rely on the comparison with another, known, species [154]. However, we note that our method of the force kick involves a dependence on the beam waists with a power 3, see Eq. 6.6, contrary to the usual harmonic frequency method for which the power is 4.

Finally, we can estimate the strength of the repulsive potentials that we can create with our setup. We have $P = 15$ mW after the optical fiber and, considering that we will lose 50 % of the power on the DMD plus other possible losses in the optical path in Fig. 6.5, we can safely estimate a power of $P = 5$ mW on the atoms. Since the laser beam will propagate in the vertical direction (parallel to the magnetic field) the angle θ is fixed and equal to $\pi/2$. The polarizability takes therefore its maximum value. With a polarizability $\alpha = -10000$ a.u. and a beam waist of $w = 60$ μm , we will obtain a ring potential with a depth $U_R = 1.5$ μK , with a lifetime of the BEC of a few seconds.

6.4 Persistent currents in the ring: preliminary numerical studies

The most direct application of the results of this thesis to the ring geometry is the study of persistent currents in the supersolid phase, realizing for the first time the seminal Leggett's

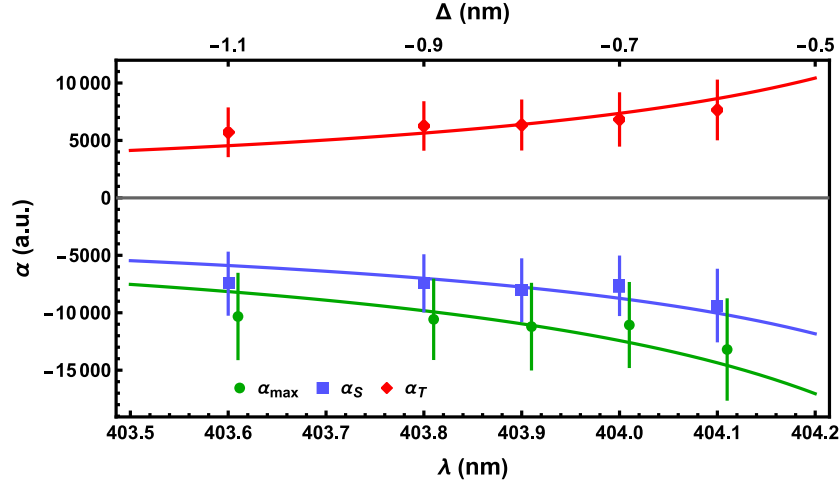


Figure 6.11: Real part of the polarizability α for the ground state of dysprosium as a function of λ , on the blue side of the resonance at 404.7 nm. Blue squares indicate α_s , red diamonds α_t and green circles $\alpha_{\max} = \alpha_s - \alpha_t/2$, obtained for a polarization angle $\theta = \pi/2$. The corresponding thick lines are theoretical calculations. The upper horizontal axis is the detuning Δ from the transition.

model discussed in section 4.1. Persistent currents in ring geometries have been studied for BECs [159, 160] and ultracold Fermi gases [161, 162], and have been among the most spectacular demonstrations of superfluidity in these systems. In this section, we present some preliminary numerical results about the excitation of persistent currents and their features both in the BEC and in the supersolid, for our experimental configuration. An extension of this work will be probably the topic of a proposal paper for experiments in the ring geometry in the near future.

The first key question is how to excite persistent currents. In the discussion at the end of section 5.5, we plotted the angular momentum of the system as a function of the angular velocity Ω of the container, which is also the conceptual situation of Leggett's model. Theoretically, this is easily simulated by adding an energy term $-\Omega L$ in the GPE equation, with L the angular momentum, and searching for the ground state in the frame rotating with velocity Ω [139]. On the experimental side, it is not obvious how to rotate the ring, if the system will come into equilibrium with the trap and how long will it take. Therefore, we take a different approach: we inject a well-defined angular momentum in the system by phase imprinting an initial velocity distribution, similar to our technique to excite the Josephson oscillations (section 5.2). Recently, persistent currents have been successfully phase-imprinted in ultracold Fermi gases [161]. Exploiting the DMD, we will be able to imprint arbitrary phase profiles along the ring.

Here we show some recent simulations of the dynamics following the imprinting of different phase profiles. All the simulations are performed with $N = 5 \times 10^4$ atoms and a harmonic trap with frequencies $(\omega_x, \omega_y, \omega_z) = 2\pi \times (20, 20, 100)$ Hz, plus the ring potential as described in section 6.1. We imprint a phase profile $\varphi(\theta)$, where θ is the angular coordinate

along the ring, by switching on a corresponding potential for 120 μs . A summary of the results so far is shown in Fig. 6.12. We tried two linear gradients, one with amplitude 2π , which is the usual one to excite one quantum of circulation in the BEC, one with amplitude π and a more complex shape corresponding to the Leggett's velocity field in Eq. 4.8. The latter reads

$$\varphi(\theta) = A \left(\theta - \bar{n} f_s \int_0^\theta \frac{d\theta'}{n(\theta')} \right), \quad (6.7)$$

where $n(\theta)$ is the number density along the ring, \bar{n} its average value, A some amplitude and f_s the superfluid fraction in Leggett's model, Eq. 4.4. We analyze the dynamic evolution of the system by calculating the angular momentum $L = \int d\theta m n(\theta) v(\theta) R$, with $v(\theta) = \hbar/m\varphi'(\theta)$, as a function of time. In Fig. 6.12(a) we plot $L(t)$ in four cases: BEC with linear gradients with amplitude π and 2π , and supersolid with 2π -linear gradient and with Leggett's profile. For the BEC, we correctly excite a persistent current with one quantum of circulation when the amplitude of the phase gradient is 2π . We indeed measure $L = N\hbar$ for the whole dynamics. If the amplitude of the gradient is lower (π) the total angular momentum is instead zero and no persistent current is excited. In Fig. 6.13, we plot density and phase snapshots for different times. The energy imprinted in the π -gradient takes the form of other excitations, such as a soliton which is clearly visible at the position of the π -jump and persists for the whole dynamic.

For the supersolid, the imprinting of the 2π phase gradient gives $L = N\hbar$ angular momentum, as in the BEC. Indeed, if the phase varies linearly $\varphi'(\theta) = 2\pi/(2\pi R) = 1/R$, the angular momentum is always $L = mR\hbar/(mR) \int d\theta n(\theta) = N\hbar$, independent from the density distribution. However, we expect that the persistent current with $L = N\hbar$ shouldn't be stable, due to the reduced superfluid fraction [139]. We indeed observe a slow decay of the current towards smaller angular momenta, even in the dissipationless system of the simulations. The lost angular momentum probably is transferred to other kinds of excitations, for example vortices inside the superfluid clusters, not detected with the current analysis. Presumably, the decay in the experiment would be faster. Interestingly, the system tends to stabilize to an angular momentum $L \sim f_s N\hbar$. The decay of the persistent current is associated with a small oscillation of the superfluid fraction, see Fig. 6.12(b), and also with structural changes of the lattice (one cluster is lost when f_s drops around $t \sim 120$ ms). Instead, when we phase imprint the Leggett's profile, we do not observe such decay and the persistent current is stable, demonstrating that the peculiar Leggett's shape of the phase corresponds to a stable rotational configuration of the supersolid, analog to the 2π linear gradient for the superfluid. Also, the superfluid fraction remains constant, reflecting a shape-preserving rotation. The angular momentum associated with this rotation is $L = f_s N\hbar$, manifesting the role of the sub-unity superfluid fraction in the persistent current. Regarding the evolution of the phase profile, in Fig. 6.13(c-d) we plot some snapshots in the case of the 2π gradient and of Leggett's profile. For the gradient, while at the beginning the phase grows linearly, we observe the appearance of an oscillating pattern on top of the linear slope at later times, similar to Leggett's profile.

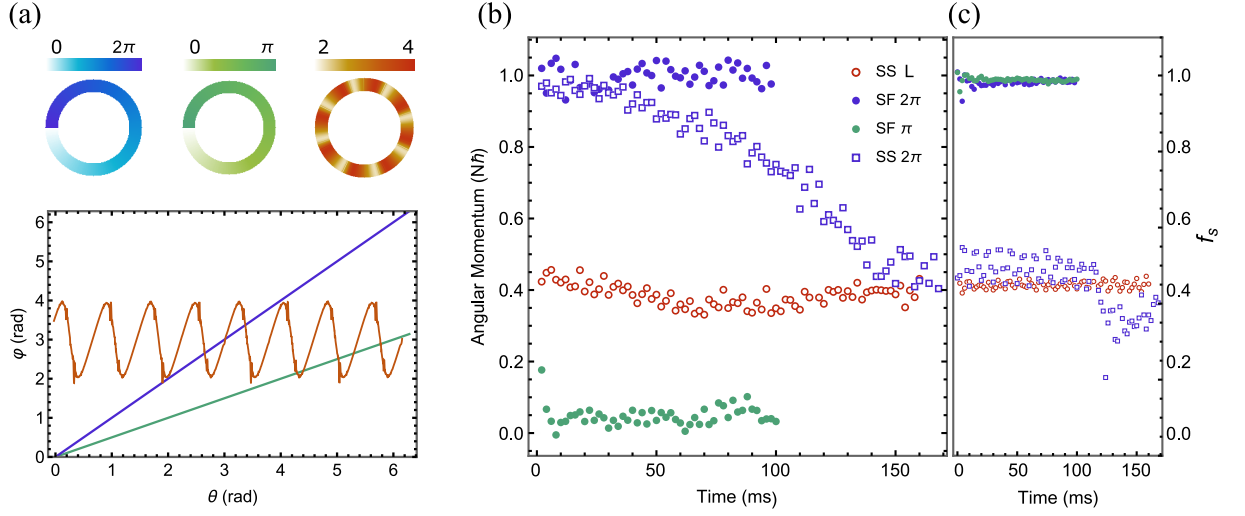


Figure 6.12: Numerical simulations of persistent currents in the ring. (a) Phase imprinting of different spatial phase profiles $\varphi(\theta)$ along the ring: linear phase gradient with amplitude 2π (blue), with amplitude π (green) and Leggett's phase profile 6.7 (red). Insets show the phase profiles in the ring geometry. (b) Angular momentum L as a function of time after phase-imprinting the spatial phase profiles in (a). Full markers refer to the BEC phase ($a_s = 150 a_0$), while open markers to the supersolid phase ($a_s = 93 a_0$). The stable persistent current in the supersolid phase brings $L = f_s N \hbar$. (c) Superfluid fraction f_s calculated with Leggett's formula 4.4 versus time in the same four cases as in (b).

Starting with Leggett's profile, instead, the shape of the phase is approximately preserved during the motion. From the density snapshots, we see that in the second case, the lattice is displaced from the starting point, demonstrating a shape-preserving rotation. In the case of the gradient, instead, the lattice is modified by other excitations at larger times.

In the short future, on the simulations side, we will extend the preliminary results presented here to include supersolids with variable f_s and with different shapes of the phase profile. It will also be interesting to study the decay of unstable persistent currents, which can give rise to topological excitations such as vortices and solitons. On the experimental side, we have to tackle and solve many challenges. The study of persistent currents requires the capability of measuring the angular momentum of the system. Of course, we will try to take advantage of both in situ and time of flight information. With phase-contrast in situ imaging, we can in principle take non-destructive images and hence extract the velocity from the movement of the real space density. We should carefully choose the detuning of the beam in order to not heat the sample between two consecutive images. However, this method only gives information on the clusters' velocity, and it wouldn't be possible to observe the peculiar counter-propagating currents of the supersolid (see Fig. 4.2). It would be possible, anyway, to determine if a current is stable or not, by observing the velocity of the clusters as a function of time. To get information on the spatial phase, we need to take time of flight measurements. A possible protocol, employed in [161], consists

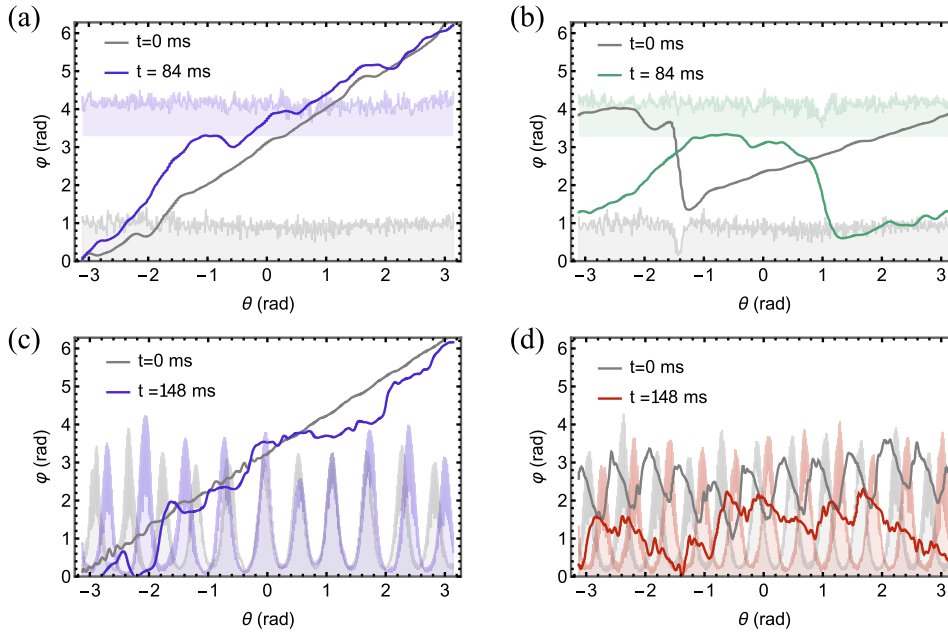


Figure 6.13: Snapshots of the dynamical simulations shown in Fig. 6.12. (a) Phase profile $\varphi(\theta)$ along the ring in the BEC phase at $t = 0$ ms just after the phase imprinting (gray line) and at $t = 64$ ms (blue line) for the imprinting of a linear gradient with amplitude 2π . The density profiles are plotted for comparison, not in scale and shifted vertically for clarity. (b) Same as in (a) for the imprinting of a linear gradient with amplitude π . The phase jump produces a soliton, detected as a dip in the density profiles. (c-d) Phase and density profiles for the supersolid after the phase imprinting of a linear gradient with amplitude 2π (c) and of Leggett's phase profile 6.7 (d). Gray lines corresponds to $t = 0$ ms while colored lines to $t = 148$ ms.

of expanding the ring together with a 'local oscillator' working as a phase reference, for example a small BEC disk at the center of the ring. In [161], the interference pattern has the form of a spiral, and the number of arms quantifies the amount of circulation in the ring. How to extend this model to the supersolid, where the density is modulated, and to partially quantized supercurrents is an open question.

Outlook

The results accomplished during my PhD can be summarized into two main groups. On one hand, I explored the character of the quantum phase transition from the superfluid to the supersolid in the cigar-shaped geometry employed so far in our experiment [15, 56]. I discovered that the transition can be experimentally tuned from discontinuous to continuous by changing the geometry of the system, increasing the degree of control over the formation process of the supersolid, and opening up new perspectives in the study of the phase transition. On the other hand, I spent a good portion of my PhD in studying the concept of superfluid fraction and its implications in the physics of supersolids. I explored the superfluid properties of the supersolid both through rotations [19, 21] and through the detection of Josephson oscillations [22]. The latter experiment allowed for the first observation of a sub-unity superfluid fraction induced by the spontaneous breaking of translational symmetry. Finally, I worked on the realization of a supersolid in a ring geometry, an exciting development that will result in the investigation of supersolids in homogeneous potentials, with applications related to persistent currents, phase transitions and hydrodynamics.

In the chapters of this thesis, I already discussed the main outlook of my research results. Particularly, in chapter 6 I described in detail possible future research lines in the ring geometry and the related extension of the research about the sub-unity superfluid fraction; in chapter 5 I pointed out the novelty of the Josephson technique to measure the superfluid fraction, that potentially can be of interest for the different systems discussed in chapter 1, in which modulated superfluid phases have been recently discovered and for which the connection to supersolidity is an open question.

Here, I want to focus on a more general outlook on future research in the field of supersolids. In my opinion, two topics about supersolids are largely unexplored so far and deserve special attention in the near future. First, the supersolid phase has been successfully described by a mean-field theory, which is a semi-classical approximation. However, quantum phases of matter are expected to host complex and rich quantum correlations and entanglement properties. Although the dipolar supersolid is a dilute system in which interactions are typically weak, I expect that interesting correlations and entanglement could emerge, also because we know that quantum fluctuations play an important role as a stabilizing mechanism. It is indeed known that entanglement can be produced crossing a quantum phase transition [163]. A study in this direction would move toward a desirable full-quantum description of the supersolid phase of matter. Imaging to move the first steps starting from our work on the Josephson effect, the reference model for the entanglement properties is the bosonic Josephson junction, which is known to host in its ground state

different kinds of entangled states, that can be also metrologically useful [142]. These squeezed states have been realized experimentally and studied through the fluctuations properties of the conjugate variables Z and $\Delta\varphi$ [164, 165]. It would be extremely interesting to explore entanglement in an extended framework in which the self-induced nature of the supersolid junction is included. Probably the low-energy Goldstone mode, which is related to the movement of the Josephson barrier, should be included as explained in chapter 5. Also a study of thermal, rather than quantum, fluctuations could be appealing to develop new thermometry methods based on the supersolid instead of the standard bosonic Josephson junctions [144].

The second outlook that I want to discuss is related to the solid nature of the supersolid. During my thesis, I mainly dealt with superfluid properties and how they are modified by the crystal structure. But how does the supersolid behave as a crystal? How much is it stiff and how much is it different from real solids? It is important to address these questions, which represent a unique novelty in the field of quantum gases, in which to my knowledge solid-like properties have never been explored. It is tempting to imagine a quantity similar to the superfluid fraction that quantifies how much the solid properties are affected by the superfluid nature. It should be 1 for the classical solid and 0 for the homogeneous superfluid: a 'solid fraction'. In this regard, an idea that I want to pursue is the following. A distinctive property of solids is that they can support shear stress and, as a consequence, a particular transverse wave can propagate in solids, the so-called shear wave. It consists of an oscillation of the atoms in a direction perpendicular to the wave propagation. The restoring force enabling the propagation of the wave is indeed shear stress. Shear waves are well known in the field of seismology because they propagate in earthquakes. The velocity of the shear wave is proportional to the shear modulus of the system: the stiffer the solid is, the faster the shear wave. Does the supersolid sustain the propagation of shear waves? Are they related to a shear modulus of the supersolid? To excite a shear wave in our small system made by a few clusters, we could consider a one-dimensional supersolid in the x direction (our cigar-shaped geometry) and apply a transverse force in the y direction to a lateral cluster. This is experimentally feasible by exploiting the DMD discussed in chapter 6. The lateral cluster will start oscillating in the harmonic trap with frequency ω_y , but will interact with the other clusters and could mediate the transverse motion. Eventually, a shear wave could propagate in the x direction. This scenario seems confirmed by some preliminary numerical simulations and is promising to understand 'how much solid' is a supersolid.

Colophon

This thesis has been written in the summer and autumn of 2023.

The L^AT_EX style has been adapted from a code developed by Niccolò Preti (niccolo.preti@unifi.it).

The images in the introduction are the Atomium, Heysel park, Bruxelles (image from [this website](#)) and a time of flight image of a dysprosium Bose-Einstein condensate.

Bibliography

- [1] A. J. Leggett. Can a solid be "superfluid"? *Phys. Rev. Lett.*, 25:1543–1546, 1970. doi: 10.1103/PhysRevLett.25.1543. URL <https://link.aps.org/doi/10.1103/PhysRevLett.25.1543>.
- [2] A. J. Leggett. *Quantum Liquids: Bose condensation and Cooper pairing in condensed-matter systems*. Oxford University Press, United States, 2008. doi: 10.1093/acprof:oso/9780198526438.001.0001.
- [3] L. Pitaevskii and S. Stringari. *Bose-Einstein Condensation and Superfluidity*. International Series of Monographs on Physics. OUP Oxford, 2016. URL <https://books.google.es/books?id=yHByCwAAQBAJ>.
- [4] E. P. Gross. Unified theory of interacting bosons. *Phys. Rev.*, 106:161–162, 1957. doi: 10.1103/PhysRev.106.161. URL <https://link.aps.org/doi/10.1103/PhysRev.106.161>.
- [5] G. V. Chester. Speculations on Bose-Einstein condensation and quantum crystals. *Phys. Rev. A*, 2:256–258, 1970. doi: 10.1103/PhysRevA.2.256. URL <https://link.aps.org/doi/10.1103/PhysRevA.2.256>.
- [6] A. F. Andreev and I. M. Lifshitz. Quantum theory of defects in crystals. *Soviet Physics Uspekhi*, 13(5):670–670, 1971. doi: 10.1070/pu1971v013n05abeh004235. URL <https://doi.org/10.1070%2Fpu1971v013n05abeh004235>.
- [7] M. Boninsegni and N. V. Prokof'ev. Colloquium: Supersolids: What and where are they? *Rev. Mod. Phys.*, 84:759–776, 2012. doi: 10.1103/RevModPhys.84.759. URL <https://link.aps.org/doi/10.1103/RevModPhys.84.759>.
- [8] S. Balibar. The enigma of supersolidity. *Nature*, 464(7286):176–182, 2010. doi: 10.1038/nature08913. URL <https://doi.org/10.1038/nature08913>.
- [9] H. Kadau, M. Schmitt, M. Wenzel, C. Wink, T. Maier, I. Ferrier-Barbut, and T. Pfau. Observing the Rosensweig instability of a quantum ferrofluid. *Nature*, 530(7589):194–197, 2016. doi: 10.1038/nature16485. URL <https://doi.org/10.1038/nature16485>.
- [10] L. Tanzi, E. Lucioni, F. Famà, J. Catani, A. Fioretti, C. Gabbanini, R. N. Bisset, L. Santos, and G. Modugno. Observation of a dipolar quantum gas

- with metastable supersolid properties. *Phys. Rev. Lett.*, 122:130405, 2019. doi: 10.1103/PhysRevLett.122.130405. URL <https://link.aps.org/doi/10.1103/PhysRevLett.122.130405>.
- [11] F. Böttcher, J.-N. Schmidt, M. Wenzel, J. Hertkorn, M. Guo, T. Langen, and T. Pfau. Transient supersolid properties in an array of dipolar quantum droplets. *Phys. Rev. X*, 9:011051, 2019. doi: 10.1103/PhysRevX.9.011051. URL <https://link.aps.org/doi/10.1103/PhysRevX.9.011051>.
- [12] L. Chomaz, D. Petter, P. Ilzhöfer, G. Natale, A. Trautmann, C. Politi, G. Durastante, R. M. W. van Bijnen, A. Patscheider, M. Sohmen, M. J. Mark, and F. Ferlaino. Long-lived and transient supersolid behaviors in dipolar quantum gases. *Phys. Rev. X*, 9:021012, 2019. doi: 10.1103/PhysRevX.9.021012. URL <https://link.aps.org/doi/10.1103/PhysRevX.9.021012>.
- [13] J. Léonard, A. Morales, P. Zupancic, T. Esslinger, and T. Donner. Supersolid formation in a quantum gas breaking a continuous translational symmetry. *Nature*, 543(7643):87–90, 2017. doi: 10.1038/nature21067. URL <https://doi.org/10.1038/nature21067>.
- [14] J. Li, J. Lee, W. Huang, S. Burchesky, B. Shteynas, F. Ç. Top, A. O. Jamison, and W. Ketterle. A stripe phase with supersolid properties in spin-orbit-coupled Bose-Einstein condensates. *Nature*, 543(7643):91–94, 2017. doi: 10.1038/nature21431. URL <https://doi.org/10.1038/nature21431>.
- [15] G. Biagioni, N. Antolini, A. Alaña, M. Modugno, A. Fioretti, C. Gabbanini, L. Tanzi, and G. Modugno. Dimensional crossover in the superfluid-supersolid quantum phase transition. *Phys. Rev. X*, 12:021019, Apr 2022. doi: 10.1103/PhysRevX.12.021019. URL <https://link.aps.org/doi/10.1103/PhysRevX.12.021019>.
- [16] N. Goldenfeld. *Lectures On Phase Transitions And The Renormalization Group*. CRC Press, 2018. URL <https://books.google.it/books?id=HQpQDwAAQBAJ>.
- [17] P. M. Chaikin and T. C. Lubensky. *Principles of Condensed Matter Physics*. Cambridge University Press, Cambridge, 1995.
- [18] W. Ketterle and M. W. Zwierlein. Making, probing and understanding ultracold Fermi gases. *La Rivista del Nuovo Cimento*, 31(5):247–422, May 2008. doi: 10.1393/ncr/i2008-10033-1. URL <https://doi.org/10.1393/ncr/i2008-10033-1>.
- [19] L. Tanzi, J. G. Maloberti, G. Biagioni, A. Fioretti, C. Gabbanini, and G. Modugno. Evidence of superfluidity in a dipolar supersolid from nonclassical rotational inertia. *Science*, 371(6534):1162–1165, 2021. doi: 10.1126/science.aba4309. URL <https://www.science.org/doi/abs/10.1126/science.aba4309>.
- [20] G. Biagioni. Evidence of superfluidity in a dipolar supersolid through non-classical rotational inertia, 2020. Master Thesis, University of Florence. Available at http://quantumgases.lens.unifi.it/theses/thesis_biagioni_master.pdf.

- [21] G. Biagioni. Evidence of superfluidity in a dipolar supersolid. *Il Nuovo Cimento C*, 44, 2021. doi: 10.1393/ncc/i2021-21107-5. URL <https://www.sif.it/riviste/sif/ncc/econtents/2021/044/04-05/article/1>.
- [22] G. Biagioni, N. Antolini, B. Donelli, L. Pezzé, A. Smerzi, M. Fattori, A. Fioretti, C. Gabbanini, M. Inguscio, L. Tanzi, and G. Modugno. Sub-unity superfluid fraction of a supersolid from self-induced Josephson effect, 2023. URL <https://doi.org/10.48550/arXiv.2311.04757>. Submitted to *Nature*.
- [23] P. Kapitza. Viscosity of liquid helium below the λ -point. *Nature*, 141(3558):74–74, 1938. doi: 10.1038/141074a0. URL <https://doi.org/10.1038/141074a0>.
- [24] J. F. Allen and A. D. Misener. Flow of liquid helium II. *Nature*, 141(3558):75–75, 1938. doi: 10.1038/141075a0. URL <https://doi.org/10.1038/141075a0>.
- [25] E. Kim and M. H. W. Chan. Probable observation of a supersolid helium phase. *Nature*, 427(6971):225–227, 2004. doi: 10.1038/nature02220. URL <https://doi.org/10.1038/nature02220>.
- [26] E. Kim and M. H. W. Chan. Observation of superflow in solid helium. *Science*, 305(5692):1941–1944, 2004. doi: 10.1126/science.1101501. URL <https://science.sciencemag.org/content/305/5692/1941>.
- [27] J. Day and J. Beamish. Low-temperature shear modulus changes in solid ^4He and connection to supersolidity. *Nature*, 450(7171):853–856, 2007. doi: 10.1038/nature06383. URL <https://doi.org/10.1038/nature06383>.
- [28] M. H. W. Chan, R. B. Hallock, and L. Reatto. Overview on solid ^4He and the issue of supersolidity. *Journal of Low Temperature Physics*, 172(5):317–363, 2013. doi: 10.1007/s10909-013-0882-x. URL <https://doi.org/10.1007/s10909-013-0882-x>.
- [29] D. Y. Kim and M. H. W. Chan. Absence of supersolidity in solid helium in porous vycor glass. *Phys. Rev. Lett.*, 109:155301, 2012. doi: 10.1103/PhysRevLett.109.155301. URL <https://link.aps.org/doi/10.1103/PhysRevLett.109.155301>.
- [30] T. Lahaye, C. Menotti, L. Santos, M. Lewenstein, and T. Pfau. The physics of dipolar bosonic quantum gases. *Reports on Progress in Physics*, 72(12):126401, 2009. doi: 10.1088/0034-4885/72/12/126401. URL <https://doi.org/10.1088/0034-4885/72/12/126401>.
- [31] L. Chomaz, I. Ferrier-Barbut, F. Ferlaino, B. Laburthe-Tolra, B. L. Lev, and T. Pfau. Dipolar physics: a review of experiments with magnetic quantum gases. *Reports on Progress in Physics*, 86(2):026401, dec 2022. doi: 10.1088/1361-6633/aca814. URL <https://dx.doi.org/10.1088/1361-6633/aca814>.
- [32] A. Campa, T. Dauxois, D. Fanelli, and S. Ruffo. *Physics of Long-range Interacting Systems*. Oxford University Press, 2014. URL https://books.google.it/books?id=AIw_BAAAQBAJ.

- [33] S. M. Roccuzzo, S. Stringari, and A. Recati. Supersolid edge and bulk phases of a dipolar quantum gas in a box. *Phys. Rev. Res.*, 4:013086, Feb 2022. doi: 10.1103/PhysRevResearch.4.013086. URL <https://link.aps.org/doi/10.1103/PhysRevResearch.4.013086>.
- [34] G. Bismut, B. Laburthe-Tolra, E. Maréchal, P. Pedri, O. Gorceix, and L. Vernac. Anisotropic excitation spectrum of a dipolar quantum Bose gas. *Phys. Rev. Lett.*, 109:155302, Oct 2012. doi: 10.1103/PhysRevLett.109.155302. URL <https://link.aps.org/doi/10.1103/PhysRevLett.109.155302>.
- [35] M. Wenzel, F. Böttcher, J.-N. Schmidt, M. Eisenmann, T. Langen, T. Pfau, and I. Ferrier-Barbut. Anisotropic superfluid behavior of a dipolar Bose-Einstein condensate. *Phys. Rev. Lett.*, 121:030401, Jul 2018. doi: 10.1103/PhysRevLett.121.030401. URL <https://link.aps.org/doi/10.1103/PhysRevLett.121.030401>.
- [36] L. Santos, G. V. Shlyapnikov, and M. Lewenstein. Roton-maxon spectrum and stability of trapped dipolar Bose-Einstein condensates. *Phys. Rev. Lett.*, 90:250403, 2003. doi: 10.1103/PhysRevLett.90.250403. URL <https://link.aps.org/doi/10.1103/PhysRevLett.90.250403>.
- [37] L. Chomaz, R. M. W. van Bijnen, D. Petter, G. Faraoni, S. Baier, J. H. Becher, M. J. Mark, F. Wächtler, L. Santos, and F. Ferlaino. Observation of roton mode population in a dipolar quantum gas. *Nature Physics*, 14(5):442–446, 2018. doi: 10.1038/s41567-018-0054-7. URL <https://doi.org/10.1038/s41567-018-0054-7>.
- [38] I. Ferrier-Barbut, H. Kadau, M. Schmitt, M. Wenzel, and T. Pfau. Observation of quantum droplets in a strongly dipolar Bose gas. *Phys. Rev. Lett.*, 116:215301, 2016. doi: 10.1103/PhysRevLett.116.215301. URL <https://link.aps.org/doi/10.1103/PhysRevLett.116.215301>.
- [39] M. Schmitt, M. Wenzel, F. Böttcher, I. Ferrier-Barbut, and T. Pfau. Self-bound droplets of a dilute magnetic quantum liquid. *Nature*, 539(7628):259–262, Nov 2016. doi: 10.1038/nature20126. URL <https://doi.org/10.1038/nature20126>.
- [40] L. Chomaz, S. Baier, D. Petter, M. J. Mark, F. Wächtler, L. Santos, and F. Ferlaino. Quantum-fluctuation-driven crossover from a dilute Bose-Einstein condensate to a macrodroplet in a dipolar quantum fluid. *Phys. Rev. X*, 6:041039, Nov 2016. doi: 10.1103/PhysRevX.6.041039. URL <https://link.aps.org/doi/10.1103/PhysRevX.6.041039>.
- [41] D. S. Petrov. Private communication.
- [42] A. R. P. Lima and A. Pelster. Beyond mean-field low-lying excitations of dipolar Bose gases. *Phys. Rev. A*, 86:063609, 2012. doi: 10.1103/PhysRevA.86.063609. URL <https://link.aps.org/doi/10.1103/PhysRevA.86.063609>.

- [43] G. Semeghini, G. Ferioli, L. Masi, C. Mazzinghi, L. Wolswijk, F. Minardi, M. Modugno, G. Modugno, M. Inguscio, and M. Fattori. Self-bound quantum droplets of atomic mixtures in free space. *Phys. Rev. Lett.*, 120:235301, 2018. doi: 10.1103/PhysRevLett.120.235301. URL <https://link.aps.org/doi/10.1103/PhysRevLett.120.235301>.
- [44] C. R. Cabrera, L. Tanzi, J. Sanz, B. Naylor, P. Thomas, P. Cheiney, and L. Tarruell. Quantum liquid droplets in a mixture of Bose-Einstein condensates. *Science*, 359(6373):301–304, 2018. doi: 10.1126/science.aa05686. URL <https://science.sciencemag.org/content/359/6373/301>.
- [45] L. Tanzi, S. M. Roccuzzo, E. Lucioni, F. Famà, A. Fioretti, C. Gabbanini, G. Modugno, A. Recati, and S. Stringari. Supersolid symmetry breaking from compressional oscillations in a dipolar quantum gas. *Nature*, 574(7778):382–385, 2019. doi: 10.1038/s41586-019-1568-6. URL <https://doi.org/10.1038/s41586-019-1568-6>.
- [46] M. Guo, F. Böttcher, J. Hertkorn, J.-N. Schmidt, M. Wenzel, H. P. Büchler, T. Langen, and T. Pfau. The low-energy Goldstone mode in a trapped dipolar supersolid. *Nature*, 574(7778):386–389, 2019. doi: 10.1038/s41586-019-1569-5. URL <https://doi.org/10.1038/s41586-019-1569-5>.
- [47] G. Natale, R. M. W. van Bijnen, A. Patscheider, D. Petter, M. J. Mark, L. Chomaz, and F. Ferlaino. Excitation spectrum of a trapped dipolar supersolid and its experimental evidence. *Phys. Rev. Lett.*, 123:050402, 2019. doi: 10.1103/PhysRevLett.123.050402. URL <https://link.aps.org/doi/10.1103/PhysRevLett.123.050402>.
- [48] T. Bland, E. Poli, C. Politi, L. Klaus, M. A. Norcia, F. Ferlaino, L. Santos, and R. N. Bisset. Two-dimensional supersolid formation in dipolar condensates. *Phys. Rev. Lett.*, 128:195302, May 2022. doi: 10.1103/PhysRevLett.128.195302. URL <https://link.aps.org/doi/10.1103/PhysRevLett.128.195302>.
- [49] Matthew A. Norcia, C. Politi, L. Klaus, E. Poli, M. Sohmen, M. J. Mark, R. N. Bisset, L. Santos, and F. Ferlaino. Two-dimensional supersolidity in a dipolar quantum gas. *Nature*, 596(7872):357–361, Aug 2021. doi: 10.1038/s41586-021-03725-7. URL <https://doi.org/10.1038/s41586-021-03725-7>.
- [50] M. Sohmen, C. Politi, L. Klaus, L. Chomaz, M. J. Mark, M. A. Norcia, and F. Ferlaino. Birth, life, and death of a dipolar supersolid. *Phys. Rev. Lett.*, 126:233401, Jun 2021. doi: 10.1103/PhysRevLett.126.233401. URL <https://link.aps.org/doi/10.1103/PhysRevLett.126.233401>.
- [51] F. Wächtler and L. Santos. Quantum filaments in dipolar Bose-Einstein condensates. *Phys. Rev. A*, 93:061603, Jun 2016. doi: 10.1103/PhysRevA.93.061603. URL <https://link.aps.org/doi/10.1103/PhysRevA.93.061603>.

- [52] D. S. Petrov. Quantum mechanical stabilization of a collapsing Bose-Bose mixture. *Phys. Rev. Lett.*, 115:155302, Oct 2015. doi: 10.1103/PhysRevLett.115.155302. URL <https://link.aps.org/doi/10.1103/PhysRevLett.115.155302>.
- [53] S. Ronen, D. C. E. Bortolotti, and J. L. Bohn. Bogoliubov modes of a dipolar condensate in a cylindrical trap. *Phys. Rev. A*, 74:013623, 2006. doi: 10.1103/PhysRevA.74.013623. URL <https://link.aps.org/doi/10.1103/PhysRevA.74.013623>.
- [54] F. Wächtler and L. Santos. Ground-state properties and elementary excitations of quantum droplets in dipolar Bose-Einstein condensates. *Phys. Rev. A*, 94:043618, 2016. doi: 10.1103/PhysRevA.94.043618. URL <https://link.aps.org/doi/10.1103/PhysRevA.94.043618>.
- [55] F. Böttcher, M. Wenzel, J.N. Schmidt, M. Guo, T. Langen, I. Ferrier-Barbut, T. Pfau, R. Bombín, J. Sánchez-Baena, J. Boronat, and F. Mazzanti. Dilute dipolar quantum droplets beyond the extended Gross-Pitaevskii equation. *Phys. Rev. Research*, 1:033088, 2019. doi: 10.1103/PhysRevResearch.1.033088. URL <https://link.aps.org/doi/10.1103/PhysRevResearch.1.033088>.
- [56] A. Alaña, N. Antolini, G. Biagioni, I. L. Egusquiza, and M. Modugno. Crossing the superfluid-supersolid transition of an elongated dipolar condensate. *Phys. Rev. A*, 106:043313, Oct 2022. doi: 10.1103/PhysRevA.106.043313. URL <https://link.aps.org/doi/10.1103/PhysRevA.106.043313>.
- [57] V. Galitski and I. B. Spielman. Spin-orbit coupling in quantum gases. *Nature*, 494 (7435):49–54, 2013. doi: 10.1038/nature11841. URL <https://doi.org/10.1038/nature11841>.
- [58] Y. Li, G. I. Martone, and S. Stringari. Spin-orbit-coupled Bose-Einstein condensates. *Annual Review of Cold Atoms and Molecules*, pages 201–250. doi: 10.1142/9789814667746_0005. URL https://www.worldscientific.com/doi/abs/10.1142/9789814667746_0005.
- [59] G. I. Martone, Y. Li, and S. Stringari. Approach for making visible and stable stripes in a spin-orbit-coupled Bose-Einstein superfluid. *Phys. Rev. A*, 90:041604, 2014. doi: 10.1103/PhysRevA.90.041604. URL <https://link.aps.org/doi/10.1103/PhysRevA.90.041604>.
- [60] G. I. Martone, T. Ozawa, C. Qu, and S. Stringari. Optical-lattice-assisted magnetic phase transition in a spin-orbit-coupled Bose-Einstein condensate. *Phys. Rev. A*, 94:043629, 2016. doi: 10.1103/PhysRevA.94.043629. URL <https://link.aps.org/doi/10.1103/PhysRevA.94.043629>.
- [61] A. Putra, F. Salces-Cárcoba, Y. Yue, S. Sugawa, and I. B. Spielman. Spatial coherence of spin-orbit-coupled Bose gases. *Phys. Rev. Lett.*, 124:053605,

2020. doi: 10.1103/PhysRevLett.124.053605. URL <https://link.aps.org/doi/10.1103/PhysRevLett.124.053605>.
- [62] K. T. Geier, G. I. Martone, P. Hauke, W. Ketterle, and S. Stringari. Dynamics of stripe patterns in supersolid spin-orbit-coupled Bose gases. *Phys. Rev. Lett.*, 130:156001, 2023. doi: 10.1103/PhysRevLett.130.156001. URL <https://link.aps.org/doi/10.1103/PhysRevLett.130.156001>.
- [63] K. Baumann, C. Guerlin, F. Brennecke, and T. Esslinger. Dicke quantum phase transition with a superfluid gas in an optical cavity. *Nature*, 464(7293):1301–1306, Apr 2010. doi: 10.1038/nature09009. URL <https://doi.org/10.1038/nature09009>.
- [64] H. Ritsch, P. Domokos, F. Brennecke, and T. Esslinger. Cold atoms in cavity-generated dynamical optical potentials. *Rev. Mod. Phys.*, 85:553–601, 2013. doi: 10.1103/RevModPhys.85.553. URL <https://link.aps.org/doi/10.1103/RevModPhys.85.553>.
- [65] J. Léonard, A. Morales, P. Zupancic, T. Donner, and T. Esslinger. Monitoring and manipulating Higgs and Goldstone modes in a supersolid quantum gas. *Science*, 358(6369):1415–1418, 2017. doi: 10.1126/science.aan2608. URL <https://www.science.org/doi/abs/10.1126/science.aan2608>.
- [66] Y. Guo, R. M. Kroeze, B. P. Marsh, S. Gopalakrishnan, J. Keeling, and B. L. Lev. An optical lattice with sound. *Nature*, 599(7884):211–215, Nov 2021. doi: 10.1038/s41586-021-03945-x. URL <https://doi.org/10.1038/s41586-021-03945-x>.
- [67] J. Nyéki, A. Phillis, A. Ho, D. Lee, P. Coleman, J. Parpia, B. Cowan, and J. Saunders. Intertwined superfluid and density wave order in two-dimensional ^4He . *Nature Physics*, 13(5):455–459, 2017. doi: 10.1038/nphys4023. URL <https://doi.org/10.1038/nphys4023>.
- [68] J. Choi, A. A. Zadorozhko, J. Choi, and E. Kim. Spatially modulated superfluid state in two-dimensional ^4He films. *Phys. Rev. Lett.*, 127:135301, Sep 2021. doi: 10.1103/PhysRevLett.127.135301. URL <https://link.aps.org/doi/10.1103/PhysRevLett.127.135301>.
- [69] L. V. Levitin, B. Yager, L. Sumner, B. Cowan, A. J. Casey, J. Saunders, N. Zhelev, R. G. Bennett, and J. M. Parpia. Evidence for a spatially modulated superfluid phase of ^3He under confinement. *Phys. Rev. Lett.*, 122:085301, Feb 2019. doi: 10.1103/PhysRevLett.122.085301. URL <https://link.aps.org/doi/10.1103/PhysRevLett.122.085301>.
- [70] A. J. Shook, V. Vadakkumbatt, P. Senarath Yapa, C. Doolin, R. Boyack, P. H. Kim, G. G. Popowich, F. Souris, H. Christani, J. Maciejko, and J. P. Davis. Stabilized pair density wave via nanoscale confinement of superfluid ^3He . *Phys. Rev. Lett.*, 124:015301, 2020. doi: 10.1103/PhysRevLett.124.015301. URL <https://link.aps.org/doi/10.1103/PhysRevLett.124.015301>.

- [71] A. B. Vorontsov and J. A. Sauls. Crystalline order in superfluid ^3He films. *Phys. Rev. Lett.*, 98:045301, Jan 2007. doi: 10.1103/PhysRevLett.98.045301. URL <https://link.aps.org/doi/10.1103/PhysRevLett.98.045301>.
- [72] M. H. Hamidian, S. D. Edkins, S. H. Joo, A. Kostin, H. Eisaki, S. Uchida, M. J. Lawler, E.-A. Kim, A. P. Mackenzie, K. Fujita, J. Lee, and J. C. S. Davis. Detection of a cooper-pair density wave in $\text{Bi}_2\text{Sr}_2\text{CaCu}_2\text{O}_{8+x}$. *Nature*, 532(7599):343–347, 2016. doi: 10.1038/nature17411. URL <https://doi.org/10.1038/nature17411>.
- [73] B. Keimer, S. A. Kivelson, M. R. Norman, S. Uchida, and J. Zaanen. From quantum matter to high-temperature superconductivity in copper oxides. *Nature*, 518(7538):179–186, Feb 2015. doi: 10.1038/nature14165. URL <https://doi.org/10.1038/nature14165>.
- [74] P. Raychaudhuri and S. Dutta. Phase fluctuations in conventional superconductors. *Journal of Physics: Condensed Matter*, 34(8):083001, 2021. doi: 10.1088/1361-648X/ac360b. URL <https://dx.doi.org/10.1088/1361-648X/ac360b>.
- [75] Z. Du, H. Li, S. H. Joo, E. P. Donoway, J. Lee, J. C. S. Davis, G. Gu, P. D. Johnson, and K. Fujita. Imaging the energy gap modulations of the cuprate pair-density-wave state. *Nature*, 580(7801):65–70, Apr 2020. doi: 10.1038/s41586-020-2143-x. URL <https://doi.org/10.1038/s41586-020-2143-x>.
- [76] Y. Liu, T. Wei, G. He, Y. Zhang, Z. Wang, and J. Wang. Pair density wave state in a monolayer high- T_c iron-based superconductor. *Nature*, 618(7967):934–939, 2023. doi: 10.1038/s41586-023-06072-x. URL <https://doi.org/10.1038/s41586-023-06072-x>.
- [77] Y. Liao, A. S. C. Rittner, T. Paprotta, W. Li, G. B. Partridge, R. G. Hulet, S. K. Baur, and E. J. Mueller. Spin-imbalance in a one-dimensional Fermi gas. *Nature*, 467(7315):567–569, Sep 2010. doi: 10.1038/nature09393. URL <https://doi.org/10.1038/nature09393>.
- [78] Y. J. Uemura, G. M. Luke, B. J. Sternlieb, J. H. Brewer, J. F. Carolan, W. N. Hardy, R. Kadono, J. R. Kempton, R. F. Kiefl, S. R. Kreitzman, P. Mulhern, T. M. Riseman, D. L. Williams, B. X. Yang, S. Uchida, H. Takagi, J. Gopalakrishnan, A. W. Sleight, M. A. Subramanian, C. L. Chien, M. Z. Cieplak, G. Xiao, V. Y. Lee, B. W. Statt, C. E. Stronach, W. J. Kossler, and X. H. Yu. Universal correlations between T_c and $\frac{n_s}{m^*}$ (carrier density over effective mass) in high- T_c cuprate superconductors. *Phys. Rev. Lett.*, 62:2317–2320, May 1989. doi: 10.1103/PhysRevLett.62.2317. URL <https://link.aps.org/doi/10.1103/PhysRevLett.62.2317>.
- [79] I. Božović, X. He, J. Wu, and A. T. Bollinger. Dependence of the critical temperature in overdoped copper oxides on superfluid density. *Nature*, 536(7616):309–311, Aug 2016. doi: 10.1038/nature19061. URL <https://doi.org/10.1038/nature19061>.

- [80] N. Chamel and P. Haensel. Physics of neutron star crusts. *Living Reviews in Relativity*, 11(1):10, Dec 2008. doi: 10.12942/lrr-2008-10. URL <https://doi.org/10.12942/lrr-2008-10>.
- [81] N. Martin and M. Urban. Superfluid hydrodynamics in the inner crust of neutron stars. *Phys. Rev. C*, 94:065801, Dec 2016. doi: 10.1103/PhysRevC.94.065801. URL <https://link.aps.org/doi/10.1103/PhysRevC.94.065801>.
- [82] G. Watanabe and C. J. Pethick. Superfluid density of neutrons in the inner crust of neutron stars: new life for pulsar glitch models. *Phys. Rev. Lett.*, 119:062701, Aug 2017. doi: 10.1103/PhysRevLett.119.062701. URL <https://link.aps.org/doi/10.1103/PhysRevLett.119.062701>.
- [83] E. Poli, T. Bland, S. J. M. White, M. J. Mark, F. Ferlaino, S. Trabucco, and M. Mannarelli. Glitches in rotating supersolids. *Phys. Rev. Lett.*, 131:223401, Nov 2023. doi: 10.1103/PhysRevLett.131.223401. URL <https://link.aps.org/doi/10.1103/PhysRevLett.131.223401>.
- [84] E. Lucioni, G. Masella, A. Fregosi, C. Gabbanini, S. Gozzini, A. Fioretti, L. Del Bino, J. Catani, G. Modugno, and M. Inguscio. A new setup for experiments with ultracold dysprosium atoms. *The European Physical Journal Special Topics*, 226(12):2775–2780, 2017. doi: 10.1140/epjst/e2016-60387-6. URL <https://doi.org/10.1140/epjst/e2016-60387-6>.
- [85] E. Lucioni, L. Tanzi, A. Fregosi, J. Catani, S. Gozzini, M. Inguscio, A. Fioretti, C. Gabbanini, and G. Modugno. Dysprosium dipolar Bose-Einstein condensate with broad Feshbach resonances. *Phys. Rev. A*, 97:060701, 2018. doi: 10.1103/PhysRevA.97.060701. URL <https://link.aps.org/doi/10.1103/PhysRevA.97.060701>.
- [86] T. Chalopin, T. Satoor, A. Evrard, V. Makhalov, J. Dalibard, R. Lopes, and S. Nascimbene. Probing chiral edge dynamics and bulk topology of a synthetic Hall system. *Nature Physics*, 16(10):1017–1021, Oct 2020. doi: 10.1038/s41567-020-0942-5. URL <https://doi.org/10.1038/s41567-020-0942-5>.
- [87] E. Lucioni, G. Masella, A. Fregosi, C. Gabbanini, S. Gozzini, A. Fioretti, L. Del Bino, J. Catani, G. Modugno, and M. Inguscio. A new setup for experiments with ultracold dysprosium atoms. *The European Physical Journal Special Topics*, 226(12):2775–2780, Jul 2017. doi: 10.1140/epjst/e2016-60387-6. URL <https://doi.org/10.1140/epjst/e2016-60387-6>.
- [88] W. Lunden, L. Du, M. Cantara, P. Barral, A. O. Jamison, and W. Ketterle. Enhancing the capture velocity of a Dy magneto-optical trap with two-stage slowing. *Phys. Rev. A*, 101:063403, Jun 2020. doi: 10.1103/PhysRevA.101.063403. URL <https://link.aps.org/doi/10.1103/PhysRevA.101.063403>.
- [89] E. Lucioni, L. Tanzi, A. Fregosi, J. Catani, S. Gozzini, M. Inguscio, A. Fioretti, C. Gabbanini, and G. Modugno. Dysprosium dipolar Bose-Einstein condensate

- with broad Feshbach resonances. *Phys. Rev. A*, 97:060701, Jun 2018. doi: 10.1103/PhysRevA.97.060701. URL <https://link.aps.org/doi/10.1103/PhysRevA.97.060701>.
- [90] Y. Castin and R. Dum. Bose-Einstein condensates in time dependent traps. *Phys. Rev. Lett.*, 77:5315–5319, Dec 1996. doi: 10.1103/PhysRevLett.77.5315. URL <https://link.aps.org/doi/10.1103/PhysRevLett.77.5315>.
- [91] A. Burchianti, C. D’Errico, L. Marconi, F. Minardi, C. Fort, and M. Modugno. Effect of interactions in the interference pattern of Bose-Einstein condensates. *Phys. Rev. A*, 102:043314, Oct 2020. doi: 10.1103/PhysRevA.102.043314. URL <https://link.aps.org/doi/10.1103/PhysRevA.102.043314>.
- [92] J. Stuhler, A. Griesmaier, T. Koch, M. Fattori, T. Pfau, S. Giovanazzi, P. Pedri, and L. Santos. Observation of dipole-dipole interaction in a degenerate quantum gas. *Phys. Rev. Lett.*, 95:150406, 2005. doi: 10.1103/PhysRevLett.95.150406. URL <https://link.aps.org/doi/10.1103/PhysRevLett.95.150406>.
- [93] G. Yang, J. Guo, and S. Zhang. Influence of the dipole–dipole interaction on the interference between Bose–Einstein condensates. *International Journal of Modern Physics B*, 33(07):1950048, 2019. doi: 10.1142/S0217979219500486. URL <https://doi.org/10.1142/S0217979219500486>.
- [94] C. C. Bradley, C. A. Sackett, and R. G. Hulet. Bose-Einstein condensation of lithium: observation of limited condensate number. *Phys. Rev. Lett.*, 78:985–989, Feb 1997. doi: 10.1103/PhysRevLett.78.985. URL <https://link.aps.org/doi/10.1103/PhysRevLett.78.985>.
- [95] J. Sánchez-Baena, C. Politi, F. Maucher, F. Ferlaino, and T. Pohl. Heating a dipolar quantum fluid into a solid. *Nature Communications*, 14(1):1868, Apr 2023. doi: 10.1038/s41467-023-37207-3. URL <https://doi.org/10.1038/s41467-023-37207-3>.
- [96] S. Sachdev. Quantum phase transitions. *Physics World*, 12(4):33, 1999. doi: 10.1088/2058-7058/12/4/23. URL <https://dx.doi.org/10.1088/2058-7058/12/4/23>.
- [97] A. del Campo and W. H. Zurek. Universality of phase transition dynamics: Topological defects from symmetry breaking. *International Journal of Modern Physics A*, 29(08):1430018, 2014. doi: 10.1142/S0217751X1430018X. URL <https://doi.org/10.1142/S0217751X1430018X>.
- [98] N. Sepúlveda, C. Josserand, and S. Rica. Superfluid density in a two-dimensional model of supersolid. *The European Physical Journal B*, 78(4):439–447, 2010. doi: 10.1140/epjb/e2010-10176-y. URL <https://doi.org/10.1140/epjb/e2010-10176-y>.
- [99] Y. Zhang, F. Maucher, and T. Pohl. Supersolidity around a critical point in dipolar Bose-Einstein condensates. *Phys. Rev. Lett.*, 123:015301, Jul 2019. doi: 10.1103/PhysRevLett.123.015301. URL <https://link.aps.org/doi/10.1103/PhysRevLett.123.015301>.

- [100] T. Macrì, F. Maucher, F. Cinti, and T. Pohl. Elementary excitations of ultracold soft-core bosons across the superfluid-supersolid phase transition. *Phys. Rev. A*, 87:061602, Jun 2013. doi: 10.1103/PhysRevA.87.061602. URL <https://link.aps.org/doi/10.1103/PhysRevA.87.061602>.
- [101] N. Sepúlveda, C. Josserand, and S. Rica. Nonclassical rotational inertia fraction in a one-dimensional model of a supersolid. *Phys. Rev. B*, 77:054513, Feb 2008. doi: 10.1103/PhysRevB.77.054513. URL <https://link.aps.org/doi/10.1103/PhysRevB.77.054513>.
- [102] S. M. Roccuzzo and F. Ancilotto. Supersolid behavior of a dipolar Bose-Einstein condensate confined in a tube. *Phys. Rev. A*, 99:041601, Apr 2019. doi: 10.1103/PhysRevA.99.041601. URL <https://link.aps.org/doi/10.1103/PhysRevA.99.041601>.
- [103] P. B. Blakie, D. Baillie, L. Chomaz, and F. Ferlaino. Supersolidity in an elongated dipolar condensate. *Phys. Rev. Res.*, 2:043318, Dec 2020. doi: 10.1103/PhysRevResearch.2.043318. URL <https://link.aps.org/doi/10.1103/PhysRevResearch.2.043318>.
- [104] J. Hertkorn, J.-N. Schmidt, M. Guo, F. Böttcher, K. S. H. Ng, S. D. Graham, P. Uerlings, T. Langen, M. Zwierlein, and T. Pfau. Pattern formation in quantum ferrofluids: from supersolids to superglasses. *Phys. Rev. Res.*, 3:033125, 2021. doi: 10.1103/PhysRevResearch.3.033125. URL <https://link.aps.org/doi/10.1103/PhysRevResearch.3.033125>.
- [105] Y. Zhang, T. Pohl, and F. Maucher. Phases of supersolids in confined dipolar Bose-Einstein condensates. *Phys. Rev. A*, 104:013310, Jul 2021. doi: 10.1103/PhysRevA.104.013310. URL <https://link.aps.org/doi/10.1103/PhysRevA.104.013310>.
- [106] J. Hertkorn, J.-N. Schmidt, M. Guo, F. Böttcher, K. S. H. Ng, S. D. Graham, P. Uerlings, H. P. Büchler, T. Langen, M. Zwierlein, and T. Pfau. Supersolidity in two-dimensional trapped dipolar droplet arrays. *Phys. Rev. Lett.*, 127:155301, Oct 2021. doi: 10.1103/PhysRevLett.127.155301. URL <https://link.aps.org/doi/10.1103/PhysRevLett.127.155301>.
- [107] D. Petter, A. Patscheider, G. Natale, M. J. Mark, M. A. Baranov, R. van Bijnen, S. M. Roccuzzo, A. Recati, B. Blakie, D. Baillie, L. Chomaz, and F. Ferlaino. Bragg scattering of an ultracold dipolar gas across the phase transition from Bose-Einstein condensate to supersolid in the free-particle regime. *Phys. Rev. A*, 104:L011302, Jul 2021. doi: 10.1103/PhysRevA.104.L011302. URL <https://link.aps.org/doi/10.1103/PhysRevA.104.L011302>.
- [108] J. Hertkorn, J.-N. Schmidt, F. Böttcher, M. Guo, M. Schmidt, K. S. H. Ng, S. D. Graham, H. P. Büchler, T. Langen, M. Zwierlein, and T. Pfau. Density fluctuations across the superfluid-supersolid phase transition in a dipolar quantum gas. *Phys.*

- Rev. X*, 11:011037, Feb 2021. doi: 10.1103/PhysRevX.11.011037. URL <https://link.aps.org/doi/10.1103/PhysRevX.11.011037>.
- [109] L.D. Landau and E.M. Lifshitz. *Statistical Physics Part One*. Pergamon Press, 1980.
- [110] Y. Imry. Finite-size rounding of a first-order phase transition. *Phys. Rev. B*, 21:2042–2043, Mar 1980. doi: 10.1103/PhysRevB.21.2042. URL <https://link.aps.org/doi/10.1103/PhysRevB.21.2042>.
- [111] G. B. Hess and W. M. Fairbank. Measurements of angular momentum in superfluid helium. *Phys. Rev. Lett.*, 19:216–218, 1967. doi: 10.1103/PhysRevLett.19.216. URL <https://link.aps.org/doi/10.1103/PhysRevLett.19.216>.
- [112] Olli V. Lounasmaa and Erkki Thuneberg. Vortices in rotating superfluid ^3He . *Proceedings of the National Academy of Sciences*, 96(14):7760–7767, 1999. doi: 10.1073/pnas.96.14.7760. URL <https://www.pnas.org/content/96/14/7760>.
- [113] F. Chevy, K. W. Madison, and J. Dalibard. Measurement of the angular momentum of a rotating Bose-Einstein condensate. *Phys. Rev. Lett.*, 85:2223–2227, 2000. doi: 10.1103/PhysRevLett.85.2223. URL <https://link.aps.org/doi/10.1103/PhysRevLett.85.2223>.
- [114] M. W. Zwierlein, J. R. Abo-Shaeer, A. Schirotzek, C. H. Schunck, and W. Ketterle. Vortices and superfluidity in a strongly interacting Fermi gas. *Nature*, 435(7045):1047–1051, 2005. doi: 10.1038/nature03858. URL <https://doi.org/10.1038/nature03858>.
- [115] O. M. Maragò, S. A. Hopkins, J. Arlt, E. Hodby, G. Hechenblaikner, and C. J. Foot. Observation of the scissors mode and evidence for superfluidity of a trapped Bose-Einstein condensed gas. *Phys. Rev. Lett.*, 84:2056–2059, Mar 2000. doi: 10.1103/PhysRevLett.84.2056. URL <https://link.aps.org/doi/10.1103/PhysRevLett.84.2056>.
- [116] O. Maragò, G. Hechenblaikner, E. Hodby, and C. Foot. Temperature dependence of damping and frequency shifts of the scissors mode of a trapped Bose-Einstein condensate. *Phys. Rev. Lett.*, 86:3938–3941, Apr 2001. doi: 10.1103/PhysRevLett.86.3938. URL <https://link.aps.org/doi/10.1103/PhysRevLett.86.3938>.
- [117] A. J. Leggett. On the superfluid fraction of an arbitrary many-body system at $T=0$. *Journal of Statistical Physics*, 93(3):927–941, 1998. doi: 10.1023/B:JOSS.0000033170.38619.6c. URL <https://doi.org/10.1023/B:JOSS.0000033170.38619.6c>.
- [118] G. E. Astrakharchik, J. Boronat, J. Casulleras, and S. Giorgini. Superfluidity versus Bose-Einstein condensation in a Bose gas with disorder. *Phys. Rev. A*, 66:023603, Aug 2002. doi: 10.1103/PhysRevA.66.023603. URL <https://link.aps.org/doi/10.1103/PhysRevA.66.023603>.

- [119] G. Chauveau, C. Maury, F. Rabec, C. Heintze, G. Brochier, S. Nascimbene, J. Dalibard, J. Beugnon, S. M. Roccuzzo, and S. Stringari. Superfluid fraction in an interacting spatially modulated Bose-Einstein condensate. *Phys. Rev. Lett.*, 130:226003, Jun 2023. doi: 10.1103/PhysRevLett.130.226003. URL <https://link.aps.org/doi/10.1103/PhysRevLett.130.226003>.
- [120] I. Zapata, F. Sols, and A. J. Leggett. Josephson effect between trapped Bose-Einstein condensates. *Phys. Rev. A*, 57:R28–R31, Jan 1998. doi: 10.1103/PhysRevA.57.R28. URL <https://link.aps.org/doi/10.1103/PhysRevA.57.R28>.
- [121] N. Lo Iudice and F. Palumbo. New isovector collective modes in deformed nuclei. *Phys. Rev. Lett.*, 41:1532–1534, Nov 1978. doi: 10.1103/PhysRevLett.41.1532. URL <https://link.aps.org/doi/10.1103/PhysRevLett.41.1532>.
- [122] M. J. Wright, S. Riedl, A. Altmeyer, C. Kohstall, E. R. Sánchez Guajardo, J. Hecker Denschlag, and R. Grimm. Finite-temperature collective dynamics of a Fermi gas in the BEC-BCS crossover. *Phys. Rev. Lett.*, 99:150403, Oct 2007. doi: 10.1103/PhysRevLett.99.150403. URL <https://link.aps.org/doi/10.1103/PhysRevLett.99.150403>.
- [123] I. Ferrier-Barbut, M. Wenzel, F. Böttcher, T. Langen, M. Isoard, S. Stringari, and T. Pfau. Scissors mode of dipolar quantum droplets of dysprosium atoms. *Phys. Rev. Lett.*, 120:160402, 2018. doi: 10.1103/PhysRevLett.120.160402. URL <https://link.aps.org/doi/10.1103/PhysRevLett.120.160402>.
- [124] D. Guéry-Odelin and S. Stringari. Scissors mode and superfluidity of a trapped Bose-Einstein condensed gas. *Phys. Rev. Lett.*, 83:4452–4455, Nov 1999. doi: 10.1103/PhysRevLett.83.4452. URL <https://link.aps.org/doi/10.1103/PhysRevLett.83.4452>.
- [125] F. Zambelli and S. Stringari. Moment of inertia and quadrupole response function of a trapped superfluid. *Phys. Rev. A*, 63:033602, Feb 2001. doi: 10.1103/PhysRevA.63.033602. URL <https://link.aps.org/doi/10.1103/PhysRevA.63.033602>.
- [126] M. A. Norcia, E. Poli, C. Politi, L. Klaus, T. Bland, M. J. Mark, L. Santos, R. N. Bisset, and F. Ferlino. Can angular oscillations probe superfluidity in dipolar supersolids? *Phys. Rev. Lett.*, 129:040403, Jul 2022. doi: 10.1103/PhysRevLett.129.040403. URL <https://link.aps.org/doi/10.1103/PhysRevLett.129.040403>.
- [127] R. M. W. van Bijnen, N. G. Parker, S. J. J. M. F. Kokkelmans, A. M. Martin, and D. H. J. O’Dell. Collective excitation frequencies and stationary states of trapped dipolar Bose-Einstein condensates in the Thomas-Fermi regime. *Phys. Rev. A*, 82:033612, Sep 2010. doi: 10.1103/PhysRevA.82.033612. URL <https://link.aps.org/doi/10.1103/PhysRevA.82.033612>.

- [128] S. M. Roccuzzo, A. Gallemí, A. Recati, and S. Stringari. Rotating a supersolid dipolar gas. *Phys. Rev. Lett.*, 124:045702, 2020. doi: 10.1103/PhysRevLett.124.045702. URL <https://link.aps.org/doi/10.1103/PhysRevLett.124.045702>.
- [129] S. M. Roccuzzo, A. Recati, and S. Stringari. Moment of inertia and dynamical rotational response of a supersolid dipolar gas. *Phys. Rev. A*, 105:023316, Feb 2022. doi: 10.1103/PhysRevA.105.023316. URL <https://link.aps.org/doi/10.1103/PhysRevA.105.023316>.
- [130] M. Modugno, G. Modugno, G. Roati, C. Fort, and M. Inguscio. Scissors mode of an expanding Bose-Einstein condensate. *Phys. Rev. A*, 67:023608, Feb 2003. doi: 10.1103/PhysRevA.67.023608. URL <https://link.aps.org/doi/10.1103/PhysRevA.67.023608>.
- [131] A. Smerzi, S. Fantoni, S. Giovanazzi, and S. R. Shenoy. Quantum coherent atomic tunneling between two trapped Bose-Einstein condensates. *Phys. Rev. Lett.*, 79:4950–4953, 1997. doi: 10.1103/PhysRevLett.79.4950. URL <https://link.aps.org/doi/10.1103/PhysRevLett.79.4950>.
- [132] M. Albiez, R. Gati, J. Fölling, S. Hunsmann, M. Cristiani, and M. K. Oberthaler. Direct observation of tunneling and nonlinear self-trapping in a single bosonic Josephson junction. *Phys. Rev. Lett.*, 95:010402, 2005. doi: 10.1103/PhysRevLett.95.010402. URL <https://link.aps.org/doi/10.1103/PhysRevLett.95.010402>.
- [133] G. Spagnolli, G. Semeghini, L. Masi, G. Ferioli, A. Trenkwalder, S. Coop, M. Landini, L. Pezzè, G. Modugno, M. Inguscio, A. Smerzi, and M. Fattori. Crossing over from attractive to repulsive interactions in a tunneling bosonic Josephson junction. *Phys. Rev. Lett.*, 118:230403, 2017. doi: 10.1103/PhysRevLett.118.230403. URL <https://link.aps.org/doi/10.1103/PhysRevLett.118.230403>.
- [134] S. Levy, E. Lahoud, I. Shomroni, and J. Steinhauer. The a.c. and d.c. Josephson effects in a Bose-Einstein condensate. *Nature*, 449(7162):579–583, 2007. doi: 10.1038/nature06186. URL <https://doi.org/10.1038/nature06186>.
- [135] G. Valtolina, A. Burchianti, A. Amico, E. Neri, K. Khani, J. A. Seman, A. Trombettoni, A. Smerzi, M. Zaccanti, M. Inguscio, and G. Roati. Josephson effect in fermionic superfluids across the BEC-BCS crossover. *Science*, 350(6267):1505–1508, 2015. doi: 10.1126/science.aac9725. URL <https://www.science.org/doi/abs/10.1126/science.aac9725>.
- [136] B.D. Josephson. Possible new effects in superconductive tunnelling. *Physics Letters*, 1(7):251 – 253, 1962. doi: [https://doi.org/10.1016/0031-9163\(62\)91369-0](https://doi.org/10.1016/0031-9163(62)91369-0). URL <http://www.sciencedirect.com/science/article/pii/0031916362913690>.
- [137] P. Ilzhöfer, M. Sohmen, G. Durastante, C. Politi, A. Trautmann, G. Natale, G. Morpurgo, T. Giamarchi, L. Chomaz, M. J. Mark, and F. Ferlaino. Phase

- coherence in out-of-equilibrium supersolid states of ultracold dipolar atoms. *Nature Physics*, 17(3):356–361, Mar 2021. doi: 10.1038/s41567-020-01100-3. URL <https://doi.org/10.1038/s41567-020-01100-3>.
- [138] S. Raghavan, A. Smerzi, S. Fantoni, and S. R. Shenoy. Coherent oscillations between two weakly coupled Bose-Einstein condensates: Josephson effects, π oscillations, and macroscopic quantum self-trapping. *Phys. Rev. A*, 59:620–633, 1999. doi: 10.1103/PhysRevA.59.620. URL <https://link.aps.org/doi/10.1103/PhysRevA.59.620>.
- [139] M. N. Tengstrand, D. Boholm, R. Sachdeva, J. Bengtsson, and S. M. Reimann. Persistent currents in toroidal dipolar supersolids. *Phys. Rev. A*, 103:013313, 2021. doi: 10.1103/PhysRevA.103.013313. URL <https://link.aps.org/doi/10.1103/PhysRevA.103.013313>.
- [140] A. Gallemí, S. M. Roccuzzo, S. Stringari, and A. Recati. Quantized vortices in dipolar supersolid Bose-Einstein-condensed gases. *Phys. Rev. A*, 102:023322, 2020. doi: 10.1103/PhysRevA.102.023322. URL <https://link.aps.org/doi/10.1103/PhysRevA.102.023322>.
- [141] F. Ancilotto, M. Barranco, M. Pi, and L. Reatto. Vortex properties in the extended supersolid phase of dipolar Bose-Einstein condensates. *Phys. Rev. A*, 103:033314, 2021. doi: 10.1103/PhysRevA.103.033314. URL <https://link.aps.org/doi/10.1103/PhysRevA.103.033314>.
- [142] L. Pezzè, A. Smerzi, M. K. Oberthaler, R. Schmied, and P. Treutlein. Quantum metrology with nonclassical states of atomic ensembles. *Rev. Mod. Phys.*, 90:035005, Sep 2018. doi: 10.1103/RevModPhys.90.035005. URL <https://link.aps.org/doi/10.1103/RevModPhys.90.035005>.
- [143] L. Pitaevskii and S. Stringari. Thermal vs quantum decoherence in double well trapped Bose-Einstein condensates. *Phys. Rev. Lett.*, 87:180402, Oct 2001. doi: 10.1103/PhysRevLett.87.180402. URL <https://link.aps.org/doi/10.1103/PhysRevLett.87.180402>.
- [144] B. Gati, R. and Hemmerling, J. Fölling, M. Albiez, and M. K. Oberthaler. Noise thermometry with two weakly coupled Bose-Einstein condensates. *Phys. Rev. Lett.*, 96:130404, Apr 2006. doi: 10.1103/PhysRevLett.96.130404. URL <https://link.aps.org/doi/10.1103/PhysRevLett.96.130404>.
- [145] L. Corman, L. Chomaz, T. Bienaimé, R. Desbuquois, C. Weitenberg, S. Nascimbène, J. Dalibard, and J. Beugnon. Quench-induced supercurrents in an annular Bose gas. *Phys. Rev. Lett.*, 113:135302, Sep 2014. doi: 10.1103/PhysRevLett.113.135302. URL <https://link.aps.org/doi/10.1103/PhysRevLett.113.135302>.
- [146] M. Šindik, T. Zawiślak, A. Recati, and S. Stringari. Sound, superfluidity and layer compressibility in a ring dipolar supersolid, 2023.

- [147] N. Preti, N. Antolini, G. Biagioni, A. Fioretti, G. Modugno, L. Tanzi, and C. Gabbanini. Blue light repulsive potentials for dysprosium atoms, 2023. in preparation.
- [148] G. Del Pace. Tunneling transport in strongly-interacting atomic Fermi gases, 2023. PhD Thesis, University of Florence. https://quantumgases.lens.unifi.it/theses/thesis_delpace_phd.pdf.
- [149] N. Preti. Towards dipolar quantum gases in a ring, 2023. Master Thesis, University of Florence.
- [150] M. E. Wickliffe, J. E. Lawler, and G. Nave. Atomic transition probabilities for Dy I and Dy II. *Journal of Quantitative Spectroscopy and Radiative Transfer*, 66(4):363–404, 2000. doi: [https://doi.org/10.1016/S0022-4073\(99\)00173-9](https://doi.org/10.1016/S0022-4073(99)00173-9). URL <https://www.sciencedirect.com/science/article/pii/S0022407399001739>.
- [151] Z. Chen, B. Seo, M. Huang, M. K. Parit, P. Chen, and G. B. Jo. Active control of a diode laser with injection locking, 2021. <https://doi.org/10.48550/arXiv.2105.11285>.
- [152] R. Grimm, M. Weidemüller, and Y. B. Ovchinnikov. Optical dipole traps for neutral atoms. *Advances In Atomic, Molecular, and Optical Physics*, pages 95–170. Academic Press, 2000. doi: [https://doi.org/10.1016/S1049-250X\(08\)60186-X](https://doi.org/10.1016/S1049-250X(08)60186-X). URL <https://www.sciencedirect.com/science/article/pii/S1049250X0860186X>.
- [153] M. Kreyer, J. H. Han, C. Ravensbergen, V. Corre, E. Soave, E. Kirilov, and R. Grimm. Measurement of the dynamic polarizability of Dy atoms near the 626-nm intercombination line. *Phys. Rev. A*, 104:033106, Sep 2021. doi: 10.1103/PhysRevA.104.033106. URL <https://link.aps.org/doi/10.1103/PhysRevA.104.033106>.
- [154] C. Ravensbergen, V. Corre, E. Soave, M. Kreyer, S. Tzanova, E. Kirilov, and R. Grimm. Accurate determination of the dynamical polarizability of dysprosium. *Phys. Rev. Lett.*, 120:223001, May 2018. doi: 10.1103/PhysRevLett.120.223001. URL <https://link.aps.org/doi/10.1103/PhysRevLett.120.223001>.
- [155] W. Kao, Y. Tang, N. Q. Burdick, and B. L. Lev. Anisotropic dependence of tune-out wavelength near dy 741-nm transition. *Opt. Express*, 25(4):3411–3419, Feb 2017. doi: 10.1364/OE.25.003411. URL <https://opg.optica.org/oe/abstract.cfm?URI=oe-25-4-3411>.
- [156] L. Du, P. Barral, M. Cantara, J. de Hond, Y.-K. Lu, and W. Ketterle. Atomic physics on a 50 nm scale: realization of a bilayer system of dipolar atoms, 2023. <https://arxiv.org/abs/2302.07209>.
- [157] V. A. Dzuba, V. V. Flambaum, and Benjamin L. Lev. Dynamic polarizabilities and magic wavelengths for dysprosium. *Phys. Rev. A*, 83:032502, Mar 2011. doi: 10.1103/PhysRevA.83.032502. URL <https://link.aps.org/doi/10.1103/PhysRevA.83.032502>.

- [158] H. Li, J. F. Wyart, O. Dulieu, S. Nascimbene, and M. Lepers. Optical trapping of ultracold dysprosium atoms: transition probabilities, dynamic dipole polarizabilities and van der Waals C_6 coefficients. *Journal of Physics B: Atomic, Molecular and Optical Physics*, 50(1):014005, 2016.
- [159] C. Ryu, M. F. Andersen, P. Cladé, Vasant Natarajan, K. Helmerson, and W. D. Phillips. Observation of persistent flow of a Bose-Einstein condensate in a toroidal trap. *Phys. Rev. Lett.*, 99:260401, Dec 2007. doi: 10.1103/PhysRevLett.99.260401. URL <https://link.aps.org/doi/10.1103/PhysRevLett.99.260401>.
- [160] S. Moulder, S. Beattie, R. P. Smith, N. Tammuz, and Z. Hadzibabic. Quantized supercurrent decay in an annular Bose-Einstein condensate. *Phys. Rev. A*, 86:013629, Jul 2012. doi: 10.1103/PhysRevA.86.013629. URL <https://link.aps.org/doi/10.1103/PhysRevA.86.013629>.
- [161] G. Del Pace, K. Khani, A. Muzi Falconi, M. Fedrizzi, N. Grani, D. Hernandez Rajkov, M. Inguscio, F. Scazza, W. J. Kwon, and G. Roati. Imprinting persistent currents in tunable fermionic rings. *Phys. Rev. X*, 12:041037, Dec 2022. doi: 10.1103/PhysRevX.12.041037. URL <https://link.aps.org/doi/10.1103/PhysRevX.12.041037>.
- [162] Y. Cai, D. G. Allman, P. Sabharwal, and K. C. Wright. Persistent currents in rings of ultracold Fermionic atoms. *Phys. Rev. Lett.*, 128:150401, Apr 2022. doi: 10.1103/PhysRevLett.128.150401. URL <https://link.aps.org/doi/10.1103/PhysRevLett.128.150401>.
- [163] X.-Y. Luo, Y.-Q. Zou, L.-N. Wu, Q. Liu, M.-F. Han, M. K. Tey, and L. You. Deterministic entanglement generation from driving through quantum phase transitions. *Science*, 355(6325):620–623, 2017. doi: 10.1126/science.aag1106. URL <https://www.science.org/doi/abs/10.1126/science.aag1106>.
- [164] J. Estève, C. Gross, A. Weller, S. Giovanazzi, and M. K. Oberthaler. Squeezing and entanglement in a Bose-Einstein condensate. *Nature*, 455(7217):1216–1219, Oct 2008. doi: 10.1038/nature07332. URL <https://doi.org/10.1038/nature07332>.
- [165] T. Berrada, S. van Frank, R. Bücke, T. Schumm, J.-F. Schaff, and J. Schmiedmayer. Integrated Mach-Zehnder interferometer for Bose-Einstein condensates. *Nature Communications*, 4(1):2077, Jun 2013. doi: 10.1038/ncomms3077. URL <https://doi.org/10.1038/ncomms3077>.